

University of Warwick institutional repository: <http://go.warwick.ac.uk/wrap>

A Thesis Submitted for the Degree of PhD at the University of Warwick

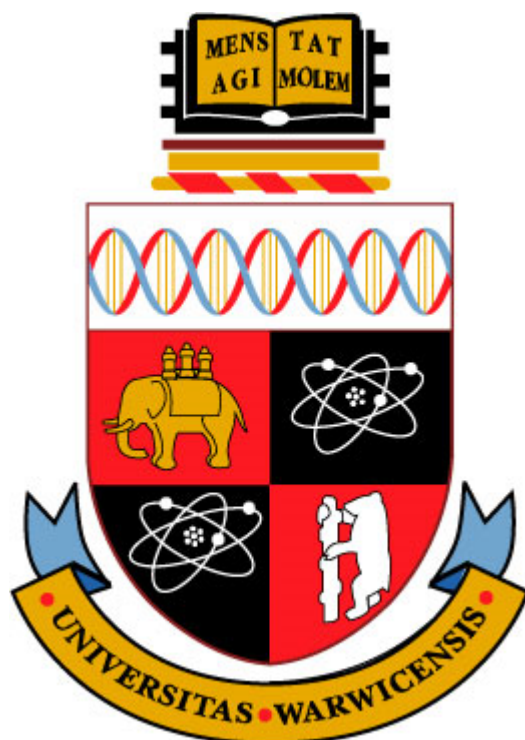
<http://go.warwick.ac.uk/wrap/60381>

This thesis is made available online and is protected by original copyright.

Please scroll down to view the document itself.

Please refer to the repository record for this item for information to help you to cite it. Our policy information is available from the repository home page.

Application of Analytical Techniques for the Study of Metal-based Anticancer Complexes



**A Thesis Submitted for the Degree of
Doctor of Philosophy**

Ruth J. McQuitty, BSc. MSc.

Supervisor: Prof. Peter J Sadler, FRS

University of Warwick, Department of Chemistry

September 2013

This thesis is dedicated in loving memory of Wilhemina.

Contents

Contents	I
Acknowledgements	IX
Declaration and publication list	XII
Abstract	XIV
Abbreviations	XVII
Chapter 1 Introduction	1
1.1 Metals in medicine	2
1.1.1 Antimicrobial agents	2
1.1.2 Gold antiarthritic drugs	4
1.1.3 Bismuth antiulcer drugs	5
1.1.4 Metal-based insulin mimics	6
1.1.5 Vasodilators	8
1.1.6 MRI contrast agents	8
1.2 Platinum-based drugs	9
1.2.1 Cisplatin	9
1.2.1.1 Mechanism of action	10
1.2.1.2 Cellular accumulation	12
1.2.1.3 Mechanism of resistance	13
1.2.2 New generation platinum-based drugs	14
1.2.2.1 Trans platinum(II) complexes	18
1.2.2.2. Delivery strategies of platinum complexes	19
	I

1.2.1.2. Photoactivation of platinum complexes	22
1.3 Photodynamic therapy	24
1.3.1 Light delivery: photonic crystal fibres (PCFs)	26
1.4 Organometallic drugs	28
1.4.1 Ruthenium complexes	28
1.4.1 Osmium and iridium complexes	30
1.5 Analytical techniques for the study of metal-based drugs	31
1.5.1 UV-Visible spectroscopy	32
1.5.2 High performance liquid chromatography (HPLC)	33
1.5.3 Mass spectrometry	35
1.6 References	40
Chapter 2 The interaction of photoactivatable Pt(IV) complexes with single strand oligonucleotides	50
2.1 Introduction	51
2.1.1 Platinum-based anticancer drugs	51
2.2.1 Platinum-based anticancer drugs and their interaction with DNA	52
2.2 Experimental	54

2.1.1 Materials	54
2.2.2 Methods	55
2.2.2.1 Cell culture	55
2.2.2.2 Platinum accumulation in A2780 human ovarian carcinoma cells	55
2.2.2.3 Inductively coupled plasma mass spectrometry (ICP-MS) instrumentation and calibrations	56
2.2.2.4 UV-Vis spectroscopy	57
2.2.2.5 Light sources	57
2.2.2.6 Chromatography	57
2.2.2.7 Mass spectrometry	59
2.3 Results	60
2.3.1 Correlation between lipophilicity and cellular accumulation of platinum complexes	61
2.3.1.1 Lipophilicity	61
2.3.1.2 Platinum accumulation in A2780 cells	63
2.3.2 Study of photoactivatable Pt(IV) diazido complex interaction with oligonucleotides by chromatography	67
2.3.2.1 Interaction of t,t,t -[Pt(N ₃) ₂ (OH) ₂ (py) ₂] with oligonucleotide d'(ATACATGCTACATA)	68
2.3.2.2 Sequence selectivity of Pt(IV) diazido complex oligonucleotide binding	72

2.3.2.3 Wavelength of activation of Pt(IV) diazido complexes	77
2.3.3 Photoactivatable Pt(IV) diazido complex interaction with an oligonucleotide by mass spectrometry	79
2.3.3.1 Interaction of <i>trans,trans,trans</i> -[Pt(N ₃) ₂ (OH) ₂ (py) ₂] and oligo 1	79
2.3.3.2 Platinum oligonucleotide interaction by mass spectrometry – ¹⁵ N labelled complexes	84
2.4 Discussion	87
2.4.1 Lipophilicity	87
2.4.2 Platinum accumulation in A2780 cells	92
2.4.3 Study of photoactivatable Pt(IV) diazido complex interaction with oligonucleotides by chromatography	97
2.4.4 Sequence selectivity of Pt(IV) diazido complex oligonucleotide binding	98
2.4.5 The effects of altering the wavelength of activation on the binding of Pt(IV) diazido complexes to a series of oligonucleotides	101
2.4.6 Photoactivatable Pt(IV) diazido complex interaction with an oligonucleotide by mass spectrometry	102
2.5 Conclusions	104
2.6 References	107

Chapter 3 Chiral chromatography of organometallic anticancer

Complexes	114
3.1 Introduction	115
3.2 Experimental	117
3.2.1 Materials	117
3.2.2 Methods	118
3.2.2.1 Sample preparation	118
3.2.2.2 HPLC	118
3.3 Results	119
3.3.1.1 Stationary phase CHIRALPAK IA, complex 11 and the stability of the enantiomers of 11	121
3.3.1.2 Stationary phase CHIRALPAK IA, complexes 12-17	124
3.3.1.3 Solution stability of the enantiomers of complex 17	127
3.3.2 Stationary phase CHIRALPAK IC, complexes 18-24	130
3.3.2.1. Complexes 18-21 : separation of enantiomers and stability of 18	131
3.3.2.2 Complexes 22 and 23 : separation of enantiomers and stability of 23	134
3.3.2.3. Complex 24 : using a system that can be separated by other means	136
3.4 Discussion	139

3.5 Conclusions	145
3.6 References	147
Chapter 4 Photonic crystal fibre mass spectrometry	150
4.1 Introduction	151
4.1.1 Photoactivatable metal-based drugs	151
4.1.2 Hyphenated mass spectrometry techniques	152
4.1.3 Photonic crystal fibres	153
4.2 Experimental	155
4.2.1 Materials	155
4.2.2 Methods	156
5.2.2.1 Sample preparation	156
4.2.2.2 Mass spectrometry	156
4.2.2.3 Light sources	157
4.3. Results	157
4.3.1 Photonic crystal fibre mass spectrometry (PCF-MS) system design and development	157
4.3.1.1 PCF-MS system design and development: metallic coupling devices	158
4.3.1.2 PCF-MS system design and development: plastic microfluidic coupling devices	165
4.3.1.3 Design of PCF-MS system: PVC coupling devices	169

4.3.1.4 Design of PCF-MS system: microfluidic devices using 'off-the-shelf' chips	173
4.3.2 Vitamin B ₁₂ - a model for PCF-MS system validation in the positive-ion mode	177
4.3.2.1 Photoaquation of vitamin B ₁₂ pH 1.7: conventional methods	178
4.3.2.2 Photoaquation of vitamin B ₁₂ pH 1.7: PCF-MS system	179
4.3.2.3 Photoaquation of vitamin B ₁₂ pH 7.9: conventional methods	179
4.3.2.4 Photoaquation of vitamin B ₁₂ pH 7.9: PCF-MS system	182
4.3.3 PCF-MS system validation: sodium nitroprusside - a model reaction for system validation in the negative-ion mode	183
4.3.4 PCF-MS system application: photoactivation of ruthenium anticancer complexes	186
4.3.5 PCF-MS system application as a rapid microreactor screening technique to gain insights into the mechanism of action of photoactivatable drugs	189
4.4 Discussion	200
4.4.1. Photonic crystal fibre mass spectrometry (PCF-MS) system design and development	200
4.4.1.2 PCF-MS system design and development: plastic microfluidic coupling devices	201

4.4.1.3 PCF-MS system design and development: PVC coupling devices	202
4.4.1.4 PCF-MS system design and development: microfluidic devices using 'off-the-shelf' chips	203
4.4.2 PCF-MS system validation: vitamin B ₁₂ - a model reaction for system validation in the positive mode	204
4.4.3 PCF-MS system validation: sodium nitroprusside - a model reaction for system validation in the negative mode	205
4.4.4 PCF-MS system application: photoactivation of ruthenium potential anticancer complexes	206
4.4.5 PCF-MS system application: PCF-MS as a rapid microreactor screening technique to gain insights into the mechanism of action of photoactivatable drugs	207
4.5 Conclusions	209
4.6 References	211
Chapter 5 Conclusions and future work	213
5.1 Conclusions	214
5.2 Future work	217
5.3 References	221
Appendices	222
Appendix I	223
Appendix II	230

Appendix III	235
Appendix III part A: desalting methods	235
Appendix III part B: method optimisation of the separation of free oligonucleotide from oligonucleotide with platinum adducts	240
Appendix III part C: oligonucleotide quality control (QC) procedure	248

Acknowledgements

I would like to thank Professor Peter J. Sadler FRS for giving me this fantastic opportunity. Your guidance and support over the past few years has been invaluable. Thank you for pushing me to do my best and making me realise that I am capable of more than I imagined.

I would also like to thank Dr Abraha Habtemariam for all of his advice and helpful discussions. More importantly I would like to thank him for his wisdom in all things, not just chemical, and his unique ability to radiate calmness to all those around him. I very much doubt that I will have the privilege to work with anyone so kind again.

To Isolda and Louisa thank you for the coffee, the laughs, the friendship and the gin. Thank you for Spain, lazy Sundays and always being there. A girl could not ask for a better duo to make a trio with. Isolda I will be eternally grateful to you and your sofa. I don't know what I would have done without you both and of course the arepas that changed my life! I would also like to thank Dr Luca Salassa for the coffee, the comedy, the pasta, the hospitality and the words of wisdom.

To PJS group members past and present I would like to say thank you for letting me be part of this big, wonderfully dysfunctional family. We have had our moments over the years but I can honestly say that it has been an absolute pleasure and I do not know how I would have made it through the last few years without you all.

Dr Ana Pizarro, what do I say? Thank you for getting me in to this mess in the first place, is a start I guess. I have met very few people in my life who, just by the

way that they live, inspire others to be better in all that they do and you are one of them. Ana, you are brave in all aspects of life and give hope to those of us who are less so, that one day we might be too. Most importantly thank you for your honesty and for always listening.

I would like to thank Dr Sarah Unterkofler for her seemingly endless patience and great skill with optical equipment. My thanks also go to Dr Tijmen Euser and Prof Philip Russell for their collaboration and input throughout my PhD. For their help with all things NMR I would like to thank Dr Ivan Prokes and Mr Edward Tunnah. To Dr Lijiang Song I will be forever grateful for his constant help with all things mass spectrometry and chromatography related. On the same note I would like to thank Mr Philp Aston for all of his help over the years and reminding me that 'it's normal for an analytical chemist to like things clean'.

To my dear friend and flatmate Becky, thank you for the late night chats and the telly evenings. Our lovely little flat was an island of peace in the ocean of chaos that was the past few years. My Wells people, I love you all! Thank you for all of the welcome distractions and some of the unwelcome ones too. To Vale, my dear, geographically we may be apart but I have drawn great strength from the knowledge that you are with me in spirit. We have had some wonderful trips these past few years, the memories of which have kept me going during the hard times. I will be forever grateful to you and Antonio for our week on the magical island of Achill. I look forward to all of the ones that we have yet to make. Thank you for listening and truly being a friend.

To gramps, thank you for inspiring me to study what I love and nanna, thank you for your constant encouragement. Ally and Amy thanks for putting up with my

weird science talk and I apologies to you both for having to have such a massive geek as a sister. Mum and dad, I was born eternally in your debt. Each day that debt grows more and more. Thank you so much for everything. This would have been impossible without your constant love and support.

Declaration

I hereby declare that the work contained in this thesis is the original work of the author, except where specific reference is made to other sources, with the nature and extent of the author's contribution indicated (as appropriate) where work was based on collaborative research. The work has not been submitted, in whole or in part, for any other degree, diploma or other qualification. A list of research papers published during the term of study is given below.

Ruth J. McQuitty

September 2013

1. R. J. McQuitty, S. Unterkofler, T. G. Euser, A. Habtermariam, P. St. J. Russell and P. J. Sadler **Rapid screening of photoactivatable drugs: photonic crystal fibre microflow reactor coupled with ESI mass spectrometry** (manuscript in preparation 2013).
2. C. R. Barone, C. Coletti, R. J. McQuitty, N. J. Farrer, G. Lorusso, L. Maresca, A. Marrone, G. Natile, C. Pacifico, S. Parsons, N. Re, P. J. Sadler and F. J. White **Photo-isomerization of alkenyl complexes of platinum(II): structural, spectroscopic, kinetic, and computational**

investigations *Dalton Trans* **2013**, 42, 6840.

3. S. Unterkofler, R. J. McQuitty, T. G. Euser, N. J. Farrer, P. J. Sadler, and P. St. J. Russell **Optofluidic hollow-core photonic crystal fiber nanoflow reactor for online photochemical reaction analysis** *Optics Letters* **2012**, 37, 1952.
4. G. Ragazzon, I. Bratsos, E. Alessio, L. Salassa, A. Habtemariam, R. J. McQuitty, G. J. Clarkson and P. J. Sadler **Design of Photoactivatable Metalldrugs: Selective and Rapid Light-induced Ligand Dissociation from Half-Sandwich [Ru([9]aneS₃)(N–N')(py)]²⁺ Complexes** *Inorg. Chim. Acta* **2012**, 393, 230.
5. L. Ronconi, A. M. Pizarro, R. J. McQuitty; P. J. Sadler **Insights into the Acid–Base Properties of Pt(IV)–Diazidodiam(m)inedihydroxido Complexes from Multinuclear NMR Spectroscopy** *Chem. Eur. J.* **2011**, 17, 12051.

Abstract

Transition metal coordination complexes show great promise as novel therapeutic agents with new mechanisms of action, but their characterisation, and identification of their target sites present significant challenges. In this thesis a variety of new analytical methods is explored for the study of platinum, ruthenium, osmium and iridium anticancer complexes.

High performance liquid chromatography (HPLC) was used to determine the relative hydrophobicity of a series of photoactivatable Pt(IV) diazido complexes of the general type *trans,trans,trans*-[Pt(N₃)₂(OH)₂(R)(R')]. Interestingly the hydrophobicities did not follow trends based on literature Log P values of individual ligands and did not correlate with the cellular uptake or antiproliferative activity of the drugs. Other factors such as the quantum yield of the complex, and the type of DNA adducts appear to be more important for their efficacy.

Chromatography and high-resolution mass spectrometry were used to study the formation of platinum adducts on DNA when the most active complex *trans,trans,trans*-[Pt(N₃)₂(OH)₂(pyridine)₂], **8** was irradiated in the presence of short single strand oligonucleotides 14 bases in length. Complex **8** was found to bind to the oligonucleotides as a {Pt(pyridine)₂}²⁺ adduct. Modifying the wavelength of activation from UVA to 420 nm had no effect on the type of adduct formed, but the higher energy irradiation achieved maximum levels of DNA platination more quickly. Changing the sequence of the oligonucleotide suggested that the photoactivated form of **8** does not favour the formation of the 1,2-(GpG) bisadduct formed by cisplatin and other clinically approved

platinum based drugs, but may form 1,3-(GpNpG) or 1,3-(ApNpG) adducts, as is the case with other *trans*-platinum complexes.

Chiral chromatography using cellulose- and amylose-based stationary phases successfully separated the enantiomers of a series of organometallic 'piano stool' anticancer complexes. This appears to be the first successful separation of facially chiral Ru(II) arene complexes, the enantiomers of which were stable in solution for over 3 h. In contrast, separated cyclopentadienyl Ir(III) complexes with chiral metal centres epimerized within 2 h in solution at ambient temperature. Under similar conditions the enantiomers of the Os(II) arene complex $[\text{Os}(\eta^6\text{-p-cym})(4\text{-}(2\text{-pyridylazo})\text{-N,N-dimethylaniline})\text{I}]^+$ remained stable, as did those of the ruthenium-based complex $[\text{Ru}(9,10\text{-dihydrophenanthrene})(\text{en})\text{Cl}]^+$. It was shown that it is possible to separate the diastereomers of $[\text{Ru}(\eta^6\text{-para-cymene})(\text{iminopyridine})\text{I}]$, that can also be resolved by crystallisation techniques, and hence, decrease the time required to separate the enantiomers. This work will therefore allow exploration of the biological properties of some of these enantiomers

A novel technique for the rapid irradiation and detection of light-sensitive species was developed. Photonic crystal fibers (PCFs) were coupled to a mass spectrometer using HPLC tubing and fittings. This continuous flow method of analysis was validated using the photoaquation of cyanocobalamin. The PCF system was compared to the conventional cuvette-based approach. No significant difference in the species detected by MS could be found, but the PCF system had the advantage of requiring 20 times less sample (25 μL), and only 15 min of irradiation compared to 10 h by conventional methods.

The new PCF-MS system was then used to study the interaction of the photoactivatable ruthenium-based drug $[\{\{\eta^6\text{-indan}\}\text{RuCl}\}_2(\mu\text{-2,3-dpp})]^{2+}$ with a range of small molecules that acted as models for intracellular components, e.g. 5'GMP for DNA. The nucleobase binding properties were consistent with those previously reported with plasmid DNA by Magennis *et al*: a small amount of binding took place in the dark in view of the aquation of the mondentate leaving groups but this dramatically increased upon photoactivation and loss of the arene ligands. The complex was also found to bind to glutathione (GSH), which is known to detoxify metal-based drugs, an observation possibly explaining its poor anticancer activity.

Abbreviations

ESI electrospray ionization

MALDI matrix assisted laser desorption ionisation

HR-MS high-resolution mass spectrometry

RP-HPLC reverse-phase high performance liquid chromatography

NP-HPLC normal-phase high performance liquid chromatography

SP stationary phase

MP mobile phase

py pyridine

LMCT ligand-to-metal charge transfer

PVC polyvinyl chloride

PTFE polytetrafluoroethylene

PEEK polyether ether ketone

DDW doubly deionised water

DACH diaminocyclohexane

GMP guanosine monophosphate

PDT photodynamic therapy

PCF photonic crystal fiber

ICP-MS inductively coupled plasma mass spectrometry

NMR nuclear magnetic resonance

UV-Vis ultraviolet-visible (spectrum)

TFA trifluoroacetic acid

DDW doubly deionised water

DNA deoxyribonucleic acid

HMG high mobility group (protein)

CTR1 copper transporter protein 1

Cp^{x_bp^h} tetramethyl(biphenyl)-cyclopentadiene

Cp^{*} pentamethylcyclopentadiene

p-cym *para*-cymene

bip biphenyl

flu fluorene

phent phenanthrene

Impy iminopyridine

en ethylenediamine

azpy-F 4-(2- pyridylazo)-N,N-fluoro

azpy-NMe₂ 4-(2- pyridylazo)-N,N-dimethylaniline)

tz thiazole

pycarboxphen 3-pyridinecarboxaldehyde, 5-phenyl-

py,4-(4tfmph) pyridine,4-[4-(trifluoromethyl)phenyl]-

py,4-(2tfmph) pyridine, 4-(2-fluorophenyl)-

dfphpy 2-(2,4-difluorophenyl)pyridine)

benzq 7,8-benzoquinoline

phenpy 2-phenylpyridine

bmp 2,2'-bipyrimidine

μ-2,3-dpp 2,3-bis(2-pyridyl)pyrazine

VWD variable wavelength detector

DEA diethylamine

TEA Triethylamine

Chapter 1

Introduction

1.1 Metals in Medicine

Traditionally the pharmaceutical industry has focused on the design and development of organic drugs. Although metals and metal-based compounds have been used for medicinal purposes for centuries, such as mercury and arsenic in the treatment of syphilis,¹ their use has not been widespread. The discovery of the antiproliferative activity of the platinum-based compound cisplatin, *cis*-[Pt(NH₃)₂Cl₂], by Rosenberg *et al.* in 1968 created a new wave of interest in metal-based therapies,^{2,3} bringing inorganic medicinal chemistry to the forefront. Since then the search for metal ions for medicinal purposes has expanded to a wide range fields in therapy and diagnosis.

1.1.1 Antimicrobial agents

Compounds of silver have been used as antimicrobial agents for a number of years, often in the form of AgNO₃.⁴ Silver has the advantage of being toxic at low levels to bacteria, but much higher levels are required to achieve toxicity in human cells. One compound in clinical use for the treatment of burns is the polymeric compound silver sulfadiazine, Figure 1.1, which like many silver antimicrobial agents has been incorporated into various materials such as bandages,^{5,6} medical instruments,⁷ shoe insoles, fabrics^{8,9} and even washing machines and food.¹⁰ Often the silver compounds are incorporated into materials such as functionalised nanoparticles or even as dendrimers.¹¹⁻¹³

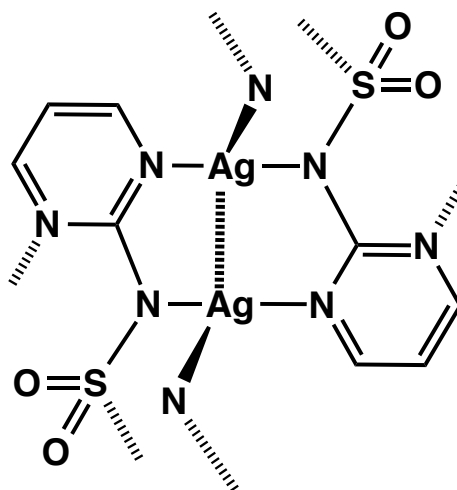


Figure 1.1 Structure of silver sulfadiazine.

Several other metal compounds have also shown efficacy as antimicrobial agents. Copper nanoparticles were shown to be inferior in activity to silver nanoparticles by Ruparelia *et al.* (2008), but a mixed nanoparticle of both metals was found to be the most effective against the four strains of bacteria tested.¹⁴ Amino acid-based complexes of Co(II), Cu(II), Ni(II) and Zn(II) were tested for their antibacterial and antifungal activity in Gram-positive, Gram-negative bacteria and fungal strains by Chohan *et al.* (2006). They were shown to be active towards *E. coli*, *B. subtilis*, *S. flexenari*, *S. aureus*, *P. aeruginosa*, and *S. typhi* bacteria, and for antifungal activity against *T. longifusus*, *C. albicans*, *A. flavus*, *M. canis*, *F. solani*, and *C. glaberata*.¹⁵ The antibacterial properties of a series of Cu(II), V(IV) and Ni(II) with Schiff bases obtained through the condensation of 4-amino-1,5-dimethyl-2-phenyl-1H-3-pyrazol-3(2H)-one (anti-pyridine) with 2-hydroxybenzaldehyde, 4-hydroxy-5-methoxyisophthalaldehyde and 4,5-dihydroxy isophthalaldehyde, respectively, were investigated by Rosu *et al.* (2010) along with their antiproliferative activity. The complexes were found to have limited activity in both bacteria and cancer cell

lines.¹⁶ The ruthenium-based complexes [Ru(phenanthroline)₂(dipyrido[3,2-d:2',3'-f]quinoxaline)]²⁺, [Ru(bipyridine)₂(dipyrido[3,2-a:2',3'-c](6,7,8,9-tetrahydro)phenazine)]²⁺, and [Ru(2,9-Me₂phenathroline)₂(dipyrido[3,2- a:2',3'-c]phenazine)]²⁺ are active towards both Gram-positive and Gram-negative bacteria.¹⁷ Ruthenium complexes have also shown promise in the treatment of the parasitic illness Chagas' disease.¹⁸ Another metal that has shown antiparasitic activity is gold; Au(I) chloroquinoline complexes are active against quinolone-resistant strains of malaria.¹⁹ A series of gold phosphine compounds has shown antimicrobial activity in Gram-positive bacteria, with the potency dependent on the structure of the phosphine ligands.²⁰

1.1.2 Gold Antiarthritic drugs

Compounds of gold are also used to treat rheumatoid arthritis. There are several forms of injectable gold antiarthritic gold drugs, including di-sodium aurothiomalate, aurothioglucose and sodium aurothiopropionol sulfonate.²¹ The orally active drug auranofin (Figure 1.2) gained approval for use in the clinic several decades ago. Its mechanism of action is thought to involve the induction of heme oxygenase-1 and the generation of reactive oxygen species (ROS), as explored in detail by Kim *et al.*²² It is known to react readily with thiols such as glutathione (GSH) and human serum albumin (HSA).²³ Using both X-ray absorption near-edge spectroscopy (XANES) and extended X-ray absorption fine structure (EXAFS), Messori *et al.* studied the interaction of auranofin with bovine serum albumin (BSA) and human serum apotransferrin.²⁴ They confirmed the findings of earlier NMR studies performed by Sadler *et al.* that auranofin loses its thiosugar ligand and

subsequently binds to the Cys-34 residue of BSA,^{25,26} and the loss of the same ligand is thought to facilitate binding to apotransferrin.²⁷ In both cases the Au(I) oxidation state is conserved upon protein binding.

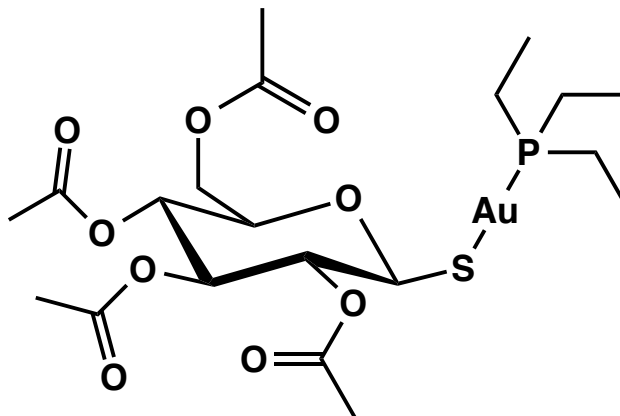


Figure 1.2 The structure of auranofin.

Auranofin has also displayed antiparasitic characteristics, thought to be derived from its ability to inhibit parasitic enzymes. The crystal structure of auranofin bound to trypanothione reductase, a key enzyme of the parasite *Leishmania infantum*, was reported by Ilari *et al.*²⁸ The structure showed that auranofin was bound to two cysteine residues of the protein, Cys-52 and Cys-57, with the thiosugar moiety of auranofin binding to the trypanothione binding site within the protein inhibiting the action of the enzyme. Auranofin has also shown promising anticancer activity against chronic lymphocytic leukemia.²⁹

1.1.3 Bismuth antiulcer drugs

Bismuth has a long history in the treatment of ulcers.²¹ These drugs, including bismuth subsalicylate (BSS), colloidal bismuthcitrate (CBS), and ranitidine bismuth citrate (RBC), which are often polymeric in structure. Target sites for

bismuth-based drugs are thought to be metalloproteins such as transferrin which can transport bismuth, and the enzyme urease in bacteria.³⁰ A study by Cun *et al.* has shown that Bi^{3+} binds to the histidine- and cysteine-rich domain at the C-terminus of the heat shock protein HspA, normally responsible for binding Ni^{2+} ions found in *Helicobacter pylori*.³¹ A proteomic study of *Helicobacter pylori* exposed to bismuth subcitrate found that the drug induced oxidative stress in the cells, suggesting that this may also be a key part of the mechanism of action of this class of drug.³² Tsang *et al.* monitored the bismuth levels of individual bacterial cells exposed to antiulcer drugs, and found that the uptake of bismuth was affected by the presence of ferric ions,³³ indicating that bismuth is taken up into the cells via iron transport pathways.

1.1.4 Metal-based insulin mimics

The signaling hormone insulin is essential for the metabolism of carbohydrates and fat.³⁴ Insulin release is prompted by high blood glucose levels and the subsequent high levels of insulin cause the liver and gut to increase the uptake of glucose. It is this function of insulin, inducing the storage of glucose, that vanadium and other metal compounds have been shown to mimic. Their efficacy is believed to be ascribable due to their interaction with phosphotyrosine phosphatases (PTPases) and tyrosine kinases that regulate insulin receptor binding.³⁵

The vanadium complex bis(maltolato)oxovanadium(IV) (BMOV), Figure 1.3, is an orally-active insulin mimic shown to be effective at reducing glucose levels in blood plasma.³⁶ To improve the uptake and efficacy of this class of drug, new generations of vanadium insulin mimics have been developed. Some of these

incorporate vanadium in different oxidation states. Rehder *et al.* synthesised and studied in detail 22 V(V) and V(IV) complexes containing –OO, –ON, –OS, –NS and –ONS donor ligands.³⁷ They found that the oxidation state of the metal had little effect on the activity of the complexes since the oxidation states of vanadium readily interconvert in cells. The most active compounds contained –ON ligands. This agrees with the findings of Gätjens *et al.* who synthesised a range of vanadium complexes derived from 5-carboalkoxypicolinates that were shown to be more active than BMOV.³⁸

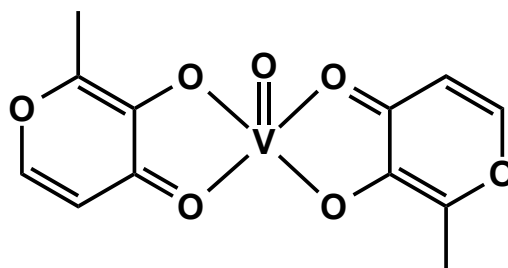


Figure 1.3 Structure of bis(maltolato)oxovanadium(IV) (BMOV).

The complexes of several other metals have shown efficacy as insulin mimics, such as molybdenum and tungsten. The Mo(VI) and W(VI) oxidation states are very similar in configuration to V(V); their similarities are discussed by Thompson *et al.* in their review of vanadium compounds as insulin mimics.³⁴ Zinc complexes may also show some efficacy as an insulin mimic.³⁴ The naturally occurring chromium-oligopeptide complex has been found to activate tyrosine kinase and some C-based complexes have been developed to explore this phenomenon further.²¹

1.1.5 Vasodilators

The release of NO from metal complexes, usually by means of photoactivation, has been shown to induce vasodilation.³⁹ The iron compound sodium nitroprusside (SNP) has been approved for clinical use to control hypertension.⁴⁰ The structure of this compound is shown in Figure 1.4. Upon irradiation with short wavelengths of light, the NO ligand of SNP is released first and subsequently small amounts of the CN⁻ ligand can also be released.^{41,39} There are also examples of ruthenium-,^{42,43} chromium-,⁴⁴ nickel-,⁴⁵ and copper-based⁴⁶ NO-releasing compounds, as well as those of other metals.⁴⁷

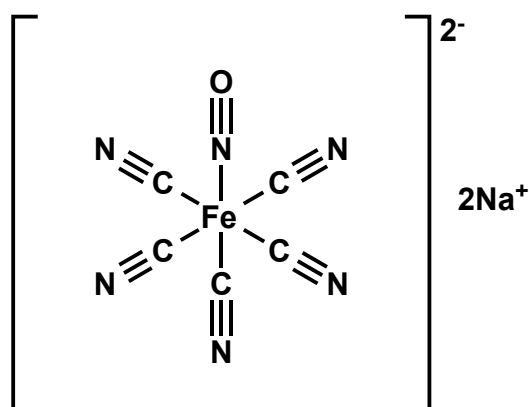


Figure 1.4 The structure of sodium nitroprusside.

1.1.6 MRI contrast agents

Advancements in other fields of medicine have led to new opportunities for inorganic drugs. The use of magnetic resonance imaging (MRI) in medical diagnosis has created a demand for contrast agents to improve the images acquired. The majority of the contrast agents in use are Gd(III)-based, though there are some iron nanoparticle agents and the Mn(II)-based agent Teloscan®. An example of the

gadolinium-based agents is shown in Figure 1.5. There are various agents for the targeting of different types of tissue, e.g. liver and brain. The different types of MRI contrast agent and their uses are reviewed extensively by Yan *et al.*⁴⁸

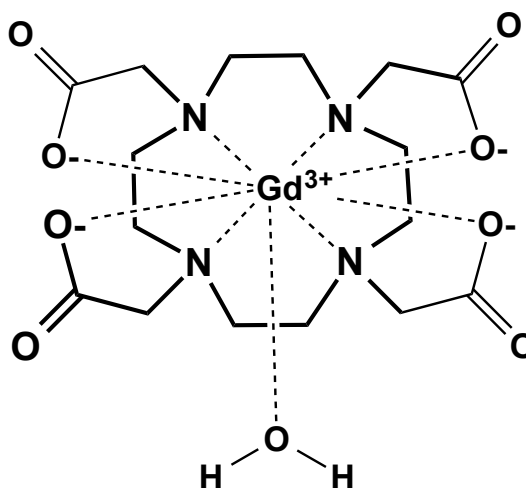


Figure 1.5 The structure of the Gd(III)-based contrast agent Dotarem®.

1.2 Platinum-based drugs

1.2.1 Cisplatin

The serendipitous discovery of the antiproliferative properties of cisplatin, Figure 1.6, sparked new interest in metal-based therapies in the late 1960s.^{2,3} In a little over a decade, it had gained FDA approval and had already begun to save lives. Cisplatin is highly effective in the treatment of testicular, ovarian, bladder, head and neck cancers.⁴⁹ Platinum-based drugs (cisplatin, carboplatin and oxaliplatin) are so successful that sales are now in the order of \$3 billion each year. Their mechanism of action, metabolism and biotransformation have been extensively studied.

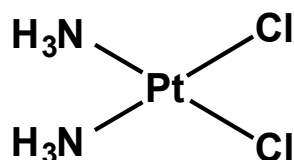


Figure 1.6 The structure of the platinum-based anticancer drug cisplatin.

1.2.1.1 Mechanism of action

The efficacy of cisplatin is thought to be attributable to its hydrolysis once it enters the cell and the subsequent binding of a small amount of the drug to nuclear DNA. Many different lesions are formed by the hydrolysed cisplatin: monoadducts, interstrand crosslinks, 1,2-intrastrand crosslinks and 1,3-intrastrand crosslinks. The adducts that are believed to induce apoptosis are the 1,2-d(GpG) and 1,2-d(ApG) intrastrand crosslinks, forming 65% and 25% of lesions (determined by high performance liquid chromatography), respectively.⁵⁰ Cisplatin binds to the N7 atom of guanine (and to some extent adenine) more favourably than other nucleotide binding sites since it is the most electron-rich, and it forms the most stable metal ion-nucleobase complex at physiological pH, see Figure 1.7.⁵¹ In single-stranded DNA, the N3 of cytidine and N1 of adenine are also possible binding sites for platinum.⁵²

The 1,2-(GpG) intrastrand crosslink causes a bending and unwinding of the duplex DNA⁵³ that is recognised by proteins. Two types of protein are known to interact with cisplatin lesions on DNA: repair proteins that recognise DNA damage and architectural proteins that are nuclear, or chromatin related proteins involved in the formation of protein-DNA or protein-protein complexes.⁵⁴ Many of these

proteins contain the high mobility group 1 box (HMG1) motif, a sequence of around 80 amino acids in length.

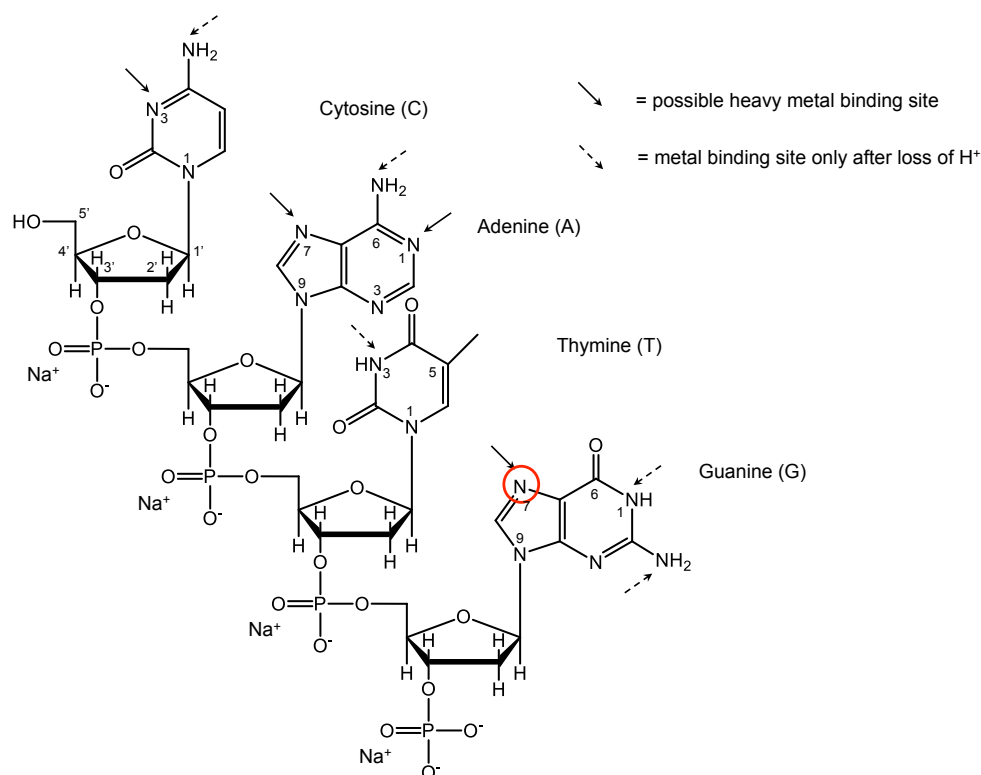


Figure 1.7 Possible binding sites for transition metal ions in a single strand deoxytetranucleotide are indicated with arrows. Adapted from ref. ⁵⁵

Ohndorf *et al.* reported the crystal structure of a HMG1 protein bound to a strand of duplex DNA, of the sequence 5'(CCT CTC TG*G* ACC TTC C)/5'(GGA GAG ACC TGG AAG G) (* indicates the position of platinum binding), containing a 1,2-c(GpG) cisplatin adduct.⁵⁶ The oligo-cisplatin adduct created a large enough bend in the duplex for a phenylalanine (Phe) residue at position 37 to partially intercalate. The binding of HMG1 was greatly reduced for a mutant protein in which Phe 37 was substituted by alanine. This suggested that such intercalation stabilised this modified DNA-protein complex. The bound HMG1 then interacts with mismatch repair protein MutS α and with the tumour-suppressor protein p53 *in vitro*, and

enhances p53 DNA-binding activity.⁵⁷ These protein interactions with the cisplatin bound DNA-HMG1 complex and other proteins initiate signaling cascades that lead to apoptosis in cells.

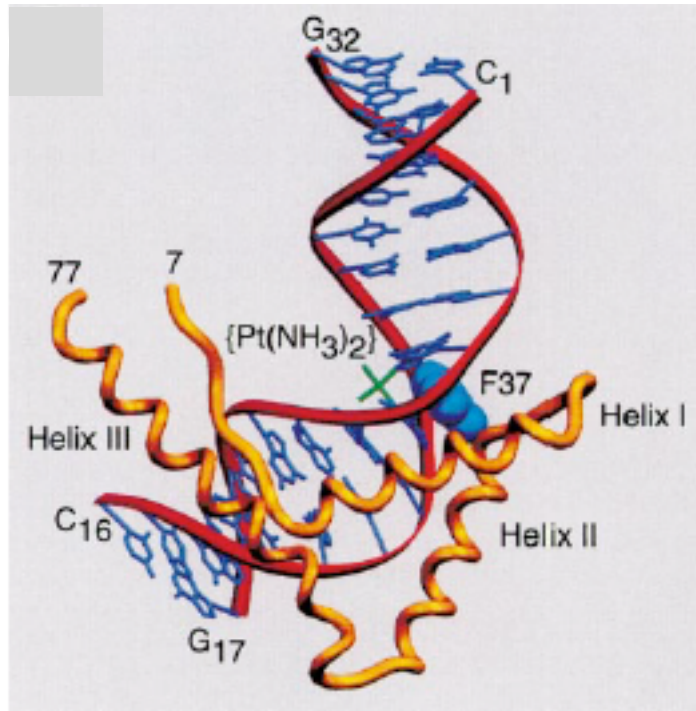


Figure 1.8 X-ray crystal structure showing the interaction of the HMG1 protein with the duplex 5'(CCT CTC TG*G* ACC TTC C)/5'(GGA GAG ACC TGG AAG G). From ref ⁵⁶

1.2.1.2 Cellular accumulation

Cisplatin uptake is not entirely understood, but it is known that it enters cells by passive diffusion. The uptake and efflux of cisplatin is also thought to be related to the high-affinity copper transporter CTR1.⁵⁷ Mutation or deletion of the CTR1 gene caused a reduction in the amount of Pt taken up by cells and an increase in cisplatin resistance. Over-expression of CTR1 increases the levels of Pt taken up.⁵⁸ Cisplatin was found to bind to the methionine residues of CTR1, perhaps allowing it to enter the cell by sulphur-sulphur ligand exchange.⁵⁹ Organic cation transporters

may also play a role in cisplatin uptake and efflux.⁶⁰

1.2.1.3 Mechanisms of resistance

Some types of cancer cells are intrinsically resistant to cisplatin, whilst others can develop resistance after prolonged exposure to the drug. One of the main sources of resistance is the reduced cellular accumulation of cisplatin by decreased influx and increased efflux.⁶¹ Additionally, an increase in levels of intracellular thiol e.g. GSH can detoxify cisplatin and increase efflux of platinum(II) from the cell. Another means of resistance is increased adduct repair and tolerance of Pt-DNA lesions resulting in failure to induce apoptosis.⁵⁷ A diagram summarising the journey of cisplatin within the cell is shown in Figure 1.9.

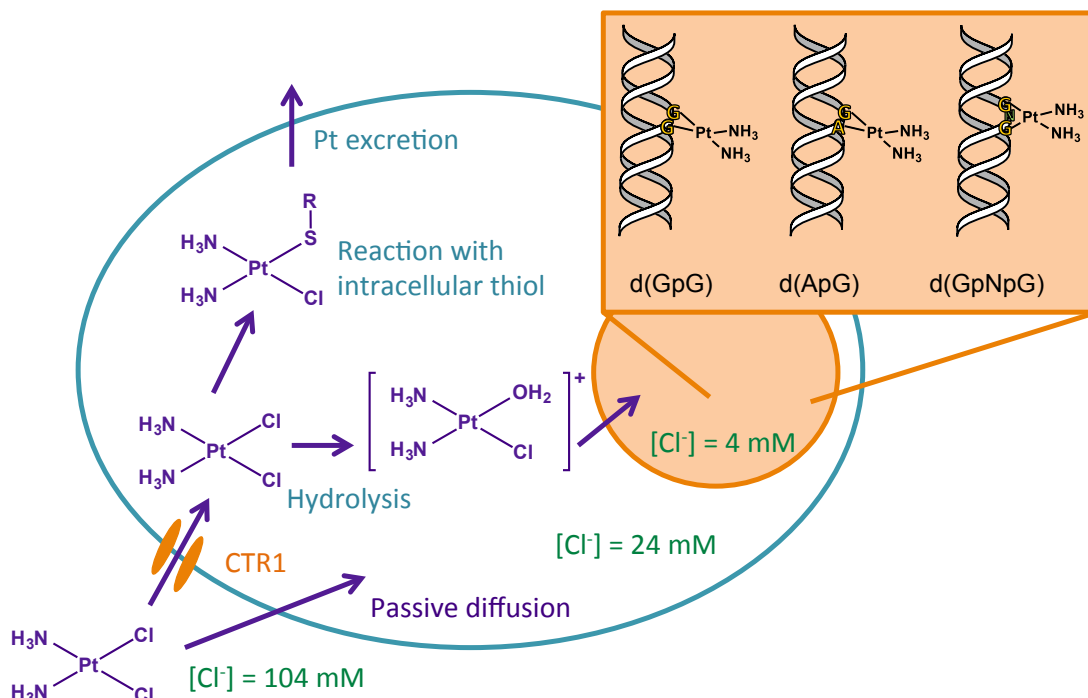


Figure 1.9 A diagram of cisplatin uptake, efflux and DNA binding (adapted from Reedijk *et al.*).⁵⁵

1.2.2 New generation platinum-based drugs

Despite its great success, cisplatin does have some disadvantages. Patients treated with cisplatin suffer from severe side-effects such as nephrotoxicity, neurotoxicity, ototoxicity, nausea and vomiting.⁴⁹ This along with the intrinsic and acquired resistance of certain cancers to cisplatin has led to the development of new platinum-based alternatives. The second generation Pt-based drug carboplatin, see Figure 1.10, was developed for these purposes.

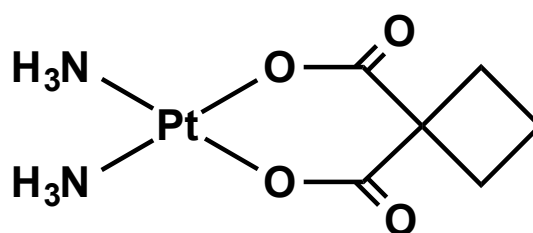


Figure 1.10 The structure of the second generation Pt-based drug Carboplatin.

The hydrolysis of carboplatin is slower than that of cisplatin as the cyclobutanedicarboxylato leaving group is not as labile as the chlorido leaving groups of cisplatin. The mechanism of carboplatin hydrolysis occurs in two stages, beginning with a ring opening process which is followed by complete loss of the ligand.⁶² This reduced rate of hydrolysis leads to fewer unwanted side reactions once carboplatin has entered the cell, and is thought to be responsible for the reduced side effects of this drug.⁶⁰ As carboplatin and cisplatin differ in structure only by the leaving groups, the resulting DNA adducts formed by carboplatin are the same as those of cisplatin.

The new generation platinum-based drug oxaliplatin (Figure 1.11), also used in the clinic, is active in some cancers that have either acquired or intrinsic resistance to cisplatin, e.g. colorectal cancers.^{63,64} This different spectrum of activity

for oxaliplatin is thought to be ascribable to the adducts that it forms with DNA. Although also a square-planar Pt(II) complex, oxaliplatin does not share any of the same ligands as cisplatin, and the lesions that it forms on DNA have a different structure and induce new changes in the duplex.

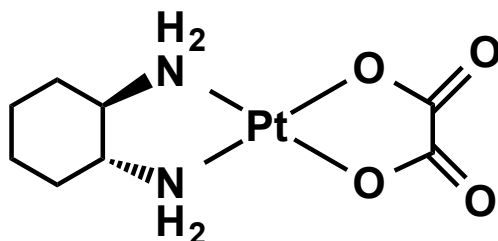


Figure 1.11 The structure of the new generation Pt-based drug oxaliplatin.

The DNA adducts of oxaliplatin, [(*R,R*)-DACH](ethanedioato-O,O')platinum(II) (where (*R,R*)-DACH is (1*R*,2*R*)-cyclohexane-1,2-diamine), have been widely studied using a range of analytical techniques. The crystal structure of the 1,2-d(GpG) oxaliplatin adduct was reported by Spingler *et al.*, with the same DNA duplex for which the crystal structure of the cisplatin adduct has also been solved.^{65,53} They found that oxaliplatin retains its diaminocyclohexane (DACH) ligand when bound to DNA. The structure contains the enantiomerically pure (*R,R*)-DACH ligand, and it was observed that there is a hydrogen bond between the pseudoequatorial NH of the (*R,R*)-DACH ligand and the O6 atom of the 3'-G of the 1,2-d(GpG) lesion. This may be an indication of why the (*R,R*)-DACH enantiomer and not the (*S,S*)-DACH is more clinically active.⁶⁶ The chirality of the DACH ligand may be very important for its interactions with DNA and subsequently the fate of the cell. This is an idea further explored by Kasparkova *et al.*, who found that the same overall structure is formed by the two enantiomers upon binding to DNA; however, there are small structural differences between the two.⁶⁷

Kasparkova *et al.* also studied the differences between the adducts formed by cisplatin and oxaliplatin on plasmid DNA. The DNA adducts of oxaliplatin were found to unwind and bend the duplex to a greater extent than those of cisplatin, reducing the ability of HMG proteins to bind to oxaliplatin-damaged DNA. Oxaliplatin also forms a greater number of interstrand crosslinks than cisplatin; this type of DNA damage is more difficult to repair than intrastrand crosslinks.⁶⁷ As well as these more qualitative biochemical experiments, several solution structures of DNA with a 1,2-d(GpG) oxaliplatin have been reported. It is difficult to compare these directly with those structures in the literature for the cisplatin 1,2-d(GpG) crosslink in view of differences in the DNA sequences used and the modelling programs. The study by Wu *et al.* allowed direct comparison between undamaged, cisplatin-bound and oxaliplatin-bound DNA under the same conditions.⁶⁸ They found that the overall bend of the duplex induced by the adducts is quite similar: $(22 \pm 10)^\circ$ for the cisplatin adduct, and $(31 \pm 10)^\circ$ for oxaliplatin. This may only be a small difference but may affect interaction of the two adducts with repair proteins. This topic has been reviewed in detail by Chaney *et al.*⁶⁹

Oxaliplatin and carboplatin have been approved for clinical use globally. There are three other Pt(II) anticancer drugs that have been licenced in individual countries. They are nedaplatin, licensed in Japan; lobaplatin, in China; and heptaplatin, in South Korea (Figure 1.12). All of these drugs contain Pt(II) with *cis* diam(m)ines; although there are examples of their activities against different tumours, there are also some examples of their cross-resistance to cisplatin.

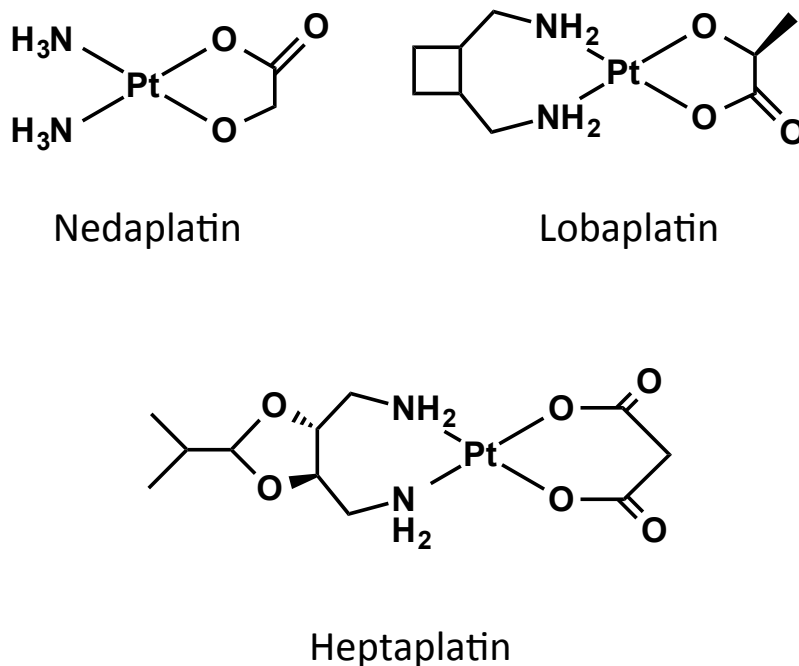


Figure 1.12 The structures of the Pt(II) drugs nedaplatin, lobaplatin and heptaplatin.

There are other Pt(II) drugs not yet licenced that have shown promise in clinical trials. One example is picoplatin, a drug that has not yet been approved for clinical use but has reached phase III clinical trials, see Figure 1.13.⁶⁴ Picoplatin has shown activity in small cell lung carcinoma, a type of cancer resistant to cisplatin and carboplatin.⁷⁰

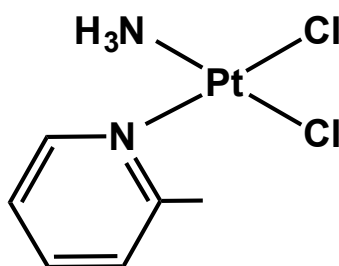


Figure 1.13 The structure of picoplatin, a Pt(II) drug in phase III trials.

1.2.2.1 *Trans* platinum(II) complexes

All of the complexes discussed above are of the *cis* configuration. Indeed, the early discovery of the inactivity of the *trans* isomer of cisplatin, transplatin, discouraged the synthesis of *trans*-platinum complexes since it was believed that they would have very little activity.⁷¹ Transplatin forms 1,3-d(GpNpG) intrastrand crosslinks on DNA and GN7-CN3 interstrand crosslinks.⁷²⁻⁷⁴ Some of the earliest *trans*-complexes were reported to have antiproliferative activity, Figure 1.14, and showed activity in cisplatin-resistant cell lines (L1210 cisplatin resistant leukaemia cells) with low IC₅₀ values comparable to their *cis* analogues, including *trans*-[PtCl₂(pyridine)₂] and *trans*-[PtCl₂(thiazole)₂].⁷⁵

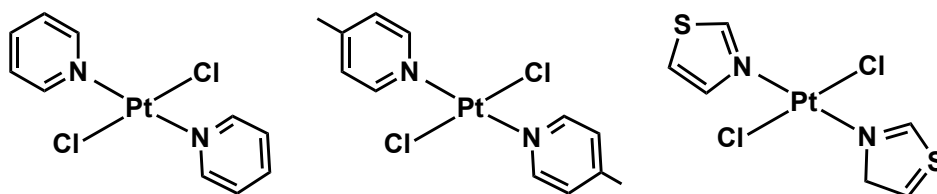


Figure 1.14 Structures of early active *trans*-platinum complexes: *trans*-[PtCl₂(pyridine)₂], *trans*-[PtCl₂(4-picoline)₂] and *trans*-[PtCl₂(thiazole)₂].^{75,76}

It was realised that *trans*-complexes could be active and possibly offer new mechanisms of action. The knowledge that it is sterically-unfavourable for them to form the 1,2-d(GpG) adduct formed by their *cis*-analogues has prompted the search for new active *trans* platinum complexes. A highly active *trans* complex that has reached clinical trials is BBR3464 *trans,trans,trans*-[[PtCl(NH₃)₂]₃ [trans-Pt(NH₃)₂{H₂N(CH₂)₆NH₂}]₂]-[PtCl(NH₃)₂]⁴⁺, the structure of which is shown in Figure 1.15. Atomic force microscopy studies of BBR3464 with DNA have shown that it causes greater compaction of the DNA than cisplatin.⁷⁷ The interaction of BBR3464

with DNA in cell free media, plasmid DNA and RNA polymerase II was reported by L. Zerzankova *et al.*⁷⁸ The adducts of BBR3464 form long range inter- and intrastrand crosslinks that inhibit RNA polymerase II more effectively than cisplatin adducts, and persist for longer but induce a smaller overall bend of the duplex.⁷⁹ The DNA adduct of BBR3464 contains a large lesion in which the two ends bind monofunctionally to the N7 of two guanine residues with the linker sitting in the minor groove. Chromatography and NMR spectroscopy were used by Ruhayel *et al.*, to confirm this structure and reveal that BBR3464 can form adducts in the 3'→3' direction as well as 5'→5, this is quite unusual as most DNA crosslinkers bind in the 5'→5' direction.⁸⁰

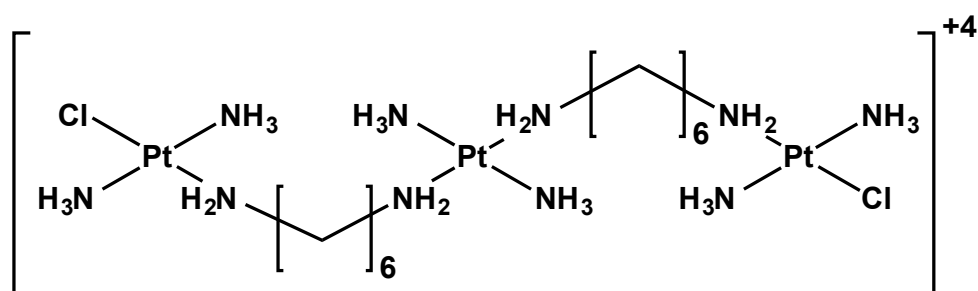


Figure 1.15 Structure of the tri-nuclear *trans*-platinum complex BBR3464.

1.2.2.2 Delivery strategies for platinum complexes

As well as increasing the spectrum of activity of platinum-based drugs by altering their geometry, targeting and delivery strategies have also been employed to help reduce their side-effects. The subject of targeting platinum based complexes has been recently reviewed in detail by Butler and Sadler⁸¹, but some of the key methods used are mentioned here. There are two types of targeting: active and passive. Active targeting and delivery relies upon the interaction of the drug

with biomolecules or biomarkers indicative of the cancerous state of the cell. Passive drug delivery is dependent on the enhanced permeability and retention effect of cancerous tissues.⁸²

Active targeting can involve many different strategies. Functionalising a drug molecule with hormones such as oestrogen allows drugs to target specific types of cancer such as oestrogen-positive breast cancers. The rapid proliferation rate of cancer cells means that they take up large amounts of sugars and carbohydrates. Some drugs utilise this to increase cellular accumulation of a drug by attaching a sugar residue.⁸³ Using cell-penetrating peptides has also proven effective in increasing drug activity.⁸⁴⁻⁸⁶

Passive targeting and delivery takes advantage of the poor vasculature structure of tumour tissue and the unique microenvironment that exists there. These 'leaky' cancer cells can allow larger molecules such as functionalised carbon nanotubes to enter, i.e. would not normally be able to do so.⁸⁷ Functionalised nanoparticles,^{88,89} dendritic structures⁹⁰ and liposomal encapsulations⁹¹ of drugs have also increased the potency of some complexes. Within solid tumours hypoxic conditions that lower the pH of the cells.⁹² Prodrugs, inactive forms of a drug that are activated within the body, can utilise these conditions to ensure activation is more likely to occur within cancer cells, or in the tumour microenvironment.

Platinum(IV) complexes can also act as prodrugs. They are less reactive towards substitution reactions than their Pt(II) analogues, lowering the likelihood of unwanted and harmful side reactions.⁹³ Within the body, Pt(IV) prodrugs are reduced to form cytotoxic Pt(II) complexes. The increased number of ligands on

octahedral Pt(IV) complexes gives the opportunity to further tune the properties of the complex to improve activity, uptake and targeting.⁹⁴

Many of these Pt(IV) drugs have shown activity across tumour cancer cells (Figure 1.16), but only a few have reached the clinic: tetraplatin (phase I) and iproplatin (phase III) were abandoned due to severe side effects and lack of significant efficacy, respectively, but LA-12 completed phase I clinical trials, and satraplatin has entered phase III clinical trials; oxoplatin has also been tested in clinical trials.^{95,96} The majority of the Pt(IV) complexes in Figure 1.16 rely upon reducing agents such as glutathione or ascorbic acid within the cell to form the active Pt(II) drug. Mitaplatin takes this one step further and combines two known active compounds in one prodrug.⁸⁹

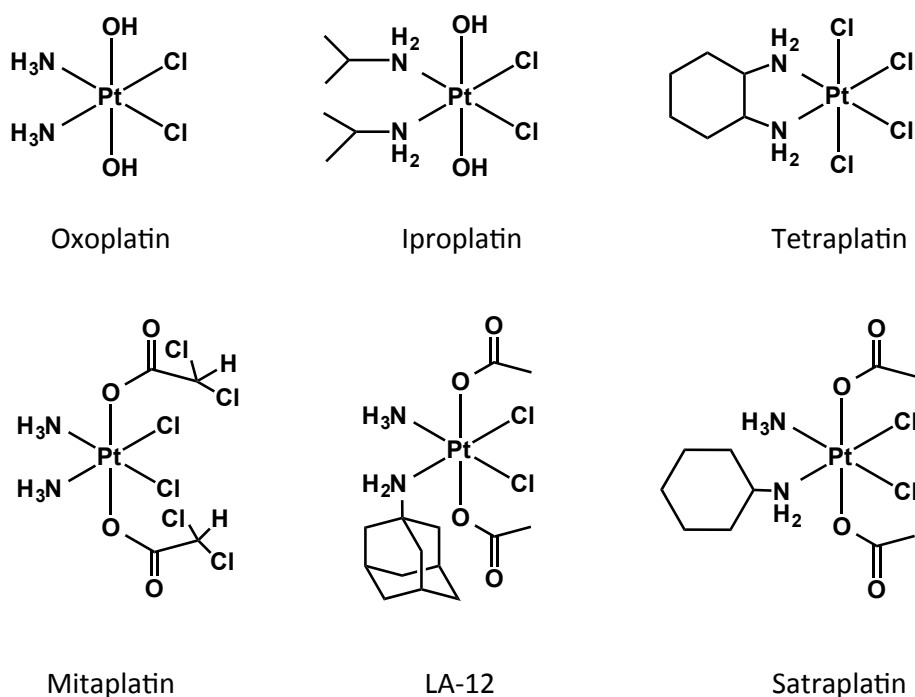


Figure 1.16 Structures of Pt(IV) prodrugs.

The majority of studies into Pt(IV) complexes and DNA are based on either their reaction with free nucleobases or the binding properties of their Pt(II) metabolites.⁹⁷⁻¹⁰¹ The emphasis has been more on using the metabolites of the Pt(IV) prodrugs rather than the complexes themselves, although some studies on Pt(IV)-DNA complexes have been carried out, and even when starting with the Pt(IV) drug the binding was found to be similar to that of their Pt(II) counterparts.^{100,97,102}

1.2.2.3 Photoactivation of platinum complexes

The Pt(IV) prodrug strategy may decrease adverse side-effects, but this reliance upon intracellular reduction is not the most reliable method of targeting and can probably be improved upon. The use of light as a method of activation via photoreduction offers spatial and temporal resolution to increase the targeting ability of Pt(IV) prodrugs.

The first Pt(IV) photoactivatable complexes reported contained two iodido ligands in order to achieve the reduction to Pt(II) by excitation of the ligand-to-metal charge-transfer bands.¹⁰³ An example of these compounds, *trans,cis,cis*-[Pt(OCOCH₃)₂(ethylenediamine)₂(I)₂], is shown in Figure 1.17. It is essential for all light-activated drugs to show minimal or preferably no dark toxicity. Unfortunately, diiodido Pt(IV) complexes only show a small difference between light and dark toxicities as a consequence of reduction by intracellular thiols.^{104,103}

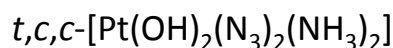
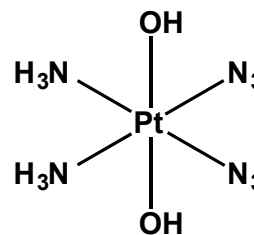
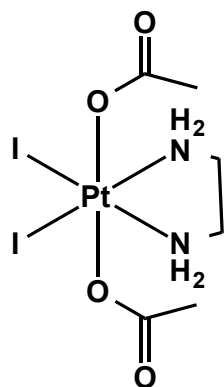


Figure 1.17 Structures of early photoactivatable Pt(IV) prodrugs.

The Sadler group has developed this class of complex, replacing the iodido ligands with azido ligands. The stability in the dark of these compounds is further increased by using *trans*-OH ligands.¹⁰⁵ These compounds have shown high activity in human cancer cells upon photoactivation with UVA. With an ability to achieve specific temporal and spatial activation, combined with tuning the activity of the complexes by changing the am(m)ine ligands, Pt(IV) diazido complexes provide interesting potential new anticancer drugs.¹⁰⁶

There have been some previous studies on the photoreduction of Pt(IV) azides and their subsequent interaction with both nucleobases and duplex DNA.^{107–}
¹¹⁰ The creation of photoproducts after irradiation with UVA was noted by the loss of the azide-to-platinum LMCT band using UV-Vis spectroscopy. For some compounds, a peak assigned to a mono-azido species was observed, which then decreased upon further irradiation. NMR studies show that when left in the dark these Pt(IV) complexes are stable (> 5 months), even in the presence of guanosine

monophosphate (GMP).¹¹¹ Irradiation in aqueous solution in the absence of reducing agents or nucleobases can produce Pt(II) hydroxides which precipitate, but in the presence of GMP, Pt(II)-GMP mono- and bis-adducts are readily formed.<sup>107–
¹¹⁰ The formation of bis-adducts suggests that, like Pt(II) drugs, these complexes can form DNA crosslinks, and this could be the cause of their cytotoxicities. The toxicity of these complexes may also be increased by the release of azide radicals upon photoactivation.¹¹²</sup>

1.3 Photodynamic therapy (PDT)

The use of light in the treatment of cancer is well established in the clinic in the form of photodynamic therapy (PDT). PDT uses photosensitisers such as porphyrin derivatives, e.g. the licenced drug Photofrin®.¹¹³ Photosensitizers usually use light to generate singlet oxygen ($^1\text{O}_2$) and radicals that cause cell damage.^{114,115} The mechanism by which photosensitisers generate free radicals and singlet oxygen is shown in Figure 1.18. The main pathway of cellular damage is the generation of singlet oxygen.¹¹⁶

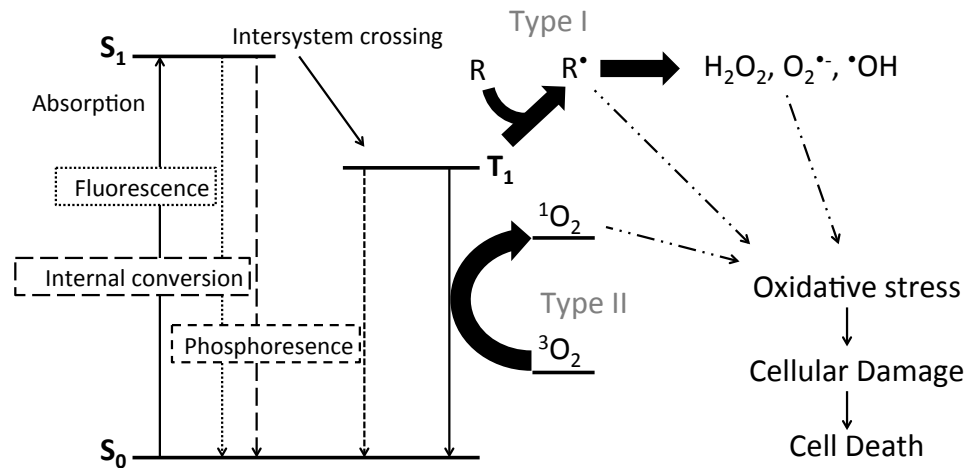


Figure 1.18 The mechanism by which an excited photosensitiser induces cellular damage and ultimately cell death. Adapted from Yoon *et al.*¹¹⁶

This form of treatment uses red light (600 - 850 nm) to achieve penetration deep into the tissue, as shown in Figure 1.19. Photodynamic therapy does, however, have its drawbacks due to its reliance on the presence of O₂. Solid tumours are often poorly vascularised resulting in a hypoxic tumour microenvironment.⁹²

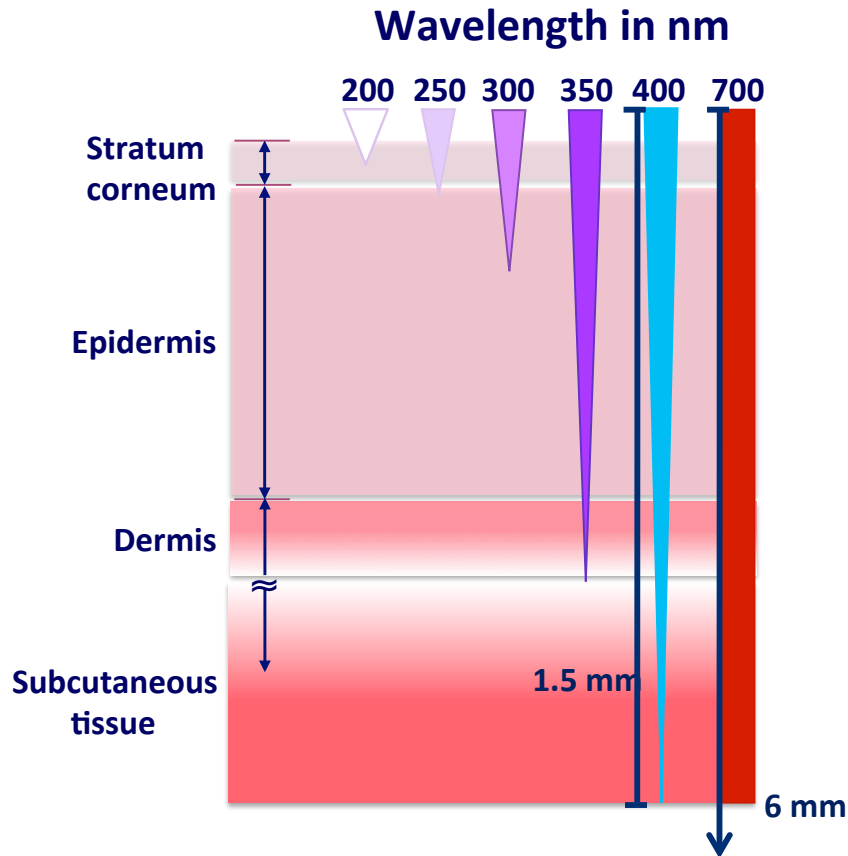


Figure 1.19 Diagram of the penetration of light into human tissue. Adapted from values given by Balaz *et al.*¹¹⁷

1.3.1 Light delivery: Photonic crystal fibres (PCFs)

The excitation of photoactivatable drugs can be achieved using various light sources, including LEDs and lasers that can then be guided to the tumour site using fibre optics. One development in the field of fibre optics in the last couple of decades is the introduction of photonic crystal fibres (PCFs).

Photonic crystal fibres are optical fibres that have unusual properties. They contain a core surrounded by a lattice structure. The gaps within the lattice are of the order of the wavelength of light that the fibre is intended to focus, and can use photonic band gaps as a waveguide mechanism.^{118–120} When light is correctly

focused into the fibre, the losses of light along the fibre as it guides the light are very small.

There are four main types of PCF structure, see Figure 1.20, solid core, suspended core, hollow-core photonic band gap and Kagomé.¹²¹ The structure of the fibre is determined by stacking very high-grade silica capillaries in a macroscopic version of the desired formation. The glass is then heated to a very high temperature and drawn out into fibres tens of micrometres thick.

Previously, these fibers have been used in gas sensing, fluorescence detection, absorption spectroscopy and as vessels for catalytic reactions. A hollow-core fibre was used as a kind of very long pathlength cuvette allowing the detection of species at much lower concentrations than conventional UV-Visible absorption spectroscopy and using very small sample volumes (1 μL).¹²² Reduced sample volumes and high optical powers are the two main advantages of these fibres over conventional irradiation methods. Those fibres that are of most interest for solution chemistry are the hollow core, the Kagomé and the suspended core fibre, as they allow for a large overlap between the sample and the light guided within the fibre.

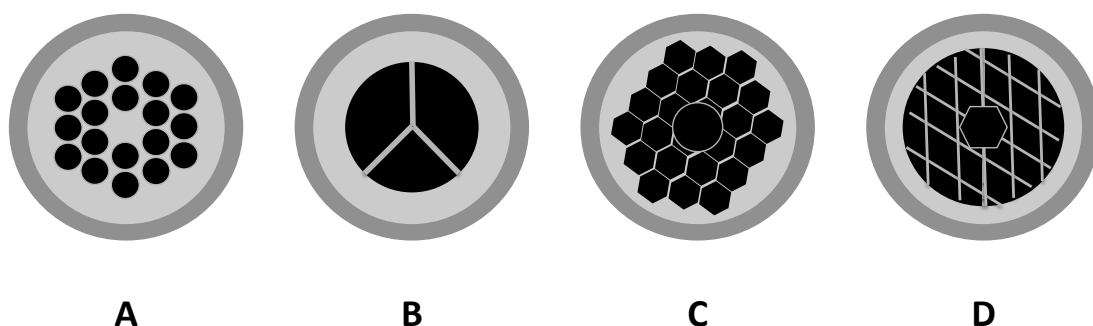


Figure 1.20 Schematics of the structures of four types of PCF: (A) solid core, (B) suspended core, (C) hollow-core photonic band gap and (D) Kagomé.¹²¹

1.4 Organometallic drugs

The search for new, effective metal-based drugs that have a different range of activity compared to cisplatin and without the side-effects associated with conventional platinum drugs, has led to the synthesis of new structures. Several of these new complexes are organometallic in nature and contain a metal ion other than those of platinum.

1.4.1 Ruthenium complexes

Ruthenium drugs were one of the first platinum alternatives to be reported, since Ru(II) and Ru(III) have similar ligand substitution kinetics to those of Pt(II).¹²³ The anticancer properties of Ru complexes, e.g. *cis*-[Ru(NH₃)₄Cl₂], were first tested by Clarke *et al.* in the late 1970s.¹²⁴ A lack of aqueous solubility prevented these complexes from reaching the clinic. However, since then several Ru-based complexes have entered clinical trials. The complexes KP1019, indazolium [*trans*-tetrachlorobis(1H-indazole)ruthenate(III)], and NAMI-A, imidazolium *trans*-[tetrachloro-(S-dimethyl-sulfoxide) 1H-(imidazole)ruthenate(III)], have both reached phase II clinical trials, see Figure 1.21.^{125–127}

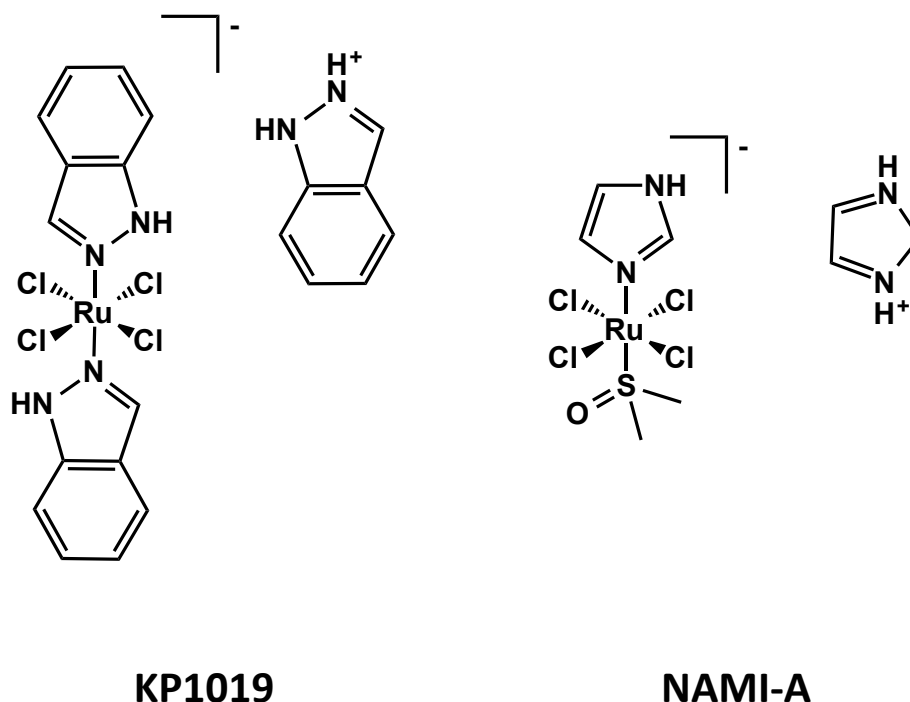


Figure 1.21 Structures of KP1019 and NAMI-A, two Ru-based drugs that have reached phase II clinical trials.

There are many other ruthenium complexes that have shown high activity in cancer cell screening. Two types of ruthenium-based complexes that have proved to be particularly successful in cell studies are the RAPTA complexes from the Dyson laboratory,¹²⁸ and another class of the so called ‘piano stool’ complexes from the Sadler group.¹²⁹ Examples of these are shown in Figure 1.22: RAPTA-C, $[(\eta^6\text{-}para\text{-cymene})\text{Ru}(\text{P-1,3,5-triaza-7-phospha-tricyclo-[3.3.1.1]decane})\text{Cl}_2]$, and complex **A** $[(\eta^6\text{-biphenyl})\text{Ru}(\text{ethylenediamine})\text{Cl}]^+$. Both of these types of complexes are prone to hydrolysis and subsequently bind to DNA.^{130–132}

New structures of complexes of the type developed by the Sadler group allow not just for direct coordination of the complex to DNA, but also for ligand intercalation and hydrogen bonding with the DNA.¹³³ As well as being important in

terms of hydrolysis, the monodentate leaving group of the ‘piano-stool’ complexes has been shown to affect the route by which the drug enters the cell.¹³⁴

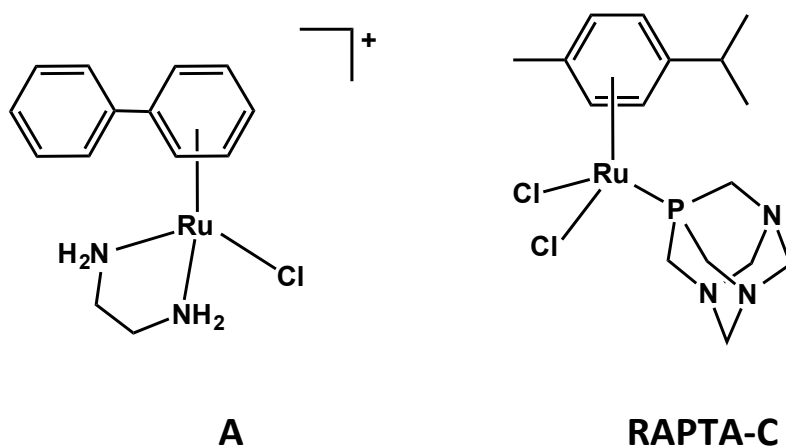


Figure 1.22 Structures of active ruthenium complexes from the Sadler laboratory, **A** $[(\eta^6\text{-biphenyl})\text{Ru}(\text{ethylenediamine})\text{Cl}]^+$, and a complex from the Dyson laboratory, **B** $\text{RATA-C}[(\eta^6\text{-}i\text{para-cymene})\text{Ru}(\text{P-1,3,5-triaza-7-phospha-tricyclo-[3.3.1.1]decane})\text{Cl}_2]$.

The chelating ligand of **A** has also been altered to include azopyridines, increasing the lability of the arene ligand when compared to the ethylenediamine analogue,¹³¹ and even to O,O-chelating ligands.¹³⁵ It was also found that increasing the size of the arene ligand (e.g. to anthracene derivatives) has led to increasing anticancer activity, this maybe due to increased DNA intercalation.

1.4.2 Osmium and iridium complexes

Within the Sadler group the ‘piano stool’ structure has been exploited further to include osmium(II) arene and iridium(III) cyclopentadienyl complexes. There are many similarities between osmium and ruthenium complexes, for example altering the monodentate leaving group can have a similar effect on complexes containing these metals.¹³⁴ However, some osmium-based drugs have been shown to be more potent in cell line testing than their ruthenium analogues

by an order of magnitude.¹³⁶ This may be ascribable to a difference in the mechanism of action of the two drugs, likely due to their very different ligand substitution kinetics. As well as binding to DNA, osmium complexes can generate reactive oxygen species (ROS) that damage cells.^{137,138} Transmission electron microscopy studies found that osmium drugs induced mitochondrial swelling and morphological changes in cancer cells, this observation suggests that mitochondrial apoptotic pathways may be implicated in cell death.¹³⁷ Osmium arene drugs have also been shown to be active *in vivo* with negligible toxicity.¹³⁹

Iridium(III) 'piano stool' complexes with N,N - and C,N - chelating ligands are highly potent against cancer cells achieving sub-micromolar activity.¹⁴⁰ The cyclopentadienyl ligands, used instead of the arene ligands in the Ru and Os complexes, have been shown to be important to hydrophobicity, DNA intercalation and can also increase the lability of the monodentate leaving group.¹⁴¹ Iridium complexes, along with some ruthenium complexes, can possess catalytic activity towards NADH which might affect the redox potential of a cell, possibly inducing oxidative stress and causing cell death in this manner.^{142,143}

1.5 Analytical techniques for the study of metal-based drugs

In this section, the methods used here for studying metal-based anticancer drugs and their interactions with biomolecules are described.

1.5.1 UV-Visible spectroscopy

UV-Visible spectroscopy is an optical technique that gives insight into the electronic structure of a molecule. The molecule absorbs a photon of light, promoting an electron from the ground state to an excited state. The amount of energy absorbed is indicative of the separation of the two energy levels. Within metal complexes there are three main types of these electronic transitions:

- Ligand field transitions, also known as metal centred transitions, are excitations of electrons from one metal orbital to another metal orbital. Examples are d-d transitions which are relatively weak.
- Ligand-to-metal charge transfer or metal-to-ligand charge transfer refers to transitions from ligand-to-metal or from metal-to-ligand. These are usually much stronger absorption bands.
- Intra-ligand transitions are those transitions that take place only from one ligand orbital to another.

The highly absorbing properties of metal complexes and the ability to study individual electronic transitions renders UV-Vis absorption spectroscopy a very useful tool for analysing metal complexes. Mackay *et al.* used these properties to great effect when studying the behaviour of photoactivatable Pt(IV) complexes, and are able to monitor the dissociation of the azide ligands by following the intensity of the LMCT band.¹⁰⁹

The Beer-Lambert law relates the absorption of a molecule to its concentration, Equation 1, where A is absorbance, I_0 and I are the intensities of the

incident and transmitted light, respectively, c is concentration, l is the pathlength of the light, and ϵ is the molar absorptivity or extinction coefficient. This formula can be used to determine the concentrations of species with known extinction coefficients that would otherwise be difficult to measure, e.g. proteins and DNA.

$$A = \log \frac{I}{I_0} = c \cdot l \cdot \epsilon \quad (1)$$

1.5.2 High-performance liquid chromatography (HPLC)

High-performance liquid chromatography forces solvent through a column filled with extremely fine particles at high pressure, resulting in highly-resolved separations.^{144,145} Liquid chromatography uses columns packed with small particles to increase the rate of equilibration of the analyte between stationary and mobile phases, and thereby increasing the efficiency of the separation. The term mobile phase refers to the solvent passed through the HPLC system, and the term stationary phase refers to the functionalised particles within the column that the solvent passes over. The smaller the particles of the stationary phase, the more efficient the column, the lower the detection limit and the faster the separation. However, with decreasing particle size, resistance to the flow of solvent also increases, causing the pressure to rise. Hence pumps and high-pressure fittings are required for the mobile phase to flow through an HPLC system.

The stationary phase support used in most HPLC columns is silica. The particle sizes are typically 3 - 5 μm in diameter, and are smaller for ultra-high pressure chromatography. Depending on the desired type of separation, these silica

particles can be functionalised with different groups to provide separation of almost any type of analyte. These groups can be functionalised by chains of sugars for chiral separation, or more commonly just carbon chains of various lengths, depending on the size of the molecules in the sample (the larger the molecule, the smaller the chain) for polarity-based separations.

The majority of HPLC analysis is carried out in what is called the 'reversed phase', in this case the particles are functionalised with hydrophobic groups, and a hydrophilic solvent is used as the mobile phase. This type of chromatography is more popular since it can easily be applied to water-soluble analytes, and typically in more biologically-relevant conditions. The opposite configuration is also used, with a hydrophilic stationary phase and a hydrophobic mobile phase. This is useful for the analysis of compounds with poor water solubility. An illustration of both types of chromatography is shown in Figure 1.23.

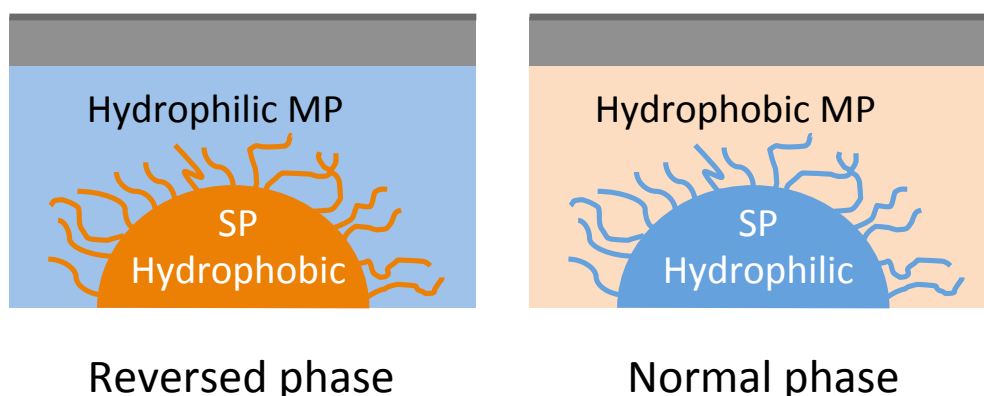


Figure 1.23 An illustration of stationary (SP) and mobile phases (MP) in reversed and normal phase HPLC.

Chromatography has been widely used in the study of metal complexes, from characterisation and purification of the complexes,¹⁴⁶⁻¹⁴⁸ monitoring reactions with

biomolecules,^{149,150} analysis of enzymatic digestions of proteins and DNA,^{151,50} and the coupling of HPLC to mass spectrometry¹⁵² or inductively-coupled plasma mass spectrometry (ICP-MS) in order to characterise species and determine metal contents.^{153,154}

1.5.3 Mass Spectrometry

Mass spectrometry (MS) is a technique used to measure the mass and give insights into the structure of a given molecule. Molecules must be in the gas phase for MS analysis and the must be ionised (either before or after entering the gas phase). Usually an electric field is applied to the gaseous ions to accelerate them and they are then separated by their mass to charge ratio (m/z).

There are many types of mass spectrometer arising from the different combinations of ionisation and detection methods. Electron impact is a method of ionisation for small volatile molecules that uses electrons to 'knock off' other electrons from the molecule of interest, creating a positively charged radical that may undergo further transformations in the gas phase. Chemical ionisation uses a reagent gas that is ionised and collided with the analyte transferring the charge. Matrix-assisted laser desorption (MALDI) uses laser light to vaporise the molecules of the matrix containing the analyte. The matrix is designed to strongly absorb the light of the laser, and it can then transfer its energy to the sample. A potential difference is then applied to the plume of analyte and the sample becomes ionised. This ionisation technique is much 'softer' than those previously described, and can be used for large molecules such as proteins.^{84,155}

In the work carried out in this thesis, only electrospray ionisation (ESI) was used. ESI is a very soft ionisation technique that requires a liquid sample input and can be used for the analysis of small ions up to large proteins. Sample solution is flowed through a capillary to the tip where a potential difference is applied. The voltage applied partly determines the charge on the sample ions. The solution forms charged droplets from which, with the aid of the sheath gas (typically N₂), the solvent molecules are evaporated. As the droplets shrink, the desolvation becomes more rapid due to Coulombic forces that eventually overcome the cohesive forces and the analyte is released from the droplet solvent-free.¹⁵⁵ Figure 1.24 shows an illustration of the process.

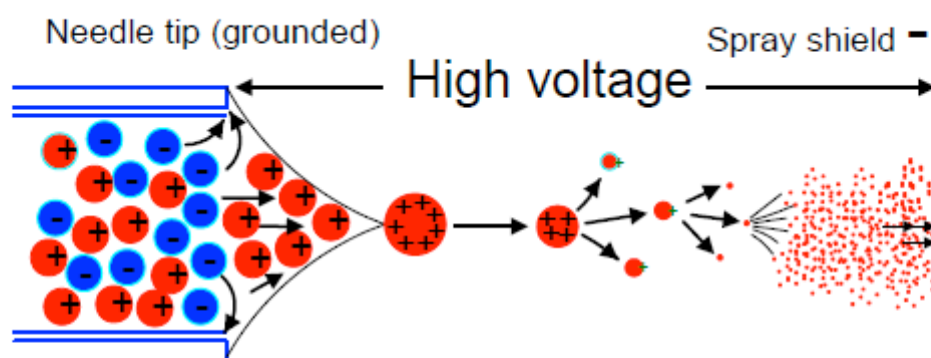


Figure 1.24 An illustration of the electrospray ionisation process.¹⁵⁶

As mentioned above different methods of ionisation can be coupled with different mass analysers, and either used on their own or in combination with each other. The following mass analysers were used to obtain data in this thesis.

One of the simplest mass analysers is a quadrupole. It consists of four parallel rods to which a constant voltage and an oscillating radio frequency are

applied to opposite pairs of rods. Ions pass through the rods and their direction of travel is controlled by the frequencies applied to the rods. Hence, certain ions may be excluded, depending on their m/z values.

Time-of-flight (TOF) analysers, as the name suggests, separate ions by the time taken for them to travel through a high vacuum drift region within the analyser called the drift region. Ions leave the ionisation chamber, and several thousands of times a second a voltage is applied adjacent to the sample stream, sending pulses of ions of the same kinetic energy into the drift region. The ions are then separated by their mass-to-charge ratios. To improve the resolution, more advanced instruments use a reflectron; this is a class of ion mirror that consists of electrodes with progressively higher charges applied to them. This, in effect, doubles the drift region and the resolving power of the analyser as well as focusing ions of the same m/z .

An ion-tap analyser shares some similarities with the quadrupole analyser. Radio frequencies and applied voltages are used to select the ions. They are then 'trapped' within the analyser and can accumulate before they are expelled towards the detector.

Tandem mass spectrometry (MS/MS) is another technique used in the course of this work. This term can be used to describe a number of ion fragmentation techniques, but in this case it refers to collision-induced dissociation (CID). For this process an ion of interest is selected and isolated, often using a quadrupole or an ion trap. An inert gas (in this case N_2) is then introduced and collisions with the gas fragment the ions.

In terms of application to the study of metal complexes, high-resolution mass spectrometry has been used for the characterisation of complexes, to study their interaction with small biomolecules such as GSH,¹⁵⁷ their interactions with proteins,^{158,159} and their interactions with DNA.¹⁶⁰⁻¹⁶⁴

Aims of this work

In order to understand the mechanisms of action of metallodrugs, it is important to develop new methods for their characterisation, and in particular their speciation in solution. It is not only important to identify target sites, but also to determine the number and types of ligands which are bound to the metal at the target site, and hence to determine how the initial ligands in the metallodrugs are involved in activation and/or target recognition.

The specific aims were as follows.

1. To use HPLC to characterise the lipophilicity of a series of photoactivatable Pt(IV) anticancer complexes for which partition coefficients could not readily be determined by conventional octanol-water shake flask methods, and to attempt to correlate their lipophilicity with cancer cell uptake and biological activity.
2. To explore the use of chiral HPLC columns to separate enantiomers of organometallic anticancer complexes, especially Ru(II) and Os(II) arenes, and cyclopentadienyl Ir(III) complexes. Such separation is important for

biological testing and target site recognition, which can show a strong dependence of the chirality of drugs. In particular, the aim was to examine the stability of separated enantiomers and complexes with subtle difference in structure such as facial chirality.

3. To explore the use of new methods involving the coupling of photonic crystal fibres with high-resolution mass spectrometry that may be more efficient both in terms of the volume of analyte required (nanolitres), in terms of the extent of photochemical conversion, and the detection of short-lived photoproducts.

1.6 References

1. K. Weismann, *Sex. Trans. Dis.*, 1995, **22**, 137–144.
2. B. Rosenberg, L. Van camp, and T. Krigas, *Nature*, 1965, **205**, 698–699.
3. B. Rosenberg, L. Van camp, J. E. Trosko, and V. H. Mansour, *Nature*, 1969, **222**, 385–386.
4. J. L. Clement and P. S. Jarrett, *Met. Based. Drugs*, 1994, **1**, 467–482.
5. S. Thomas and P. McCubbin, *J Wound Care*, 2003, **12**, 101–107.
6. M. Ip, S. L. Lui, V. K. M. Poon, I. Lung, and A. Burd, *J. Med. Microbiol.*, 2006, **55**, 59–63.
7. L. Taylor, P. Phillips, and R. Hastings, *J. Infect. Prev.*, 2009, **10**, 6–12.
8. U. Klueh, V. Wagner, S. Kelly, A. Johnson, and J. D. Bryers, *J. Biomed. Mat. Res.*, 2000, **53**, 621–631.
9. M. Mirjalili, N. Yaghmaei, and M. Mirjalili, *J. Nanostruc. Chem.*, 2013, **3**, 43–48.
10. A. Martínez-Abad, G. Sánchez, J. M. Lagaron, and M. J. Ocio, *Food Chem.*, 2013, **139**, 281–288.
11. A. Melaiye, Z. Sun, K. Hindi, A. Milsted, D. Ely, D. H. Reneker, C. A. Tessier, and W. J. Youngs, *J. Am. Chem. Soc.*, 2005, **127**, 2285–2291.
12. P. Dallas, V. K. Sharma, and R. Zboril, *Adv. Colloid Interface Sci*, 2011, **166**, 119–135.
13. L. Balogh, D. R. Swanson, D. a. Tomalia, G. L. Hagnauer, and A. T. McManus, *Nano Letts.*, 2001, **1**, 18–21.
14. J. P. Ruparelia, A. K. Chatterjee, S. P. Duttagupta, and S. Mukherji, *Acta Biomater.*, 2008, **4**, 707–716.
15. Z. H. Chohan, M. Arif, M. a Akhtar, and C. T. Supuran, *Bioinorg. Chem. Appli.*, 2006, **2006**, 83131–83144.
16. T. Rosu, M. Negoiu, S. Pasculescu, E. Pahontu, D. Poirier, and A. Gulea, *Eur. J. Med. Chem.*, 2010, **45**, 774–781.
17. A. Bolhuis, L. Hand, J. E. Marshall, A. D. Richards, A. Rodger, and J. Aldrich-Wright, *Eur. J. Pharma. Sci.*, 2011, **42**, 313–317.

18. L. Otero, P. Noblia, and D. Gambino, *Inorg. Chim. Acta.*, 2003, **344**, 1–10.
19. M. Navarro, H. Pérez, and R. a Sánchez-Delgado, *J. Med. Chem.*, 1997, **40**, 1937–1939.
20. F. Novelli, M. Recine, F. Sparatore, and C. Juliano, *Farm.*, 1999, **54**, 232–236.
21. Z. Guo and P. J. Sadler, *Angew. Chem. Int. Ed.*, 1999, **38**, 1512–1531.
22. N.-H. Kim, M.-K. Oh, H. J. Park, and I.-S. Kim, *J. Pharmacol. Sci.*, 2010, **113**, 246–254.
23. A. Albert, C. Brauckmann, F. Blaske, M. Sperling, C. Engelhard, and U. Karst, *J. Anal. Atom. Spectrom.*, 2012, **27**, 975–981.
24. L. Messori, A. Balerna, I. Ascone, C. Castellano, C. Gabbiani, A. Casini, C. Marchioni, G. Jaouen, and A. Congiu Castellano, *J. Biol. Inorg. Chem.*, 2011, **16**, 491–499.
25. A. Dhubhghaill, OM N., Sadler, PJ., Tucker, *J. Am. Chem. Soc.*, 1992, **114**, 1118–1120.
26. J. Christodoulou, P. J. Sadler, and a Tucker, *FEBS Lett.*, 1995, **376**, 1–5.
27. R. C. Coffey, M T; Shaw, C F; Eidsness, M K; Watkins, J W ; Elder, *Inorg. Chem.*, 1986, **25**, 333–339.
28. A. Ilari, P. Baiocco, L. Messori, A. Fiorillo, A. Boffi, M. Gramiccia, T. Di Muccio, and G. Colotti, *Amino Acids*, 2012, **42**, 803–811.
29. J. M. Madeira, D. L. Gibson, W. F. Kean, and A. Klegeris, *Inflammopharmacol.*, 2012, **20**, 297–306.
30. R. Ge and H. Sun, *Acc. Chem. Res.*, 2007, **40**, 267–274.
31. S. Cun, H. Li, R. Ge, M. C. M. Lin, and H. Sun, *J. Bio. Chem.*, 2008, **283**, 15142–15151.
32. R. Ge, X. Sun, Q. Gu, R. M. Watt, J. a Tanner, B. C. Y. Wong, H. H. Xia, J.-D. Huang, Q.-Y. He, and H. Sun, *J. Biol. Inorg. Chem.*, 2007, **12**, 831–842.
33. C.-N. Tsang, K.-S. Ho, H. Sun, and W.-T. Chan, *J. Am. Chem. Soc.*, 2011, **133**, 7355–7357.
34. K. H. Thompson, J. H. McNeill, and C. Orvig, *Chem. Rev.*, 1999, **99**, 2561–2572.
35. C. R. Kahn and M. F. White, *J. Clin. Invest.*, 1988, **82**, 1151–1156.

36. V. G. Yuen, C. Orvig, and J. H. McNeill, *C. J. Phys. Pharmacol.*, 1995, **73**, 55–64.
37. D. Rehder, J. Costa Pessoa, C. F. G. C. Geraldés, M. C. a Castro, T. Kabanos, T. Kiss, B. Meier, G. Micera, L. Pettersson, M. Rangel, A. Salifoglou, I. Turel, and D. Wang, *J. Biol. Inorg. Chem.*, 2002, **7**, 384–396.
38. J. Gätjens, B. Meier, T. Kiss, E. M. Nagy, P. Buglyó, H. Sakurai, K. Kawabe, and D. Rehder, *Chem. Eur. J.*, 2003, **9**, 4924–4935.
39. W. P. Arnold, D. E. Longnecker, and R. M. Epstein, *Anesthesiol.*, 1984, **61**, 254–260.
40. A. R. Butler and C. Glidewell, *Chem. Soc. Rev.*, 1987, **16**, 361–380.
41. S. M. Shishido and M. G. de Oliveira, *Prog. React. Kinet. Mech.*, 2001, **26**, 239–261.
42. P. G. Zanichelli, A. M. Miotto, H. F. G. Estrela, F. R. Soares, D. M. Grassi-Kassisse, R. C. Spadari-Bratfisch, E. E. Castellano, F. Roncaroli, A. R. Parise, J. a Olabe, A. R. M. S. de Brito, and D. W. Franco, *J. Biol. Inorg. Chem.*, 2004, **98**, 1921–1932.
43. F. G. Marcondes, A. a Ferro, A. Souza-Torsoni, M. Sumitani, M. J. Clarke, D. W. Franco, E. Tfouni, and M. H. Krieger, *Life Sci.*, 2002, **70**, 2735–2752.
44. Y. Wang, P. Legzdins, J. Poon, and C. Pang, *J. Cardiovas. Pharmacol.*, 2000, **35**, 73–77.
45. M. A. Zoroddu, S. Medici, and M. Peana, *J. Coord. Chem.*, 2009, **62**, 3828–3836.
46. M. Ziche, S. Donnini, L. Morbidelli, E. Monzani, R. Roncone, R. Gabbini, and L. Casella, *ChemMedChem*, 2008, **3**, 1039–1047.
47. J. Reglinski, A. R. Butler, and C. Glidewell, *Appl. Organomet. Chem.*, 1994, **8**, 25–31.
48. G.-P. Yan, L. Robinson, and P. Hogg, *Radiography*, 2007, **13**, e5–e19.
49. *FDA drug data- Platinol*,
http://www.accessdata.fda._docs/label/2010/018057s.
50. A. Eastman, *Biochemistry*, 1986, **25**, 3912–3915.
51. N. A. F. E. Sletten, *Metal Complex-DNA Interactions*, Sons, John Wiley & Sons, Chichester, West Sussex, UK, 2009.

52. J. Reedijk, *Chem. Rev.*, 1999, **99**, 2499–2510.
53. P. Takahara, A. Rosenzweig, C. Frederick, and S. Lippard, *Nature*, 1995, **377**, 6477–6487.
54. J. Zlatanova, J. Yaneva, and S. H. Leuba, *FASEB J.*, 1998, **12**, 791–799.
55. J. Reedijk, *Eur. J. Inorg. Chem.*, 2009, **2009**, 1303–1312.
56. U. M. Ohndorf, M. a Rould, Q. He, C. O. Pabo, and S. J. Lippard, *Nature*, 1999, **399**, 708–712.
57. D. Wang and S. J. Lippard, *Nat. Rev. Drug Discov.*, 2005, **4**, 307–320.
58. S. Ishida, J. Lee, D. J. Thiele, and I. Herskowitz, *Proc. Natl. Acad. Sci. USA*, 2002, **99**, 14298–14302.
59. X. Wang, X. Du, H. Li, D. S.-B. Chan, and H. Sun, *Angew. Chem. Int. Ed.*, 2011, **50**, 2706–2711.
60. F. Arnesano and G. Natile, *Coord. Chem. Rev.*, 2009, **253**, 2070–2081.
61. B. Köberle, M. T. Tomicic, S. Usanova, and B. Kaina, *Biochim. Biophys. Acta*, 2010, **1806**, 172–182.
62. T. Boulikas, A. Pantos, E. Bellis, and P. Christofis, *Cancer Ther.*, 2007, **5**, 537–583.
63. S. Nannizzi, G. J. Veal, E. Giovannetti, V. Mey, S. Ricciardi, C. J. Ottley, M. Del Tacca, and R. Danesi, *Cancer Chemother. Pharmacol.*, 2010, **66**, 547–558.
64. L. Kelland, *Nat. Rev. Cancer*, 2007, **7**, 573–584.
65. B. Spingler, D. a Whittington, and S. J. Lippard, *Inorg. Chem.*, 2001, **40**, 5596–5602.
66. J. L. Misset, *Brit. J. Cancer*, 1998, **77 Suppl 4**, 4–7.
67. J. Kasparkova, M. Vojtiskova, G. Natile, and V. Brabec, *Chem. Eur. J.*, 2008, **14**, 1330–1341.
68. Y. Wu, D. Bhattacharyya, C. L. King, I. Baskerville-abraham, S. Huh, G. Boysen, J. A. Swenberg, B. Temple, S. L. Campbell, S. G. Chaney, V. Recci, V. No, V. Re, M. Recci, and V. February, *Biochemistry*, 2007, **46**, 6477–6487.
69. S. G. Chaney, S. L. Campbell, E. Bassett, and Y. Wu, *Crit. Rev. Oncol. Hematol.*, 2005, **53**, 3–11.

70. C.-H. Tang, C. Parham, E. Shocron, G. McMahon, and N. Patel, *Cancer Chemother. Pharmacol.*, 2011, **67**, 1389–1400.
71. J. M. Pérez, M. a Fuertes, C. Alonso, and C. Navarro-Ranninger, *Crit. Rev. Oncol. Hematol.*, 2000, **35**, 109–120.
72. R. Dalbiès, D. Payet, and M. Leng, *Proc. Natl. Acad. Sci. USA*, 1994, **91**, 8147–8151.
73. F. Paquet, M. Boudvillain, G. Lancelot, and M. Leng, *Nucleic Acids Res.*, 1999, **27**, 4261–4268.
74. M. Boudvillain, R. Dalbiès, C. Aussourd, and M. Leng, *Nucleic Acids Res.*, 1995, **23**, 2381–2388.
75. N. Farrell, L. Kelland, J. Roberts, and M. Van Beusichem, *Cancer Res.*, 1992, **52**, 5065–5072.
76. N. P. J. N. Farrell, T. T. B. Ha, J.-P. Souchard, F. L. Wimmer, S. Cros, *J. Med. Chem.*, 1989, **32**, 2240–2241.
77. T. Banerjee, P. Dubey, and R. Mukhopadhyay, *Biochimie*, 2012, **94**, 494–502.
78. L. Zerzankova, T. Suchankova, O. Vrana, N. P. Farrell, V. Brabec, and J. Kasparkova, *Biochem. Pharmacol.*, 2010, **79**, 112–121.
79. J. Kasparkova, N. Farrell, and V. Brabec, *J. Bio. Chem.*, 2000, **275**, 15789–15798.
80. R. A. Ruhayel, S. J. Berners-Price, and N. P. Farrell, *Dalton Trans.*, 2013, **42**, 3181–3187.
81. J. S. Butler and P. J. Sadler, *Curr. Opin. Chem. Biol.*, 2013, **17**, 175–188.
82. X. Wang and Z. Guo, *Chem. Soc. Rev.*, 2013, **42**, 202–224.
83. R. W.-Y. Sun, D.-L. Ma, E. L.-M. Wong, and C.-M. Che, *Dalton Trans.*, 2007, 4884–4892.
84. F. Barragán, V. Moreno, and V. Marchán, *Chem. Comm.*, 2009, 4705–4707.
85. M. W. Ndinguri, R. Solipuram, R. P. Gambrell, S. Aggarwal, and R. P. Hammer, *Bioconj. Chem.*, 2009, **20**, 1869–1878.
86. L. Cardo and M. J. Hannon, *Inorg. Chim. Acta.*, 2009, **362**, 784–792.
87. J. Li, S. Q. Yap, C. F. Chin, Q. Tian, S. L. Yoong, G. Pastorin, and W. H. Ang, *Chem. Sci.*, 2012, **3**, 20832087.

88. J. Della Rocca, R. C. Huxford, E. Comstock-Duggan, and W. Lin, *Angew. Chem. Int. Ed.*, 2011, **50**, 10330–10334.
89. S. Dhar and S. J. Lippard, *Proc. Natl. Acad. Sci. USA*, 2009, **106**, 22199–22204.
90. A. Abderrezak, P. Bourassa, J.-S. Mandeville, R. Sedaghat-Herati, and H.-A. Tajmir-Riahi, *PLoS One*, 2012, **7**, e33102.
91. T. Tippayamontri, R. Kotb, B. Paquette, and L. Sanche, *Invest. New Drugs*, 2011, **29**, 1321–1327.
92. T. W. Hambley, *Aust. J. Chem.*, 2008, **61**, 647–653.
93. M. Hall and T. Hambley, *Coord. Chem. Rev.*, 2002, **232**, 49–67.
94. M. D. Hall, H. R. Mellor, R. Callaghan, and T. W. Hambley, *J. Med. Chem.*, 2007, **50**, 3403–3411.
95. M. R. Reithofer, S. M. Valiahdi, M. a Jakupec, V. B. Arion, A. Egger, M. Galanski, and B. K. Keppler, *J. Med. Chem.*, 2007, **50**, 6692–6699.
96. C. N. Sternberg, D. P. Petrylak, O. Sartor, J. A. Witjes, T. Demkow, J.-M. Ferrero, J.-C. Eymard, S. Falcon, F. Calabrò, N. James, I. Bodrogi, P. Harper, M. Wirth, W. Berry, M. E. Petrone, T. J. McKearn, M. Noursalehi, M. George, and M. Rozenzweig, *J. Clin. Oncol.*, 2009, **27**, 5431–5438.
97. J. F. Hartwig and S. J. Lippard, *J. Am. Chem. Soc.*, 1992, **114**, 5646–5654.
98. M. Wei, S. M. Cohen, a P. Silverman, and S. J. Lippard, *J. Biol. Chem.*, 2001, **276**, 38774–38780.
99. L. Pendyala, A. V Arakali, P. Sansone, J. W. Cowens, and P. J. Creaven, *Cancer Chemother. Pharmacol.*, 1990, **27**, 248–250.
100. R. Roat and J. Reedijk, *J. Inorg. Biochem.*, 1993, **214**, 263–274.
101. A. P. Silverman, W. Bu, S. M. Cohen, and S. J. Lippard, *J. Biol. Chem.*, 2002, **277**, 49743–49749.
102. O. Nováková, O. Vrána, V. I. Kiseleva, and V. Brabec, *Eur. J. Bio*, 1995, **228**, 616–624.
103. N. A. Kratochwil, P. J. Bednarski, H. Mrozek, A. Vogler, and J. K. Nagle, *Anti-Cancer Drug Des.*, 1996, **11**, 155–171.
104. N. A. Kratochwil, M. Zabel, K. J. Range, and P. J. Bednarski, *J. Med. Chem.*, 1996, **39**, 2499–2507.

105. L. Ellis, H. Er, and T. Hambley, *Aust. J. Chem.*, 1995, **48**, 793–806.
106. S. J. Berners-Price, *Angew. Chem. Int. Ed.*, 2011, **50**, 804–805.
107. N. A. Kratochwil, J. a. Parkinson, P. J. Bednarski, and P. J. Sadler, *Angew. Chem. Int. Ed.*, 1999, **38**, 1460–1463.
108. P. Müller and B. Schröder, *Angew. Chem. Int. Ed.*, 2003, **42**, 335–339.
109. F. S. Mackay, N. J. Farrer, L. Salassa, H.-C. Tai, R. J. Deeth, S. a Moggach, P. a Wood, S. Parsons, and P. J. Sadler, *Dalton Trans.*, 2009, **2009**, 2315–2325.
110. F. S. Mackay, S. A. Moggach, A. Collins, S. Parsons, and P. J. Sadler, *Inorg. Chim. Acta.*, 2009, **362**, 811–819.
111. F. S. Mackay, J. a Woods, P. Heringová, J. Kaspárková, A. M. Pizarro, S. a Moggach, S. Parsons, V. Brabec, and P. J. Sadler, *Proc. Nat. Acad. Sci.*, 2007, **104**, 20743–20748.
112. J. S. Butler, J. a Woods, N. J. Farrer, M. E. Newton, and P. J. Sadler, *J. Am. Chem. Soc.*, 2012, **134**, 16508–16511.
113. R. R. Allison and C. H. Sibata, *Photodiagnosis Photodyn. Ther.*, 2010, **7**, 61–75.
114. C. A. Robertson, D. H. Evans, and H. Abrahamse, *J. Photochem. Photobiol. B*, 2009, **96**, 1–8.
115. Y. Tian, L. Wang, and W. Wang, *Laser Phys.*, 2008, **18**, 1119–1123.
116. I. Yoon, J. Z. Li, and Y. K. Shim, *Clini. Endosc.*, 2013, **46**, 7–23.
117. M. Balaz, H. a Collins, E. Dahlstedt, and H. L. Anderson, *Org. Biomol. Chem.*, 2009, **7**, 874–888.
118. J. Knight, T. Birks, and R. Cregan, *Opt. Mat.*, 1999, **11**, 143–151.
119. J. C. Knight, *Science*, 1998, **282**, 1476–1478.
120. P. Russell, *Science*, 2003, **299**, 358–362.
121. A. M. Cubillas, S. Unterkofler, T. G. Euser, B. J. M. Etzold, A. C. Jones, P. J. Sadler, P. Wasserscheid, and P. S. J. Russell, *Chem. Soc. Rev.*, 2013, **42**, 8629–8648.
122. J. S. Y. Chen, T. G. Euser, N. J. Farrer, P. J. Sadler, M. Scharrer, and P. S. J. Russell, *Chem. Eur. J.*, 2010, **16**, 5607–5612.
123. S. H. van Rijt and P. J. Sadler, *Drug discov. Today*, 2009, **14**, 1089–1097.

124. H. J. P. A.D. Kelman, M.J. Clarke, S.D. Edmonds, *J. Clin. Hematol. Oncol.*, 1977, **7**, 274–288.
125. G. Süss-Fink, *Dalton Trans.*, 2010, **39**, 1673–1688.
126. E. Alessio and G. Mestroni, *Curr. Top. Med. Chem.*, 2004, **4**, 1525–1535.
127. F. Garzon and M. Berger, *Cancer Chemother. Pharmacol.*, 1987, 347–349.
128. W. H. Ang, A. Casini, G. Sava, and P. J. Dyson, *J. Organomet. Chem.*, 2011, **696**, 989–998.
129. S. Dougan and P. Sadler, *Chimia*, 2007, **61**, 704–715.
130. W. H. Ang, E. Daldini, C. Scolaro, R. Scopelliti, L. Juillerat-Jeannerat, and P. J. Dyson, *Inorg. Chem.*, 2006, **45**, 9006–9013.
131. S. J. Dougan, M. Melchart, A. Habtemariam, S. Parsons, and P. J. Sadler, *Inorg. Chem.*, 2006, **45**, 10882–10894.
132. F. Wang, J. Bella, J. a Parkinson, and P. J. Sadler, *J. Biol. Inorg. Chem.*, 2005, **10**, 147–155.
133. A. M. Pizarro and P. J. Sadler, *Biochimie*, 2009, **91**, 1198–1211.
134. I. Romero-Canelón, L. Salassa, and P. J. Sadler, *J. Med. Chem.*, 2013, **56**, 1291–1300.
135. M. Melchart, A. Habtemariam, S. Parsons, and P. J. Sadler, *J. Inorg. Biochem.*, 2007, **101**, 1903–1912.
136. Y. Fu, A. Habtemariam, A. M. Pizarro, S. H. van Rijt, D. J. Healey, P. a Cooper, S. D. Shnyder, G. J. Clarkson, and P. J. Sadler, *J. Med. Chem.*, 2010, **53**, 8192–8196.
137. S. H. van Rijt, A. Mukherjee, A. M. Pizarro, and P. J. Sadler, *J. Med. Chem.*, 2010, **53**, 840–849.
138. S. H. Van Rijt, H. Kosthunova, V. Brabec, and P. J. Sadler, *Bioconj. Chem.*, 2011, **22**, 218–226.
139. S. D. Shnyder, Y. Fu, A. Habtemariam, S. H. van Rijt, P. a Cooper, P. M. Loadman, and P. J. Sadler, *Medchemcomm*, 2011, **2**, 666–668.
140. Z. Liu, L. Salassa, A. Habtemariam, A. M. Pizarro, G. J. Clarkson, and P. J. Sadler, *Inorg. Chem.*, 2011, **50**, 5777–5783.

141. Z. Liu, A. Habtemariam, A. M. Pizarro, S. a Fletcher, A. Kisova, O. Vrana, L. Salassa, P. C. a Bruijnincx, G. J. Clarkson, V. Brabec, and P. J. Sadler, *J. Med. Chem.*, 2011, **54**, 3011–3026.
142. Z. Liu, R. J. Deeth, J. S. Butler, A. Habtemariam, M. E. Newton, and P. J. Sadler, *Angew. Chem. Int. Ed.*, 2013, **52**, 4194–4197.
143. S. Betanzos-Lara, Z. Liu, A. Habtemariam, A. M. Pizarro, B. Qamar, and P. J. Sadler, *Angew. Chem. Int. Ed.*, 2012, **51**, 3897–3900.
144. D. C. Harris, *Quantitative Chemical Analysis*, W.H. Freeman and Compnay, New York, 2007.
145. J. L. Snyder, L. R., Kirkland, J. J., and Galjch, *No Title Practical HPLC Method Development*, Wiley, New York, 1997.
146. V. Pichler, S. Göschl, S. M. Meier, A. Roller, M. a Jakupec, M. Galanski, and B. K. Keppler, *Inorg. Chem.*, 2013, **52**, 8151–8162.
147. A. Grau-Campistany, A. Massaguer, D. Carrion-Salip, F. Barragán, G. Artigas, P. López-Senín, V. Moreno, and V. Marchán, *Mol. Pharm.*, 2013, **10**, 1964–1976.
148. M. El-Khateeb, T. G. Appleton, B. G. Charles, and L. R. Gahan, *J. Pharma. Sci.*, 1999, **88**, 319–326.
149. G. Ma, E. Wang, H. Wei, K. Wei, P. Zhu, and Y. Liu, *Metallomics*, 2013, **5**, 879–887.
150. F. Wang, H. Chen, J. a Parkinson, P. D. S. Murdoch, and P. J. Sadler, *Inorg. Chem.*, 2002, **41**, 4509–4523.
151. A. Eastman, *Biochemistry*, 1983, **22**, 3927–3933.
152. C. G. Huber and H. Oberacher, *Mass Spectrom. Rev.*, 2002, **20**, 310–343.
153. R. A. Diaz-Bone, M. Hollmann, O. Wuerfel, and D. Pieper, *J. Anal. Atom. Spectrom.*, 2009, **24**, 808–814.
154. M. Hollmann, J. Boertz, E. Dopp, J. Hippler, and A. V. Hirner, *Metallomics*, 2010, **2**, 52–56.
155. I. Williams, D. H., Flemming, *Spectroscopic methods in Organic Chemistry*, McGraw-Hill Higher Education, London, 6th edn., 2008.
156. B. Daltonics, *MaXis User Manual*, 2008, vol. 1.

157. F. Wang, S. Weidt, J. Xu, C. L. Mackay, P. R. R. Langridge-Smith, and P. J. Sadler, *J. Am Soc. Mass Spectrom.*, 2008, **19**, 544–549.
158. C. G. Hartinger, Y. O. Tsybin, J. Fuchser, and P. J. Dyson, *Inorg. Chem.*, 2008, **47**, 17–19.
159. A. Casini, C. Gabbiani, E. Michelucci, G. Pieraccini, G. Moneti, P. J. Dyson, and L. Messori, *J. Biol. Inorg. Chem.*, 2009, **14**, 761–770.
160. T. Urathamakul, D. J. Waller, J. L. Beck, J. R. Aldrich-Wright, and S. F. Ralph, *Inorg. Chem.*, 2008, **47**, 6621–6632.
161. J. L. Beck, M. L. Colgrave, S. F. Ralph, and M. M. Sheil, *Mass Spectrom. Rev.*, 2001, **20**, 61–87.
162. J. Talib, C. Green, K. J. Davis, T. Urathamakul, J. L. Beck, J. R. Aldrich-Wright, and S. F. Ralph, *Dalton Trans.*, 2008, **9226**, 1018–1026.
163. J. Talib, J. L. Beck, T. Urathamakul, C. D. Nguyen, J. R. Aldrich-Wright, J. P. Mackay, and S. F. Ralph, *Chem. Comm.*, 2009, 5546–5548.
164. J. Talib, D. G. Harman, C. T. Dillon, J. Aldrich-Wright, J. L. Beck, and S. F. Ralph, *Dalton Trans.*, 2009, 504–513.

Chapter 2

The interaction of photoactivatable Pt(IV) complexes with single strand oligonucleotides

In this Chapter, ten photoactivatable platinum(IV) diazido complexes of the general formula *trans,trans,trans*-[Pt(N₃)₂(OH)₂(R)(R')] are discussed. The lipophilicity of each complex is compared to its intracellular accumulation and IC₅₀ values in A2780 human ovarian cancer cells. The DNA binding of complex *trans,trans,trans*-[Pt(N₃)₂(OH)₂(pyridine)₂] is investigated by means of mass spectrometry and chromatography.

2.1 Introduction

2.1.1 Platinum-based anticancer drugs

As discussed in Chapter 1, platinum-based drugs have a long and successful history in anticancer therapy, first gaining FDA approval in 1978.¹ Despite their success they do suffer from two major drawbacks, namely severe side effects and both intrinsic as well as acquired resistance of certain types of cancers. To overcome these problems, new generations of platinum based drugs have emerged.

In the Sadler group a new generation of potential platinum drugs are under development that could overcome the problems of traditional platinum-based therapies, whilst retaining and even improving their efficacies.² The approach taken utilises a Pt(IV) prodrug, a strategy that has been widely explored and has seen Pt(IV)-based complexes reach clinical trials.^{3,4} These Pt(IV) prodrugs are reduced by intracellular species to form a cytotoxic Pt(II) complex that has a similar mechanism

of action to that of established platinum-based agents. The method of Pt(IV) reduction utilised by the Sadler group is light activation. This enables both spatial and temporal resolution of the treatment, allowing only tumour tissue to be targeted and hence, reducing any potentially harmful side effects in healthy cells.

Light activation is already in the clinic in the form of photodynamic therapy (PDT). This treatment uses long wavelength light (600 – 850 nm) to achieve activation of the photosensitiser within the tumour.^{5,6} This therapy is discussed more fully in Section 1.3 of Chapter 1.

2.1.2 Platinum-based anticancer drugs and their interaction with DNA

The DNA binding of platinum-based drugs is key to their activity, and therefore is an important area of study. The DNA damage induced by the platinum drug is believed to attract intracellular proteins and cause the binding of the HMG1 region of proteins, triggering a signalling cascade that leads to apoptosis.

Mass spectrometry is a highly sensitive analytical technique. It is capable of using very small sample volumes and low concentrations, allowing the observation of species undetectable by other methods. Mass spectrometry has been widely used in the past to study drug-DNA interactions, including metal-based drugs such as cisplatin, and has proven to be very effective in determining the site of binding and the structure of the adduct.⁷⁻⁹

To determine the binding site of the drug, tandem mass spectrometry (MS/MS) is often used to fragment the DNA strand. These fragmentations are

dependent upon whether the MS is in the positive or the negative mode, the ionisation method, e.g. ESI and MALDI, and the type of fragmentation employed, e.g. collision induced dissociation (CID). The nomenclature for the cleavages of the oligonucleotide, shown in Figure 2.1, is analogous to that widely used for the fragmentation of peptide chains.¹⁰ There are four possible cleavages of the phosphate backbone, fragments containing the 5' terminus of the oligonucleotide are labelled a, b, c and d depending upon the position of the cleavage, with the corresponding fragments w, x, y, and z containing the 3' end of the strand. The number of the fragment indicates how many bases from the terminus that the cleavage occurred at.

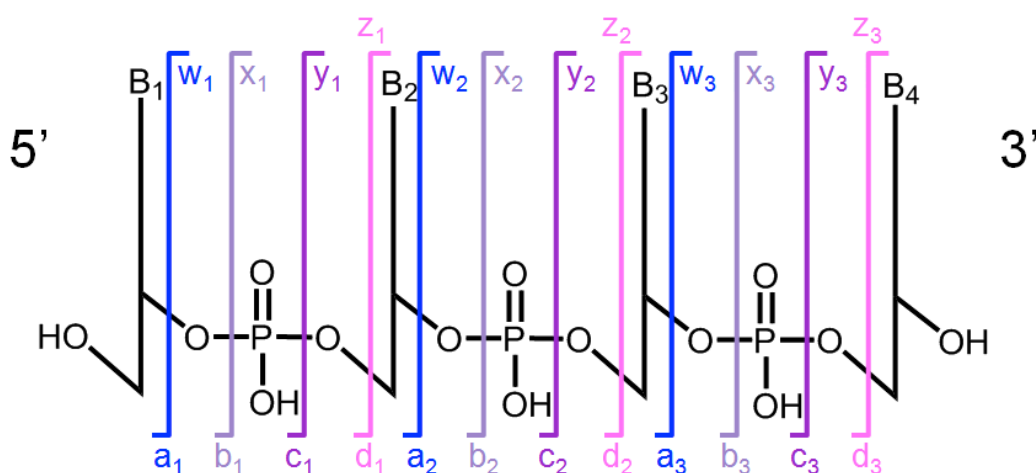


Figure 2.1 Nomenclature of oligonucleotide fragments caused by cleavage of the phosphate backbone (B represents a nucleobase). Figure adapted from McLuckey *et al.*¹⁰

2.2 Experimental

2.2.1 Materials

Complexes **1-10**, **8X** and **8Y** were synthesised according to literature procedures and characterised by ^1H NMR and elemental analysis.^{2,11-14} The purity and the 24-hour stability under low lighting conditions were determined by HPLC. The purity of the complexes was determined as > 96% for complexes **1-8**, 86% for **9** and 89% for **10**. The decrease in complex stability over 24 hours varied from \leq 5% decomposition for **1,2,5,6** and **8**, 5-10% for **4** and **10**, and 15-17% for **3**, **7** and **9** as determined by chromatogram peak areas (see Appendix II).

HPLC grade methanol and water for HPLC mobile phase were purchased from Fisher Scientific. Trifluoroacetic acid (TFA), spectrophotometric grade (99+%), was purchased from Sigma-Aldrich. Unless otherwise stated, all of the water used was doubly deionised water (DDW, with the exception of that used for HPLC), purified using a Multipore Milli Q and a USF Elga UHQ water deioniser. Omix pipette tips for micro extraction were purchased from Varian Inc. Amicon Stirred Cell and regenerated cellulose ultrafiltration membranes (25 mm diameter, 1 kDa cut-off) were purchased from Millipore.

Oligonucleotides. All oligonucleotides were purchased from DNA Technology A/S (Denmark), with sodium as the counter ion, and were purified twice by reversed-phase high performance liquid chromatography (RP-HPLC). All of the oligonucleotides used in these experiments were subject to in-house quality control checks. Quantification of these agents was carried out using UV-Vis spectroscopy,

Chapter 2 - Chapter 2 The interaction of photoactivatable Pt(IV) complexes with single strand oligonucleotides

recording the absorbance at 260 nm of a dilution of the stock sample and using the Beer-Lambert law to calculate the concentration of the original solution. The extinction coefficients were calculated with software using base composition and nearest neighbour models:¹⁵ oligo 1 $\epsilon_{260 \text{ nm}} = 145,100 \text{ M}^{-1}\text{cm}^{-1}$, oligo2 $\epsilon_{260 \text{ nm}} = 149800 \text{ M}^{-1}\text{cm}^{-1}$, and oligo 3 $\epsilon_{260 \text{ nm}} = 143,000 \text{ M}^{-1}\text{cm}^{-1}$. Mass spectrometry and HPLC were also used to confirm that the strand was of the correct mass and that it was of high purity.

2.2.2 Methods

2.2.2.1 Cellular uptake of Pt(IV)-diazido complexes and platinum content determination.

All of the work related to the culturing of cells, platinum accumulation studies and platinum detection by ICP-MS was carried out by Dr Ana Pizarro.

2.2.2.1.1 Cell Culture

The A2780 ovarian cancer cell line was obtained from the ECACC (European Collection of Animal Cell Culture, Salisbury, UK). The cells were maintained in RPMI 1640 media, which was supplemented with 10% foetal calf serum, 1% L-glutamine, and 1% penicillin/streptomycin. All cells were grown at 310 K in a humidified atmosphere containing 5% CO₂.

2.2.2.1.2 Platinum Accumulation in A2780 Human Ovarian Carcinoma Cells

A2780 cells were plated at a density of 5×10^6 cells/100 mm Petri dish in 10 mL of culture medium (three dishes were prepared per compound tested, and three untreated control dishes). After 24 h incubation, cells were treated with the Pt(IV) complexes and cisplatin for 1 h in the dark. Solutions of the platinum compounds (100 μ M) were prepared in 0.9% (w/v) saline and fresh media (1:10) containing 1% (v/v) DMSO. After 1 h of drug exposure at 310 K on a 5% CO₂ incubator, the drug-containing medium was removed, and the cell monolayers were washed with warm PBS twice, trypsinised, harvested and counted using a haemocytometer in the dark. The cells were centrifuged, quickly washed with cold PBS, and the cell pellets were stored at 253 K for determination of total cell accumulation (the net effect of uptake and efflux) of platinum in the dark. The cell pellets were digested in freshly distilled 72% (w/v) HNO₃ in Wheaton V-Vials with a PTFE-faced rubber-lined cap (Sigma-Aldrich) for 16 h at 373 K. After they were cooled, the samples were diluted with doubly dionised water (DDW) to a maximum final concentration of 7.2% (w/v) HNO₃ (suitable for ICP-MS analysis) prior to quantification of ¹⁹⁵Pt. The standard deviations are based on experiments performed in triplicate.

2.2.2.1.3 Inductively Coupled Plasma Mass Spectrometry (ICP-MS) Instrumentation and Calibration

All ICP-MS analyses were carried out on an Agilent Technologies 7500 series ICP-MS instrument (California, USA). The solvent used for ICP-MS analysis was

doubly deionized water (DDW). The Platinum Standard for ICP (Fluka, 1000 mg/L in 5% (w/v) HCl) was diluted with 7.2% HNO₃ (diluted with DDW from 72% (w/v) HNO₃, doubly distilled on-site) to freshly prepare calibrants at concentrations ranging from 200 to 0.1 ppb. The ICP-MS instrument was set to detect ¹⁹⁵Pt with a detection limit of 6.5 ppt using no-gas mode. The forward power was set to 1550 W, argon flow was 15 L/min, and the auxiliary gas flow was 0.9 L/min, with ¹⁶⁶Er used and the internal standard.

2.2.2.2 UV-Vis Spectroscopy

All UV-Vis electronic absorption spectra were performed on a Varian Cary 300 UV-Vis spectrophotometer with a temperature control block using 1 cm path-length cuvettes. All spectra were baseline corrected using pure solvent as a background. Data were processed using Microsoft Office Excel.

2.2.2.3 Light Sources

Photoactivation of Pt(IV) complexes was conducted using a LZC-ICH2 photoreactor (Luzchem Research Inc) with a temperature controller set at 310 K and fitted with LZC 420 lamps (Luzchem Research Inc., $\lambda_{\text{max}} = 420 \text{ nm}$).

2.2.2.4 Chromatography

Conditions for the lipophilicity studies to determine both purity and retention time determinations of Pt(IV)-diazido complexes were as follows. All experiments were carried out on the Agilent 1200 system using an Agilent Zorbax eclipse plus C18 column (5 μm particle size, 4.6 x 250 mm) column. Solvent A was

Chapter 2 - Chapter 2 The interaction of photoactivatable Pt(IV) complexes with single strand oligonucleotides

H₂O containing 0.1% TFA (v/v); Solvent B, MeOH containing 0.1% TFA (v/v); with a flow-rate of 1.00 mL/min. The solvent gradient began at 0% B rising to 30% B over 30 minutes. All injections were 50 µL of 100 µM solutions of each complex in DDW. All solutions were prepared with minimal exposure to light. The column was cleansed after each run with a high percentage of organic solvent, the column was then allowed to equilibrate to the starting conditions. The wavelength of detection was set at 254 nm.

HPLC studies of Pt-oligonucleotide interactions were carried out on an Agilent Technologies 1100 system with a Rheodyne 7725i manual injector fitted with a 100 µL loop and a variable wavelength UV detector. The mobile phases for all analyses were: solvent A, H₂O 10 mM NH₄OAc; solvent, B acetonitrile 10 mM NH₄OAc. All chromatograms were processed using ChemStation and Microsoft Office Excel.

All oligonucleotide purity tests were carried out on a Zorbax eclipse C18 strong-bond 250 x 4.6 mm column, with a particle size of 5 µm with 300 Å pores, a flow rate of 1.00 mL/min, wavelength of detection 260 nm and 50 µL injections. The gradients used were either 0 – 30 % B over 30 min, or 0 – 60 % B over 60 min, and the column oven was set to either 35°C or 40°C.

Separations involving the single-strand oligonucleotide were carried out on a Hichrom Ace C8 250 x 4.6 mm column, with a particle size of 5 µm with 300 Å pores. The solvent gradient was isocratic for the first 15 min at 7 % B, increased to 80 % B between 15 and 21 min, with a flow rate of 1 mL/min. The gradient

remained isocratic at 80 % until 30 min into the run, then decreased to 7 % B by 30.5 min, where it remained until the end of the run at 37 min, for the column to equilibrate back to the starting conditions. The flow rate was 1.00 mL/min, injections were of 50 μ L, the column oven was at 55°C and the wavelength of detection was set at 260 nm.

2.2.2.5 Mass spectrometry

Mass spectrometry was carried out on a Bruker HCT Ultra ion trap instrument in both positive and negative modes. The sample flow rate was 240 μ L/h, and scan ranges varied from 50 – 1000 m/z to 500 – 3000 m/z . The solvent used, cone voltage and source temperature varied depending on the sample analysed.

Most of the mass spectrometric data was high resolution mass spectrometry (HR-MS), and was carried out on a Bruker MaXis mass spectrometer. DNA samples were analysed in the negative mode (sample flow rate 100 μ L/h) Mass spectrometry work with the oligonucleotides was carried out in the negative mode (290 – 5000 m/z scan range), capillary 4000 V, end plate offset –500 V, dry gas 4.0 L/min, dry heater 180°C, nebuliser 0.4 bar. The acquisition parameters for spectra obtained in the positive mode are as follows: scan range 50 – 3000 m/z , set capillary 3000 V, end plate off-set –500 V, nebuliser pressure 0.4 bar, dry heater 180 °C, and dry gas 4.0 L/min. All data were acquired and processed with Bruker MicroTOF control Bruker Compas DataAnalysis (version 4.0) and OriginPro8.1.

All oligonucleotide samples analysed by MS were desalted to remove peaks due to sodium and potassium adducts, as well as improving signal intensity. Two different desalting methods were employed. The first method was to desalt using an Amicon Stirred Cell under N₂ gas (70 bar) using ultrafiltration membranes with a 1 kDa cut off. The sample volume was first reduced from 400 µL to 50 µL whilst stirring, and was then washed with two aliquots of 200 µL of DDW. The samples were then diluted 1 in 2 in 40 mM NH₄OAc in MeOH. The second method was to use Omix micro extraction C18 pipette tips, typically used to desalt peptides. The manufacturer's protocol was followed, eluting the sample in 20 mM NH₄OAc (Sigma Aldrich, 99.99%) and 80:20 MeOH/H₂O (v/v).

2.3 Results

The complexes studied in this work are platinum(IV)-diazido ones of the general formula *trans,trans,trans*-[Pt(N₃)₂(OH)₂(R)(R')], where R and R' are NH₃, methylamine, ethylamine, pyridine, 2-picoline, 3-picoline or thiazole. The structures of the 10 complexes and that of cisplatin, the standard metal-based anticancer drug, are shown in Figure 2.2. All of the following work was carried out under low-light conditions unless stated otherwise.

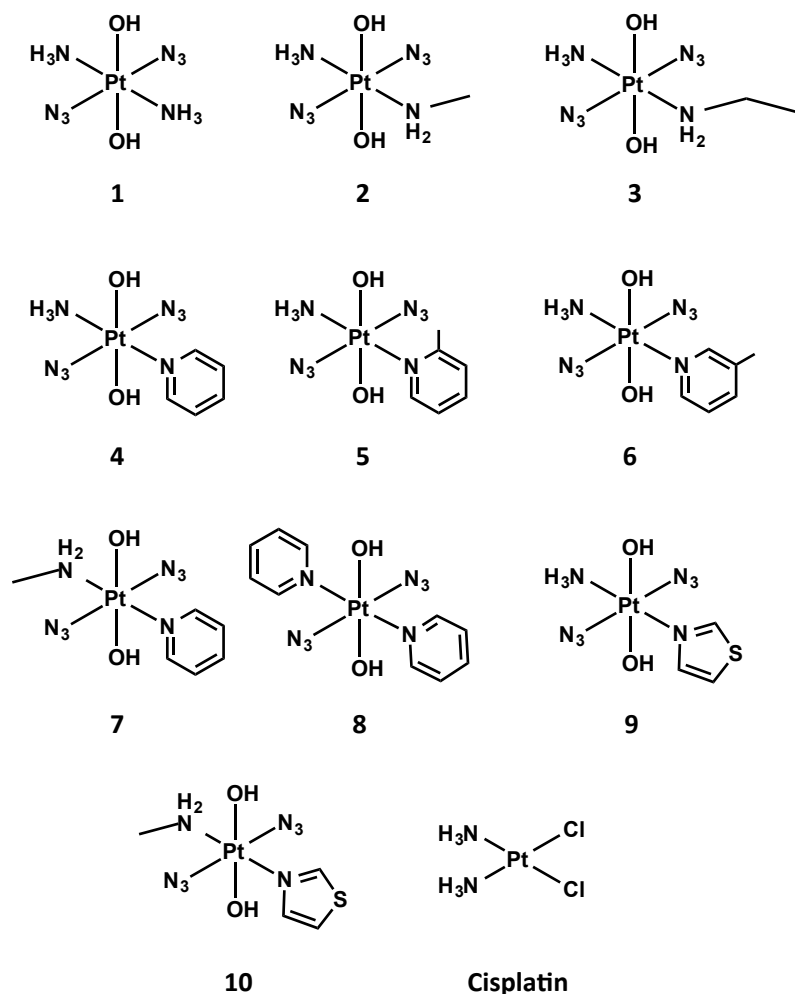


Figure 2.2 Structures of the Pt(IV) diazido complexes studied here and that of cisplatin.

2.3.1 Correlation between Lipophilicity and Cellular Accumulation of Platinum Complexes

2.3.1.1 Lipophilicity

The lipophilicity of the complexes **1** – **10** was initially studied using the shake flask octanol/water partition method.¹⁶ However, this method proved to be ineffective due to the very high hydrophilicity of the compounds. Instead, the time taken for the complexes to elute from a reversed phase (RP) HPLC column was used

as a measure of their lipophilicity for the purposes of comparison. This method also measures the partition between hydrophilic (mobile phase) and hydrophobic (stationary phase) phases, with the resulting retention time being intrinsic to that particular complex. The retention times (t_R) of the complexes are shown in Figure 2.3.

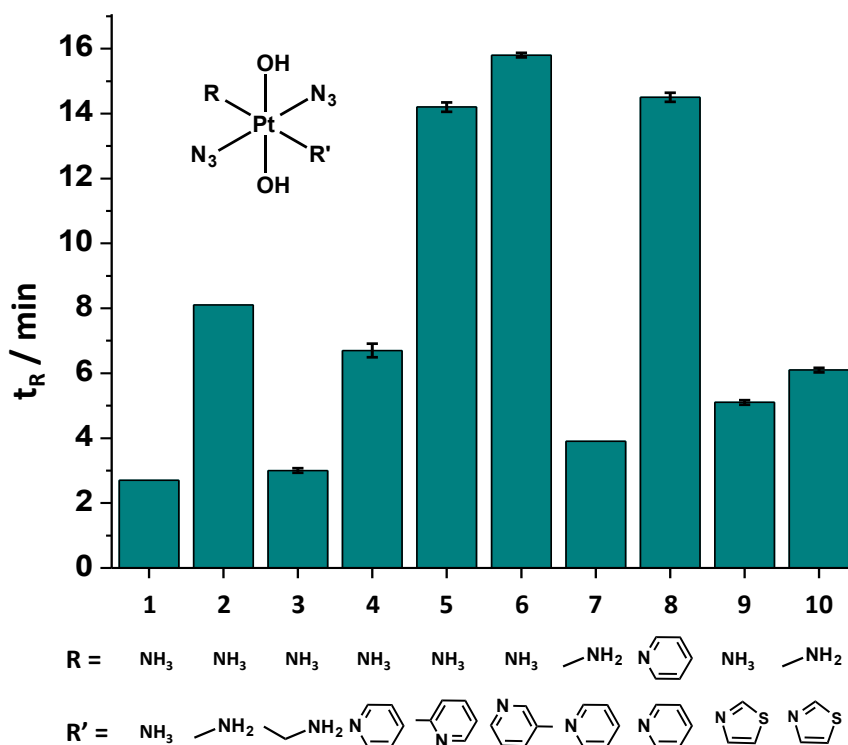


Figure 2.3 Retention times (t_R) of complexes **1-10** on a RP HPLC column. Solvent A was H₂O 0.1% TFA; solvent B, MeOH 0.1% TFA; with a flow rate of 1.00 mL/min. The solvent gradient began at 0% B rising to 30% B over 30 minutes. Solutions for the complexes were 100 μ M, and a 50 μ L aliquot of each solution was injected onto the column. The general structure of the complexes and the different ligands are also shown. Error bars are the standard deviation of two independent measurements.

Some trends observed are expected, for example complexes **1**, **4** and **8**. This series shows an increase in retention times and therefore in lipophilicity with the

sequential substitution of NH_3 groups for more hydrophobic pyridine (py) ligands. The series of complexes **4-6**, in which the py R' ligand has a methyl substituent at two different positions (2-picolino and 4-picolino) increasing both the hydrophobicity and the t_R . These complexes also fit into a series with complex **1**.

Complexes **2** and **7**, which contain methylamine ligands, have retention times that sit 'out of series'. Complexes **1** – **3** form a series of compounds that have an increasing carbon chain (from **1** to **3**), while the retention time of **3** (3.0 min) is longer than that of **1** (2.7 min), as expected due to the increased lipophilicity of the ethylamine ligand compared to the $-\text{NH}_3$ one. Compound **2** has a much higher retention time than that of **3** (8.1 min), and even higher than that of complex **4** (6.7 min), which has a more hydrophobic py ligand. Conversely, the retention time of complex **7** is shorter than expected in the series **4**, **7** and **8**. All of these complexes have a py R' group and the R group increases in hydrophobicity from **4** to **8**. The retention time of **7** (3.9 min) is less than that of **4** (6.7 min) and **8** (14.5 min).

The complex with a methylamine ligand that has a retention time that follows the predicted series is complex **10** (6.1 min). This compound is more hydrophobic than the amino complex **9** (5.1 min). The two compounds **9** and **10** with thiazole R' ligands have shorter t_{RS} values than those with py R' groups, with the exception of complex **7**.

2.3.1.2 Platinum Accumulation in A2780 Cells

The cellular accumulation studies in this section were carried out by Dr Ana Pizarro as were the measurements determining cellular Pt content. The conditions for the cellular accumulation tests were designed to mimic those used to determine the IC₅₀ values of the complexes.¹¹ The human ovarian A2780 cancer cells were exposed to 100 µM solutions of the drugs for 1.00 h in the dark. The platinum-based anticancer drug cisplatin was included as a positive control. The results for the cellular uptake are shown in terms of ng of platinum per million cells. This was determined by acidic digestion of the collected cells and the determination of their platinum content by ICP-MS. The results are shown in the form of a bar chart in Figure 2.4.

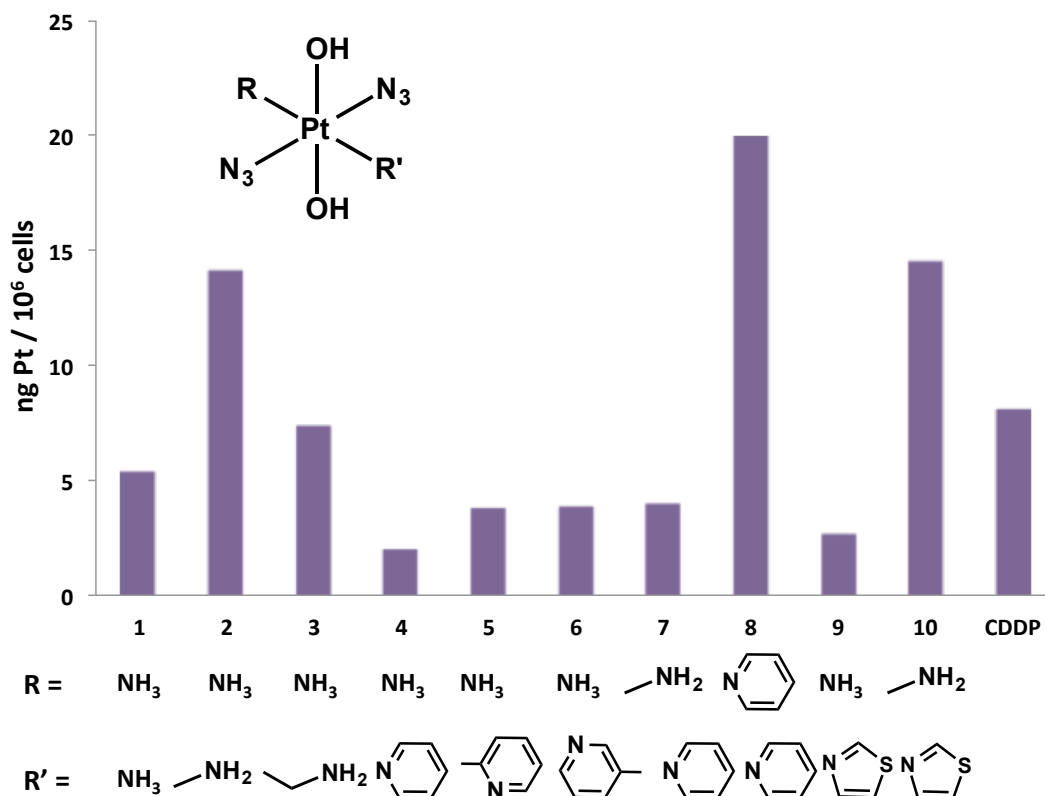


Figure 2.4 Cellular uptake of Pt(IV) diazido anticancer complexes (100 μ M solutions) in the dark and the established metal-based anticancer drug cisplatin. The results are represented in terms of ng of Pt accumulated per million cancer cells.

Complexes **1** – **3** are taken up into the cells following the same trend as that hydrophobicity, as determined by HPLC. Complexes **4**, **5** and **6** also follow the same trend as their lipophilicity, but their uptake is less than that of compound **1**. Overall, the compounds with a py or thiazole group have a lower cellular accumulation than those complexes without an aromatic ligand. The exceptions are complexes **8** and **10**, which are also the compounds with the highest cellular accumulation of platinum. The lack of correlation between t_R and cellular accumulation of platinum over the whole series is summarised in Figure 2.5.

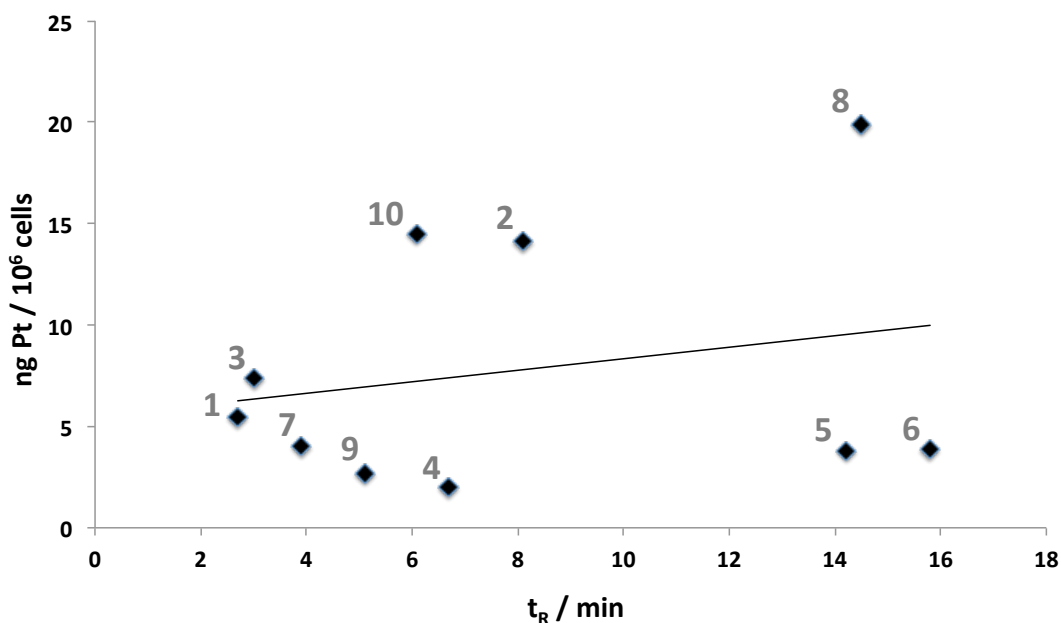


Figure 2.5 Plot of the HPLC retention times of compounds **1 – 10** and their cellular accumulation over 1 h of drug exposure to A2680 human ovarian carcinoma cells (ng of platinum/ million cells). The trendline is included to show a lack of correlation between IC₅₀ value and cellular accumulation of platinum (shown by the low correlation coefficient, R² value of 0.0531).

The relationship between the cellular accumulation in the dark and the IC₅₀ values, when irradiated with 365 nm light, of complexes **1-10** and cisplatin (CDDP) is shown in Figure 2.6. Complexes **1, 2, 3, 8** and **10** support the hypothesis that higher drug accumulation leads to greater potency. However, compounds **6, 7** and **9** are very active (< 6 μM) with low cellular accumulation (< 5 μM). This illustrates that many other factors, including quantum yield of the compound and the potency of the products of the photoreaction, are important for the efficacy of a photoactivatable drug. A summary of the chemical biological properties of complexes **1-10** is shown in Table 2.1.

Chapter 2 - Chapter 2 The interaction of photoactivatable Pt(IV) complexes with single strand oligonucleotides

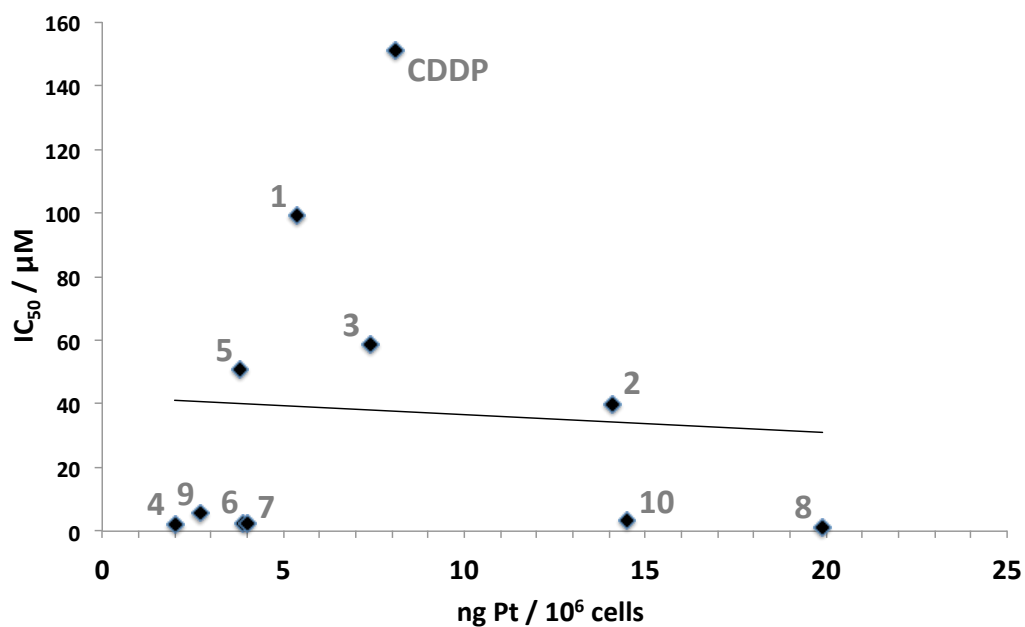


Figure 2.6 IC₅₀ for A2780 cancer cells after 1 h drug exposure (in the dark) and then irradiated for 1.00 h with 365 nm, in A2780 cancer cells of complexes **1 – 10** and cisplatin (CDDP) compared to the cellular accumulation of the complexes (ng of platinum/million cells). The trendline is included to show a lack of correlation between IC₅₀ value and cellular accumulation of platinum (R² value of 0.0227).

Table 2.1 Summary of the lipophilicity, cellular accumulation, IC₅₀ (365 nm irradiated) and IC₅₀ (dark). IC₅₀ values obtained by Dr Julie Woods of Ninewells Hospital, University of Dundee.^{13,11,14} Retention times are an average of 2 measurements ± the standard deviation.

Complex	t _R /min	Pt accumulation in A2780 ng Pt/10 ⁶ cells	IC ₅₀ irradiated with 365 nm light/μM	IC ₅₀ in the dark/μM
1	2.7 ± 0.0	5.4	99.2	> 287.9
2	8.1 ± 0.0	14.1	39.8	> 276.8
3	3.0 ± 0.07	7.4	58.4	> 266.3
4	6.7 ± 0.21	2.0	1.9	> 224.4
5	14.2 ± 0.14	3.8	51.0	> 236.3
6	15.8 ± 0.07	3.9	2.6	26.8
7	3.9 ± 0.0	4.0	2.3	> 236.3
8	14.5 ± 0.14	19.9	1.1	212.3
9	5.1 ± 0.07	2.7	5.5	186.9
10	6.1 ± 0.07	14.5	3.2	> 232.9
CDDP	NT	8.1	151.3	152

2.3.2 Study of photoactivatable Pt(IV) diazido complex interaction with oligonucleotides by chromatography

The most active Pt(IV) diazido complex studied in the previous section against A2780 cancer cell lines was compound **8** (*t,t,t*-[Pt(N₃)₂(OH)₂(py)₂). As DNA binding is thought to be the mechanism of action of Pt-based drugs currently in the

clinic,¹⁷ the interaction of the most promising drug candidate from the previous series of 10 compounds (complex **8**) with short single strand oligonucleotides is studied in this section of the chapter.

2.3.2.1 Interaction of t,t,t -[Pt(N₃)₂(OH)₂(py)₂] with oligonucleotide d'(ATACATGCTACATA)

A single strand oligonucleotide of sequence d'(ATACATGCTACATA), oligo 1, was purchased from DNA Technologies Europe A/S. This sequence contains one guanine residue, the preferred binding site for platinum-based drugs.¹⁸ The oligonucleotide was twice RP-HPLC purified and with Na⁺ as the counter ion. The oligonucleotide was quantified using UV-Vis absorption at 260 nm using a calculated extinction coefficient.¹⁵ An example of the UV-Vis spectrum of oligo 1 is shown in Figure 2.7. The purity of the oligonucleotide used was confirmed by HPLC (data not shown).

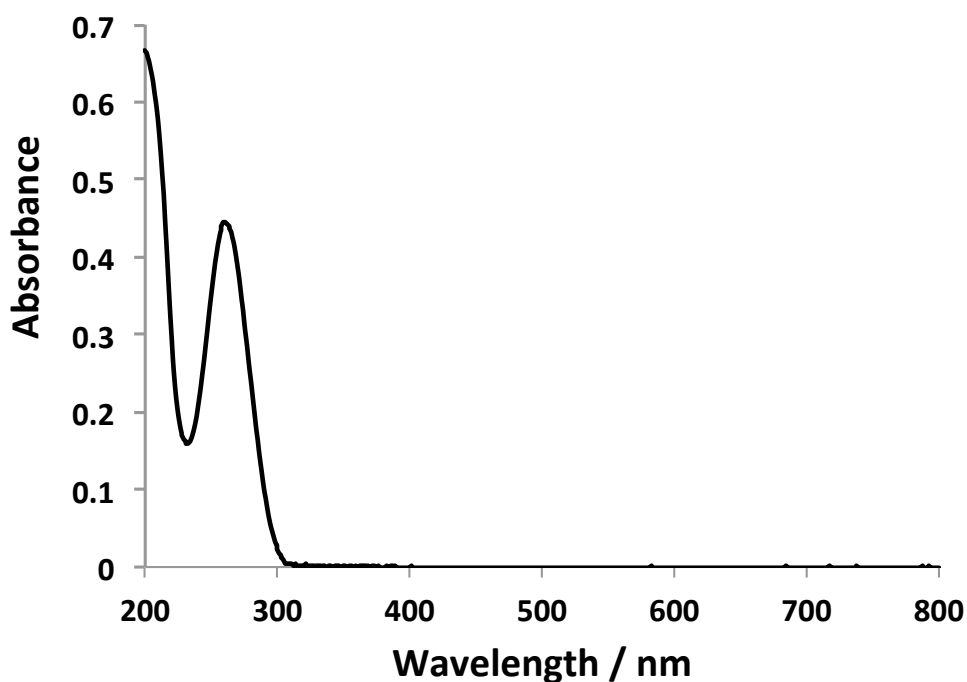


Figure 2.7 UV-Vis spectrum of d'(ATACATGCTACATA), oligo 1, in water used to determine the concentration of the oligonucleotide stock solution ($\epsilon_{260\text{nm}} = 145100 \text{ M}^{-1}\text{cm}^{-1}$).

The light source used to activate complex **8** in the presence of the oligonucleotide was a temperature-controlled photoreactor (Luzchem Research Inc). The arrangement of the bulbs within the photoreactor is shown in Figure 2.8. Each bulb was labelled with its corresponding position in the photoreactor so that the irradiation of each sample remained the same for all experiments. The temperature of the photoreactor was set at 37°C, to mimic biological conditions, for all experiments.

Chapter 2 - Chapter 2 The interaction of photoactivatable Pt(IV) complexes with single strand oligonucleotides

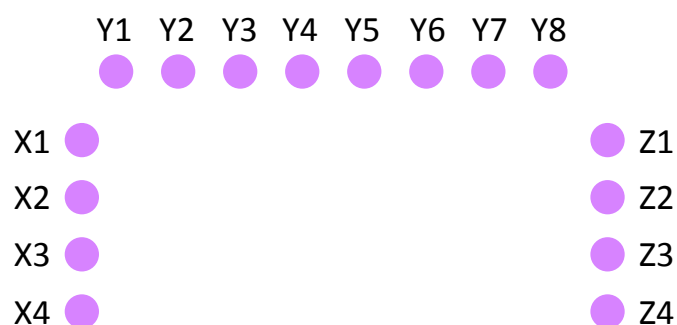


Figure 2.8 Top: photoreactor used for the sample irradiations in this chapter, bottom: schematic diagram of the bulb layout within the photoreactor.

A HPLC method was developed and optimised for the separation of single strand oligonucleotides from platinated oligonucleotides (Appendix III). The method was used to analyse the following reaction. A solution of complex **8** (500 μM) and oligo **1** (250 μM) in H_2O was irradiated for a 2 h period with aliquots taken every 30 min. Figure 2.9 shows the chromatograms of the aliquots taken before irradiation and after 30 min of irradiation with 365 nm light. Chromatogram A, a 1 in 10 dilution (in water) of the solution in the dark 2.00 min after solution mixing in the dark, shows 3 peaks, the first peak (t_R 3.9 min) corresponding to the oligonucleotide. This was confirmed by analysing an injection of just oligo **1** using

the same gradient. The following peaks (t_R 4.6 min and t_R 5.1 min) may be attributable to a folding of the oligonucleotide or a short-lived platinum-oligonucleotide adduct. It was not possible to characterise this species (nor to determine whether it contained platinum) due to its very low concentration. In chromatogram B (after 30 min of irradiation with 365 nm light) a new peak, (t_R 19.7 min) was observed, and this is assigned to a Pt-oligonucleotide adduct.

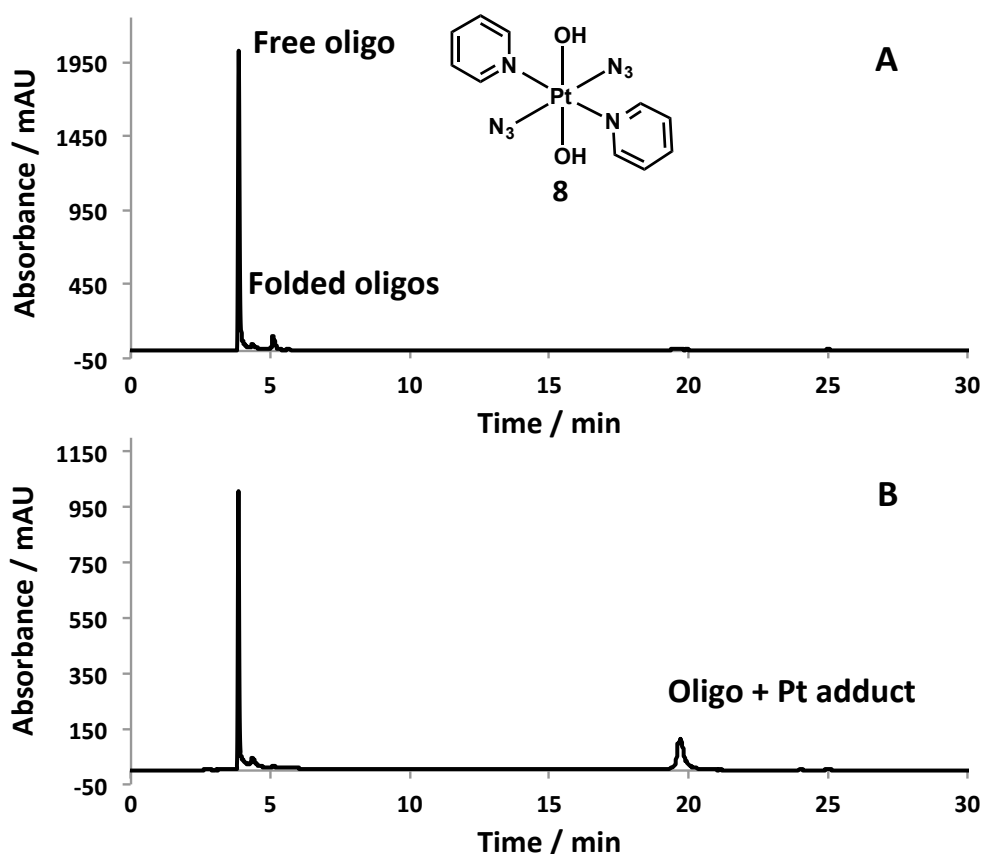


Figure 2.9 A solution of **8** (500 μM) and oligo 1, d'(ATACATGCTACATA), (250 μM): chromatogram A is a 1 in 10 dilution (in water) of the solution after 2 min of mixing in the dark; chromatogram B is a 1 in 10 dilution (in H_2O) of the solution after 30 min of irradiation with 365 nm at 37°C. Separation gradient was isocratic for the first 15 min at 7% B (v/v), increased to 80% B (v/v) between 15 and 21 min, with a flow rate of 1.00 mL/min, column oven temperature 55°C. Solvent A, 10 mM NH_4OAc H_2O ; solvent B, 10 mM NH_4OAc acetonitrile; wavelength of detection 260 nm.

The percentage of the integrated peak areas assigned as Pt-oligonucleotide adduct over the course of the 2.0 h irradiation period is shown in Figure 2.10. After 30 min the maximum amount of platinum is bound to the DNA and then reduces slightly over the next 90 min. It is within the error of the experiment that this reduction is not significant, and the maximum level of the platinated oligonucleotide is reached before 30 min and remains constant thereafter.

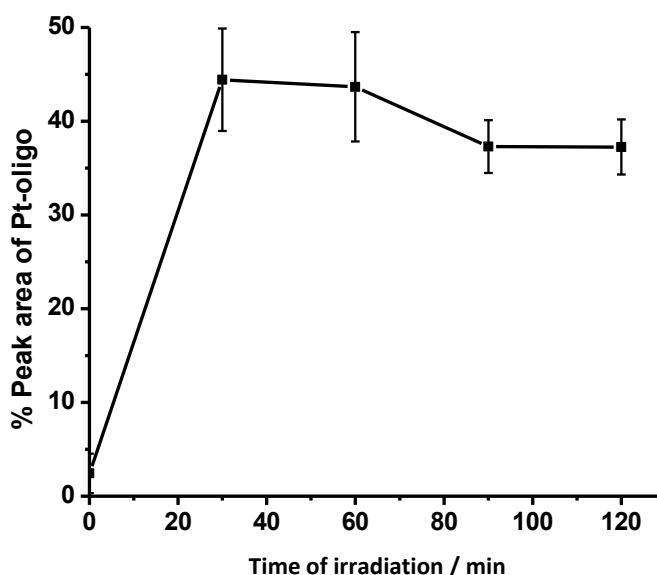


Figure 2.10 The percentage of the peak area corresponding to the Pt-oligonucleotide adduct (t_R 19.7 min) against the time of sample irradiation (complex **8**, 500 μM and oligo **1**, 250 μM) with 365 nm light at 37°C. Error bars are the standard deviation of 5 manual peak integrations of 3 independent experiments.

2.3.2.2 Sequence selectivity of Pt(IV) diazido complex oligonucleotide binding

The sequence selectivity for complex **8**, (t,t,t -[Pt(N₃)₂(OH)₂(py)₂], binding to single strand DNA was explored using three different oligonucleotides, each 14 bases in length.

Chapter 2 - Chapter 2 The interaction of photoactivatable Pt(IV) complexes with single strand oligonucleotides

The sequences are as follows:

oligo 1 d'(ATACATGCTACATA)

oligo 2 d'(ATACATGGTACATA)

oligo 3 d'(ATACGTGCTACATA)

The same irradiation procedure as stated for oligo 1 in Section 2.3.2 was applied to oligo 2 and 3. Chromatograms of **8** (500 μ M) and oligo 2 (250 μ M) in water are shown in Figure 2.11. Analysis of the solution in the dark, with 2.0 min after mixing, shown in chromatogram A indicates the presence of unreacted oligonucleotide (peak **1** t_R 3.86 min) and another species, possibly a folded strand, (peak **2** t_R 5.1 min). In chromatogram B, the solution irradiated with 365 nm for 30 min, contains a third peak attributable to a Pt-oligonucleotide adduct at 19.7 min.

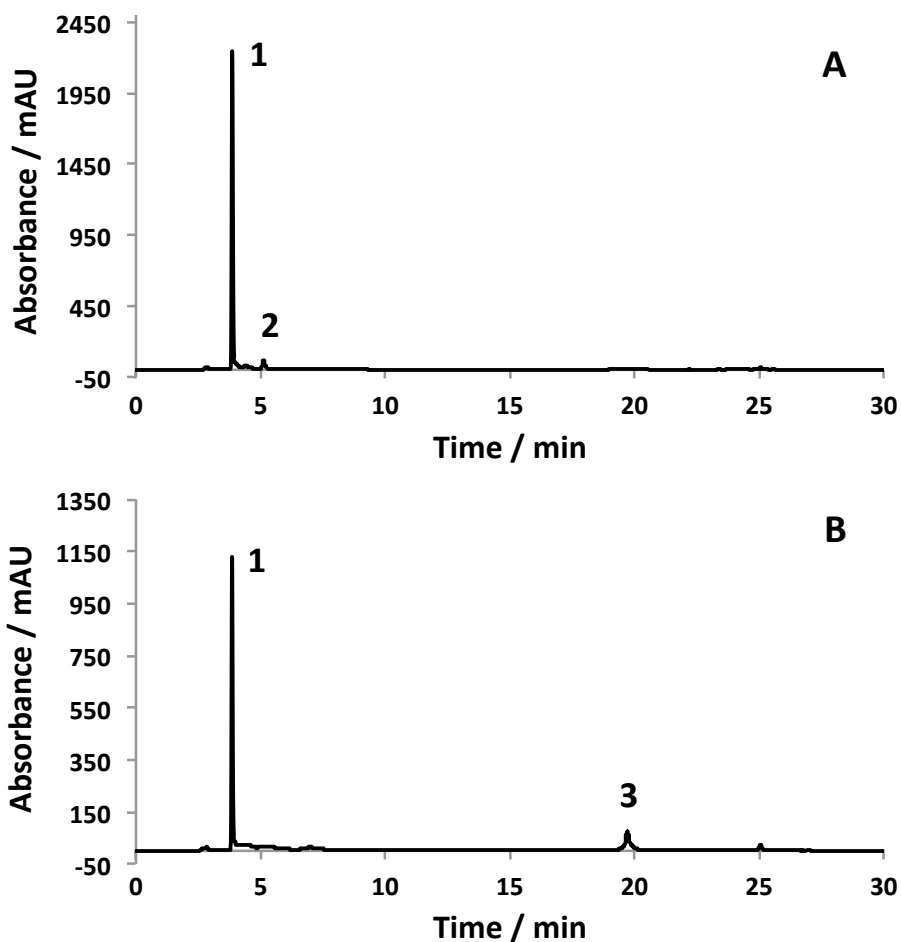


Figure 2.11 A solution of **8** (500 μM) and oligo 2 (250 μM) in water. Chromatogram A: a 1 in 10 dilution of the solution after 2 min mixing in the dark. Chromatogram B: a 1 in 10 dilution of the solution after 30 min of irradiation with 365 nm light at 37°C. Separation gradient was isocratic for the first 15 min at 7% B (v/v), increased to 80% B (v/v) between 15 and 21 min, with a flow rate of 1.00 mL/min, column oven temperature 55°C. Solvent A, 10 mM NH_4OAc H_2O ; solvent B, 10 mM NH_4OAc acetonitrile; wavelength of detection 260 nm.

The same protocol was also applied to oligo 3, with the results shown in Figure 2.12. The peak assigned as the oligonucleotide (t_R 3.9 min) can clearly be seen in the chromatogram of the solution in the dark (A). After irradiation a peak is observed at 19.67 min that is attributed to platinated oligonucleotide. This peak is

of a similar intensity to that of the platinated oligo 1 after 30 min of irradiation, but of a greater area than that of platinated oligo 2.

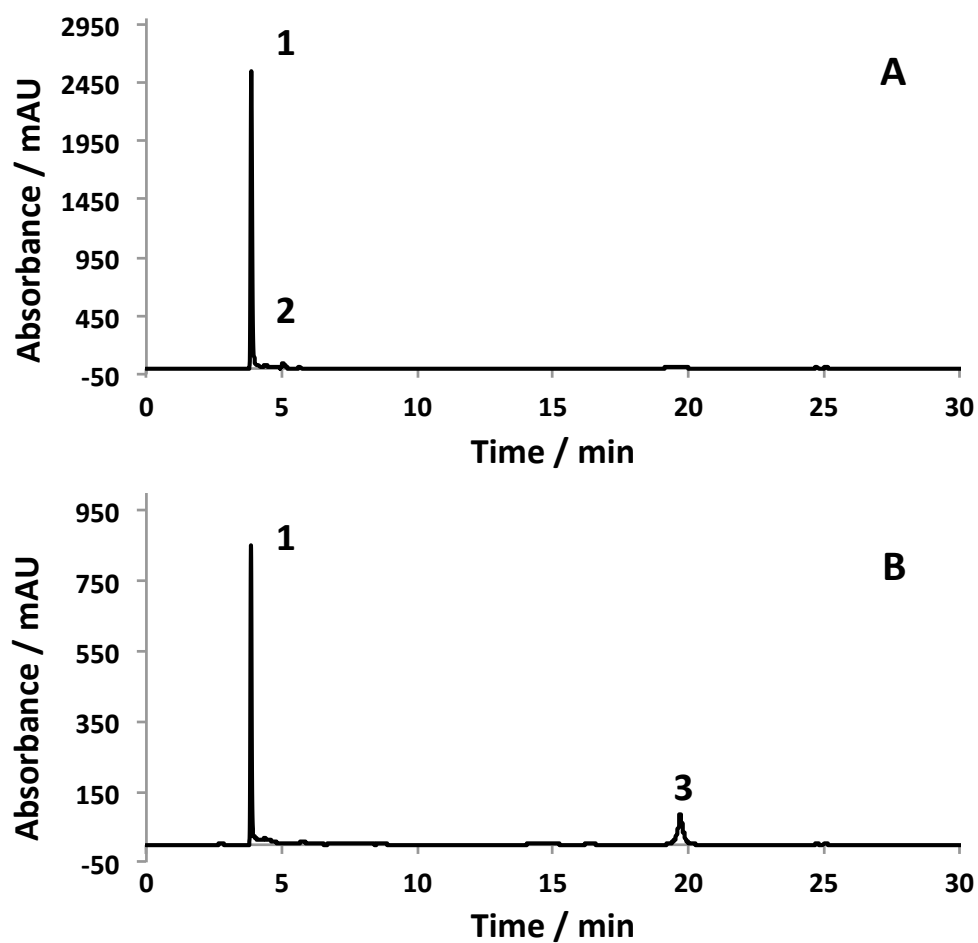


Figure 2.12 A solution of **8** (500 μ M) and oligo **3** (250 μ M) in H₂O. Chromatogram A: a 1 in 10 dilution of the solution after 2 min mixing in the dark. Chromatogram B: a 1 in 10 dilution of the solution after 30 min of irradiation with 365 nm light at 37°C. Separation gradient was isocratic for the first 15 min at 7% B (v/v), increased to 80% B (v/v) between 15 and 21 min, with a flow rate of 1.00 mL/min, column oven temperature 55°C. Solvent A, 10 mM NH₄OAc H₂O; solvent B, 10 mM NH₄OAc acetonitrile; wavelength of detection 260 nm.

The rates of platination of the three oligonucleotides are compared in Figure 2.13. After 30 min of irradiation with 365 nm UVA, the maximum level of platination was attained or had almost been reached, regardless of the oligonucleotide sequence. The percentage peak area attributed to the platinated oligonucleotide after 120 min of irradiation with 365 nm UVA for each of the strands follows the following trend: oligo 1 > oligo 3 > oligo 2, see Table 2.2. There is very little difference between the percentage peak areas attributed to platinated DNA for oligo 1 and 3. The percentage peak areas of platinated oligonucleotide for oligo 2 is almost a third less than that for the other strands, suggesting that oligo 2 offers less favourable binding sites.

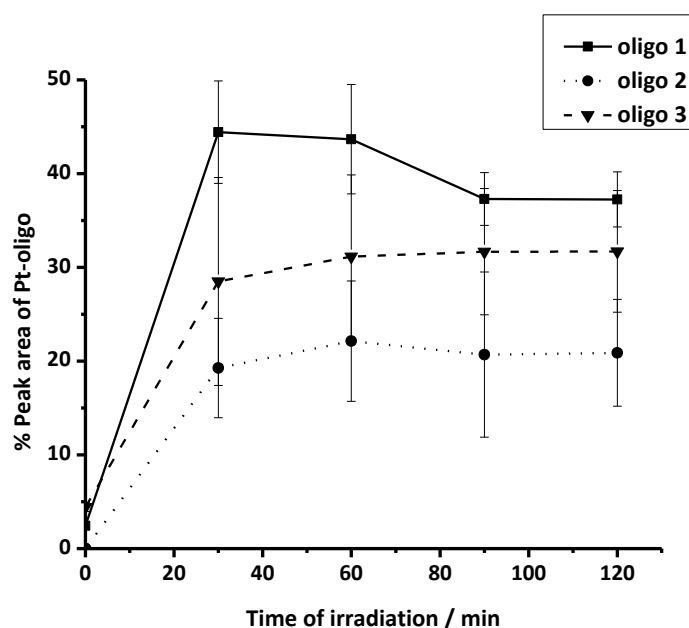


Figure 2.13 The percentage of the peak area within the chromatogram attributed to the three platinated oligonucleotides and how this changes when irradiated with 365 nm light. Values are averaged over a minimum of 2 experiments, with 5 manual integrations taken for each experiment (error bars are the standard deviations of these values).

Table 2.2 The percentage peak area attributable to platinated oligonucleotide for oligo 1, d'(ATACATGCTACATA), oligo 2, d'(ATACATGGTACATA), and oligo 3, d'(ATACGTGCTACATA) at time 0 and 120 min of irradiation. Error bars are the standard deviations of a minimum of 2 independent experiments, each manually intergrated 5 times.

Time of irradiation (365 nm) / min	Oligo 1 % peak area of platinated DNA	Oligo 2 % peak area of platinated DNA	Oligo 3 % peak area of platinated DNA
0	3.52 (\pm 2.10)	0 (\pm 0.0)	4.44 (\pm 0.47)
120	33.92 (\pm 2.94)	20.88 (\pm 5.70)	31.70 (\pm 6.49)

2.3.2.3 Wavelength of activation of Pt(IV) diazido complexes

Longer wavelength light is preferred for *in vivo* drug activation, as it penetrates further into tissue.^{19,20} Complex **8** can be activated by wavelengths of light as long as green light.¹³ To investigate if a different wavelength of activation produces a change in the DNA adduct formed by **8** and oligo 1, a set of 420 nm bulbs was fitted in the photoreactor (in the same arrangement as shown in Figure 2.8). The same protocol as in Section 2.3.2.1 was then carried out using this longer wavelength of light. Figure 2.14 (chromatogram A) shows the solution of **8** (500 μ M) and oligo 1, d'(ATACATGCTACATA), (250 μ M) 2 min after mixing in the dark (and diluted 1 in 10 in water). Three peaks can be observed in this chromatogram: **1** is attributable to oligo 1 (t_R 3.9 min), the second (**2** t_R 4.5 min) and third (**3** t_R 5.1 min) to folded forms of the oligonucleotide. After the solution had been irradiated for 30 min with 420 nm light (chromatogram B, Figure 2.14) a new peak (**4**) at 19.7 min is detected. This is the same retention time as the peak assigned as the platinated oligo 1 when a similar solution was irradiated with 365 nm UVA, Fig 2.9.

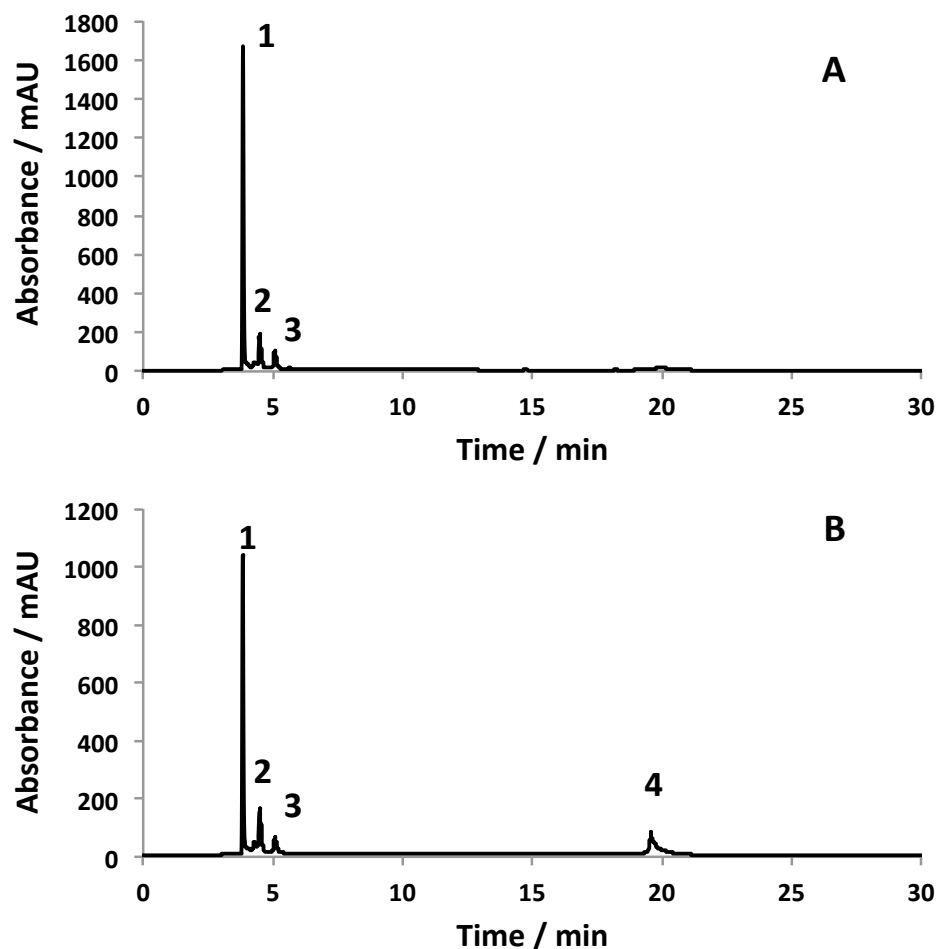


Figure 2.14 A solution of **8** (500 μM) and oligo **1** (250 μM) in H_2O . Chromatogram A: a 1 in 10 dilution of the solution after 2 min mixing in the dark. Chromatogram B: a 1 in 10 dilution of the solution after 30 min of irradiation with 420 nm light at 37°C. Separation gradient was isocratic for the first 15 min at 7% B (v/v), increased to 80% B (v/v) between 15 and 21 min, with a flow rate of 1.00 mL/min, column oven temperature 55°C. Solvent A, 10 mM NH_4OAc H_2O ; solvent B, 10 mM NH_4OAc acetonitrile; wavelength of absorption 260 nm.

The platination of oligo **1** in the presence of **8** irradiated with either 365 nm or 420 nm light over a period of 2 h are compared in Figure 2.15. The solution irradiated with 365 nm light reaches a maximum amount of oligonucleotide platination after 30 min of irradiation. The solution irradiated with the longer wavelength of 420 nm light takes 60 min to achieve the same level of platination.

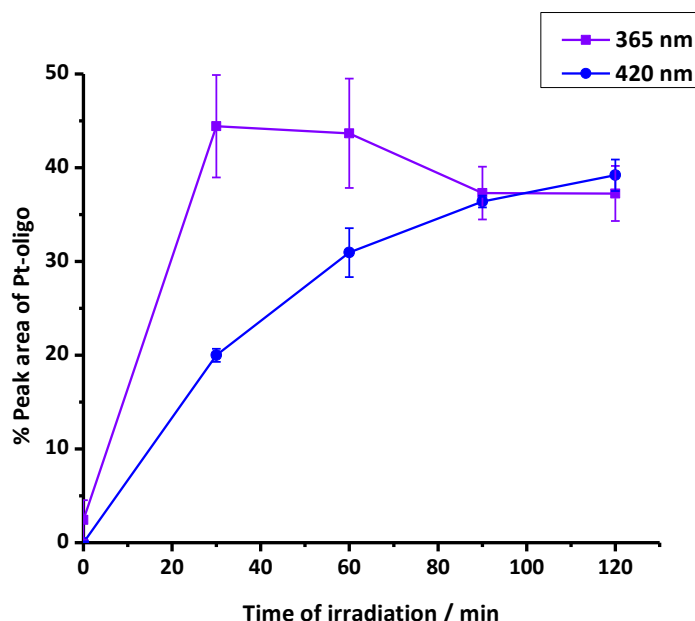


Figure 2.15 Graph of the percentage of the peak area within the chromatogram attributed to the platinated oligonucleotide and how this percentage changes with irradiation with 365 nm and 420 nm light over a period of 2 h. Values are averaged over a minimum of 2 experiments, with 5 manual integrations taken for each experiment (error bars are the standard deviations of these values).

2.3.3 Photoactivatable Pt(IV) diazido complex interaction with an oligonucleotide

by mass spectrometry

2.3.3.1 Interaction of *trans,trans,trans*-[Pt(N₃)₂(OH)₂(py)₂] and oligo 1

The chromatography-based studies of Section 2.3.2 suggest that the irradiation of **8** (*t,t,t*-[Pt(N₃)₂(OH)₂(py)₂]) in the presence of an oligonucleotide generates a platinum species that binds to the DNA. Mass spectrometry was used to characterise this new adduct once it was bound to the oligonucleotide. Initially, a de-salting protocol was developed as the excess salt bound to the oligonucleotide in solution could potentially damage the mass spectrometer, if it was sprayed into the instrument, e.g. block the skimmer cone. Salt adducts of the DNA would also be

detected and could potentially overlap with species of interest in the resulting mass spectrum. An Amicon stirred cell with 1 kDa cut-off ultrafiltration membrane was used, as outlined in Section 2.2.1.7, in order to de-salt the oligonucleotide samples. The spectrum of an 8 μ M solution of desalted oligo 1, d'(ATACATGCTACATA), in 40 mM NH₄OAc 80% MeOH/20% H₂O in the negative-ion mode is shown in Figure 2.16; the ⁻4 at 1056.179 *m/z* (predicted 1056.184 *m/z*) and ⁻3 at 1408.574 *m/z* (predicted 1408.581 *m/z*) charge states were observed. Throughout this work the fully protonated form of an oligonucleotide will be referred to as M, i.e. the ⁻4 charge state of oligo 1 has 9 additional protons.

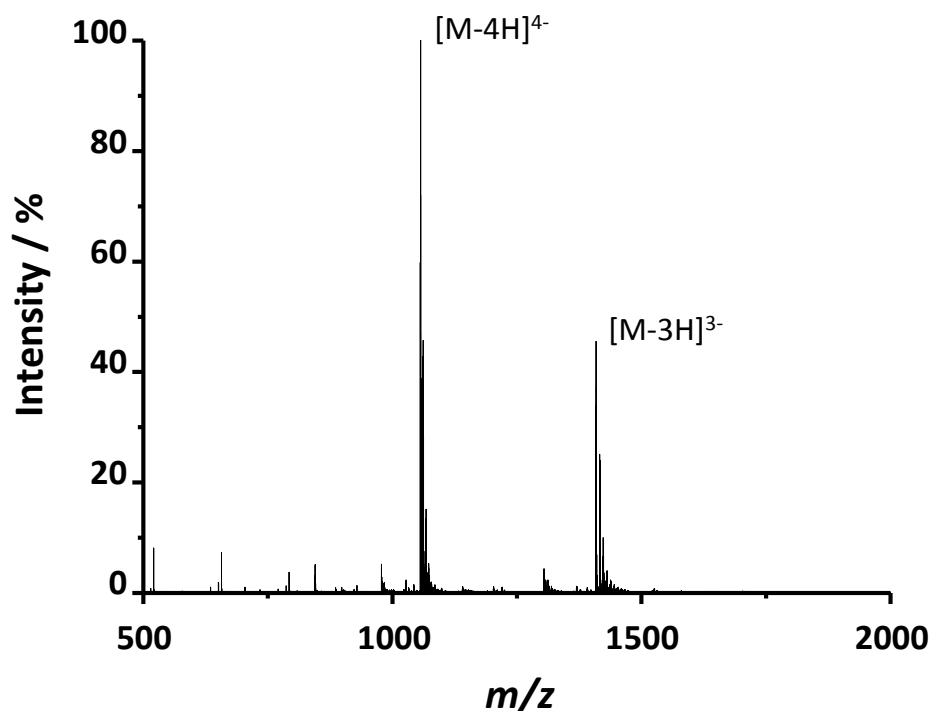


Figure 2.16 High resolution mass spectrum of oligo 1 (8 μ M) in 40 mM NH₄OAc 80% MeOH/20% H₂O (v/v) in the negative ion mode.

Analogous experiments to those analysed by chromatography in section 2.3.2 were carried out and the resulting solutions investigated by mass spectrometry. The spectrum of **8** (250 μ M) irradiated with 365 nm light in the presence of oligo 1 (250 μ M), following de-salting, is shown in Figure 2.17. The $^{-3}$ (1408.913 m/z) and $^{-4}$ (1056.439 m/z) charge states of oligo 1 were detected, as well as the $^{-3}$ at 1525.601 m/z (1525.592 m/z) and $^{-4}$ at 1143.946 m/z (1143.943 m/z) charge states of another species. The isotopic pattern of these peaks suggest that they contain platinum, and the m/z values would suggest that the new species is [oligo 1 + [Pt(py)₂]]. This is believed to be the Pt-oligonucleotide adduct observed after irradiation with 365 nm light at 19.67 min in Chromatogram B, Figure 2.12.

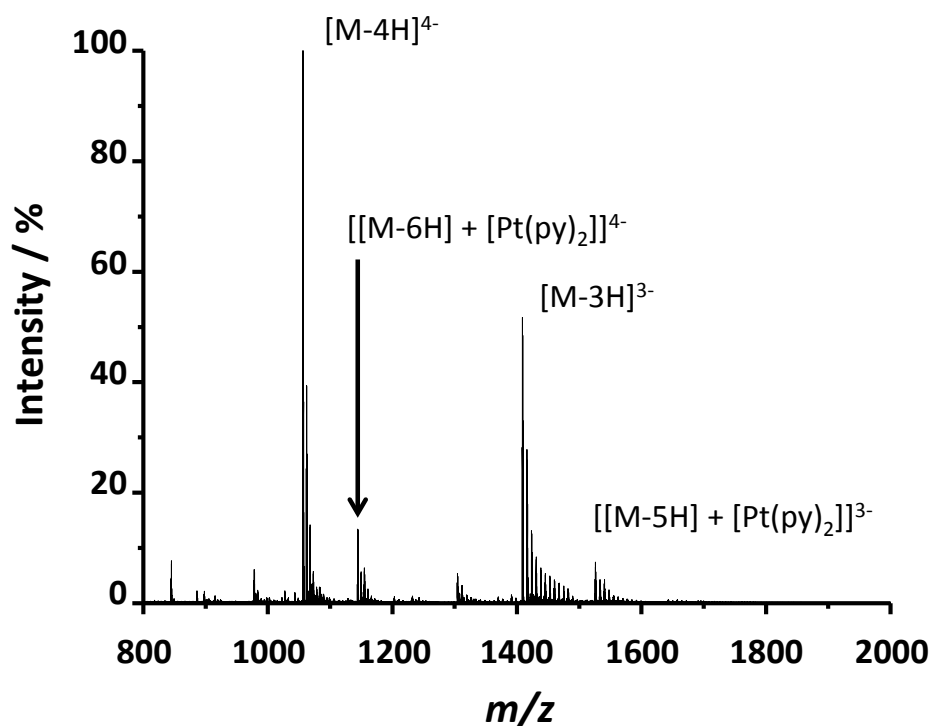


Figure 2.17 A solution of **8** (250 μ M) and oligo 1 (250 μ M) irradiated with 365 nm light for 30 min. High resolution mass spectrum of the desalted solution, final oligo concentration approx. 8 μ M, in 40 mM NH₄OAc 80% MeOH/20% H₂O in the negative ion mode.

The chromatographic data in Section 2.3.2 suggest only a difference in the rate of Pt-oligonucleotide adduct formation and not in the type of DNA lesion formed when the wavelength of activation of **8** is changed. To confirm this, a solution of **8** (250 μM) was irradiated with 420 nm light for 60 min in the presence of oligo 1 (250 μM). This solution was then de-salted and the mass spectrum recorded, see Fig.2.18. The $^{-3}$ and $^{-4}$ charge states of oligo 1 and [oligo 1 + [Pt(py)₂]] were again observed as shown in Figure 2.17.

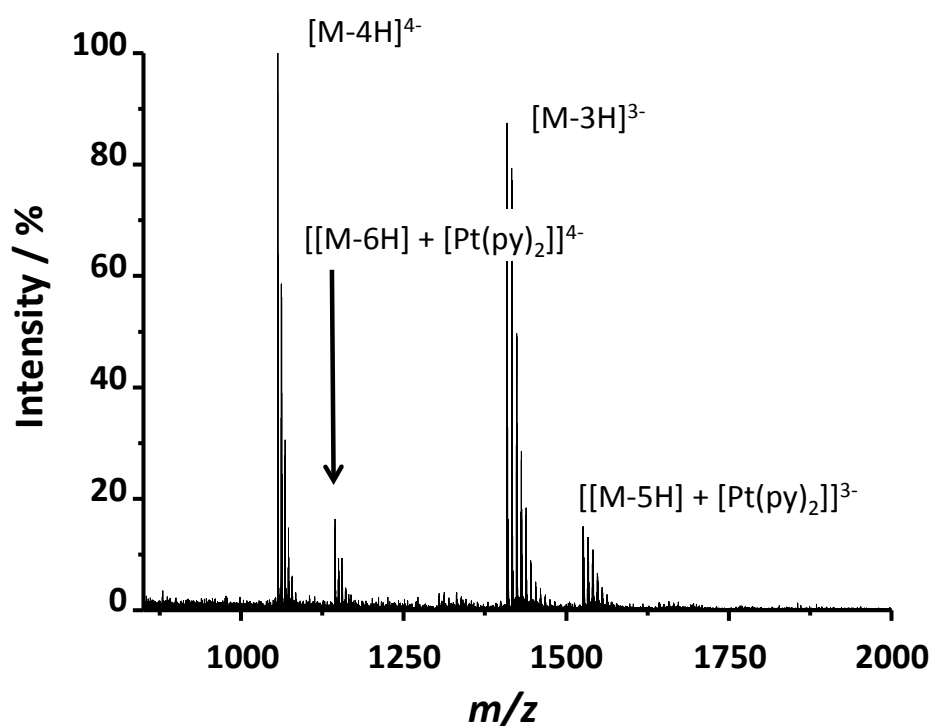


Figure 2.18 A solution of **8** (250 μM) and oligo 1 (250 μM) irradiated with 420 nm light for 60 min. High resolution mass spectrum of the desalted solution, final oligo concentration approx. 8 μM , in 40 mM NH₄OAc 80% MeOH 20% H₂O in the negative ion mode.

The effect of using a 1:1 molar ratio of **8** to oligo 1 in the irradiation experiments studied by mass spectrometry (instead of the 2:1 molar ratio used in

the chromatographic experiments) was explored by analysing a solution with a 2:1 ratio by mass spectrometry. A solution of **8** (500 μM) was irradiated with 420 nm light for 60 min in the presence of oligo 1 (250 μM) and de-salted. The mass spectrum of this solution is shown in Figure 2.19. In addition to the $\bar{3}$ (1408.574 m/z) and $\bar{4}$ (1056.179 m/z) charge states of oligo 1, and the same charge states of [oligo 1 + $[\text{Pt}(\text{py})_2]$] (1525.601 m/z and 1143.456 m/z , respectively), a set of low intensity peaks, also with $\bar{3}$ at (1642.556 m/z) (1642.604 m/z) and $\bar{4}$ at 1231.667 m/z (1231.701 m/z) charge states, assigned as [oligo 1 + 2 $[\text{Pt}(\text{py})_2]$], was observed.

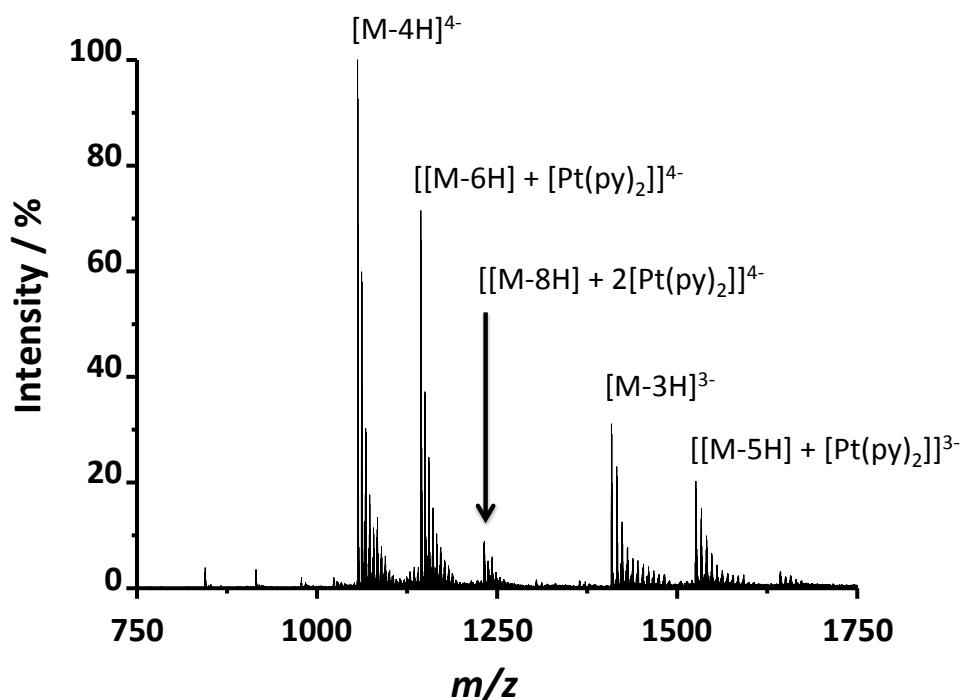


Figure 2.19 A solution of **8** (500 μM) and oligo 1 (250 μM) irradiated with 420 nm light for 60 min. High resolution mass spectrum of the desalted solution, final oligo concentration approx. 8 μM , in 40 mM NH_4OAc 80% MeOH/20% H_2O in the negative ion mode.

2.3.3.2 Platinum oligonucleotide interaction monitored by mass spectrometry – ¹⁵N labelled complexes

In the previous section the platinum adduct formed after photoactivation of **8** (*t,t,t*-[Pt(N₃)₂(OH)₂(py)₂) in the presence of oligo 1, d'(ATACATGCTACATA), was characterised as [oligo 1 + [Pt(py)₂]]. Figure 2.20 shows the fit of the deconvoluted observed peak due to [oligo 1 + [Pt(py)₂]] to the predicted pattern (Bruker Daltonics data analysis). To confirm the assignment in section 2.3.3.1 ¹⁵N labelled complex **8** was also photoactivated in the presence of oligo 1.

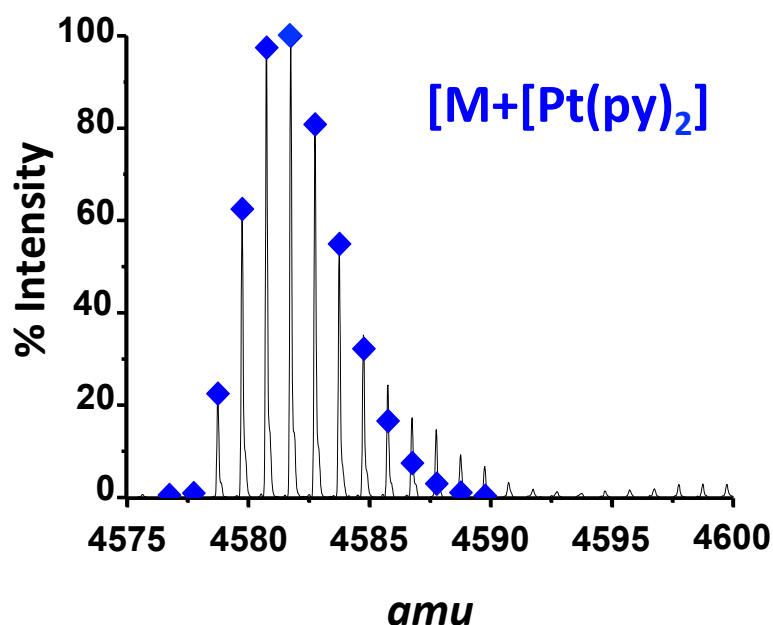


Figure 2.20 Deconvoluted spectra of (–) observed and (◆) predicted peak patterns of [M+[Pt(py)₂]].

An isotopically-labelled complex **8**, **8X** *trans,trans,trans*-[Pt(N₃)₂(OH)₂(¹⁵Npy)₂], (500 μM) containing two ¹⁵N atoms, one in each of the py

ligands, was irradiated with 420 nm light in the presence of oligo 1 (250 μ M). The same protocol was carried out using complex **8Y**, *trans,trans,trans*-[Pt(15 N₃)₂(OH)₂(15 Npy)₂], compound **8** with an 15 N label on each of the py ligands, and one 15 N atom on each of the azido ligands. The resulting deconvoluted spectra of the de-salted solutions, and of complex **8** with oligo 1, are shown in Figure 2.21. When the strand was reacted with **8X**, the platinated oligonucleotide peak shifts by 2 atomic mass units (see Fig. 2.21 spectra X and Z), indicating the presence of two 15 N labelled atoms. The same reaction with the doubly-labelled complex **8Y** gave an identical spectrum to that of the singly-labelled complex (Fig. 2.21 spectrum Y). It can therefore be concluded that the azide ligands are no longer bound to the platinum metal centre after the adduct is formed.

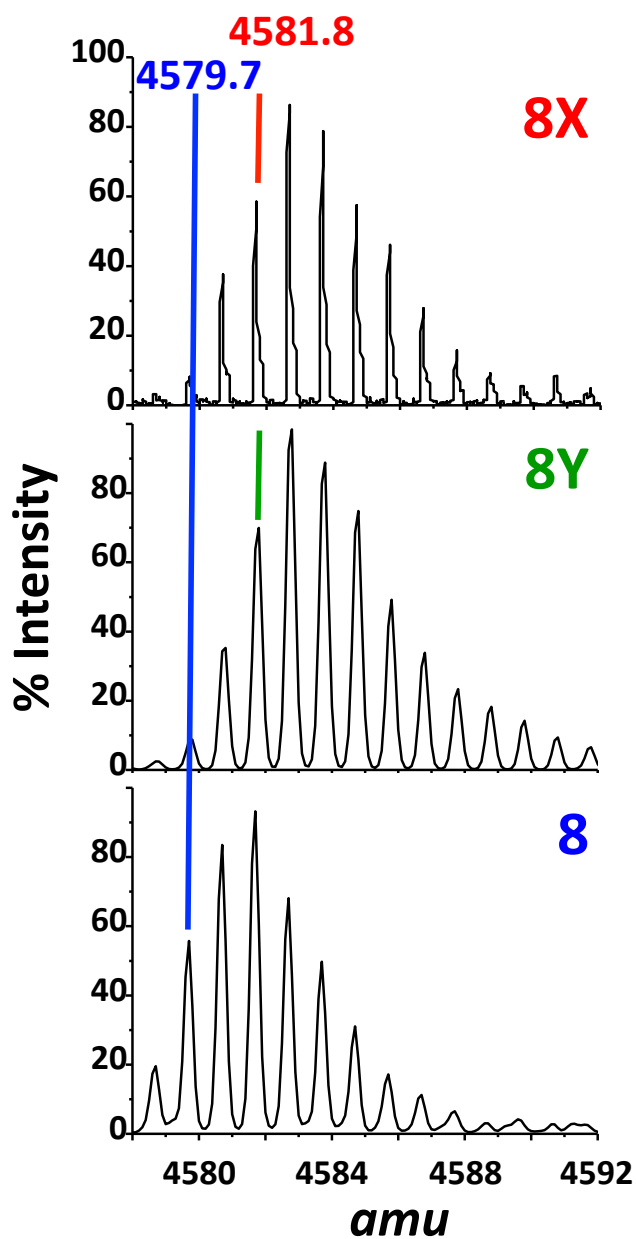


Figure 2.21 Deconvoluted spectra of the photoproducts of oligo 1, d'(ATACATGCTACATA), irradiated for 60 min in the presence of **8X**: t,t -[Pt(N₃)₂(OH)₂(¹⁵Npy)₂]; **8Y**: t,t -[Pt(¹⁵N₃)₂(OH)₂(¹⁵Npy)₂]; and **8**: compound **8**, t,t -[Pt(N₃)₂(OH)₂(py)₂]. In 80% MeOH, 40 mM NH₄OAc.

2.4 Discussion

2.4.1 Lipophilicity

The lipophilicity of a potential drug is an important property and can prove useful in the selection of promising new candidates. Indeed a drug's lipophilicity is key to its pharmacokinetics and its pharmaceutical properties. It can be used as an indication of how well a drug can pass through the cell membrane, and hence this can influence its activity *in vivo*. The hydrophobicity of a drug is thought to be crucial for its adsorption, distribution, metabolism and excretion in patients. It is one of only four fundamental properties listed in Lipinski's rules for an ideal organic drug molecule,²¹ and although they were not intended for inorganic drugs they can be applied to their design. Lipinski's 'rules of five' states that an orally-active drug should have a Log P value of less than 5 (later revised to between -0.4 and 5.6).²²

Typically the shake-flask method is used to determine the octanol/water partition factor Log P. Use of triplicates of triplicate measurements by the shake flask method, using ICP-MS for platinum detection, did not produce a single reproducible value and hence the method was abandoned in favour of measuring relative hydrophobicities by HPLC. Chromatography is often used to investigate the lipophilicity of compounds using octanol and water as the mobile phase,²³ or more commonly determining the retention times in RP-HPLC²⁴⁻²⁷. This involves determining the relative hydrophobicity of the compounds by a chromatographic method, and the retention times of a range of compounds with known Log P values. The k' value of each compound is then calculated according to equation 1, where t_R

is the retention time of the compound and t_0 is the dead time of the system. The value of k' can then be input into equation 2,²⁴ where a and b are constants, and by plotting the known Log P values, against the log of their k' values a, and b can be determined, and the unknown Log P values calculated.

$$k' = \frac{(t_R - t_0)}{t_0} \quad (1)$$

$$\text{Log P} = a \log k' + b \quad (2)$$

Unfortunately, this method requires a range of calibrants that have a similar range of Log P values to those under investigation. As noted above, it has not been possible to determine Log P values for such hydrophilic platinum complexes. The Log P value of cisplatin has been determined as -2.19, but Hambley *et al.* it found to be as low as -2.53, an average of all of the reported values is -2.32.²⁸⁻³² Since complexes **1-10**, of the general formula *trans,trans,trans*-[Pt(N₃)₂(OH)₂(R)(R')], contain two hydroxido ligands, it is expected that they would be even more hydrophilic than cisplatin. Complex **4**, *t,t,t*-[Pt(N₃)₂(OH)₂(py)(NH₃)], for example, has a solubility of 50 mM in H₂O.¹¹ As it was not possible to obtain a range of compounds with known Log P values similar to those predicted for complexes **1 – 10**, only relative comparisons between the complexes can be made.

Assumptions about the lipophilicity of a given compound based on the properties of a set of ligands, in this case the literature Log P values of R and R' (see Table 2.3), were not in agreement with the data obtained; for example, the methylamine-containing complex **2**, *t,t,t*-[Pt(N₃)₂(OH)₂(NH₃)(NH₂CH₃)], is more

Chapter 2 - Chapter 2 The interaction of photoactivatable Pt(IV) complexes with single strand oligonucleotides

lipophilic than complex **7**, t,t,t -[Pt(N₃)₂(OH)₂(NH₂CH₃)(py)]. Compounds **1** (t,t,t -[Pt(N₃)₂(OH)₂(NH₃)₂]), **2** and **3** (t,t,t -[Pt(N₃)₂(OH)₂(NH₃)(NH₂CH₂CH₃)]) comprise a series of increasingly hydrophobic compounds on consideration of to the R' ligands. However, **2** had the highest retention time of the series (t_R =8.1 min), see Fig 2.3, higher than that of complex **4** (t_R =6.7 min), where R' = py. In the case of compound **7**, in the series **4**, **7**, **8**, t,t,t -[Pt(N₃)₂(OH)₂(NH₂CH₃)(py)], where the R group increases in hydrophobicity from **4** (t_R =6.7 min) to **8** (t_R =14.5 min), the retention time of **7** (t_R =3.9 min) is much shorter than expected. The unusual behaviour of these two complexes cannot be attributed to the methylamine ligand alone, as compound **10**, t,t,t -[Pt(N₃)₂(OH)₂(NH₂CH₃)(thiazole)], has a retention time that follows a lipophilic trend with complex **9**, t,t,t -[Pt(N₃)₂(OH)₂(NH₃)(thiazole)].

Table 2.3 Literature Log P values for the R and R' ligands of complexes **1 – 10**, * indicates a predicted value.

Ligand	Log P
NH ₃	-1.38 ³³
NH ₂ CH ₃	-0.57 ³⁴
NH ₂ CH ₂ CH ₃	-0.13 ³⁴
py	0.65 ³⁴
2-pic	1.19±0.19* ³⁵
4-pic	1.22 ³³
tz	0.44±0.29* ³⁶

Chapter 2 - Chapter 2 The interaction of photoactivatable Pt(IV) complexes with single strand oligonucleotides

There are some theoretical trends in lipophilicity, based on the values in Table 2.3, that are borne out by data acquired. For example, with the sequential substitution of NH_3 groups by more hydrophobic pyridine (py) ligands in the series **1**, t,t,t -[Pt(N_3)₂(OH)₂(NH_3)₂] ($t_R = 2.7$), **4**, t,t,t -[Pt(N_3)₂(OH)₂(NH_3)(py)], ($t_R = 6.7$ min), **8**, t,t,t -[Pt(N_3)₂(OH)₂(py)₂], ($t_R = 14.5$ min) leads to increased retention times. This is also true of the series **4-6** in which the py R' ligand has a methyl substituent added at two different positions (2-picoline, complex **5**, and 4-picoline, complex **6**). However, this series, whilst in agreement with the retention time of **1**, has an unexpectedly high t_R value, **5** (14.2 min)

These results suggest that the overall lipophilicity of a metal complex is affected by more than just the properties of the individual ligands. Indeed, attempts to predict the lipophilicity of Pt(IV) compounds by computational methods have had to take this into account. Oldfield *et al.* developed a quantitative structure-property relationship (QSPR) for platinum complexes based on density functional theory (DFT) calculations, and reported literature Log P values.^{31,32} This proved much more effective than relying upon predictions made using values based on the ligand properties alone, consistent with the discrepancies in the data reported here. Gramatica *et al.* report a similar approach to modelling QSPRs for platinum based complexes, where a lipophilic descriptor and an electronic descriptor are used to predict the lipophilicity of the whole compound.³⁷ This type of method has been refined by Ermondi *et al.* to include VolSurf descriptors (descriptors based on 3D molecular fields) for improving the accuracy of the

predictions.³⁸ This new QSPR model shows the importance, not just of the lipophilicity of the substituent parts of the molecule, but also of its size and hydrophobic interactions, specifically, that ligand orientation and subsequent surface exposure to solvent are very important in determining the overall lipophilicity of the complex. This supports data reported in Section 2.3.1.1 and the findings that the lipophilicity cannot be predicted merely by ligand structure alone and the solvation of the molecule must be considered.

The findings of Oldfield^{31,32} and Ermondi³⁸ go some way to explaining the anomalous results observed in Section 2.3.1.1, but there are other factors to consider. The partitioning of a complex between the mobile and stationary chromatographic phases is a pH dependent process. This phenomenon was used by Wiczling *et al.* to develop an HPLC-based approach to deriving Log P and pK_a values of drugs by altering the pH value of the mobile phase.³⁹ The experiments reported in this chapter used a mobile phase containing an ion-pairing agent to ensure that any charged species could be detected according to their hydrophobicity. In this case the ion-pairing agent used was trifluoroacetic acid (TFA), which reduced the pH of the mobile phase to 1.7. Ronconi *et al.* found that for complexes of the type $[\text{Pt}(\text{N}_3)_2(\text{OH})_2(\text{R})(\text{R}')]]$, the pK_a for the deprotonation of the first hydroxyl group is around pH 3, for example for complex **1** the pK_a value is 3.42 ± 0.01 .⁴⁰ Alteration of the am(m)ine ligands in the *trans,trans,cis*- $[\text{Pt}(\text{N}_3)_2(\text{OH})_2(\text{R})(\text{R}')]]$ isomer had little effect on the pK_a of the hydroxyl group. Hence, all of the complexes should be protonated in the aqueous mobile phase at pH 1.7.

The use of an ion-pairing agent, combined with the low pH value indicates that the complexes are protonated in the mobile phase and associated with the ion pairing agent, i.e. the surface presented to the solvent molecules and the stationary phase may be different from that of the complex alone. As previously discussed, the interaction of a complex with solvent can have a significant effect on its retention time and perceived lipophilicity. This suggests that the relative hydrophobicities measured are of the TFA-associated molecules not of complexes **1** – **10**. However, it was necessary to include the TFA to allow for the separation and detection of any charged Pt(II) impurities, and also to prevent peak broadening. This problem associated with measuring lipophilicities by HPLC again highlights the fact that there are many factors that contribute to a compound's lipophilicity, and it is not determined by the properties of the ligands alone.

2.4.2 Platinum Accumulation in A2780 Cells

It has previously been reported that, as is the case with many drugs, the lipophilicity of Pt(IV) drugs has a positive correlation with their cellular accumulation.^{30,41} In the case of the complexes investigated by Oldfield *et al*, this relationship showed a dramatic increase in uptake for complexes with positive Log P values.³¹ The reported higher Log P values were achieved by modifying the axial ligands, and hence, increasing their hydrophobicity. The work in this chapter compares the relative lipophilicity of ten Pt(IV) diazido complexes, of the general formula *trans,trans,trans*-[Pt(N₃)₂(OH)₂(R)(R')], with their cellular accumulation after 1 h of exposure to 100 μM drug solutions in the dark. Data presented in

Figures 2.4 and 2.5 show no correlation between the relative lipophilicity of the complexes and their cellular accumulation across the series **1** – **10**. However, there are some sub-series that do exhibit the expected relationship: complexes **1** – **3**, and complexes **9** and **10**. Of these two sub series **9** and **10** also followed the predicted pattern of relative lipophilicity. The trend in cellular accumulation for complexes **1** – **3** followed the same, if unexpected, pattern as that of their relative lipophilicity. However, the cellular uptake of the sub-series **4** – **6** shows a slightly different trend to that of their lipophilicities. The cellular accumulation of **5** (3.8 ng Pt / 10⁶ cells), and **6** (3.9 ng Pt / 10⁶ cells) is slightly higher than that of **4** (2.0 ng Pt / 10⁶ cells) and there is a much smaller difference between their retention times, **4** (t_R = 6.7 min), **5** (t_R = 14.2 min), **6** (t_R = 15.8 min). The sub-series **1**, **4**, and **8**, contains the complex accumulated the most in the cells, complex **8**, *t,t,t*-[Pt(N₃)₂(OH)₂(py)₂], which also has the longest retention time of the *t* (t_R = 14.5 min) and so follows the expected lipophilic trend. Of the other complexes in the sub-series (complexes **1** and **4**), complex **1** also seems to exhibit a correlation between lipophilicity and cellular accumulation, but complex **4** shows only a poor uptake (2.0 ng / 10⁶ cells), the lowest of all ten compounds investigated.

There is a lack of correlation between the lipophilicity of complexes **1-10**, as determined by their chromatographic retention time, and their cellular accumulation in A2780 cancer cells. A correlation between these two properties, along with linear uptake, non-saturable uptake kinetics, and a lack of competitive uptake inhibition by analogues, are indicative of passive diffusion.^{42,43} Platinum(II)

Chapter 2 - Chapter 2 The interaction of photoactivatable Pt(IV) complexes with single strand oligonucleotides

complexes have already been reported as entering cells by active transport via the copper transporter CTR1 and organic cation transporters 1 and 2.⁴⁴⁻⁴⁸ Active efflux of cisplatin by the copper efflux transporters ATP7A and ATP7B, or efflux of Pt-glutathione conjugates by the GS-X efflux transporters, has also been reported.⁴² Therefore it may be possible for these Pt(IV) diazido complexes to enter cells by similar means.

This particular class of Pt(IV) diazido complex is highly water soluble, typically in the tens of millimolar range, and yet 4 out of 10 of the series are accumulated to a similar or to a higher level than the established platinum-based drug cisplatin, see Table 2.1. The lack of correlation between their lipophilicity and cellular accumulation suggests that these Pt(IV) diazido complexes enter cells by more than passive diffusion alone. It is also possible that the Pt(IV) complexes have been reduced before they enter the cell, explaining the lack of correlation. The cell culture medium used in the drug accumulation experiments (RPMI) contains amino acids and, phosphate in large excess (when compared to the platinum complexes) that are capable of reducing the complexes. The -OH axial ligands employed do increase the stability of Pt(IV) complexes, as shown by Hambley et al.⁴⁹ This along with the short exposure time used in the experiments minimises the likelihood of reduction taking place but may not prevent it entirely. The new Pt(II) species then may react further with species in the media.

The relationship between the cellular accumulation of complexes **1** – **10** and their antiproliferative activity in A2780 cancer cells, after activation for 1 h with 365

nm UVA, is summarised in Figure 2.6. There is no correlation across the whole series between the two, but this could arise for several reasons. The complexes under investigation are prodrugs that must be photoactivated to become effective. Therefore, the quantum yield (the amount of complex converted per photon of energy absorbed) is a key factor in generating enough of the active species to achieve cell death. The efficacy of established platinum-based drugs such as cisplatin is attributed to the activation of apoptotic pathways by the binding of DNA repair proteins to lesions formed on DNA by the metal complex. The nature of the lesion formed by different platinum complexes is thought to be responsible for their differences in their activities.⁵²⁻⁵⁵ It is worth noting that the most active complex, **8**, had the highest level of cellular accumulation, the highest relative lipophilicity (see Table 2.1) and has a quantum yield of 0.105 at 365 nm (for a 3.00 mM solution).¹³ All of these factors may contribute to the increased potency of this complex.

As a class of compound these potential anticancer drugs have been shown to be highly active when irradiated with 365 nm UVA in A2780 cancer cells, in some cases (complexes **6-10**) more than an order of magnitude more active than cisplatin. They are highly active, even with the very short 1.00 h drug exposure time and 1 h irradiation time. Only two compounds, **6** ($IC_{50} = 26.8 \mu M$) and **9** ($IC_{50} = 186.9 \mu M$), exhibit any significant dark toxicity, and only one of these two (**6**) is more active in the dark cisplatin ($IC_{50} = 152 \mu M$). All other compounds have a dark IC_{50} value higher than 210 μM , greater than the concentration range used. These data

highlight the temporal and spatial targeting offered by this exciting class of drug. Further investigation of their behaviour once they have entered the cell is required to gain more insight into the mechanism of action of these drugs.

2.4.3 Study of photoactivatable Pt(IV) diazido complex interaction with oligonucleotides by chromatography

The very low IC_{50} of photoactivated complex **8**, *t,t,t*-[Pt(N₃)₂(OH)₂(NH₂CH₃)(py)] in cancer cells, along with its high cellular accumulation and relative lipophilicity make it an interesting candidate for study. As much is already known about the most of the factors affecting the efficacy of this photoactivatable drug, such as the quantum yield, the DNA adducts formed by the complex upon activation with light was investigated. Some studies involving the interaction of **8** with calf thymus DNA have been reported,⁵⁶ suggesting that after photactivation **8** binds to DNA 16 times more than cisplatin and forms lesions distinctly different to that of those formed by transplatin and cisplatin. In the study reported here, short single strand oligonucleotides were selected for analysis by mass spectrometry in order to replicate the increased concentration of single stranded DNA in the rapidly proliferating cancer cells.

Chromatography is an analytical technique that has been used to study the interaction of metal-based drugs with DNA. The early work of Eastman followed the reaction of cisplatin with deoxyribonucleosides by HPLC and ¹H NMR.⁵⁷ More common metal-based drugs are reacted with calf thymus DNA, enzymatically digested and the resulting mixture is analysed by HPLC.^{58-61,17} The use of controls

and reactions of the drug with individual nucleotides allowed for the identification and quantification of the adducts formed with calf thymus DNA or cellular DNA. In this study, undigested DNA was used as only short strands were reacted with the drug. An HPLC method was developed specifically for the separation of short-strand oligonucleotides, and those with platinum adducts bound to them.

Complex **8** (500 μM) was irradiated with 365 nm UVA in the presence of d'(ATACATGCTACATA), oligo 1, (250 μM) in water at 37°C for 2.00 h. Aliquots were taken every 30 min and analysed by HPLC. Time points at 0 and 30 min of irradiation are shown in Figure 2.9. After 30 min of irradiation, a new peak was detected at 19.7 min, assigned as a platinated strand oligo 1. There appears to be only one new species generated by the photoactivation of **8** in the presence of oligo 1. However, due to the steep solvent gradient at this point of the HPLC method, it is possible that more than one species may be contained within one peak of the chromatogram. In the case of cisplatin it is known that there are several types of Pt(II)-DNA adducts formed, 1,2-d(GpG), 1,2-d(ApG), and 1,3-d(GpNpG).^{62,63} The second generation platinum drug carboplatin displays a similar DNA-binding profile,⁶⁴ as does oxaliplatin.^{65,54,66} The efficacy of all three drugs is reliant upon the 1,2-d(GpG) adducts. There is a smaller peak at 5.1 min possibly due to a folding of the oligonucleotide, the DNA folding prediction programme mfold predicts the formation of a hairpin at 37°C, and 0.5 mM Na⁺ see Figure 2.22,⁶⁷ as the retention time is very similar to that of oligo 1 and is also present in the chromatogram of the solution on the dark.

Chapter 2 - Chapter 2 The interaction of photoactivatable Pt(IV) complexes with single strand oligonucleotides

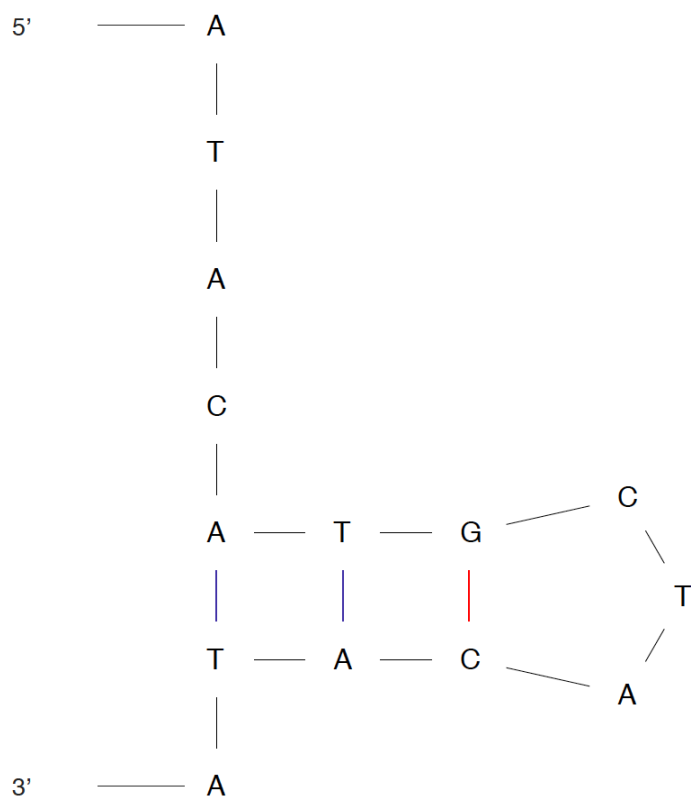


Figure 2.22 Structure of the hairpin formed by oligo 1, d'(ATACATGCTACATA), at 37°C, 0.5 mM Na⁺.⁶⁷

2.4.4 Sequence selectivity of Pt(IV) diazido complex oligonucleotide binding

The binding of **8** to three different oligonucleotide sequences was compared. The sequences of the strands are:

oligo 1 d'(ATACATGCTACATA)

oligo 2 d'(ATACATGGTACATA)

oligo 3 d'(ATACGTGCTACATA)

Chapter 2 - Chapter 2 The interaction of photoactivatable Pt(IV) complexes with single strand oligonucleotides

Each strand offers the possibility of the formation of several bis- and mono-adducts of Pt complexes. Oligo 1 would allow the Pt(II) photoactivated form of complex **8** to create mono-adducts, likely at N7 of guanine and N7 or N1 of adenine, 1,3-d(ApNpG) bis-adducts. All of these adducts could still be formed when **8** is irradiated in the presence of oligo 2, with the additional possibility of forming a 1,2-d(GpG) bis-adduct (the type of adduct responsible for the antiproliferative activity of cisplatin). Photoactivation of **8** in the presence of oligo 3 can, once again, lead to the formation of the same type of adducts that could be formed with oligo 1, with the addition of a 1,3-d(GpNpG) bis-adduct.

The three oligonucleotides (250 μ M) were reacted with complex **8** (500 μ M) and oligo 2 (250 μ M) in water was then irradiated with 365 nm UVA for 2.00 h, with aliquots taken every 30 min. The results for oligo 1, oligo 2 and oligo 3 are shown in Figures 2.9, 2.10 and 2.11 respectively. All of the solutions, when equilibrated in the dark for 2 min after mixing, showed no reaction with **8**. The chromatograms of the solutions irradiated with 365 nm for 30 min, labelled as chromatogram B in the figures, contains a peak at 19.7 min attributable to a Pt-oligonucleotide adduct. Comparing the rates of platination of the three oligonucleotides, see Figure 2.13, the percentage peak area attributed to the platinated oligonucleotide follows the trend: oligo 1 > oligo 3 > oligo 2.

The fact that binding of the photoactivated form of **8** to oligo 2 is disfavoured supports the findings of Pracharova *et al.* that the DNA lesions of **8** are different to those formed by cisplatin, since oligo contains the classical cisplatin

1,2(GpG) DNA binding site.⁵⁶ Small differences in the bend induced in the double helix of DNA by the 1,2-d(GpG) lesion caused by oxaliplatin, are 3° - 4° less compared to that of cisplatin,⁶⁸ is thought to be responsible for oxaliplatin's increased potency in colorectal cancer cells, previously not treatable with cisplatin.⁶⁹ However, the interaction of the multinuclear platinum-base drug BBR3464 of Farrell *et al.* with DNA gives rise to a unique binding mode.⁷⁰ The mechanism of these multinuclear drugs involves the induction of cell autophagy, before the activation of apoptotic pathways in order to achieve cell death;⁷¹ this may give rise to their activity in cisplatin-resistant cell lines.

Prachova *et al.*, reported that **8** forms a 1,3-d(GpNpG) bis-adduct. The findings of this study that binding to oligos 1 and 3 both containing either 1,3-d(ApNpG) or 1,3-d(GpNpG) binding modes supports their findings. The increased steric bulk of the py ligands of **8** (compared to the NH₃ ligands of cisplatin) could cause the 1,2-d(GpG) adduct to be disfavoured. It is also widely reported that other platinum complexes of *trans*-configuration form 1,3-bisadducts.⁷² Computational and theoretical studies by Tai *et al.* indicates that the reaction of duplex DNA with photoactivated **8** may lead to GG interstrand crosslinks, and there is some evidence that GC interstrand crosslinks may be formed.^{73,74,14} The unusual binding mode of **8** to DNA indicates that the mechanism of action of this drug is different from that of conventional platinum-based drugs, offering a new spectrum of activity in cancer cells.

2.4.5 The effects of altering the wavelength of activation on the binding of Pt(IV) diazido complexes to a series of oligonucleotides

The activation of light-sensitive drugs within tissue is optimal if the compound can be activated by wavelengths within the therapeutic window of 600 - 850 nm.⁷⁵ This is because longer wavelengths of light penetrate further into tissue up to the point that coloured proteins such as haemoglobin begin to absorb the longer wavelengths. Various constituent amino acids, small molecules and lipids etc absorb the shorter wavelengths of light.¹⁹ It has been shown that complex **8** can be activated not just by UVA but by wavelengths as long as green light.¹³ The effect of altering the wavelength of activation of **8** from 365 nm to 420 nm on binding to oligo 1 was investigated in Section 2.3.2.

For both wavelengths of irradiation, a solution of complex **8** (500 µM) and oligo 1 (250 µM) in water was irradiated for a 2 h period with aliquots taken every 30 min. Chromatogram B (Fig. 2.9) shows the appearance of a new peak at 19.7 min after 30 min of irradiation with 365 nm light, assigned as a Pt-oligonucleotide adduct. After irradiation for 30 min with 420 nm light, chromatogram B Figure 2.14, again a peak at 19.7 min was detected.

When comparing the two wavelengths of activation the solution irradiated with 365 nm reaches a maximum amount of oligonucleotide platination after 30 min of irradiation, whereas the solution irradiated with 420 nm light takes 90 min to achieve the same levels of platination. This would seem to be the only notable difference between the two solutions. This agrees with the findings of Prachova *et*

al.,⁵⁶ who found little difference when comparing 365 nm and 420 nm light activation of **8** in transcription-mapping experiments using plasmid DNA. This work also gives some insight into the low overall amount of oligonucleotide platination of **8** observed in this study. The experiments of Prachova *et al* followed the reaction of **8** with calf thymus DNA over a 24 h period using thiourea to trap mono-adducts shows that the concentration of bis-adducts formed is initially very low, and increases during the first 10 h. The rapid analysis of the samples in this investigation may indicate that these chromatographic studies did not detect similar levels to those observed in biological assays.^{56,13}

2.4.6 Photoactivatable Pt(IV) diazido complex interaction with an oligonucleotide by mass spectrometry

It was established by chromatographic methods in Section 2.3.2 that upon photoactivation of **8** in the presence of an oligonucleotide a new species, thought to be a platinated oligonucleotide, is formed. To identify the platinum-DNA adduct formed by **8** after irradiation, mass spectrometric methods were employed. Solutions of **8** and oligo 1 in a 1 to 1 molar ratio were irradiated with 365 nm and 420 nm light. Both solutions (Figures 2.18 and 2.19) were analysed by mass spectrometry and were found to contain unreacted oligo 1 and [oligo 1 + [Pt(py)₂]]. Where two equivalents of **8** were used the species [oligo 1 + 2[Pt(py)₂]] was also detected. The nature of the remaining ligands bound to the platinum centre after adduct formation was confirmed by the use of ¹⁵N labelled versions of **8**, Figure 2.21.

Chapter 2 - Chapter 2 The interaction of photoactivatable Pt(IV) complexes with single strand oligonucleotides

From the MS data and the four coordinate square-planar binding nature of Pt(II), we can deduce that there are two pyridines coordinated to the metal centre and binding to a DNA base accounts for another coordination site, leaving one binding site unaccounted for. One possibility is that a mono-adduct is formed and a solvent molecule that is lost during the ionisation process could occupy the remaining platinum(II) coordination site. Alternatively, the platinum could bind to the oligonucleotide at two points, e.g. through the N7 of guanine and the N3 of cytosine as noted in the interstrand crosslinks of *trans*-Pt(II) complexes.⁵²⁻⁵⁶ The low relative intensity of the [oligo 1 + [Pt(py)₂]] species, -3 charge state (1525.601 *m/z*) and -4 (1143.456 *m/z*), revealed that although individual peaks could be isolated, the fragments of the oligonucleotide could not be detected above the background noise of the instrument. The use of very low collision energies (1-2 eV), in an attempt to try to maintain peak intensity was not effective. This shows that it was not possible to locate the platinum binding site by utilising the protein-like fragmentation of oligonucleotides^{8,76,7} undergoing CID, although this has been achieved with metal-based drugs and oligonucleotides before by Groessl *et al.* and others.⁷⁶⁻⁷⁹

If the adduct formed is a bis-adduct with two pyridine ligands, it would be consistent with previous MS and NMR studies of **5** with GMP after irradiation at 420 nm.⁵ However, unlike the reaction with GMP, no azide-containing mono-adduct and no Pt(IV) species were observed. This may be due to the fact that these are short-lived species, with a lifetime of less than 10 h, and the relatively long overnight

sample preparation for the oligonucleotide MS required me to desalt the oligonucleotide indicates that they have decomposed or converted into bis-adducts by the time that the analysis took place.⁵⁶

The DNA adducts formed by platinum complexes are believed to be the reason for their anticancer efficacy. Platinum(IV) diazido complexes of the formula structure t,t,t -[Pt(N₃)₂(OH)₂(R)(R')] are no exception to this, but they have an additional facet to their toxicity. Recently Butler *et al.* found that upon photoactivation, **8** releases azide radicals that contribute to the induction of cell death.⁸⁰ It was found that the radicals could be quenched by the amino acid L-tryptophan, a molecule in lower concentrations in some patients with breast cancer when compared to those of healthy controls.⁸¹ This additional affect of the azide radicals may go some way to explaining the unusual method of cell death induced by **8** after irradiation. The cells do not experience apoptosis, as is the case with cisplatin-induced cell death, but autophagy was implied via biological assays.⁸²

2.5 Conclusions

The relative lipophilicity a series of ten platinum(IV) diazido complexes of general formula t,t,t -[Pt(N₃)₂(OH)₂(R)(R')] was determined by HPLC. The trend in observed lipophilicity was different to the expected trend when considering just the lipophilicity of the R and R' ligands. These observed lipophilicities were then compared to the accumulation of compounds **1** – **10** in A2780 human ovarian

carcinoma cells. There appears to be no overall trend relating hydrophobicity and cellular accumulation of these complexes. In turn, their potency in cancer cells (as IC_{50} values) has no obvious relationship with the cellular accumulation of the complexes. It seems likely that because other factors, such as the quantum yield of the complex, and the type of DNA lesion formed after photoactivation, have a greater influence over the efficacy of this class of drug.

The DNA-binding properties of one of these complexes, **8** *t,t,t*-[Pt(N₃)₂(OH)₂(py)₂], was investigated by HPLC and mass spectrometry. Upon irradiation with UVA light in the presence of a single strand oligonucleotide, oligo 1 d'(ATACATGCTACATA), a new species was created. When the sequence of the oligonucleotide was changed to include the 1,2-d(GpG) binding mode, the amount of platinum bound to the DNA reduced by one third. Levels of DNA platination for oligo 3, d'(ATACGTGCTACATA) were similar to that of oligo 1.

The adduct formed by **8** upon photoactivation in the presence of oligo 1 was characterised by mass spectrometry, and the species was found to be [oligo 1 + [Pt(py)₂]]. This was confirmed by the photoactivation of ¹⁵N labelled versions of **8**, *t,t,t*-[Pt(N₃)₂(OH)₂(¹⁵Npy)₂] (**8X**) and *t,t,t*-[Pt(¹⁵N₃)₂(OH)₂(¹⁵Npy)₂] (**8Y**), in the presence of oligo 1. By both mass spectrometry and chromatography the wavelength of activation of **8** was found to have no effect on the DNA adduct formed, but the shorter wavelength of light caused more rapid platination of the strand.

Chapter 2 - Chapter 2 The interaction of photoactivatable Pt(IV) complexes with single strand oligonucleotides

These studies indicate that Pt(IV) diazido complexes are a highly potent class of new anticancer drug with complicated structure-activity relationships. They offer many advantages when compared to conventional platinum-based treatments. The light activation offers spatial and temporal resolution of cancer therapy, as well as a new spectrum of activity and an extra potency attributed to the release of highly damaging azide radicals.

2.6 References

1. B. Rosenberg and L. VanCamp, *Cancer Res.*, 1970, **30**, 1799–802.
2. F. S. Mackay, J. A. Woods, H. Moseley, J. Ferguson, A. Dawson, S. Parsons, and P. J. Sadler, *Chem. Eur. J.*, 2006, **12**, 3155–3161.
3. C. N. Sternberg, D. P. Petrylak, O. Sartor, J. A. Witjes, T. Demkow, J.-M. Ferrero, J.-C. Eymard, S. Falcon, F. Calabrò, N. James, I. Bodrogi, P. Harper, M. Wirth, W. Berry, M. E. Petrone, T. J. McKearn, M. Noursalehi, M. George, and M. Rozenzweig, *J. Clin. Oncol.*, 2009, **27**, 5431–5438.
4. M. R. Reithofer, S. M. Valiahdi, M. a Jakupec, V. B. Arion, A. Egger, M. Galanski, and B. K. Keppler, *J. Med. Chem.*, 2007, **50**, 6692–6699.
5. M. Mitsunaga, M. Ogawa, N. Kosaka, L. T. Rosenblum, P. L. Choyke, and H. Kobayashi, *Nat. Med.*, 2011, **17**, 1685–1691.
6. T. J. Dougherty, C. J. Gomer, B. W. Henderson, G. Jori, D. Kessel, M. Korbelik, J. Moan, and Q. Peng, *J. Nat. Cancer Inst.*, 1998, **90**, 889–905.
7. J. Wu and S. A. McLuckey, *Int. J. Mass Spectrom.*, 2004, **237**, 197–241.
8. K. K. Murray, *J. Mass Spectrom.*, 1996, **31**, 1203–1215.
9. P. Nordhoff, E; Kirpekar, F and Roepstorff, *Mass Spectrom. Rev.*, 1996, **15**, 67–138.
10. S. McLuckey, G. Van Berker, and G. Glish, *J. Am Soc. Mass Spectrom.*, 1992, **3**, 60–70.
11. F. S. Mackay, J. a Woods, P. Heringová, J. Kaspárková, A. M. Pizarro, S. a Moggach, S. Parsons, V. Brabec, and P. J. Sadler, *Proc. Nat. Acad. Sci.*, 2007, **104**, 20743–20748.
12. F. S. Mackay, S. a Moggach, A. Collins, S. Parsons, and P. J. Sadler, *Inorg. Chim. Acta.*, 2009, **362**, 811–819.
13. N. J. Farrer, J. A. Woods, L. Salassa, Y. Zhao, K. S. Robinson, G. Clarkson, F. S. Mackay, and P. J. Sadler, *Angew. Chem. Int. Ed.*, 2010, **49**, 8905–8908.

14. Y. Zhao, J. A. Woods, N. J. Farrer, K. S. Robinson, J. Pracharova, J. Kasparkova, O. Novakova, H. Li, L. Salassa, A. M. Pizarro, G. J. Clarkson, L. Song, V. Brabec, and P. J. Sadler, *Chem. Eur. J.*, 2013, **19**, 9578–9591.
15. A. V Tataurov, Y. You, and R. Owczarzy, *Biophys. Chem.*, 2008, **133**, 66–70.
16. S. H. van Rijt, A. Mukherjee, A. M. Pizarro, and P. J. Sadler, *J. Med. Chem.*, 2010, **53**, 840–849.
17. A. . M. Fichtinger-Schepman, J. L. van der Veer, J. H. den Hartog, P. H. Lohman, and J. Reedijk, *Biochemistry*, 1985, **24**, 707–713.
18. J. Reedijk, *Eur. J. Inorg. Chem.*, 2009, **2009**, 1303–1312.
19. R. Rox Anderson and J. A. Parish, *J. Invest. Dermatol.*, 1981, **77**, 13–19.
20. M. Balaz, H. A. Collins, E. Dahlstedt, and H. L. Anderson, *Org. Biomol. Chem.*, 2009, **7**, 874–888.
21. C. A. Lipinski, F. Lombardo, B. W. Dominy, and P. J. Feeney, *Adv. Drug Deliv. Rev.*, 2001, **46**, 3–26.
22. A. K. Ghose, V. N. Viswanadhan, and J. J. Wendoloski, *J. Comb. Chem.*, 1999, **1**, 55–68.
23. M. S. Mirrlees, S. J. Moulton, C. T. Murphy, and P. J. Taylor, *J. Med. Chem.*, 1976, **19**, 615–619.
24. D. Minick and J. Frenz, *J. Med. Chem.*, 1988, **31**, 1923–1933.
25. M. Abraham, H. Chadha, and A. Leo, *J. Chromatogr. A*, 1994, **685**, 203–211.
26. C. J. Ward and G. A. Codd, *J. Appl. Microbiol.*, 1999, **86**, 874–882.
27. F. K. Główka, M. Romański, and A. Siemiątkowska, *J. Chromatogr. B*, 2013, **923-924**, 92–97.
28. D. Screnci, M. J. McKeage, P. Galettis, T. W. Hambley, B. D. Palmer, and B. C. Baguley, *Brit. J. Cancer*, 2000, **82**, 966–972.
29. J. Souchard and T. Ha, *J. Med. Chem.*, 1991, 863–864.

30. M. D. Hall, S. Amjadi, M. Zhang, P. J. Beale, and T. W. Hambley, *J. Inorg. Biochem.*, 2004, **98**, 1614–1624.
31. S. P. Oldfield, M. D. Hall, and J. a Platts, *J. Med. Chem.*, 2007, **50**, 5227–5237.
32. J. A. Platts, S. P. Oldfield, M. M. Reif, A. Palmucci, E. Gabano, and D. Osella, *J. Inorg. Biochem.*, 2006, **100**, 1199–1207.
33. C. Hansch, A. Leo, and D. Hoekman, *Exploring QSAR: Fundamentals and applications in chemistry and biology*, American Chemical Society, Washington, DC, 1995.
34. E. L. Willighagen, H. M. G. W. Denissen, R. Wehrens, and L. M. C. Buydens, *J. Chem. Info. Model.*, 2006, **46**, 487–94.
35. RSC, <http://www.chemspider.com/Chemical-Structure.13839199.html?rid=0bb52c53-018f-4b18-a334-47a5fe14ae5c>.
36. RSC, <http://www.chemspider.com/Chemical-Structure.8899.html>.
37. P. Gramatica, E. Papa, M. Luini, E. Monti, M. B. Gariboldi, M. Ravera, E. Gabano, L. Gaviglio, and D. Osella, *J. Biol. Inorg. Chem.*, 2010, **15**, 1157–1169.
38. G. Ermondi, G. Caron, M. Ravera, E. Gabano, S. Bianco, J. A. Platts, and D. Osella, *Dalt. Trans.*, 2013, **42**, 3482–3489.
39. P. Wiczling, A. Nasal, Ł. Kubik, and R. Kaliszan, *Eur. J. Pharmaceu. Sci.*, 2012, **47**, 1–5.
40. L. Ronconi, A. M. Pizarro, R. J. McQuitty, and P. J. Sadler, *Chem. Eur. J.*, 2011, **17**, 12051–12058.
41. J. A. Platts, D. E. Hibbs, T. W. Hambley, and M. D. Hall, *J. Med. Chem.*, 2001, **44**, 472–474.
42. Y. Jung and S. J. Lippard, *Chem. Rev.*, 2007, **107**, 1387–1407.
43. D. P. Gately and S. B. Howell, *Brit. J. Cancer*, 1993, **67**, 1171–1176.
44. F. Arnesano and G. Natile, *Coord. Chem. Rev.*, 2009, **253**, 2070–2081.

45. S. B. Howell, R. Safaei, C. A. Larson, and M. J. Sailor, *Mol. Pharm.*, 2010, **77**, 887–894.
46. S. Ishida, F. McCormick, K. Smith-McCune, and D. Hanahan, *Cancer Cell*, 2010, **17**, 574–583.
47. C. A. Rabik, E. B. Maryon, K. Kasza, J. T. Shafer, C. M. Bartnik, and M. E. Dolan, *Cancer Chemother. Pharmacol.*, 2009, **64**, 133–142.
48. D. Sinani, D. Adle, H. Kim, and J. Lee, *J. Biol. Chem.*, 2007, **282**, 26775–26785.
49. L. Ellis, H. Er, and T. Hambley, *Aust. J. Chem.*, 1995, **48**, 793–806.
50. J. Reedijk, *Proc. Natl. Acad. Sci. USA*, 2003, **100**, 3611–3616.
51. J. Reedijk, *Plat. Met. Rev.*, 2008, **52**, 2–11.
52. Y. Wu, P. Pradhan, J. Havener, G. Boysen, J. a Swenberg, S. L. Campbell, and S. G. Chaney, *J. Mol. Biol.*, 2004, **341**, 1251–1269.
53. V. Brabec, J. Reedijk, and M. Leng, *Biochemistry*, 1992, **31**, 12397–12402.
54. B. Spingler, D. A. Whittington, and S. J. Lippard, *Inorg. Chem.*, 2001, **40**, 5596–5602.
55. S. Mowaka and M. Linscheid, *Anal. Bioanal Chem.*, 2008, **392**, 819–830.
56. J. Pracharova, L. Zerzankova, J. Stepankova, O. Novakova, N. J. Farrer, P. J. Sadler, V. Brabec, and J. Kasparkova, *Chem. Res. Toxicol.*, 2012, **25**, 1099–1111.
57. A. Eastman, *Biochemistry*, 1982, **21**, 6732–6736.
58. A. Eastman, *Biochemistry*, 1986, **25**, 3912–3915.
59. A. Zayed, T. Shoeib, S. E. Taylor, G. D. D. Jones, A. L. Thomas, J. P. Wood, H. J. Reid, and B. L. Sharp, *Int. J. Mass Spectrom.*, 2011, **307**, 70–78.
60. J. F. Hartwig and S. J. Lippard, *J. Am. Chem. Soc.*, 1992, **114**, 5646–5654.

61. Y. Wu, D. Bhattacharyya, C. L. King, I. Baskerville-abraham, S. Huh, G. Boysen, J. A. Swenberg, B. Temple, S. L. Campbell, S. G. Chaney, V. Recci, V. No, V. Re, M. Recci, and V. February, *Biochemistry*, 2007, **46**, 6477–6487.
62. P. Takahara, A. Rosenzweig, C. Frederick, and S. Lippard, *Nature*, 1995, **377**, 6477–6487.
63. A. Pinto and S. Lippard, *Biochim. Biophys. Acta*, 1985, **780**, 167–180.
64. R. J. Knox, F. Friedlos, D. A. Lydall, T. Li, and J. J. Roberts, *Cancer Res.*, 1986, **46**, 1972–1979.
65. S. L. Kerr, T. Shoeib, and B. L. Sharp, *Anal. Bioanal Chem.*, 2008, **391**, 2339–2348.
66. J. Kasparkova, M. Vojtiskova, G. Natile, and V. Brabec, *Chem. Eur. J.*, 2008, **14**, 1330–1341.
67. M. Zuker, *Nucleic Acids Res.*, 2003, **31**, 3406–3415.
68. J. Malina, O. Novakova, M. Vojtiskova, G. Natile, and V. Brabec, *Biophys. J*, 2007, **93**, 3950–3962.
69. B. Desoize and C. Madoulet, *Crit. Rev. Oncol. Hematol.*, 2002, **42**, 317–325.
70. J. Malina, J. Kasparkova, N. P. Farrell, and V. Brabec, *Nucleic Acids Res.*, 2011, **39**, 720–728.
71. T. Shingu, *Neuro. Oncol.*, 2010, **12**, 1269–1277.
72. R. Dalbiès, D. Payet, and M. Leng, *Proc. Natl. Acad. Sci. USA*, 1994, **91**, 8147–8151.
73. H. Tai, R. Brodbeck, J. Kasparkova, N. J. Farrer, V. Brabec, P. J. Sadler, and R. J. Deeth, *Inorg. Chem.*, 2012, **2**, 6830–6841.
74. F. Paquet, M. Boudvillain, G. Lancelot, and M. Leng, *Nucleic Acids Res.*, 1999, **27**, 4261–4268.
75. R. B. Sears, L. E. Joyce, M. Ojaimi, J. C. Gallucci, R. P. Thummel, and C. Turro, *J. Inorg. Biochem.*, 2013, **121**, 77–87.
76. J. L. Beck, M. L. Colgrave, S. F. Ralph, and M. M. Sheil, *Mass Spectrom. Rev.*, 2001, **20**, 61–87.

77. K. G. Samper, C. Vicente, V. Rodríguez, S. Atrian, N. Cutillas, M. Capdevila, J. Ruiz, and Ö. Palacios, *Dalt. Trans.*, 2012, **41**, 300–306.
78. M. Groessl, Y. O. Tsybin, C. G. Hartinger, B. K. Keppler, and P. J. Dyson, *J. Biol. Inorg. Chem.*, 2010, **15**, 677–688.
79. T. Urathamakul, D. J. Waller, J. L. Beck, J. R. Aldrich-Wright, and S. F. Ralph, *Inorg. Chem.*, 2008, **47**, 6621–6632.
80. J. S. Butler, J. A. Woods, N. J. Farrer, M. E. Newton, and P. J. Sadler, *J. Am. Chem. Soc.*, 2012, **134**, 16508–16511.
81. D. E. Lyon, J. M. Walter, A. R. Starkweather, C. M. Schubert, and N. L. McCain, *BMC Res. Notes*, 2011, **4**, 156–163.
82. A. F. Westendorf, J. A. Woods, K. Korpis, N. J. Farrer, L. Salassa, K. Robinson, V. Appleyard, K. Murray, R. Grünert, A. M. Thompson, P. J. Sadler, and P. J. Bednarski, *Mol. Cancer Ther.*, 2012, **11**, 1894–1904.

Chapter 2 - Chapter 2 The interaction of photoactivatable Pt(IV) complexes with
single strand oligonucleotides

Chapter 3

Chiral chromatography of organometallic anticancer complexes

3.1 Introduction

As outlined in Chapter 1, the efficacy of the platinum-based anticancer drugs currently in the clinic is attributed to their interactions with DNA.^{1,2,3} New generation drugs may also target DNA,^{4,5} but can also be multi-targeted, activating cellular pathways by means of, e.g., protein binding.^{6,7} Drugs can interact with various molecules before reaching the intra cellular target. Some of these are proteins involved in cellular uptake, or efflux, or in side reactions that are responsible for deactivation of the drug or can cause unwanted side effects. When considering these interactions, it must be remembered that the human body contains many chiral molecules: L-amino acids, D-sugars and even secondary structures such as α -helices in proteins the right-handed twist of the double helix in B-DNA, and the left-handed twist of Z-DNA. Therefore if a potential new drug is also chiral, then the 'handedness' of this molecule is crucial for its cellular uptake, transport, metabolism, interaction with DNA and proteins.⁸

There are many examples in the literature of chiral drugs, the different enantiomers of which have varying effects on the human body. As recorded in the 1992 statement on the development of new stereoisomeric drugs by the FDA, there are categories in which chiral drugs can be placed.⁹ The first comprises of drugs for which both enantiomers give the desired effect e.g. ibuprofen and β -lactam antibiotics. The second are where one enantiomer has the desired effect and the other is inactive e.g. propranolol. The third category comprises of drugs with enantiomers that have differing activities. These potential differences in the activity

of enantiomers has led the FDA and other regulatory bodies to require the testing of individual isomers before a drug can be licensed.

There are several means of achieving optically pure enantiomers: by crystallisation, by using an optically pure second molecule to form pairs of diastereomers, and by using stereo-selective syntheses. For example Kilpin *et al.* (2013) used optically pure ligands to synthesise the two different enantiomers of organometallic ruthenium(II) compounds, and compared their antiproliferative activity in ovarian cancer cells.¹⁰ The Smith laboratory uses stereo-selective synthesis to create ferrocene- and ruthenocene-based complexes that have antimalarial activity.^{11,12}

This work is concerned with the separation of enantiomers by chiral chromatography. The technique employed utilises high performance liquid chromatography (HPLC) with columns containing a chiral stationary phase, with which the different enantiomers will interact to a varying extent depending on their stereochemistry, thus allowing the enantiomers to be separated. Indeed, the stationary phases of these columns are often sugar based, utilising amylose and functionalised supports.¹³⁻¹⁵ There have been previous successes in using these stationary phases to separate the enantiomers of organometallic compounds.¹⁶⁻¹⁸

The complexes studied in this work have a 'piano stool' structure of the general formula shown in Fig 3.1, where M is the metal centre, X is the halide leaving group, A is the arene ligand and L-L' is the bidentate ligand. This study will encompass Ir-, Os- and Ru-based organometallic complexes. These compounds also exhibit different types of chirality. The Ir-based complexes have chiral metal

centres, as do the Os-based compounds. The ruthenium complexes fall into two categories: those that have an asymmetric arene ligand and have facial chirality, and those that have a chiral centre at the metal and on the bidentate ligand.

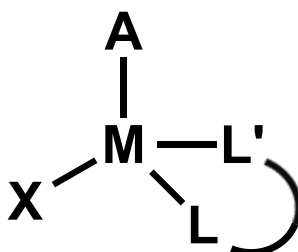


Figure 3.1 General structure of the complexes studied. Where M is the metal, A is the arene ligand, X is the halide leaving group, and L-L' is the bidentate ligand.

3.2 Experimental

3.2.1 Materials

All solvents used were HPLC-grade and obtained from Fischer Scientific, except for *n*-heptane which was purchased from Sigma Aldrich. Trifluoroacetic acid (TFA, 99.99%, spectrophotometric grade) and diethylamine (DEA, 99.5%, purified by re-distillation) were purchased from Sigma Aldrich, and triethylamine (TEA, HPLC grade) was purchased from VWR. All of the metal complexes analysed were synthesised within the Sadler group.

3.2.2 Methods

3.2.2.1 Sample preparation

All samples were dissolved in HPLC grade EtOH unless stated otherwise, and filtered using 0.45 μm , 4 mm, PTFE, SUPELCO Iso-Disc syringe filters if there was sufficient sample volume. If there was a limited amount of sample, the solution was centrifuged at 14,000 rpm, 5°C for 10 min and the supernatant used for analysis. In the case of the poorly soluble complexes **12** and **13**, 1.00 mL of EtOH was added to 1 mg of each compound. These samples were then sonicated for 5 min and vortexed for 10 min. The solutions were then centrifuged and the supernatant filtered using 0.45 μm syringe filters and the filtrate used for analysis.

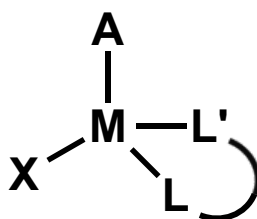
3.2.2.2 HPLC

All of the following work was carried out on an Agilent 1200 series HPLC system equipped with a binary pump, a variable wavelength detector (VWD) and fitted with a 100 μL loop in normal phase. The columns used were a CHIRALPAK IA column (250 mm x 4.6 mm) with an isocratic gradient of heptane:ethylacetate containing 0.1% (v/v) diethylamine (DEA), flow-rate 1.00mL/min, wavelength of detection 260 nm and a CHIRALPAK IC column (250 mm x 4.6 mm) with an isocratic gradient of heptane:ethanol 0.5% triethylamine (TEA), 0.3% trifluoroacetic acid(TFA) (v/v), flow-rate 1.00mL/min, wavelength of detection 300 nm. Initial method development for the separation of complexes **11**, $[\text{Ir}(\eta^5\text{-Cp}^{\text{xbph}})(\text{phenpy})\text{Cl}]$, on CHIRALPAK IA and **18**, on CHIRALPAK IC was carried out by Chiral Technologies Europe. The initial methods for **11** had to be further optimised. Data were

processed using ChemStation and Microsoft Excel. The resolution of the separations was calculated using the formula $R_s = 2(t_1 - t_2) / (w_1 + w_2)$, where t_1 is the retention time of the first peak, t_2 of the second, w_1 is the width of the first peak, and w_2 that of the second.

3.3 Results

The organometallic complexes studied in this chapter are listed in Table 3.1 below. They include different metals and display several types of chirality. The separation of the enantiomers of the chiral anticancer complexes was carried out using HPLC columns with two different stationary phases: CHIRALPAK IA and CHIRALPAK IC, see Figure 3.2. Of the two stationary phases used, CHIRALPAK IA was selected for the separation of neutral complexes and CHIRALPAK IC, with its chloro groups, was employed for positively charged complexes. Compounds **11-17** were analysed using CHIRALPAK IA and **18-24** using CHIRALPAK IC.

Table 3.1 Summary of the structures of the complex studied in this work.

Complex	M	A	L-L'	X
11	Ir(III)	tetramethyl(biphenyl)-cyclopentadiene (Cp ^{x_{bph}})	2-phenylpyridine (phenpy)	Cl
12	Ir(III)	pentamethylcyclopentadiene (Cp [*])	7,8-benzoquinoline (benzq)	Cl
13	Ir(III)	pentamethylcyclopentadiene (Cp [*])	2-(2,4-Difluorophenyl)pyridine (dfphpy)	Cl
14	Ir(III)	pentamethylcyclopentadiene (Cp [*])	Pyridine, 4-(2-fluorophenyl)-(py,4-(2fph))	Cl
15	Ir(III)	pentamethylcyclopentadiene (Cp [*])	Pyridine, 4-(4-fluorophenyl)-(py,4-(4fph))	Cl
16	Ir(III)	pentamethylcyclopentadiene (Cp [*])	Pyridine,4-[4-(trifluoromethyl)phenyl]-(py,4-(4tfmph))	Cl
17	Ir(III)	pentamethylcyclopentadiene (Cp [*])	3-Pyridinecarboxaldehyde, 5-phenyl-(pycarboxphen)	Cl
18	Os(II)	<i>para</i> -cymene (<i>p</i> -cym)	4-(2- pyridylazo)-N,N-dimethylaniline) (azpy-NMe ₂)	I
19	Os(II)	<i>para</i> -cymene (<i>p</i> -cym)	4-(2- pyridylazo)-N,N-dimethylaniline) (azpy-NMe ₂)	Br
20	Os(II)	biphenyl (bip)	4-(2- pyridylazo)-N,N-dimethylaniline) (azpy-NMe ₂)	I
21	Os(II)	biphenyl (bip)	4-(2- pyridylazo)-N,N-fluoro (azpy-F)	I
22	Ru(II)	fluorene (flu)	Ethylenediamine (en)	Cl
23	Ru(II)	phenanthrene (phent)	Ethylenediamine (en)	Cl
24	Ru(II)	<i>para</i> -cymene (<i>p</i> -cym)	iminopyridine (Impy)	I

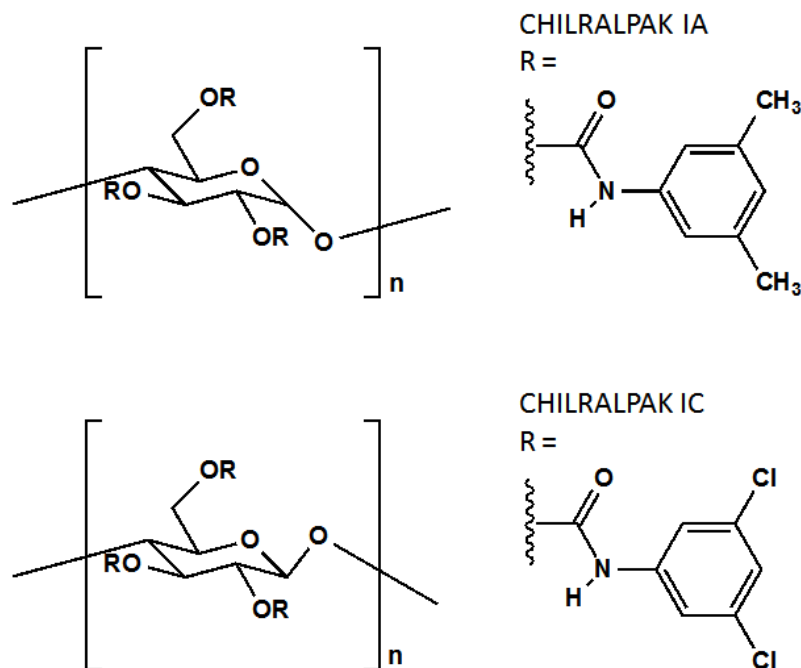


Figure 3.2 Structures of the stationary phases CHIRALPAK IA (top) and CHIRALPAK IC (bottom).

3.3.1.1 Stationary phase CHIRALPAK IA, complex **11** and the stability of its enantiomers

A method was developed to separate the enantiomers of compound **11**, $[\text{Ir}(\eta^5\text{-Cp}^{\text{xbph}})(\text{phenpy})\text{Cl}]$, provided by Dr Zhe Lui see Figure 3.3. A 10 μL injection of a solution of 1 mg of **11** dissolved in 1 mL of EtOH (HPLC-grade) was analysed with an isocratic gradient of 60:40 heptane:ethylacetate 0.1% DEA. The chromatogram (Figure 3.4, top) shows two well-resolved (R_S 2.76) peaks, peak 1 t_R at 7.65 min and peak 2 t_R 9.97 min.

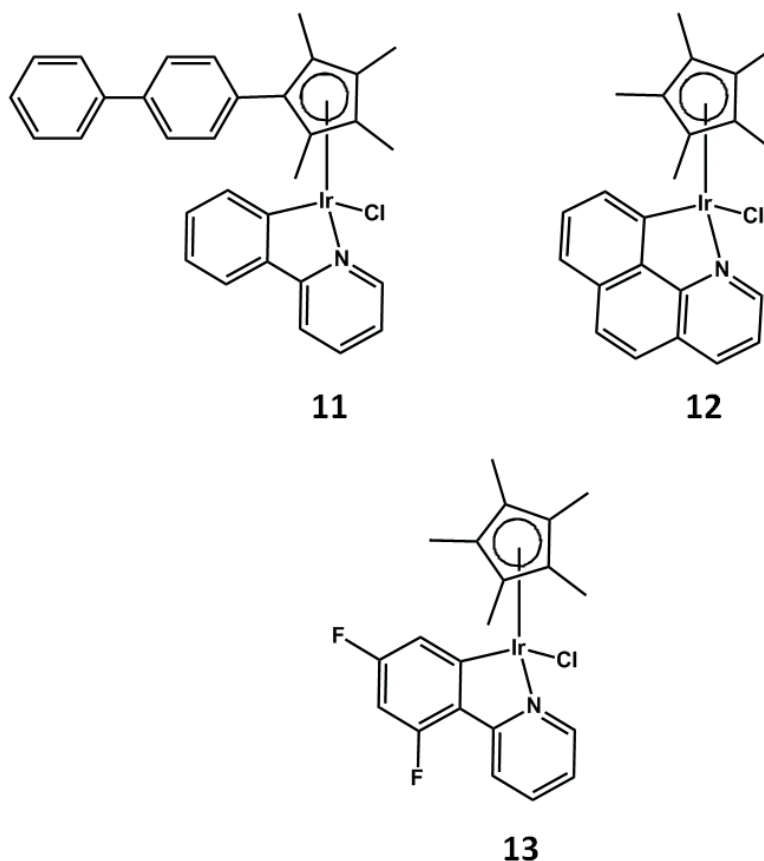


Figure 3.3 Structures of complexes **11**, $[\text{Ir}(\eta^5\text{-Cp}^{\text{xbph}})(\text{phenpy})\text{Cl}]$, **12**, $[\text{Ir}(\eta^5\text{-Cp}^*)(\text{benzq})\text{Cl}]$, and **13**, $[\text{Ir}(\eta^5\text{-Cp}^*)(\text{dfphpy})\text{Cl}]$.

To establish whether the isolated purified single isomers will revert back to a racemic mixture or remain pure, the individual peaks were then collected during the course of eight analyses (to obtain enough material for subsequent analysis). All of the fractions containing peak 1 (t_R 7.65 min, Fig 3.3) were combined together and evaporated to dryness on a vacuum line, and this procedure was repeated for the second peak, peak 2 (t_R 9.97 min). The solid samples of each individual isomer were then re-dissolved in 100 μL of EtOH, left in solution for 2 h at ambient temperature and subjected to the original separation protocol. The chromatograms for both

collected peaks, see Figure 3.4 (bottom), clearly show that both single peaks transformed into two peaks, indicating a return to a racemic mixture.

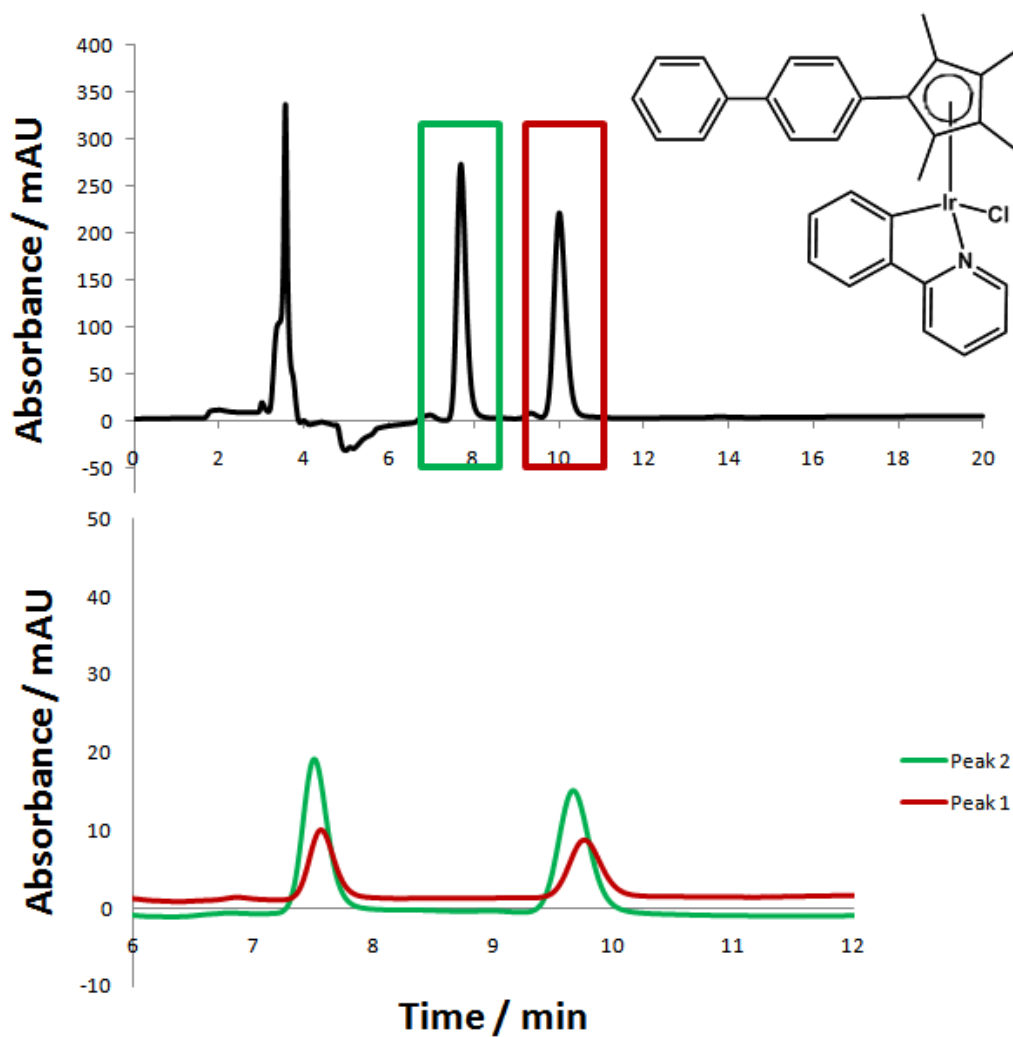


Figure 3.4 Top: chromatogram of a solution of **11** in EtOH, peak 1 t_R 7.65 min, peak 2 t_R 9.97 min, R_S 2.76. Bottom: chromatograms of repeat collections of peaks 1 and 2 of **11** also in EtOH. All separations carried out using an isocratic flow of 60:40 heptane/EtOAc 0.1% DEA (v/v) on a CHIRALPAK IA 4.6 x 250 mm column.

3.3.1.2 Stationary phase CHIRALPAK IA, complexes 12-17

The initial conditions used to separate the enantiomers of **11** provided a starting point for all subsequent separations of neutral enantiomers. Hence, solutions of **12**, $[\text{Ir}(\eta^5\text{-Cp}^*)(\text{ben})\text{Cl}]$, and **13**, $[\text{Ir}(\eta^5\text{-Cp}^*)(\text{dfphpy})\text{Cl}]$, (compounds provided by Dr Zhe Lui) in EtOH were analysed under these conditions. The solubility of both compounds in EtOH and the mobile phase is very poor, and it was not possible to achieve a solution of 1.0 mg/mL for either of the complexes. In view of the slightly better solubility of these molecules in EtOH when compared to that in the mobile phase alone, a 1.0 mg/mL solution of each was made up in EtOH as outlined in the experimental Section 3.2.1.1. The resulting chromatograms are shown in Figure 3.5.

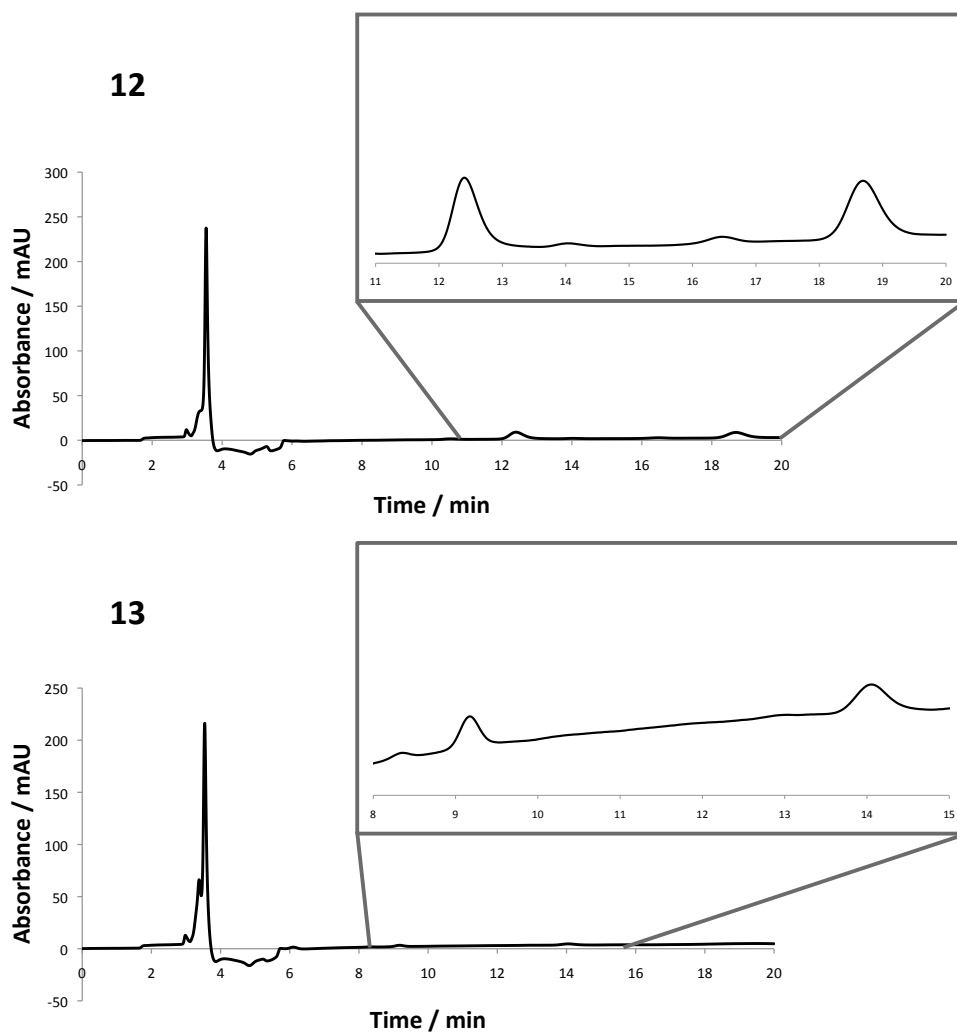


Figure 3.5 Top: chromatogram of the separation of the two enantiomers of **12**, peak1 t_R 12.33 min, peak 2 t_R 18.61 min, R_S 4.39. Bottom: chromatogram of the separation of the enantiomers of **13**, peak 1 t_R 9.11 min, peak 2 t_R 13.98 min, R_S 5.83. The conditions used for both analyses were isocratic of 60:40 heptane/EtOAc 0.1% DEA (v/v) on a CHIRALPAK IA 4.6 x 250 mm column.

There is a peak in both chromatograms at around 3.5 min, corresponding to the dead time of the instrument, and attributable to the EtOH used to dissolve the sample is the solvent front. In the case of both of these complexes, the peaks attributable to the separated enantiomers are very small, due to the low concentration of the sample. Several other complexes similar in structure were also separated using the same protocol, see Figure 3.6.

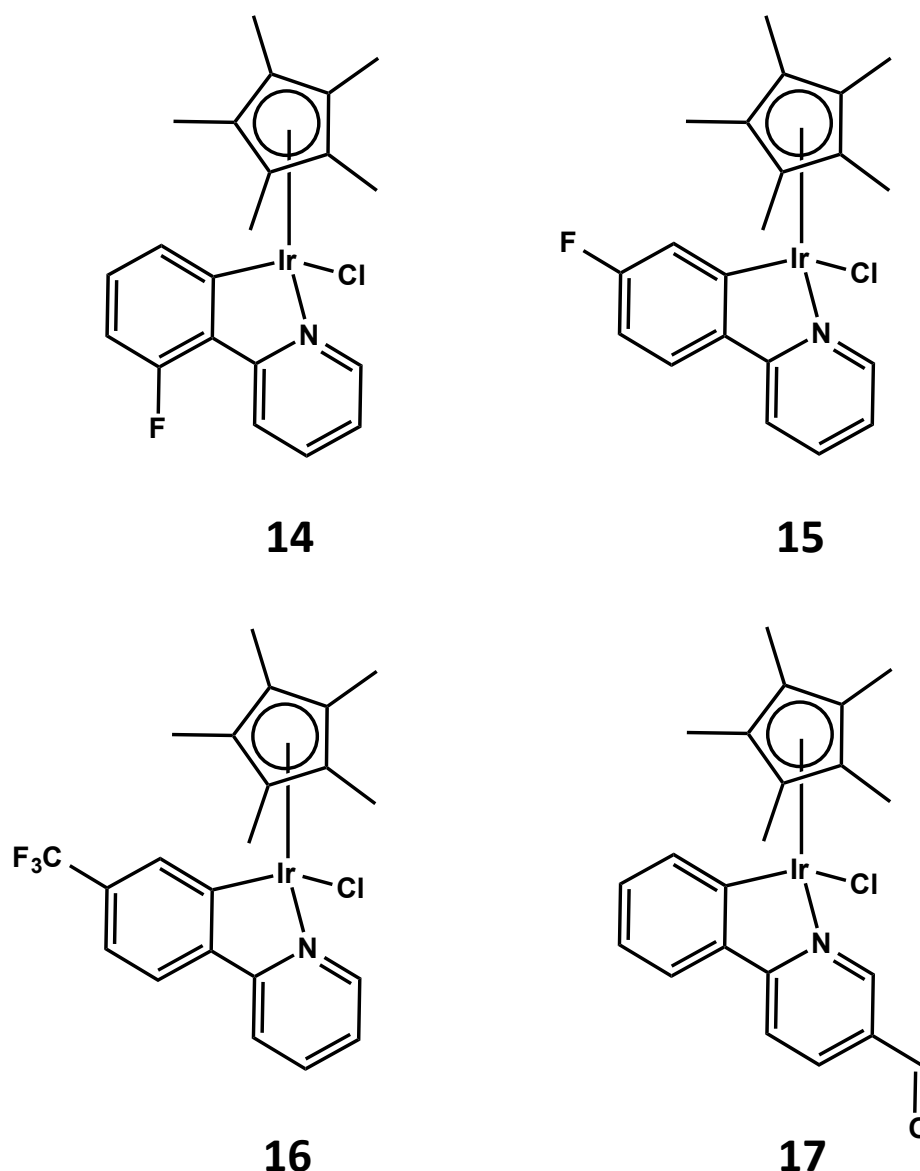


Figure 3.6 Structures of complexes **14**, $[\text{Ir}(\eta^5\text{-Cp}^*)(\text{py},4\text{-}(2\text{fph}))\text{Cl}]$, **15**, $[\text{Ir}(\eta^5\text{-Cp}^*)(\text{py},4\text{-}(4\text{fph}))\text{Cl}]$, **16**, $[\text{Ir}(\eta^5\text{-Cp}^*)(\text{py},4\text{-}(4\text{tfmph}))\text{Cl}]$, and **17**, $[\text{Ir}(\eta^5\text{-Cp}^*)(\text{pycarboxphen})\text{Cl}]$.

Complexes **14-17**, provided by Adam Millett, have improved solubility when compared to **12** and **13**. Solutions of 1 mg/mL of each compound were made using the mobile phase as a solvent. This removes the large signal at 3.5 min ascribable to ethanol observed in the previous chromatograms. The improved solubility also gives rise to an improved separation of the two enantiomers, i.e. it was easier to

observe, Figure 3.7. The chromatograms in Fig. 3.7 show clear resolution of the enantiomers of **14**, **15** and, with a somewhat reduced resolution, **16**. Previously, the resolution of the separated enantiomers for complexes **11**, **13** and **13** has been such that there is a difference of between 8 and 3 min. This is also true of complexes **14** and **15**, but for complex **16** the difference in retention times is reduced to less than a minute.

3.3.1.3 Solution stability of the enantiomers of complex **17**

As with **14**, **15** and **16**, compound **17** displayed improved solubility and a solution of 1.0 mg/mL was made up using the mobile phase as a solvent. In biological testing complex **17** has shown great promise with an IC₅₀ value of 4.4 μM in A2780 human carcinoma cells (A. Millett, I. Romero-Canelon, unpublished). For this reason, the stability of its two enantiomers was tested in the same manner as those of **11**. The two peaks, highlighted in red and blue in Fig. 3.8, were individually collected over the course of eight separations. The fractions for each separated peak were then combined and evaporated to dryness under vacuum. The resulting solid was re-dissolved in 100 μL of mobile phase (60:40 heptane/EtOAc 0.1% DEA), allowed to sit for 3 h in solution at approximately 20°C, and analysed as described above. The chromatograms in Figure 3.8 clearly show that the purified peaks of **17** revert back to a mixture of enantiomers. The retention times of all of the peaks and the resolutions of these separations performed on the stationary phase CHIRALPAK IA are shown in Table 3.2.

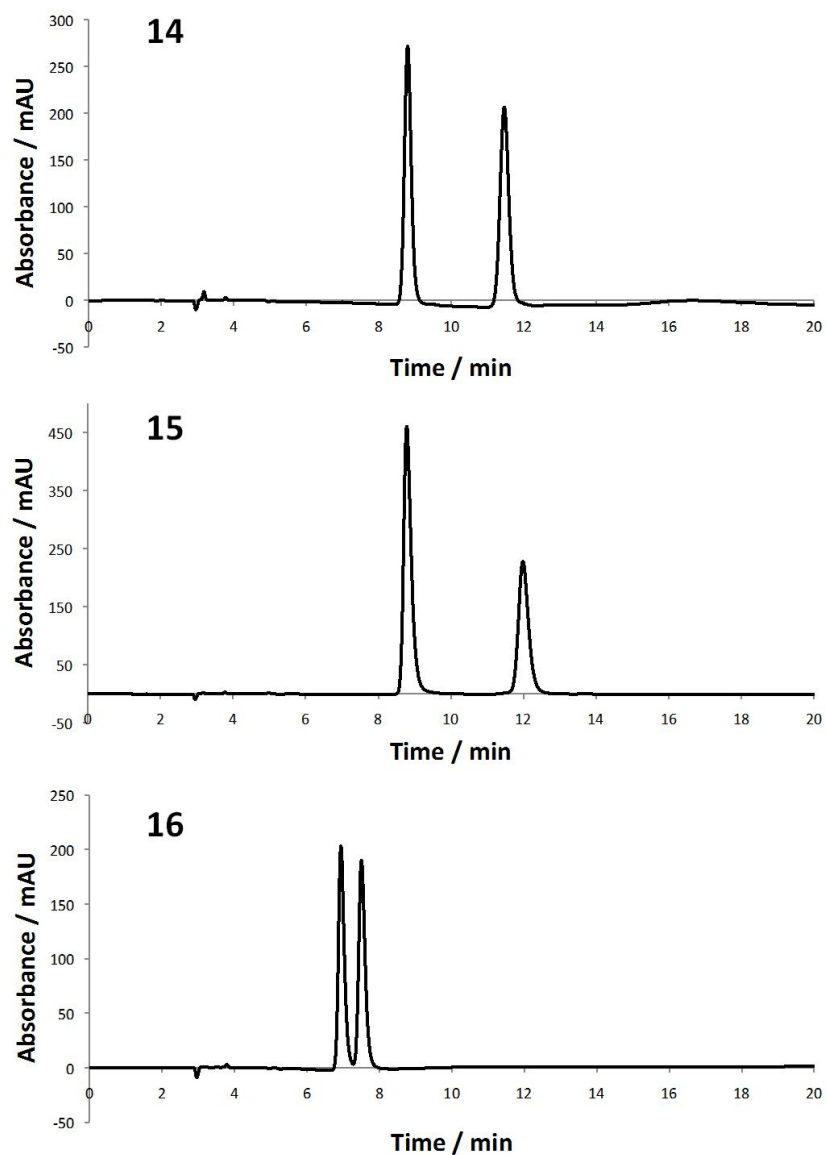


Figure 3.7 Chromatograms of the chiral separation of the different enantiomers of **14** (top), peak1 t_R 8.79 min, peak 2 t_R 11.42 min, R_S 2.86, **15** (middle) , peak1 t_R 8.76 min, peak 2 t_R 11.94 min, R_S 3.12, and **16** (bottom) , peak1 t_R 6.93 min, peak 2 t_R 7.50 min, R_S 0.97. Separations of 20 μ L injections (1.0 mg/mL) were carried out on a column CHIRALPAK IA 4.6 x 250 mm, isocratic 60:40 heptane/EtOAc 0.1% DEA (v/v).

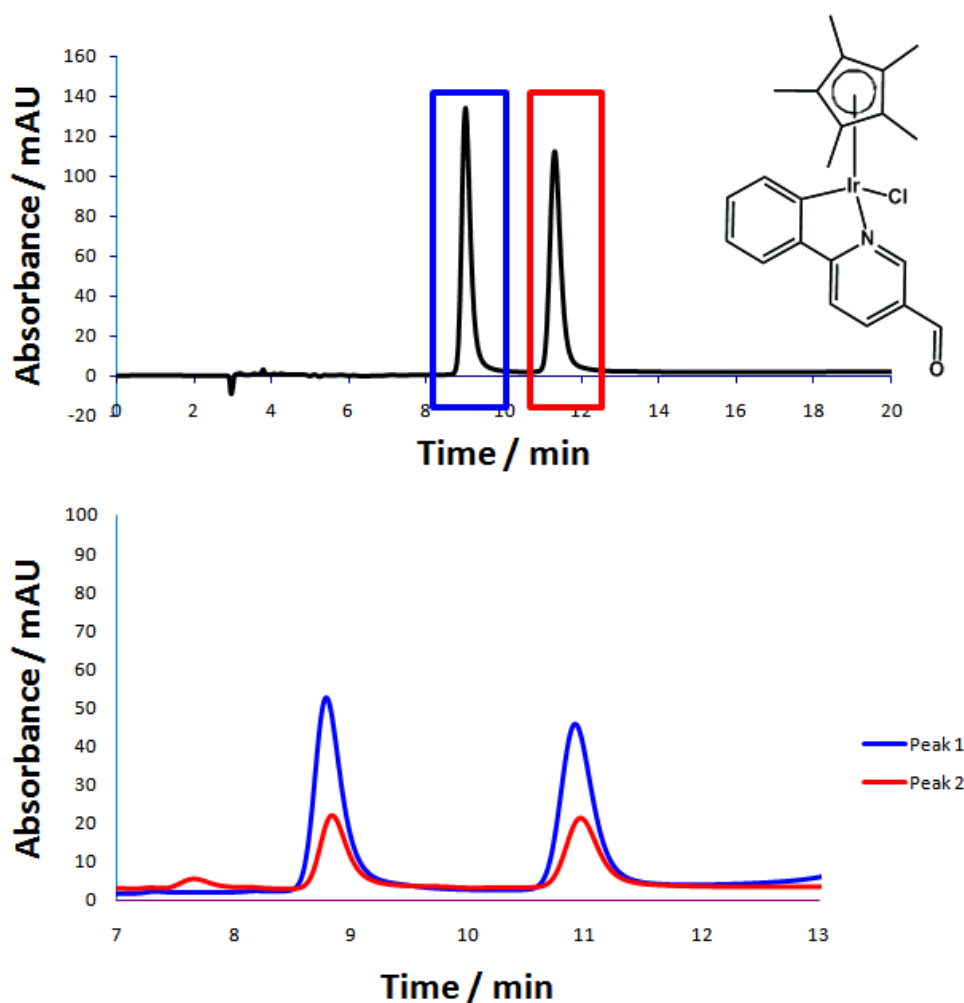


Figure 3.8 Top: Chromatogram of the chiral separation of the enantiomers of **17**, R_S 2.35, peak 1 in blue, t_R 8.98 min, peak 2 in red, t_R 11.28 min. Bottom: chromatograms of the repeat collections of peak 1 (blue) and peak 2 (red) showing conversion back to a mixture of enantiomers. Separation conditions were as follows 20 μ L injections, samples dissolved in mobile phase, carried out on a column CHIRALPAK IA 4.6 x 250 mm, isocratic flow of 60:40 heptane/EtOAc 0.1% DEA (v/v).

Table 3.2 Retention times (t_1 and t_2) and resolution of peaks eluted from the CHIRALPAK IA column.

Complex	t_1 / min	t_2 / min	R_s
11	7.65	9.97	2.76
12	12.33	18.61	4.39
13	9.11	13.98	5.83
14	8.79	11.42	2.86
15	8.76	11.94	3.12
16	6.93	7.50	0.97
17	8.98	11.28	2.35

3.3.2 Stationary phase CHIRALPAK IC analysis of, complexes 18-24

Several charged chiral drugs synthesised within the Sadler group have shown great promise in biological assays for their anticancer properties.¹⁹⁻²² The separation of the enantiomers of several of these compounds was performed on an HPLC column with the stationary phase CHIRALPAK IC. Unlike the neutral iridium complexes previously described, these compounds are osmium- and ruthenium-based. The osmium-based complexes are shown in Fig. 3.9, **18** $[\text{Os}(\eta^6\text{-p-cym})(\text{azpy-NMe}_2)\text{I}]^+$, **19** $[\text{Os}(\eta^6\text{-p-cym})(\text{azpy-NMe}_2)\text{Br}]^+$, **20** $[\text{Os}(\eta^6\text{-bip})(\text{azpy-NMe}_2)\text{I}]^+$, and **21** $[\text{Os}(\eta^6\text{-bip})(\text{azpy-f})\text{I}]^+$. These compounds are all very similar in structure to one another, and their enantiomers were separated using the same conditions. The compounds were provided by Russell Needham.

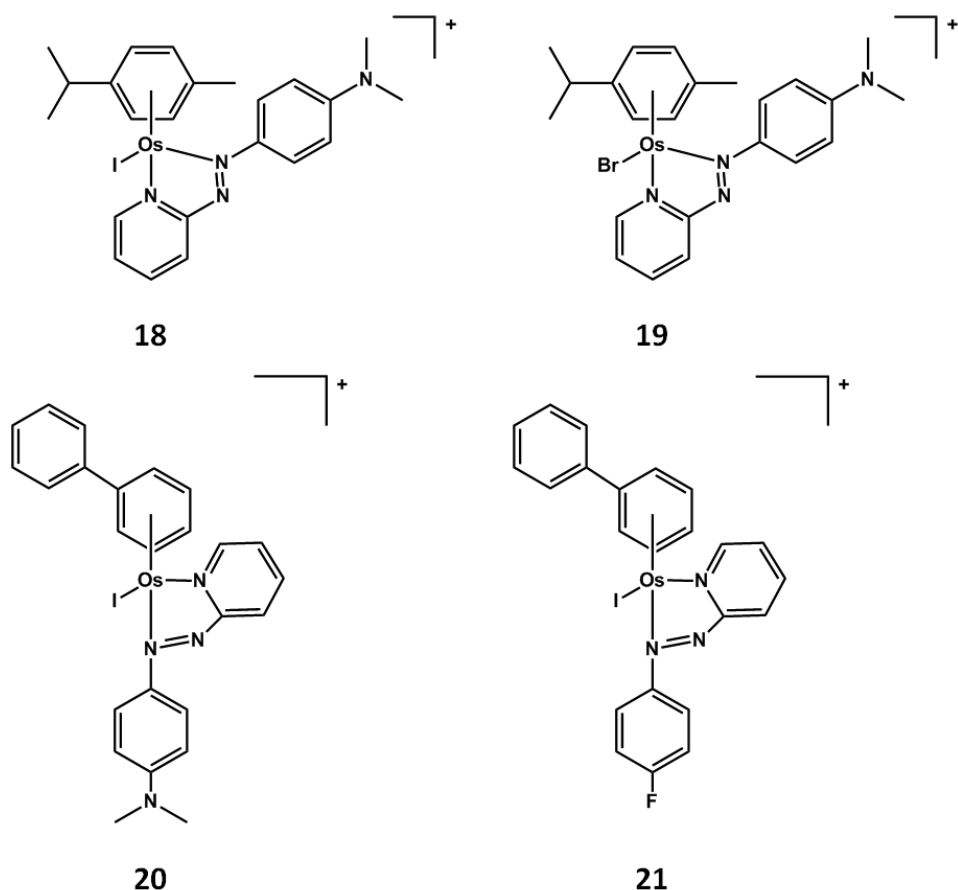


Figure 3.9 Structures of Os-based complexes **18** $[\text{Os}(\eta^6\text{-p-cym})(\text{azpy-NMe}_2)\text{I}]^+$, **19** $[\text{Os}(\eta^6\text{-p-cym})(\text{azpy-NMe}_2)\text{Br}]^+$, **20** $[\text{Os}(\eta^6\text{-bip})(\text{azpy-NMe}_2)\text{I}]^+$, and **21** $[\text{Os}(\eta^6\text{-bip})(\text{azpy-f})\text{I}]^+$.

3.3.2.1. Complexes 18-21: separation of enantiomers and stability of 18

The enantiomers of complex **18** were separated using an isocratic gradient of 50:50 heptane:ethanol 0.5% TEA, 0.3% TFA, flow rate 1.00 mL/min, on a CHIRALPAK IC column. The injections of sample **18**, 1.0 mg/mL in EtOH, were 25 μL in volume. The resolution of 0.93 is significantly less than that achieved in previous experiments (complexes **11-15** and **17**), but there are still two separate peaks, see Figure 3.10 (top). Repeated collections of the individual peaks, as detailed in

Section 3.3.1, were carried out. The chromatogram in Fig 3.10 clearly shows that the two enantiomers are stable over 4 h in solution at approximately 20°C.

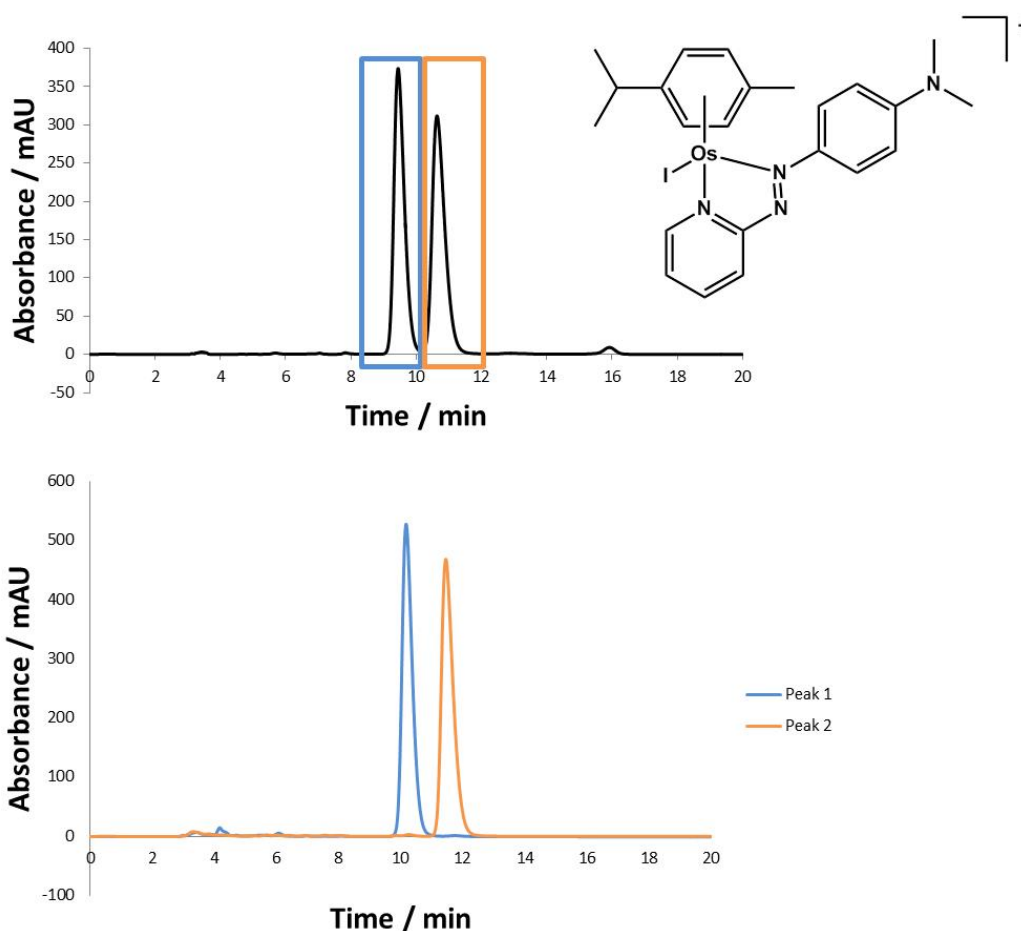


Figure 3.10 Top: Chromatogram of the separated isomers of **18**, R_S 0.93, bottom: re-injection of repeat collections of peak 1 (blue), t_R 9.05 min, and peak 2 (orange), t_R 10.15, of **18**. Separation conditions were the same for both analyses: 25 μ L injections of a 1.0 mg/mL solution of **18**, isocratic 50:50 heptane:ethanol containing 0.5% TEA and 0.3% TFA (v/v), flow rate 1.00 mL/min, on a CHIRALPAK IC column.

Separations, carried out under the same conditions as those for complex **18**, were carried out successfully for complexes **19**, **20** and **21** (R_S 1.08, 1.34 and 0.87, respectively). Separation of the enantiomers of each complex **19** and **20** can clearly be observed in Figure 3.11. However, the enantiomers of complex **21** are not fully resolved, and there appears to be a second set of peaks at ca. 9 min, 3 min after the first set, possibly as a result of hydrolysis of the complex.

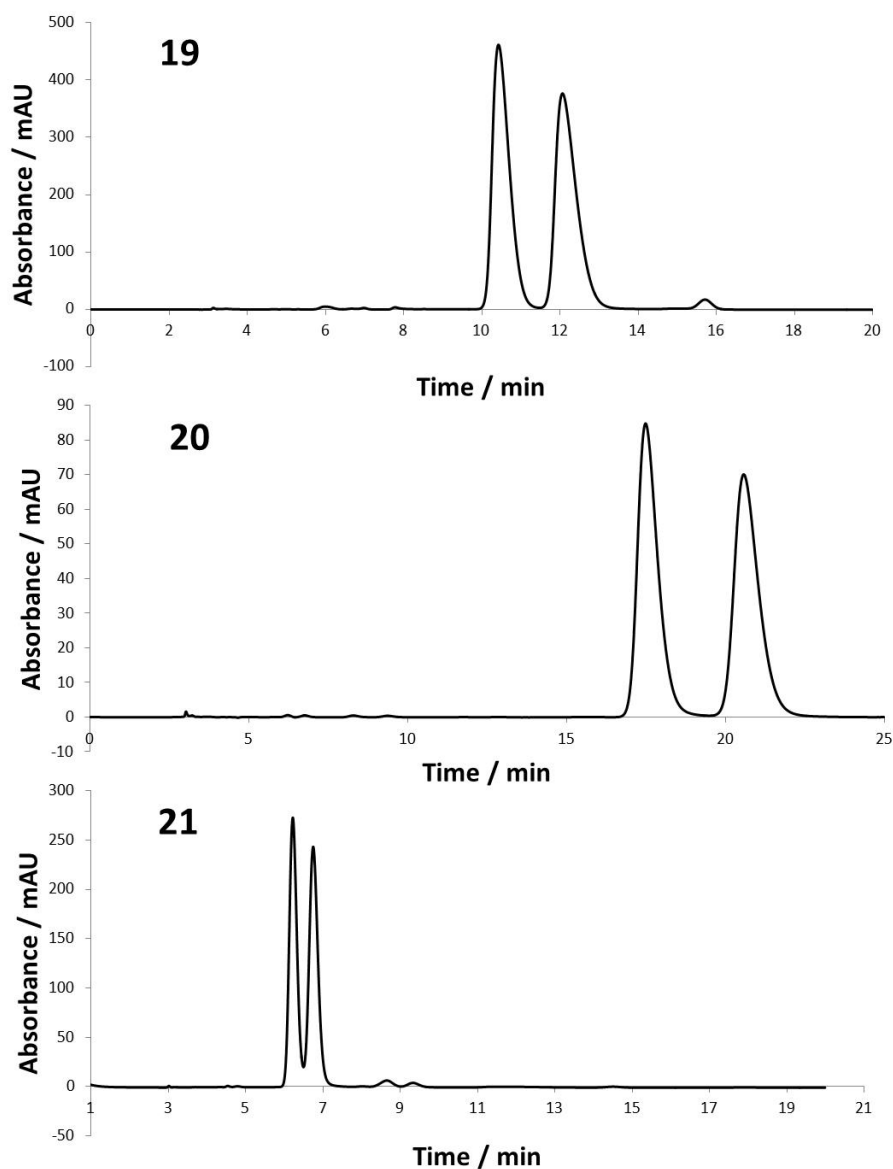


Figure 3.11 Separation of the enantiomers of **19**, peak1 t_R 10.40 min, peak 2 t_R 12.02 min, R_S 1.08, **20**, peak1 t_R 17.43 min, peak 2 t_R 20.52 min, R_S 1.34, and **21**, peak1 t_R 6.20 min, peak 2 t_R 6.72 min, R_S 0.87, using 25 μ L injections of a 1.0 mg/mL solution of **18**, isocratic 50:50 heptane:ethanol containing 0.5% TEA and 0.3% TFA, flow rate 1.00 mL/min, on a CHIRALPAK IC column.

3.3.2.2 Complexes **22** and **23**: separation of enantiomers and stability of **23**

As well as osmium-based compounds, the enantiomers of some ruthenium-based compounds were also separated. Complexes **22**, $[\text{Ru}(\eta^6\text{-flu})(\text{en})\text{Cl}]^+$, and **23**, $[\text{Ru}(\eta^6\text{-phent})(\text{en})\text{Cl}]^+$, are shown in Figure 3.12, they are Ru-based compounds that have facial chirality due to the unsymmetric aromatic ligands. The compounds were provided by Dr Abraha Habtemariam. A method was developed that successfully separated the enantiomers of both complexes: 70:30 isocratic of heptane:ethanol containing 0.5% TEA, and 0.3% TFA (v/v), flow rate 1.00 mL/min, 25 μL injection of a 1.0 mg/mL solution in EtOH, on a CHIRALPAK IC column. The results are shown in Figures 3.13 and 3.14. The bottom of Figure 3.14 also shows the chromatograms of the individual collected enantiomers of **23**, as detailed in Section 3.3.1. After 5 h in solution at approximately 20°C, the enantiomers appear stable.

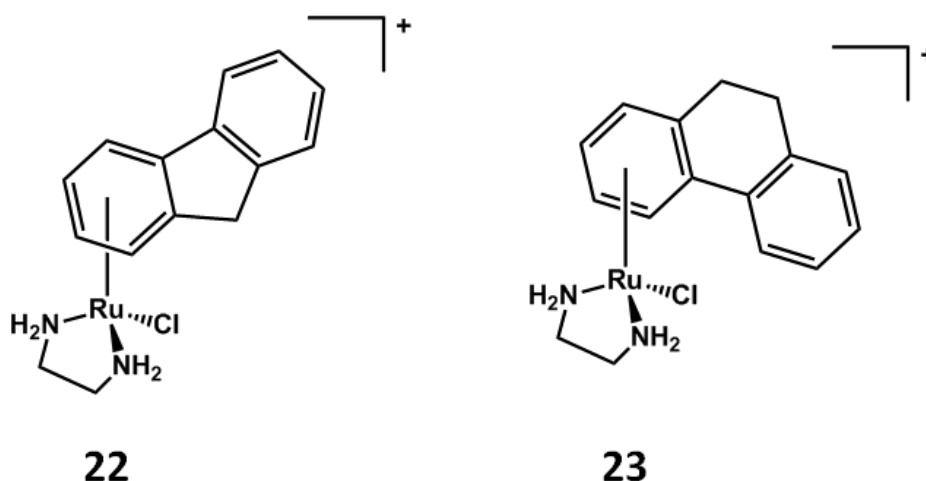


Figure 3.12 Structures of complexes **22**, $[\text{Ru}(\eta^6\text{-flu})(\text{en})\text{Cl}]^+$ and **23**, $[\text{Ru}(\eta^6\text{-phent})(\text{en})\text{Cl}]^+$.

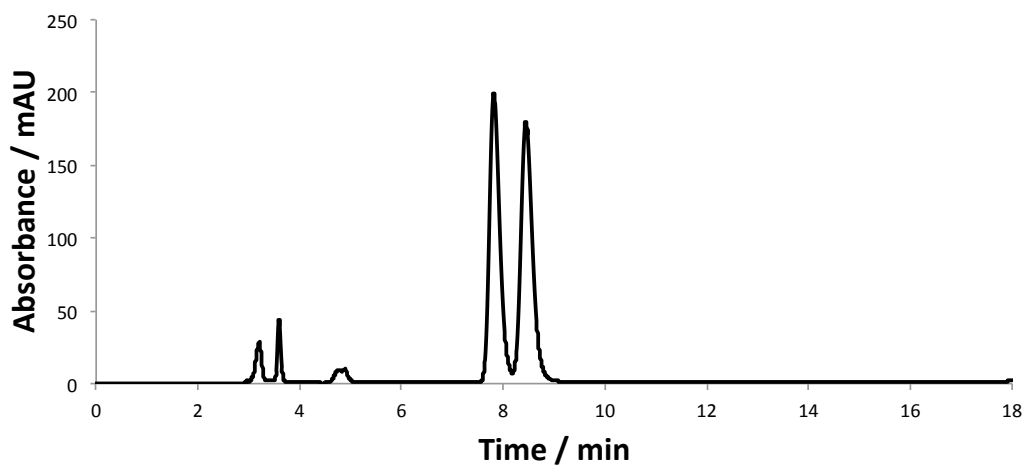


Figure 3.13 Chromatogram for the separation of the two enantiomers of **22**, peak 1 t_R 7.80 min, peak 2 t_R 8.43 min, R_S 0.92, isocratic 70:30 heptane:ethanol containing 0.5% TEA, and 0.3% TFA (v/v), flow rate 1.00 mL/min, on a CHIRALPAK IC column.

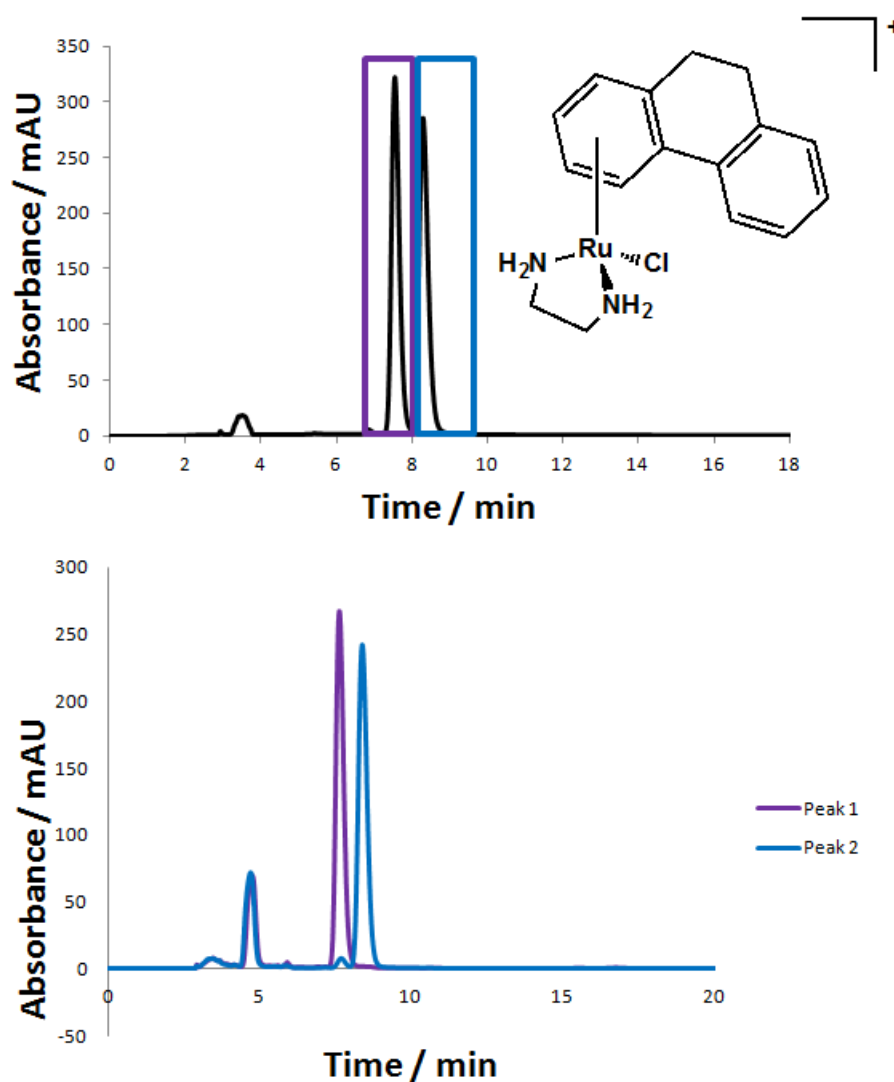


Figure 3.14 Top: Chromatogram for the separation of the two enantiomers of **23**, R_S 0.98, using an isocratic gradient of 70:30 heptane:ethanol containing 0.5% TEA, and 0.3% TFA (v/v), flow rate 1.00 mL/min, on a CHIRALPAK IC column. Bottom: chromatograms of the collected peaks 1 (purple), peak1 t_R 7.52 min, and 2 (blue), peak 2 t_R 8.27 min, of **23**.

3.3.2.3. Complex 24: using a system that can be separated by other means

Compound **24**, $[\text{Ru}(\eta^6\text{-p-cym})(\text{Impy})\text{I}]^+$, contains two chiral centres, i.e. there are four possible diastereomers of the compound. The four different diastereomers can be separated by crystallisation. In this section complexes using

only one set of the diastereomers, those with the R-configured bidentate ligand (separated by crystallisation) are studied, see Fig 3.15. Both compounds were provided by Dr María Xosé Romero Castro. The method of separation of the diastereomers with differing chirality at the metal centre was an isocratic flow of 70:30 heptane:ethanol containing 0.5% TEA, and 0.3% TFA, flow rate 1.00 mL/min, 25 μ L injection of a 1.0 mg/mL solution in EtOH, on a CHIRALPAK IC column. This was not optimised for complex **24**, and the peaks are not fully resolved, Figure 3.16 (bottom). The retention times of all of the peaks and the resolutions of the separations carried out on the stationary phase CHIRALPAK IC are shown in Table 3.3. However, since the enantiomers can be separated via crystallisation, these pure enantiomers were also analysed. From the chromatograms of the diastereomers separated by crystallisation, used as controls to establish retention times, (Fig. 3.16, top), the two diastereomers of **24** can be distinguished. Diastereomer **24-B** shows a small amount of **24-A** since it converts back to a mixture of enantiomers over time when in solution. In solution, the enantiomers are in the proportion of 1:3 for controls A and B. The intergrations of the peaks agree with this.

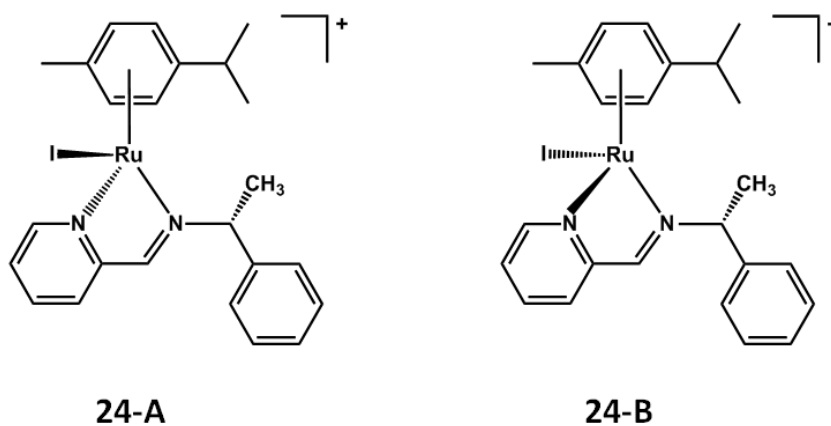


Figure 3.15 Structures of the two diastereomers of complex **24**, $[\text{Ru}(\eta^6\text{-p-cym})(\text{Impy})\text{I}]^+$.

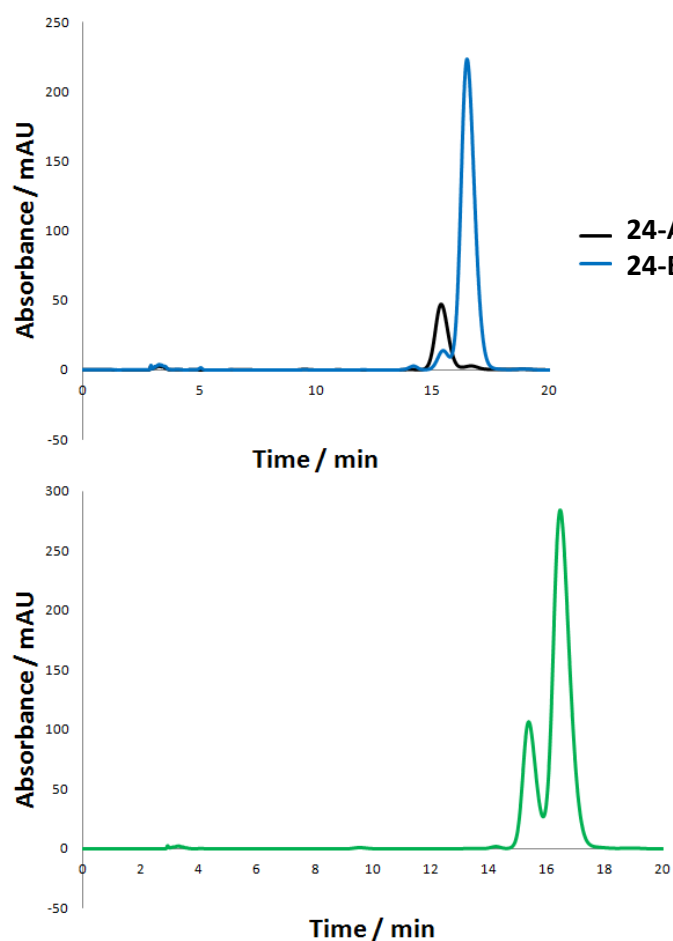


Figure 3.16 Top: chromatograms of the diastereomers separated by crystallisation **24-A**, t_R 15.36 min, and **24-B**, t_R 16.43 min. Bottom: chromatogram of a mixture of the diastereomers in EtOH, R_S 0.64. separation was carried out using an isocratic flow of 70:30 heptane:ethanol 0.5% TEA, 0.3% TFA, flow rate 1.00 mL/min, 25 μL injection of a 1.0 mg/mL solution in EtOH, on a CHIRALPAK IC column.

Table 3.3 Retention times (t_1 and t_2) and resolution of peaks eluted from the CHIRALPAK column.

Complex	t_1 / min	t_2 / min	R_s
18	9.05	10.15	0.93
19	10.40	12.02	1.08
20	17.43	20.52	1.34
21	6.20	6.72	0.87
22	7.80	8.43	0.92
23	7.52	8.27	0.98
24	15.36	16.43	0.64

3.4 Discussion

Chiral compounds can often be separated by crystallisation, using an optically-pure second molecule to form pairs of diastereomers. They can also be made by using stereo-selective syntheses.²³ They can be separated by capillary electrophoresis using micellar electrokinetic chromatography.²⁴ This work has been concerned with separations achieved by chiral chromatography. Typically, this involves sugar-based, e.g. amylose, stationary phases,^{15,25,26} but all chiral stationary phases rely on the same basic principles to achieve enantiomeric separation. They contain structural features like cavities and, as in the case of polysaccharides, grooves. The enantiomeric purity of the stationary phase means that these features have a specific stereochemistry or 'handedness', which, in turn governs its interactions with the different molecular configurations of the analyte. The enantiomer with the better 'fit' for the groove/cavity is retained on the column for

longer. Functionalisation of the sugars affects other types of interaction important in the separation process, such as: hydrogen bonding, electrostatic forces, π - π stacking, and steric effects.²⁷ The solvent mixture and the mobile phase additives used dictate the extent of interaction between the analyte and the stationary phase. The long chains of sugars that make up the stationary phase are functionalised with a range of different substituents in order to be able to separate the enantiomers of a range of different molecules.^{28-30,13} However, Further types of stationary phase have proven to be useful for the separation of chiral molecules, such as the glycopeptide antibiotic teicoplanin,³¹ and even the use of metal complexes such as the octahedral ruthenium(II)-based ones used by Sun et al.³²

Previously the chiral stationary phases (supplied by Chiral Technologies Europe) used in this study have been used to separate various metal-based complexes, such as the ruthenium-based half-sandwich complexes of Meggers et al.³³ These complexes were found to racemise up to 2% after 24 h at approximately 20°C in DMSO. There are various factors that contribute to the conformational lability at the metal centre of organometallic complexes, such as solvent, temperature and the nature of the ligands.³⁴⁻³⁸ Temperature can be an important factor as shown in the ¹H NMR experiments carried out by Brunner et al. on Ru(II) and Os(II) half-sandwich complexes. They found that at low temperatures (193-195 K), solutions prepared from enantiomerically-pure crystals remain as such in solution, but when the temperature increases (223-294 K), the concentration of the other epimer increases.³⁷ It has also been shown that chelating bi-dentate ligands increase the stability of a complex when compared to mono-dentate ligands

The stationary phase CHIRALPAK IA under the same chromatographic

protocol was shown to separate the enantiomers of a range of Ir-based complexes, differing only in the structure of the bi-dentate ligand, but all are chiral at the metal centre. This series of complexes has shown great potential in biological assays. Complex **11**, $[\text{Ir}(\eta^5\text{-Cp}^{\text{xbph}})(\text{phenpy})\text{Cl}]$, is highly cytotoxic with an IC_{50} value of $0.70 \mu\text{M}$ in A2780 human ovarian cancer cells.³⁹ Slight modifications to the ligands of these complexes can produce large changes in retention times. When the 2-phenylpyridine (2-phenpy) ligand of **11** is switched to 7,8-benzoquinoline and a less extended arene ligand (Cp^*) is used, complex **12**, $[\text{Ir}(\eta^5\text{-Cp}^*)(\text{benzq})\text{Cl}]$ is formed. A less hydrophobic arene ligand is used and so the retention time of the compound is increased; as with normal-phase chromatography, the more hydrophobic the complex, the quicker it will elute. The higher hydrophobicity of the bi-dentate ligand, unusually, results in the retention times of both peaks almost doubling (9.97 min to 18.61 min), as does the resolution (2.76 min to 4.39 min), as noted in Table 4.2.

Complexes **14**, $[\text{Ir}(\eta^5\text{-Cp}^*)(\text{py},4\text{-}(2\text{fph}))\text{Cl}]$, and **15**, $[\text{Ir}(\eta^5\text{-Cp}^*)(\text{py},4\text{-}(4\text{fph}))\text{Cl}]$, differ from **11** by a fluoro group on the phenyl ring, in the *ortho* position for **14**, and the *para* position for **15**, and the changing of the arene ligand to Cp^* . Once again, substitution of Cp^{xbph} for Cp^* results in an increase in retention time. When comparing the complexes **14** and **15**, the retention times of the two enantiomers of these compounds are very similar. The enantiomers of **15** elute slightly further apart than those of **14**, giving a resolution 0.26 higher. The complex with two fluorine substituents on the bi-dentate ligand **13**, $[\text{Ir}(\eta^5\text{-Cp}^*)(\text{dfphpy})\text{Cl}]$, however, has an increased retention time for both peaks, $t_1 = 9.11 \text{ min}$ and $t_2 = 13.98 \text{ min}$; along with a high resolution of the separation, $R_S = 5.38$. This suggests that

increasing the bulkiness of the bi-dentate ligand increases the retention times of both the species eluted, and also the resolution of the separation. However, this is only true up to a point, and when a bulkier substituent is added to the bi-dentate ligand, as in complex **16**, $[\text{Ir}(\eta^5\text{-Cp}^*)(\text{py},4\text{-}(4\text{tfmph}))\text{Cl}]$, ($R_S = 0.97$), there is a dramatic loss of resolution when compared to complex **14**, ($R_S = 2.86$), and even greater still when compared to the other complex with a *para* substituted ring, **15**, ($R_S = 3.12$). This is presumably attributable to steric hindrance caused by the larger group on the phenyl ring a phenomenon which reduces interaction of the molecule with the CHIRALPAK IA stationary phase.

All the complexes with a Cp^* arene ligand experience the largest change in retention time for the second enantiomer t_2 (when compared to **11**); this is the dominant factor in any change of resolution. In the case of complex **17**, $[\text{Ir}(\eta^5\text{-Cp}^*)(\text{pycarboxphen})\text{Cl}]$, where the substitution is on the pyridine ring, both retention times are shifted, causing the loss of resolution. The change in retention times may also be due to the ligand altering the overall hydrophobicity of the complex, a property which can also be crucial for the passive uptake of such drugs into cells.⁴⁰ From literature values of Log P values of the octanol/water partitions for similar iridium-based complexes,⁴¹ some observed trends could be related to the work reported here. A series of complexes: $[\text{Ir}(\eta^5\text{-Cp}^*)(1,10\text{-phenanthroline})\text{Cl}]^+$, $[\text{Ir}(\eta^5\text{-Cp}^{\text{xph}})(1,10\text{-phenanthroline})\text{Cl}]^+$, and $[\text{Ir}(\eta^5\text{-Cp}^{\text{xbph}})(1,10\text{-phenanthroline})\text{Cl}]^+$ have reported Log P values of -0.82, 0.48 and 1.11 respectively.⁴¹ This increasing lipophilicity, conceivably attributable, to the extension of the arene ligand, was also observed when comparing complex **11** with those containing the shorter Cp^* ligand. The unusual observation that increasing the hydrophobicity of the bi-dentate ligand

increases the retention time of the complex for normal phase chromatography may arise from the shape of the bi-dentate ligand. As the measured hydrophobicity of the complexes $[\text{Ir}(\eta^5\text{-Cp}^{\text{xph}})(\text{biphenyl})\text{Cl}]^+$, and $[\text{Ir}(\eta^5\text{-Cp}^{\text{xph}})(1,10\text{-phenanthroline})\text{Cl}]^+$, demonstrates an increase in Log P values from -0.95 to 0.48. The shape of the extended bi-dentate ligand could give rise to increased interactions with the functionalised sugars that comprise up the stationary phase.

The stationary phase CHIRALPAK IA has previously been shown to separate the enantiomers of $[\text{tris}(2\text{-phenylpyridine})\text{iridium(III)}]$ using an isocratic mix of hexane/ $\text{CHCl}_3/\text{CH}_2\text{Cl}_2$ (75:20:5).⁴² Unlike the complexes analysed here, Chen *et al.*⁴² showed that the separated enantiomers of $[\text{tris}(2\text{-phenylpyridine})\text{iridium(III)}]$ did not undergo racemisation after purification. This may suggest that the octahedral structure of the complexes studied by Chen *et al.* may be more stable than the piano-stool configuration of those investigated in this work.

In view of the wider range of charged anticancer organometallic complexes available, a much broader range of structures could be compared. In the case of the Os-based complexes, the effect of changing the arene, the bi-dentate ligand and the halide leaving ligand, an alteration already shown to be significant in cellular uptake for Ru-based complexes,⁴³ can be explored. By replacing the iodido ligand (**18**, $[\text{Os}(\eta^6\text{-p-cym})(\text{azpy-NMe}_2)\text{I}]^+$) with bromido (**19** $[\text{Os}(\eta^6\text{-p-cym})(\text{azpy-NMe}_2)\text{Br}]^+$), the retention times of both peaks are longer and t_2 (the retention time of the second peak to be eluted) even longer, thereby increasing the resolution. Extension of the arene ligand from *para*-cymene (**18**) to biphenyl (**20**, $[\text{Os}(\eta^6\text{-bip})(\text{azpy-NMe}_2)\text{I}]^+$) leads to a large modification in the chromatograms of the Os-based complexes, the value t_1 changes by 8.38 min, that of t_2 by 10.37 min, and the

resolution increases by 0.42. This is ascribable to the increased hydrophobicity of the complex by adding an extra phenyl ring. However, the most dramatic shift is the considerable reduction in retention times of both enantiomers when the bi-dentate ligand is changed from azpy-NMe₂ (**20**) to azpy-F (**21**, [Os(η^6 -bip)(azpy-f)I]⁺); indeed, t_1 shortens by 11.23 min, and t_2 by 13.8 min. The chromatogram of **20** shows very broad peaks over 2 min, and with the introduction of the new ligand the peaks for **21** narrow to under one minute in width, resulting in only a small loss of resolution (0.47).

Compounds with a ruthenium centre were also analysed. **22**, [Ru(η^6 -flu)(en)Cl]⁺, and **23**, [Ru(η^6 -phent)(en)Cl]⁺ which are facially chiral and only have a small difference in their aromatic ligands from fluorene (**22**) to phenanthrene (**23**). This is reflected in a maximum difference of 0.28 min between the retention times of the enantiomers eluted first, and only a difference of 0.06 in the resolution of the two chromatograms. Upon separation of the two enantiomers of **22**, they remain stable in solution, Fig 3.14. There is a small amount of contamination observed in the chromatogram shown in Fig. 3.14 this is believed to be due to grease from the vacuum line. This stability means that it is possible to scale up the separation and collect enough of each purified enantiomer in order to carry out kinetic studies, cell testing and further experiments required for potential new drugs that are chiral. This is also the case for the Os-based complex **18**, which has already shown promising activity as a racemic mixture.¹⁹

Studies on the other Ru-based complex investigated, **24** ([Ru(η^6 -p-cym)(Impy)I]⁺), show that diastereomers with two chiral centres, one of which is in the R- configuration, can be separated by chromatographic methods. Studies of the

stability of the separated enantiomers of the Os- and Ru-based complexes suggest that the iridium(II) Cp ligands are more labile than the Os(II) and Ru(II) arene ligands.

3.5 Conclusions

In conclusion, the enantiomers and diastereomers of several metal-based compounds were separated by chromatographic methods using CHIRALPAK IA and CHIRALPAK IC columns. The stability of some of these enantiomers was also assessed. All of the neutral Ir(Cp*)-based complexes tested reverted to a racemic mixture after a minimum of 2 h in solution at approximately 20°C, however, the Ru- and Os-based enantiomers maintained stability over 2 or more hours in ethanol at approximately 20°C. Separations of these enantiomers can, in the future, be scaled up to obtain enough material for cell testing and further biological assays.

Small structural differences, such as changing the halide leaving group (complexes **11-17**), were found to have a substantial effect on the retention time of the enantiomers and the resolution of the separation. Alteration of any of the ligands of the complex was shown to give rise to change in retention times, but the most dramatic changes were caused by the addition of either hydrophilic or hydrophobic groups to the bi-dentate ligand. In summary, these studies have provided an important step towards the preparation of chirally pure organometallic complexes which can undergo clinical development. In principle, biological assays can now be carried out using both the racemate and the individual

enantiomers of those compounds which are stable in solution, or only the racemate for those that were shown to be unstable.

3.6 References

1. S. E. Sherman and S. J. Lippard, *Chem. Rev.*, 1987, **87**, 1153–1181.
2. A. Pinto and S. Lippard, *Biochim. Biophys. Acta*, 1985, **780**, 167–180.
3. J. Reedijk, *Eur. J. Inorg. Chem.*, 2009, **2009**, 1303–1312.
4. P. J. Dyson and G. Sava, *Dalt. Trans.*, 2006, **2006**, 1929–1933.
5. F. S. Mackay, J. A. Woods, H. Moseley, J. Ferguson, A. Dawson, S. Parsons, and P. J. Sadler, *Chem. Eur. J.*, 2006, **12**, 3155–3161.
6. G. Sava, G. Jaouen, E. a Hillard, and A. Bergamo, *Dalt. Trans.*, 2012, **41**, 8226–8234.
7. A. Casini, C. G. Hartinger, A. A. Nazarov, and P. J. Dyson, *Medicinal Organometallic Chemistry*, Springer Berlin Heidelberg, Berlin, Heidelberg, 2010, vol. 32.
8. S. W. Smith, *Toxicolo. Sci.*, 2009, **110**, 4–30.
9. FDA, *Chirality*, 1992, **4**, 338–340.
10. K. J. Kilpin, S. M. Cammack, C. M. Clavel, and P. J. Dyson, *Dalt. Trans.*, 2013, **42**, 2008–2014.
11. P. Beagley, M. a. L. Blackie, K. Chibale, C. Clarkson, J. R. Moss, and P. J. Smith, *J. Chem. Soc. Dalt. Trans.*, 2002, **2002**, 4426–4433.
12. P. Beagley, M. Blackie, and K. Chibale, *Dalt. ...*, 2003, **2003**, 3046–3051.
13. B. Chankvetadze, *J Chromatogr. A*, 1997, **787**, 67–77.
14. C. Yamamoto, S. Inagaki, and Y. Okamoto, *J. Sep. Sci.*, 2006, **29**, 915–923.
15. B. Chankvetadze, *J. Chromatogr. A*, 2012, **1269**, 26–51.
16. S. N. Paisner and R. G. Bergman, *J. Organomet. Chem.*, 2001, **621**, 242–245.
17. T. Nagai, *J. Chromatogr. A*, 1992, **606**, 33–42.
18. P. Sun, A. Krishnan, A. Yadav, S. Singh, F. M. MacDonnell, and D. W. Armstrong, *Inorg. Chem.*, 2007, **46**, 10312–10320.

19. Y. Fu, A. Habtemariam, A. M. Pizarro, S. H. van Rijt, D. J. Healey, P. a Cooper, S. D. Shnyder, G. J. Clarkson, and P. J. Sadler, *J. Med. Chem.*, 2010, **53**, 8192–8196.
20. S. D. Shnyder, Y. Fu, A. Habtemariam, S. H. van Rijt, P. a. Cooper, P. M. Loadman, and P. J. Sadler, *Medchemcomm*, 2011, **2**, 666–668.
21. Y. Fu, M. J. Romero, A. Habtemariam, M. E. Snowden, L. Song, G. J. Clarkson, B. Qamar, A. M. Pizarro, P. R. Unwin, and P. J. Sadler, *Chem. Sci.*, 2012, **3**, 2485–2494.
22. A. Habtemariam and M. Melchart, *J. Med. Chem.*, 2006, **49**, 6858–6868.
23. G. Büchel, I. Stepanenko, and M. Hejl, *J. Inorg. Bio. Chem.*, 2012, **113**, 47–54.
24. A. R. Timerbaev, C. G. Hartinger, and B. K. Keppler, *Trends Anal. Chem.*, 2006, **25**, 868–875.
25. B. Chankvetadze, C. Yamamoto, and Y. Okamoto, *J. Chromatogr. A*, 2001, **922**, 127–137.
26. B. Chankvetadze, E. Yashima, and Y. Okamoto, *J. Chromatogr. A*, 1995, **694**, 101–109.
27. I. Ali, K. Kumerer, and H. Y. Aboul-Enein, *Chromatographia*, 2006, **63**, 295–307.
28. L. Peng, S. Jayapalan, B. Chankvetadze, and T. Farkas, *J. Chromatogr. A*, 2010, **1217**, 6942–6955.
29. P. Wang, D. Liu, X. Lei, S. Jiang, and Z. Zhou, *J. Sep. Sci.*, 2006, **29**, 265–271.
30. K. S. S. Dossou, P. Chiap, B. Chankvetadze, A.-C. Servais, M. Fillet, and J. Crommen, *J. Chromatogr. A*, 2009, **1216**, 7450–7455.
31. F. Gasparrini, I. D'Acquarica, J. G. Vos*, C. M. O'Connor, and C. Villani, *Tetrah. Asymm.*, 2000, **11**, 3535–3541.
32. P. Sun, A. Krishnan, A. Yadav, F. M. MacDonnell, and D. W. Armstrong, *J. Mol. Struct.*, 2008, **890**, 75–80.
33. G. Atilla-Gokcumen and D. Williams, *ChemBioChem*, 2006, **7**, 1443–1450.
34. H. Brunner, *Angew. Chem. Int. Ed.*, 1969, **8**, 382–383.
35. H. Brunner and J. Aclasis, *Angew. Chem. Int. Ed.*, 1974, **31**, 13–14.
36. H. Brunner, R. Oeschey, and B. Nuber, *Organomet.*, 1996, **7333**, 3616–3624.

37. H. Brunner, T. Zwack, and M. Zabel, *Polyhedron*, 2003, **22**, 861–865.
38. C. G. Hartinger, M. a Jakupec, S. Zorbas-Seifried, M. Groessl, A. Egger, W. Berger, H. Zorbas, P. J. Dyson, and B. K. Keppler, *Chem. Biodiver.*, 2008, **5**, 2140–2155.
39. Z. Liu, A. Habtemariam, A. M. Pizarro, G. J. Clarkson, and P. J. Sadler, *Organomet.*, 2011, **30**, 4702–4710.
40. M. J. McKeage, S. J. Berners-Price, P. Galettis, R. J. Bowen, W. Brouwer, L. Ding, L. Zhuang, and B. C. Baguley, *Cancer Chemother. Pharmacol.*, 2000, **46**, 343–350.
41. Z. Liu, A. Habtemariam, A. M. Pizarro, S. a Fletcher, A. Kisova, O. Vrana, L. Salassa, P. C. a Bruijninx, G. J. Clarkson, V. Brabec, and P. J. Sadler, *J. Med. Chem.*, 2011, **54**, 3011–3026.
42. X. Chen, Y. Okamoto, T. Yano, and J. Otsuki, *J. Sep. Sci.*, 2007, **30**, 713–716.
43. I. Romero-Canelón, L. Salassa, and P. J. Sadler, *J. Med. Chem.*, 2013, **56**, 1291–1300.

Chapter 4

Photonic crystal fibre mass spectrometry

In this chapter the development of a new analytical technique that couples mass spectrometry and photonic crystal fibres is reported. Initially the use of different types of sample cell construction was explored and the system optimised. The efficacy of the technique will then be assessed by using it to study a well known photoreaction. The system was proven successful, and the technique was then applied to a new system to gain insight into the mechanism of action of a new potential phototherapy.

4.1 Introduction

4.1.1 Photoactivatable metal-based drugs

Metal-based anticancer drugs have had success in the clinic for over 30 years,¹ and are used in the treatment of a wide range of cancers such as bladder, head, neck, testicular and cervical.² However, as discussed in Chapter 1 many cancers are intrinsically resistant to platinum-based, others may develop resistance over time and it can also cause multiple unwanted side effects such as nephrotoxicity and ototoxicity. These problems have led to the use of new strategies in the development of metal-based drugs to reduce side-effects and have a different spectrum of activity to established platinum-based treatments. This quest for new, better, metal-based treatments has led to exploration of the use of different oxidation states of the metal centre, with the inclusion of more stable Pt(IV) drugs to reduce unwanted side effects, and even the use of different metal centres, such as ruthenium, osmium and iridium.

Various methods have been employed to improve the targeting of these exciting new drugs such as the attachment of cell-penetrating peptides,^{3,4} using them to functionalise nanoparticles⁵ and the inclusion of enzyme inhibitors to block detoxification pathways⁶ (these are discussed at greater length in Chapter 1). Another strategy to reduce unwanted side-effects is to use a prodrug that can then be activated once it has reached the tumour site. This can be performed using a variety of techniques, one of which is photoactivation, where a prodrug is converted into the active form of the drug using light. The Sadler group have synthesised a range of promising potential light activated drugs using both platinum and ruthenium.⁷⁻⁸ Light therapies are already in the clinic in the form of photodynamic therapy (PDT). This therapy involves porphyrin-based drugs being activated by 600 - 850 nm light and generating reactive oxygen species that induce cell death.

4.1.2 Hyphenated mass spectrometry techniques

Mass spectrometry has long been used in conjunction with other analytical techniques, such as gas chromatography and capillary electrophoresis.^{9,10} The advent of electrospray ionisation in the field of mass spectrometry not only increased the types of sample that could be analysed but also the ease with which a range of techniques could be coupled with mass spectrometry. Liquid chromatography-mass spectrometry (LC-MS) is used in laboratories all over the world every day, and has been combined with other analytical methods to create techniques such as LC-ICP-MS¹¹ and LC-MS-NMR, giving great insight into sample composition and structures. Recent advances have led to the development of ultra-

high performance liquid chromatography-mass spectrometry (UPLC-MS), dramatically shortening analysis times, and the inclusion of nano liquid chromatography reducing sample and solvent volumes. The reduction in solvent consumed and waste generated by these developments in the field of chromatography not only reduces costs, but also minimises the environmental impact of a given analysis.

The tendency towards miniaturisation, requiring less sample for essentially the same analysis has led to the inclusion of microfluidics¹² into the field, and in recent years lab-on-a-chip approaches.^{13,14} Emphasis has also been placed on the speed of analysis and the possibility of online mass spectrometry measurements like those used by Yu et al. to monitor protease-catalysed reactions such as the trypsinolysis of cytochrome *c* and for online quality control sampling of industrial reactions.¹⁵ The aim of this chapter is to bring together these elements of dual analysis, reduced sample volumes, online sampling and the *in situ* irradiation adaptations already embraced by some analytical techniques, e.g. NMR probes fitted with lasers to study photochemical reactions in real time.

4.1.3 Photonic crystal fibres

Photonic crystal fibres (PCFs) are a type of optical fibre with unusual properties.¹⁶ They typically consist of a core surrounded by a photonic crystal cladding of very high-grade silica glass. They are fabricated by arranging capillaries and rods of high-grade silica into the shape of the desired structure of the fibre. The glass is then heated to extremely high temperatures (2000°C), and the silica is stretched out using a drawing tower; the resulting fibre has a diameter of around

40 μm . These fibres exhibit characteristically low guidance and transmission losses either by funnelling the light using a photonic bandgap, or a modified form of total internal reflection.^{17,18} The fibres can have either a solid or a hollow core (an example of a hollow core fibre is show in Figure 4.1). The immediate advantage of these structures when considering the analysis of solutions are the gaps in the cladding, and in some cases the core, i.e. those which allow liquids to pass through the fibres. This work will be primarily concerned with the applications of hollow core photonic crystal fibres (HC-PCFs)

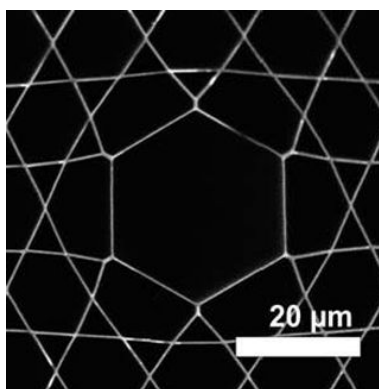


Figure 4.1 Scanning electron micrograph of a cross-section of a Kagomé hollow-core PCF.¹⁹

Previous uses of these fibres are discussed in Chapter 1, Section 1.3.1. In this chapter PCFs are put to a new use, in combination with a high-resolution mass spectrometer using a coupling device, on a microfluidic scale to reduce analysis times (microfluidics have been previously coupled to a mass spectrometer for various applications²⁰). This fusion of analyses aims to create a new analytical technique that allows samples to be irradiated rapidly analysed and any photoproducts characterised using minimal sample volume with low

concentrations. It may also allow the detection of short-lived species that are not observed by standard methods.

4.2 Experimental

4.2.1 Materials

All of the water used was doubly deionised water (DDW), purified using a Multipore Milli Q and a USF Elga UHQ water deioniser. Coupling devices and microfluidic mounts were constructed 'in-house' at the Max Plank institute of light in Erlangen; the initial microfluidic sample cells were constructed by Grayme White (Cambridge University). The microfluidic chips were purchased from the microfluidic ChipShop and the flow meter from (SLG1430-150) Sensirion. For sample introduction, a 500 μ L-glass syringe from Hamilton was used, and a syringe pump from kdScientific. Cyanocobalamin (99.99%) and aquacobalamin were from Sigma-Aldrich, as was the sodium nitroprusside (99.99%), 5'-GMP, as a sodium salt, (99.99%) and L-cysteine (99.99%). Both the 5'-AMP (99.99%) and glutathione (GSH) (99.99%) were purchased from Acros Organics. The metal-based drug complex **8** (*t,t,t*-[Pt(py)₂(N₃)₂(OH)₂]) was synthesised according to literature methods,⁷ **24** [(*p*-cym)Ru(bpm)(py)][PF₆]₂ by Dr Soledad Betanzos-Lara and **25** [{(η^6 -indan)RuCl]₂(μ -2,3-dpp)](PF₆)₂ was donated by Dr Abraha Habtemariam.

4.2.2 Methods

5.2.2.1 Sample preparation

All MS samples were filtered using NALGENE 0.2 μm polyethersulfone (PES) filters and then centrifuged at 14,000 rpm, 5°C for a period of 10 min. The pH of samples was measured using a Mettler-Toledo glass microelectrode connected to a Martini instruments Mi150 pH/temperature bench meter calibrated at pH values of 4, 7 and 10 using pH buffers from Mettler-Toledo

4.2.2.2 Mass spectrometry

Preliminary mass spectra, to test for interactions between **8**, *t,t,t*-[Pt(N₃)₂(OH)₂(py)₂], and the PCF were carried out on a Bruker HCT Ultra ion trap mass spectrometry in the positive mode. Sample flow rate was 240 $\mu\text{L/h}$, with scan ranges varied from 50 – 1000 *m/z* to 500 – 3000 *m/z*. The solvent used, cone voltage and source temperature varied depending on the sample. All other spectra were obtained on a Bruker MaXis high-resolution mass spectrometer (HR-MS). Samples were introduced to the MS at a flow rate of 100 $\mu\text{L/h}$. The acquisition parameters for spectra obtained in the positive ion mode are as follows: scan range 50 – 3000 *m/z*, set capillary 3000 V, end plate off-set –500 V, nebuliser pressure 0.4 bar, dry heater 180 °C, and dry gas 4.0 L/min. Negative ion spectra were obtained using the same conditions as those in the positive ion mode except that the set capillary was 4000 V and the ion polarity was set to negative. MS/MS experiments were carried using the conditions detailed above with an isolation width of 6 *m/z*,

and the collision energy varied depending on the sample. All spectra were processed using Bruker Daltonics Analysis software and Origin Pro 8.1.

4.2.2.3 Light sources

The 405 nm laser used was purchased from Thorlabs, the 488 nm laser from Topptica, and operated using Top Control software.

4.3. Results

4.3.1 Photonic crystal fibre mass spectrometry (PCF-MS) system design and development

As outlined in Chapter 2, it is thought that there may be some DNA adducts formed when complex **8**, $ttt\text{-[Pt(py)}_2\text{(N}_3\text{)}_2\text{(OH)}_2\text{]}$, is irradiated in the presence of oligonucleotides, that are currently undetectable by conventional methods due to the lengthy sample preparation. Reactions of **8** with 5'-GMP not only produce the $[\text{Pt(py)}_2\text{(5'-GMP)}_2]$ adduct observed on oligonucleotides in Chapter 2, but also the monoazido adduct $[\text{Pt(py)}_2\text{(N}_3\text{)(5'-GMP)}]$.⁷ These species are not detected by conventional MS methods, an observation possibly ascribable to the time taken to prepare the sample for analysis and the fact some platinum DNA adducts transform over time.²¹ With this in mind, a system incorporating the use of PCFs was been designed to characterise short-lived photoproducts that had not previously been detected.

4.3.1.1 PCF-MS system design and development: metallic coupling devices

For the purposes of this chapter, the term ‘direct infusion’ will be used for samples that have been directly injected into a mass spectrometer via PEEK tubing using a syringe and syringe pump. This is a conventional method for the introduction of samples into the mass spectrometer, and was used as a means of producing a ‘standard’ mass spectrum for comparison with those generated by the PCF-MS system. The vast majority of work in this chapter concerning fibre fabrication, optical coupling, and the introduction of solutions to the PCFs was carried out by Dr Sarah Unterkofler. My work was concerned with optimisation of the microfluidic circuitry, achieving successful coupling of the system to the mass spectrometer, carrying out control reactions by ‘conventional methods’ for comparison purposes and the selection of appropriate photoreactions for analysis. It was first necessary to establish if there was any interaction between the bare silica of the PCF and the metal complex that may affect the mass spectrum observed. Preliminary experiments carried out on an ion-trap mass spectrometer indicated that there were no major differences between the spectra of a 10 μM solution of complex **8** in a 50:50 water/methanol solvent mix when flowed through a PCF or PEEK tubing (both when in the dark and irradiated). These initial experiments were then repeated on a high-resolution instrument (Bruker MaXis) using a solution of 100 μM solution of **8** in 50:50 DDW and acetonitrile, with the addition of the steel coupling devices; see Figure 4.2, to the PCF. The solvent was changed to acetonitrile, since this produced a lower signal-to-noise ratio than that of the water methanol mix. This inclusion of metallic coupling devices to allow the

introduction of sample and light to the PCF (set-up shown in Figure 4.3) introduced several new, unknown platinum containing species at 579.2, 750.2 and 857.2 m/z , see Figure 4.4. MS/MS of the peak at 750.2 m/z shows fragments at 383.1, 411.1, 579.2 and 732.2 m/z . The ions 383.1 and 411.1 m/z are also observed in the spectrum of the direct infusion of **8**, Figure 4.5. This would suggest that the coupling devices have introduced a contaminant.



Figure 4.2 An example of an initial metallic (steel) coupling device built in the Max Plank Institute of Light, Erlangen used in the first PCF-MS system (Figure 4.3).

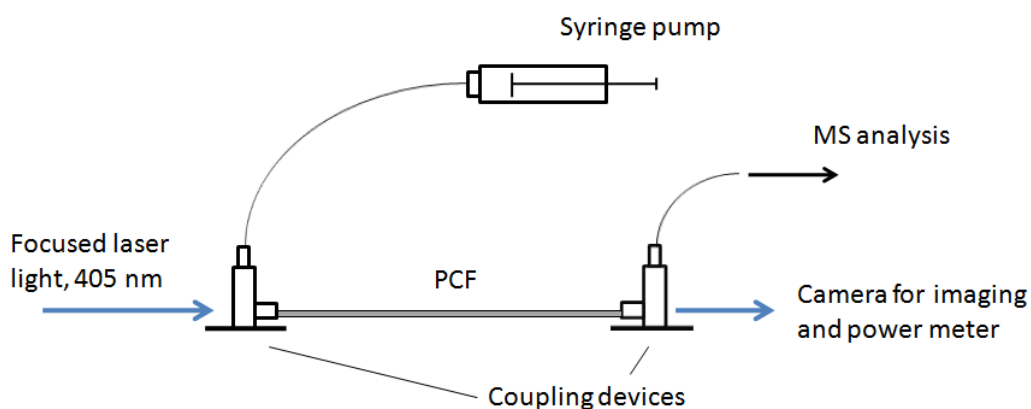


Figure 4.3 Schematic of a PCF sample injection system when coupled to 405 nm laser light.

For completeness of the comparison, the sample was then irradiated within the system using 405 nm laser light. The photoactivation of **8** resulted in the creation of several species that were also previously detected by direct infusion. The molecular formulae of some of the ions was determined: 382.0 m/z PtC₁₀H₁₁N₄, 430.0 m/z PtC₁₀H₁₂O₂N₅, 388.0 m/z PtC₁₀H₁₃O₂N₂. A structure is proposed for one of the photoproducts (388.0 m/z): this is a Pt(III) ion. Indeed, the photoactivation of Pt(IV) diazido complexes have previously been reported to generate this type of species (see Figure 4.6).²² The intensity of the unknown species 579.2, 750.2 and 857.2 m/z decreases over the time of irradiation, Figure 4.7. The system was then cleaned by continual flushing with acetonitrile. Further new unknown platinum-containing peaks then appeared at 382.0 m/z and 619.1 m/z , Figure 4.8. Even under dark conditions, and a continual flow of clean solvent, these species remained.

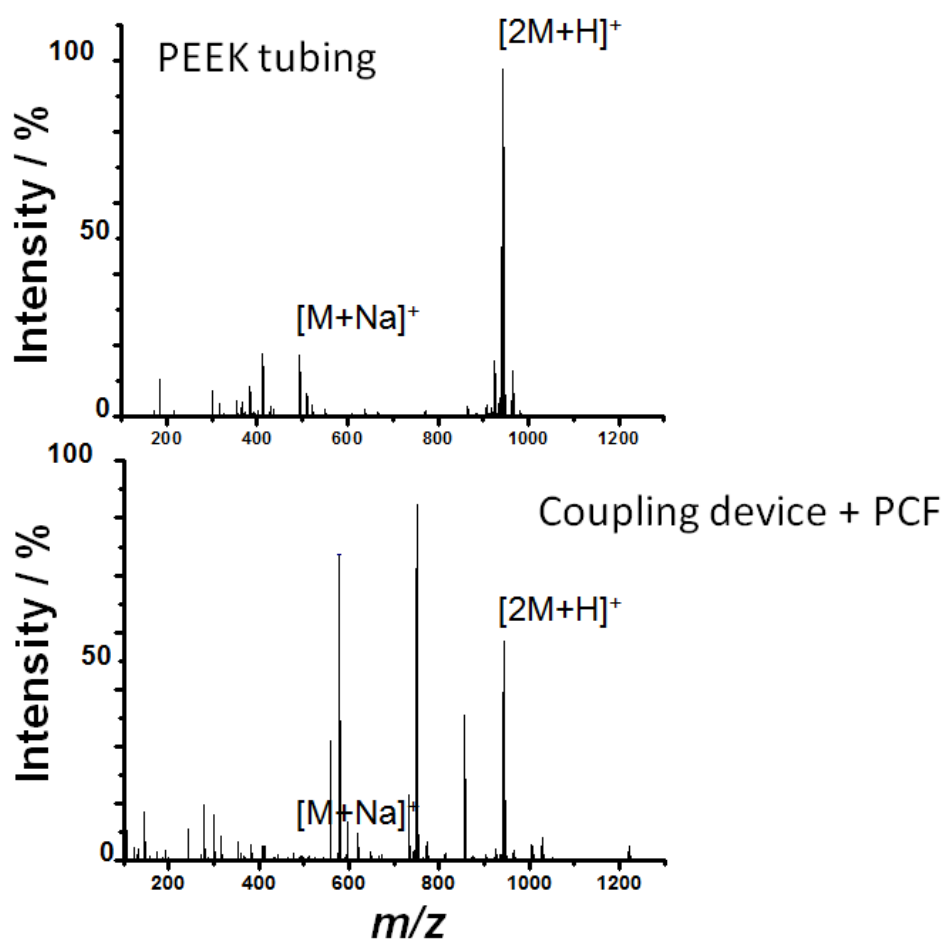


Figure 4.4 Top spectrum is of complex **8**, 10 μM in 50:50 methanol and DDW, in the dark flowed through PEEK tubing only; the bottom spectrum is the complex, 100 μM in 50:50 acetonitrile and DDW, flowed through the coupling device and PCF system in the dark. Additional unknown peaks appear in this spectrum at 579.2, 750.2 and 857.2 m/z . The peak at 388.1 m/z is assigned as $[\text{Pt(III)}(\text{py})_2(\text{OH})_2]^+$, 494.1 m/z as $[\text{M} + \text{Na}]^+$, and 943.1 m/z as $[2\text{M} + \text{H}]^+$.

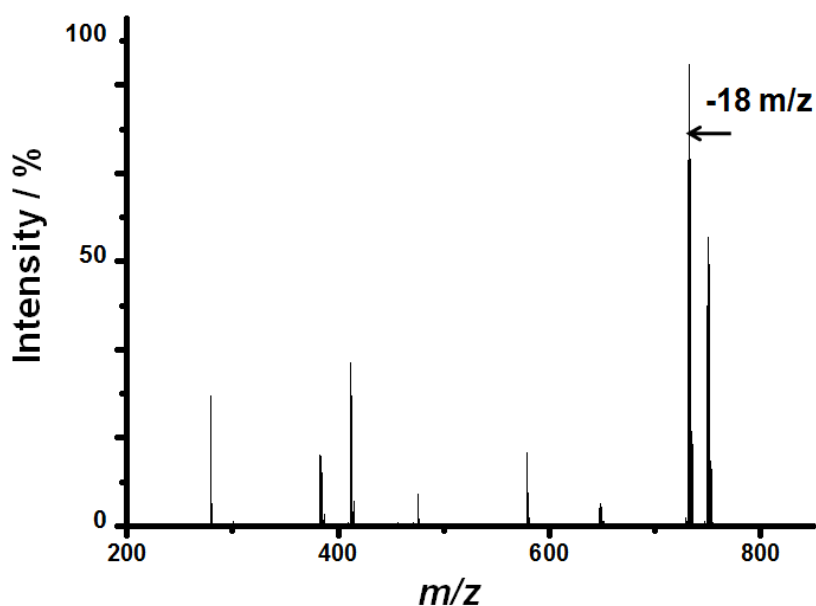


Figure 4.5 MS/MS of 750.2 m/z peak ascribable to contamination introduced by the coupling device, possibly from glue used in the construction. Peak isolation width of 6 m/z collision energy 15 eV. Its isotopic pattern suggests the presence of Pt in the ion, as would the smaller fragments 383.1 and 411.1 m/z also seen by direct infusion. The loss of 18 m/z is attributed to the loss of H_2O .

The photostability of these contaminant peaks was then tested by switching the laser back on. The post-irradiation contaminants appear to be highly photostable, and did not break down after 28 min of irradiation and constant flushing with acetonitrile. The sample cells provided effective optical coupling from the laser to the fibre, but also introduced contamination and have large pre- and post-irradiation mixing volumes of 60 μL each. These large mixing volumes increase the time of analysis, and the possibility of photoactivated species interacting with each other and solvent molecules. An alternative method of sample and light introduction was therefore deemed to be required. Preferably, the construction would be of a less reactive material and the mixing volumes would be smaller whilst retaining the optical properties of the sample cell.

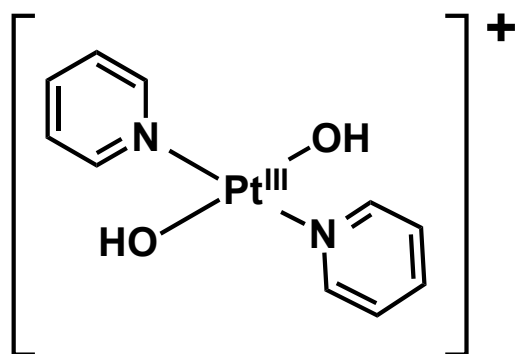


Figure 4.6 Proposed structure of the photoproduct of **8**, 388.0 m/z .

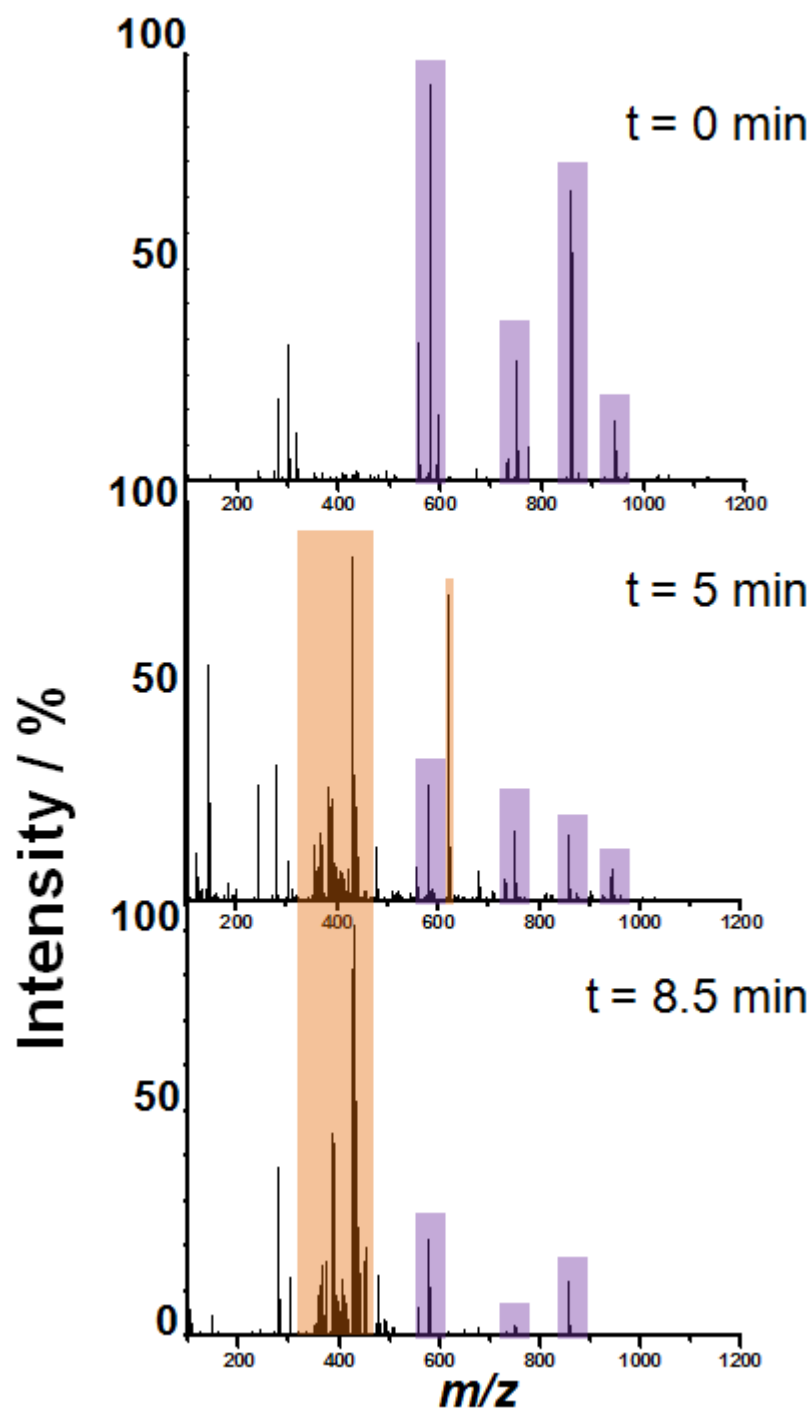


Figure 4.7 Irradiation of complex 8 (100 μM) in acetonitrile over time ($t = 0, 5, 8.5$ min), infused through the PCF-MS system. Ions that reduced in intensity with irradiation are highlighted in purple, whilst those that increase are highlighted in orange.

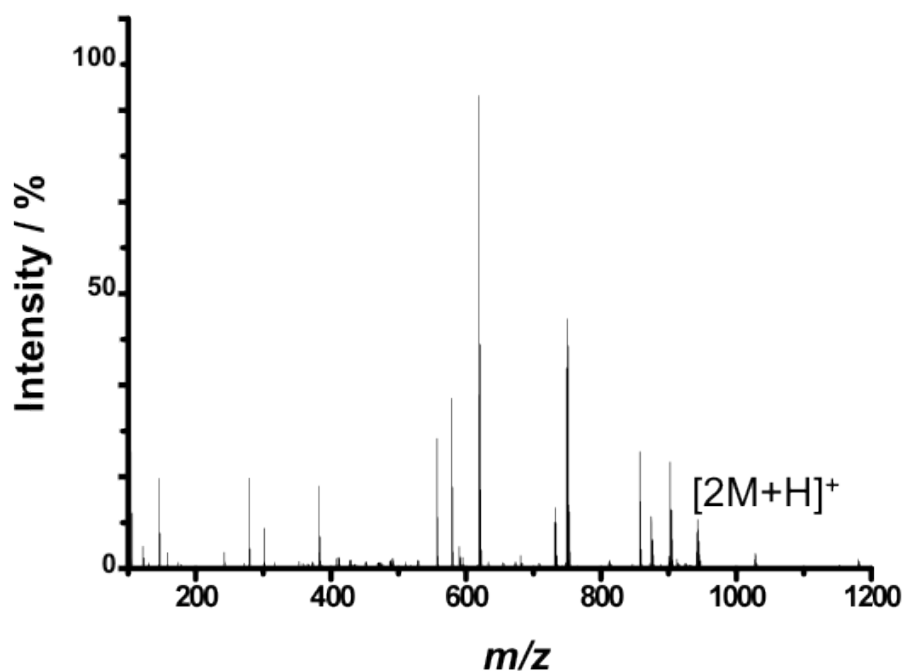


Figure 4.8 The initial mass spectrum of the instrument being flushed with HPLC-grade acetonitrile, showing the contamination from the metallic coupling devices, after irradiation. Ions 619.1 and 382.0 m/z are photostable. A small amount of 943.1 m/z , $[2M + H]^+$ was also detected.

4.3.1.2 PCF-MS system design and development: plastic microfluidic coupling devices

It was thought that the introduction of plastic (Teflon) microfluidic devices would improve the system since they would have smaller mixing volumes than the metallic coupling devices, reducing the analysis time, see Figure 4.9. An additional improvement was the drawing of a new photonic crystal fibre (Figure 4.10) that would guide the light better at 405 nm. The core of the fibre is smaller by 5 μm and the cladding has been altered to better 'trap' 405 nm light. When using the microfluidic devices, the fibre had to be placed inside one of the three PEEK tubing outlets (Figure 4.9 and Figure 4.11); however, the inner diameter of the tubing was

too small to fit the fibre and its protective cladding. To overcome this problem, the cladding was removed with a razor blade, leaving the fibre exposed. Without any cladding, the fibre is brittle and was prone to breakage when the ferrules are tightened to create a closed system.

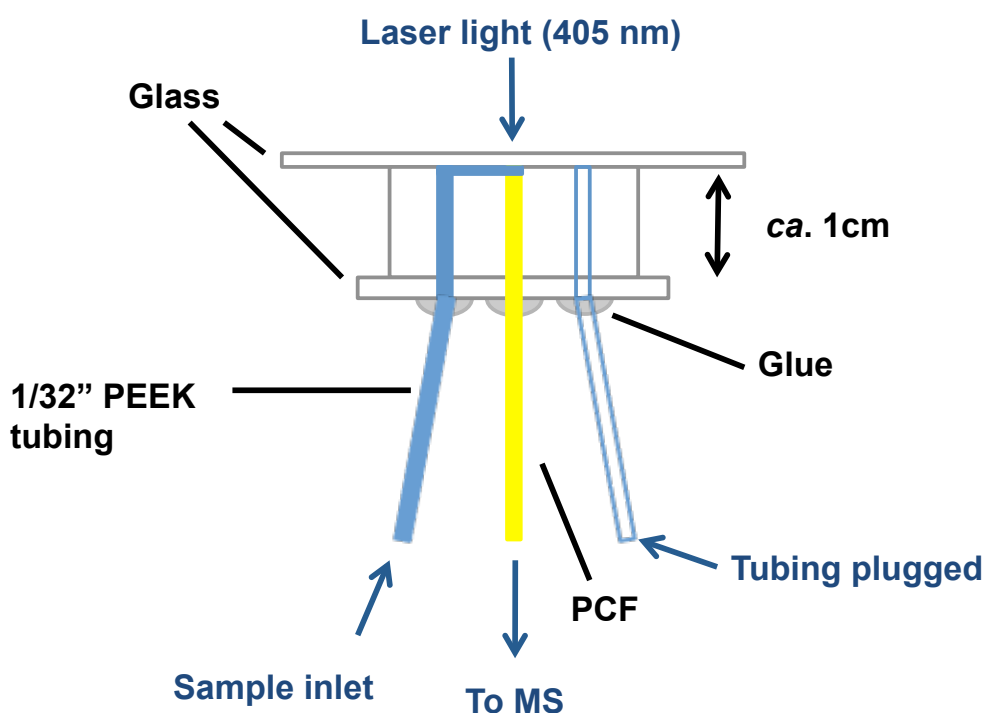


Figure 4.9 Diagram of the microfluidic device used as an interface to introduce sample solution and light into the PCF and allow for MS analysis.

The microfluidics proved problematic when it came to guiding the light to the PCF. Even in just an air-filled system, it was not possible to guide the light efficiently into the core of the fibre. This may have been due to breakages in the section of the fibre with the cladding removed close to the coupling interface. There also appeared to be imperfections in the glass coverslip where the light was coupled to the device, possibly arising from the adhesive used in the construction of the unit. The glue-based construction also prevented the passage of organic solvents through the device, since it would dissolve the adhesive. Overall, these

microfluidic devices did not prove successful. It was then proposed that PVC coupling devices, constructed using Teflon tape instead of glue, would be used. This would result in a return to large pre- and post-irradiation mixing volumes.

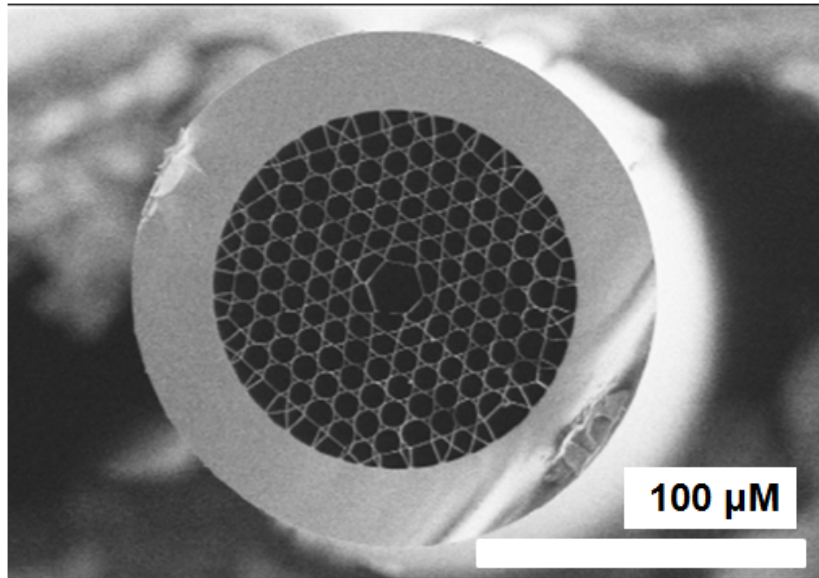


Figure 4.10 Cross-section of the new Kagomé fibre with improved 405 nm light guiding properties by changing the core size, the internal structure of the fibre and the cladding thickness (core approx. 15 μm).

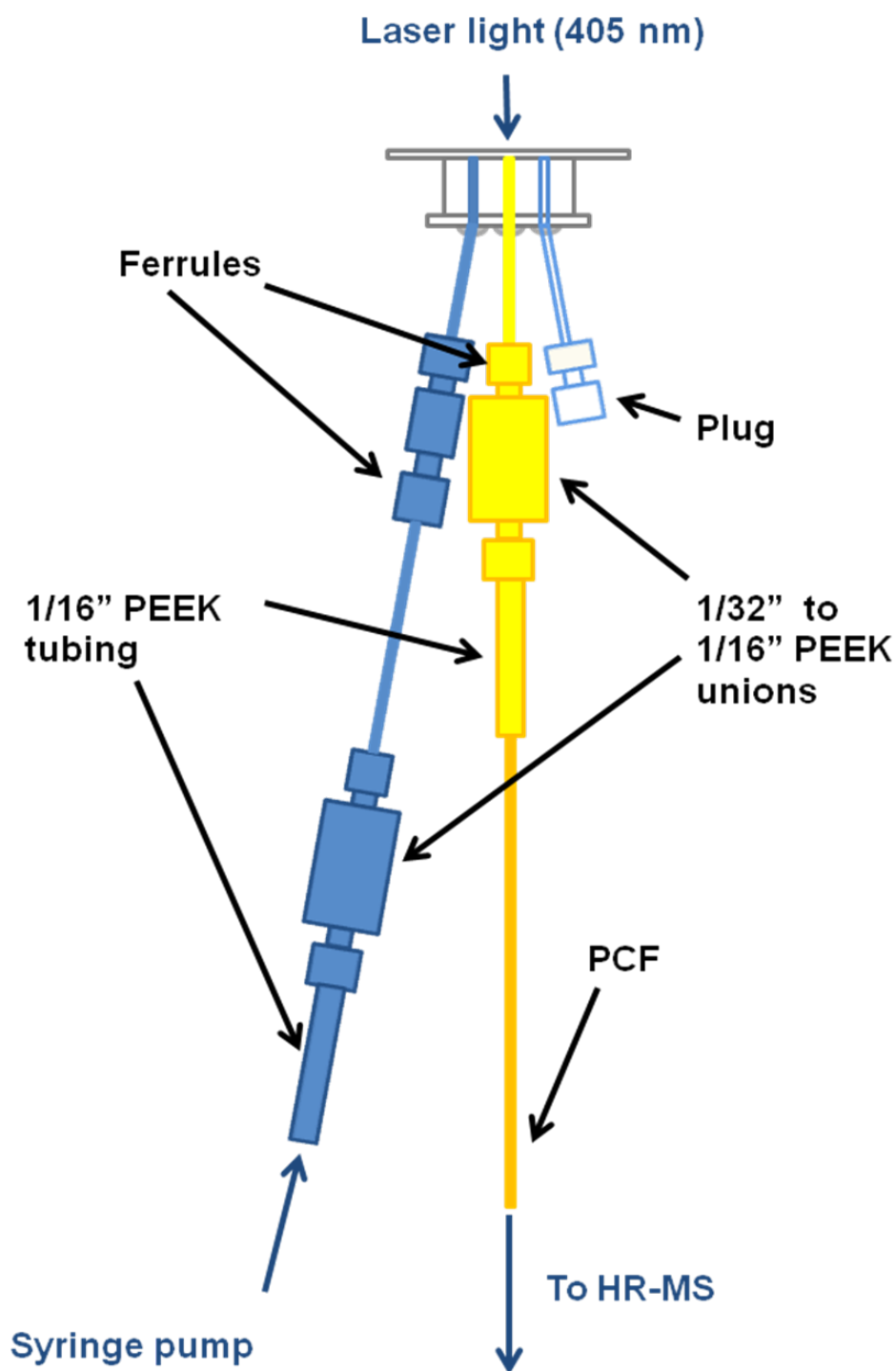


Figure 4.11 Schematic of the coupling of a microfluidic device into the system using PEEK HPLC fittings.

4.3.1.3 Design of PCF-MS system: PVC coupling devices

The system previously described in Section 4.3.1.2 was further adapted by the substitution of the microfluidic cells for new PVC pressure cells (Figure 4.12). It was hoped that they would aid the coupling of light into the fibre using optically accessible windows constructed from a high-grade glass and reduce the contamination problems associated with past systems.

After focusing the laser light into the core of the fibre, the flow rate through the system was measured in order to establish the rate required for the syringe pump to reach the ideal flow into the mass spectrometer. The tubing was detached from the MS at the end of the system. The volume of liquid that flowed through over a 15 min period was collected in an Eppendorf tube and its volume determined. This is a very crude approximation of the flow within the system, but should be enough to obtain a spectrum of high enough intensity. In view of the back-pressure within the system the syringe pump had to be set to 200 $\mu\text{L}/\text{h}$ to achieve the desired 100 $\mu\text{L}/\text{h}$ flow-rate. The flow rate of the sample is an important consideration when using ESI, since it affects both the desolvation and ionisation processes.

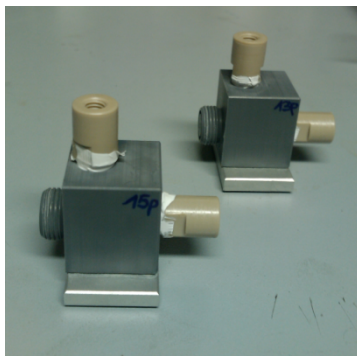


Figure 4.12 Picture of the new PVC coupling devices replacing the old microfluidic ones.

First 0.2 μm filtered DDW was flowed through the system, followed by the calibrant, sodium formate. At this point it was established that the intrinsic dead volume of the system was problematic for the low flow-rate (100 μL) of the system. Although the volume of the fibre itself is very small (65 nL in the core), the internal volume of each PVC pressure cell is 60 μL , requiring over an hour to run solution through the system.

A 500 μM solution of **8**, $\text{t}t\text{t}-[\text{Pt}(\text{py})_2(\text{N}_3)_2(\text{OH})_2]$, in DDW was then pumped into the system. The set flow rate was increased from 200 μL to 500 μL to reduce the dead time but this gave rise to the spray in to the MS taking longer to stabilise, a phenomenon which increased the pressure within the system.

The first spectrum was obtained after 1 h, Fig. 4.13. The sodium adduct of the complex is clearly observed at 494.1 m/z , as well a dimer of the complex at 943.1 m/z , and some fragment ions/photoproducts at 388.1 and 412.1 m/z . When the PCF-MS spectrum is compared to the spectrum of the complex directly infused into the MS, both under dark conditions (Fig. 4.14) and after irradiation at 420 nm (Fig. 4.15), significant differences were observed.

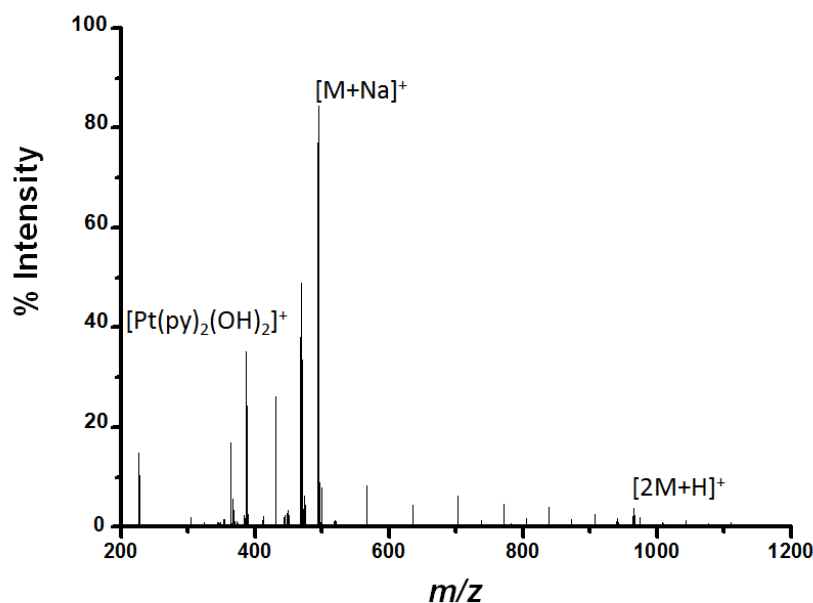


Figure 4.13 Mass spectrum of 500 μM complex **8**, $\text{t}t\text{t}$ -[Pt(py)₂(N₃)₂(OH)₂], in DDW, irradiated with 405 nm laser light in the PCF-MS system. Peak at 388.1 m/z assigned as [Pt(py)₂(OH)₂]⁺, 494.1 m/z as [M + Na]⁺ and 943.1 m/z as [2M + H]⁺.

The directly infused sample in the dark, Figure 4.14, contains a relatively high abundance of the complex with a sodium ion and the fragment ion/photoproduct 388.0 m/z [Pt(py)₂(OH)₂]⁺; a dimer of this complex is also detected at 943.1 m/z . In the irradiated sample, Figure 4.15 there is a complete absence of dimer formation and very low intensity of the peak assigned to the complex with a sodium ion. This may indicate that the dimer is likely to be formed during the ionisation process; as the droplet size shrinks and complex ions are forced closer together. The dominant peak in the spectrum in Figure 4.15 is the fragment ion/photoproduct [Pt(py)₂(OH)₂]⁺ at 388.0 m/z , indicating that photoreduction had taken place.

Comparison of the spectrum of the sample irradiated within the PCF-MS system (Figure 4.13) with directly infused samples reveals similarities with the spectrum of **8** in the dark (Figure 4.14), such as the presence of dimer and high proportions of the complex with a sodium ion. This suggests that the solution may not have been fully irradiated. The PCF-MS spectrum also contains a peak not observed in either of the other two spectra at 469.1 m/z . From the isotopic pattern of the peak, it is highly likely that the species contains platinum, but its structure is as yet undetermined. Tentative assignment to a short-lived species not detected by direct infusion can be ruled out in view of the long period of time between the sample being exposed to the laser light and acquisition of the PCF-MS spectrum (1.0 h).

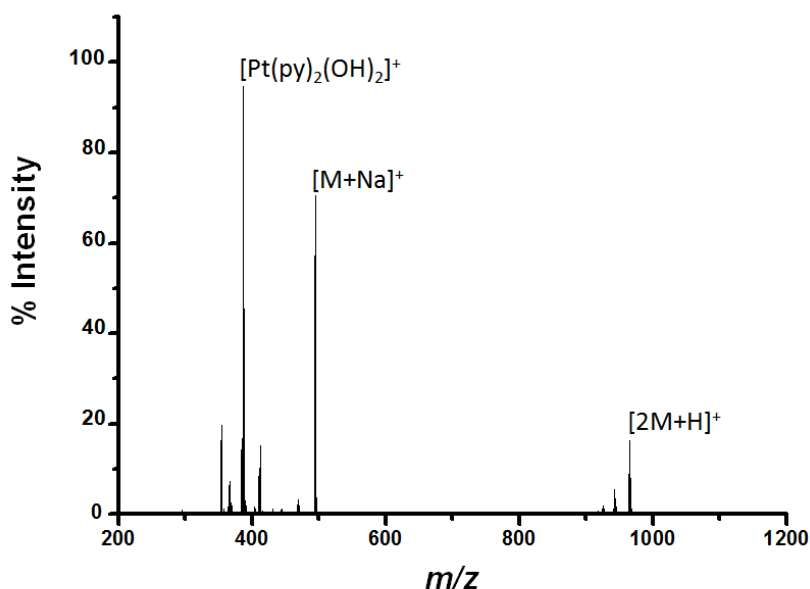


Figure 4.14 Mass spectrum of a dark solution containing 500 μM of **8** in DDW directly infused. Peaks at 388.1 m/z are assigned as $[\text{Pt}(\text{py})_2(\text{OH})_2]^+$, 494.1 m/z as $[\text{M} + \text{Na}]^+$, and 943.1 m/z as $[2\text{M} + \text{H}]^+$.

Another reason for the PCF-MS sample having greater similarity to the dark directly infused sample is that during the time taken for the sample to flow through the system, the light drifted from the core of the fibre as indicated by the post-fibre imaging camera (Fig. 4.3). This could occur for several reasons; the generation of small bubbles of N₂ gas from the photoreduction reaction;⁷ the high flow-rate through the system could have placed it under strain causing movement of the fibre, and also the limited ability of the fibre to guide light at 405 nm.

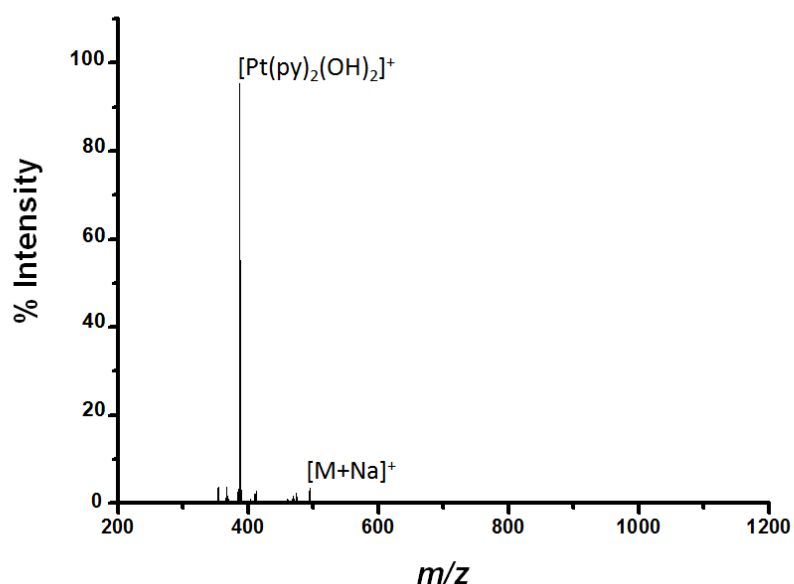


Figure 4.15 Mass spectrum of the direct infusion of a 500 μ M solution of **8** after 30 min of irradiation at 420 nm in a photoreactor. Peaks at 388.1 m/z are assigned as $[\text{Pt}(\text{py})_2(\text{OH})_2]^+$ and 494.1 m/z as $[\text{M} + \text{Na}]^+$.

4.3.1.4 Design of PCF-MS system: microfluidic devices using ‘off-the-shelf’ chips

To reduce drifting of the light out of the core, as described at the end of the previous section, the set up was modified so that the sample is introduced at the opposite end to which the light is coupled into the system. This is intended to

reduce movement at the end of the fibre that the laser is focused into, preventing the light from moving out of the core once focused. A flow meter was also introduced to obtain accurate, online measurements of the flow-rate, see Figure 5.16. The wavelength of laser light used was also changed to 488 nm for two reasons: firstly, PCFs are better at guiding longer wavelengths of light, and secondly this is a better wavelength for medical application, with a view to working with photoactivatable anticancer complexes with potential for clinical use. A cross-section of this new fibre can be seen in Figure 4.17.

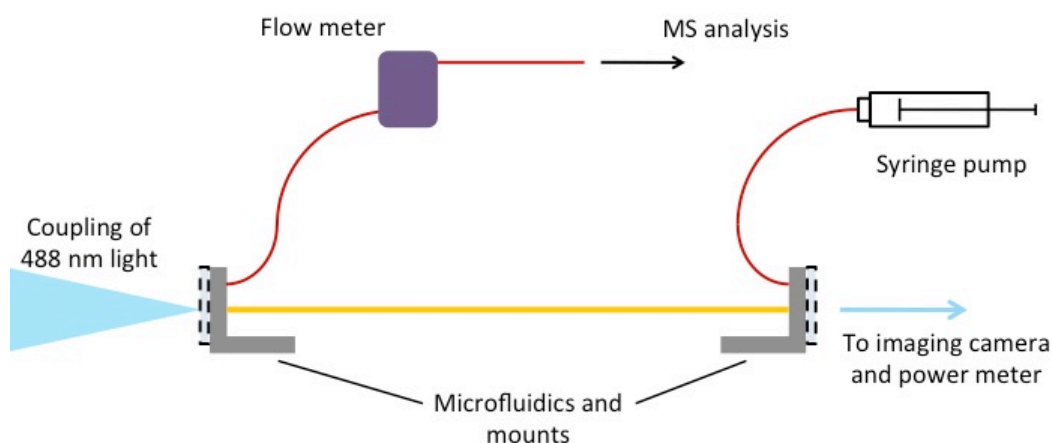


Figure 4.16 Schematic of the updated system, complete with flow-meter and microfluidics chips with mounts (Figure 4.18). PEEK tubing in red, PCF in yellow, light in blue, and the microfluidics are surrounded by a dashed line.

The connection of the fibre to the rest of the system was also modified. Commercially available polymeric microfluidic chips consisting of 16 separate channels were mounted onto a specially made metal frame. The PCF and the PEEK tubing were connected to a single channel in each chip using HPLC PEEK fittings, and as with previous systems the fiber ends remain optically-accessible, see Figure 4.18. These individual channels have a volume less than 400 nL, and when combined with the volume of the PCF

(average length 25 cm) gives a total volume of 3.1 μL (not including PEEK tubing), the smallest volume of this system to date.

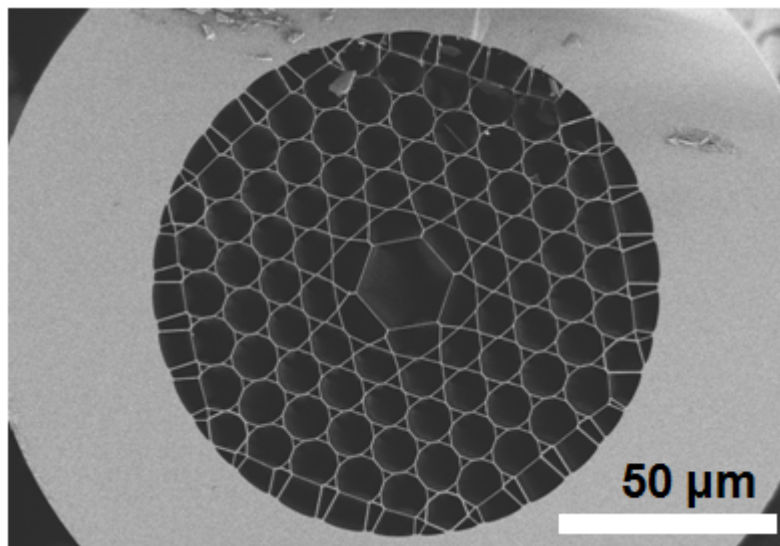


Figure 4.17 A cross section of the Kagomé fibre designed to guide 488 nm light; the core size has been increased, as has the cladding.

This system has the potential to give the quickest delivery of irradiated sample to the mass spectrometer. The system was validated before any conclusions were drawn from the data that it yielded. Previously complex **8** was used for this purpose and signal intensity was a continual problem. This may be due to the fact that this class of complex is neutral and usually detected by mass spectrometry as a sodium or potassium adduct.²³ The bare silica walls of the PCF may be affecting the process by which the complex acquires these ions, so that it may be detected. Therefore, a new model photoreaction was required as a proof-of-concept means of testing the efficacy of the system.

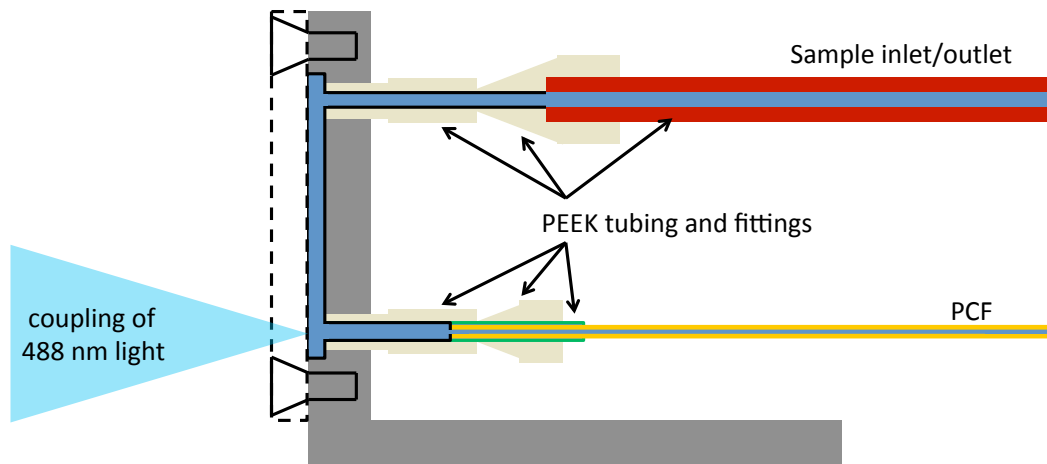


Figure 4.18 Schematic of the microfluidic chip in its mount and how it is connected to the rest of the system. Sample in dark blue, PEEK tubing in red and green, laser light in blue; the dashed line represents the microfluidic chip and dark grey the metal mount.

4.3.2 Vitamin B₁₂ - a model for PCF-MS system validation in the positive-ion mode

The photodissociation of vitamin B₁₂, cyanocobalamin, has been the subject of much research and involves the loss of the Co-bound cyano group upon irradiation, and its replacement with a water molecule to give aquacobalamin (Figure 4.19).^{24,25,26} This is a pH dependent process and normally only occurs at high or low pH values.^{27,19} As with the previous experiments to validate the PCF-MS system (in this case the system shown in Section 4.3.1.4), it must be compared with conventional methods. In this case, as well as directly infusing sample solutions in the dark, an aliquot of the sample was placed in a quartz cuvette and irradiated using a 488 nm laser set at the same power as for the PCF-MS experiments (5 mW). For all future experiments, this is referred to as the ‘conventional method of irradiation’. For the purpose of system validation in the positive-ion mode, a solution of cyanocobalamin at pH 1 and another at pH 8 were irradiated by conventional and PCF-MS methods for comparison.

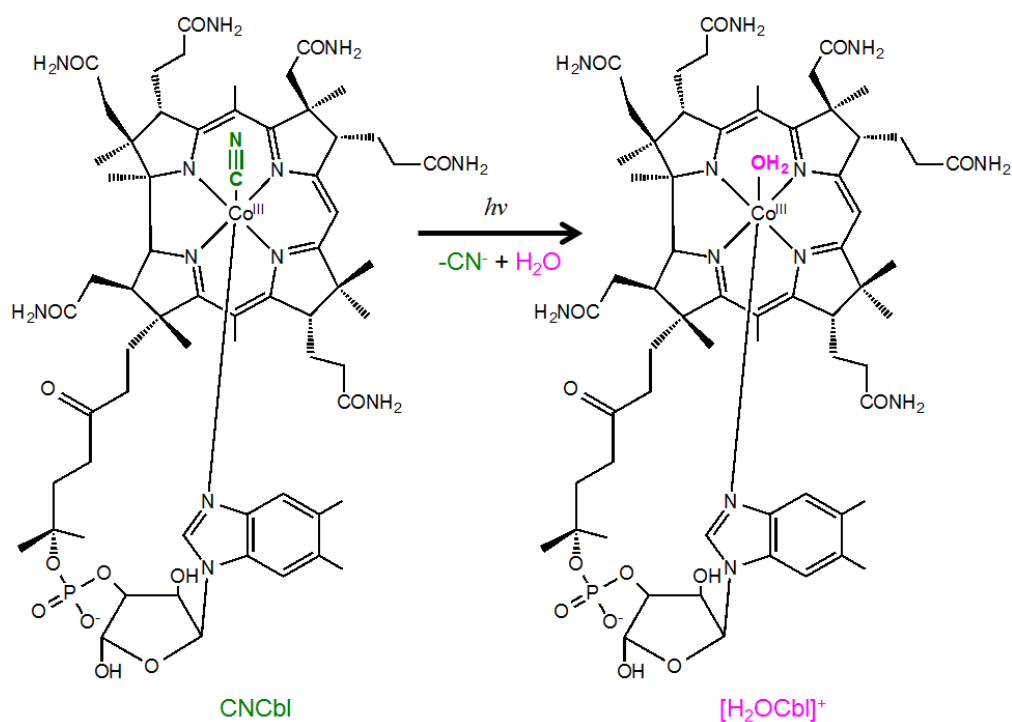


Figure 4.19 Photosubstitution of cyanocobalamin, [CNCbl], to give aquacobalamin, [H₂OCbl]⁺.

4.3.2.1 Photoaquation of vitamin B₁₂ at pH 1.7: conventional method

The photoaquation of cyanocobalamin has been shown to occur more rapidly at lower pH.²⁸ A solution of 100 μM of cyanocobalamin (pH 1.7) was directly infused into the mass spectrometer under dark conditions. The resulting spectrum is shown in Figure 4.20. The most abundant ions in the spectrum are 678.3 m/z assigned as the doubly protonated molecular ion ($[\text{CNCbl} + 2\text{H}]^{2+}$), and 689.3 m/z as a doubly-charged sodium adduct ($[\text{CNCbl} + \text{H} + \text{Na}]^{2+}$).

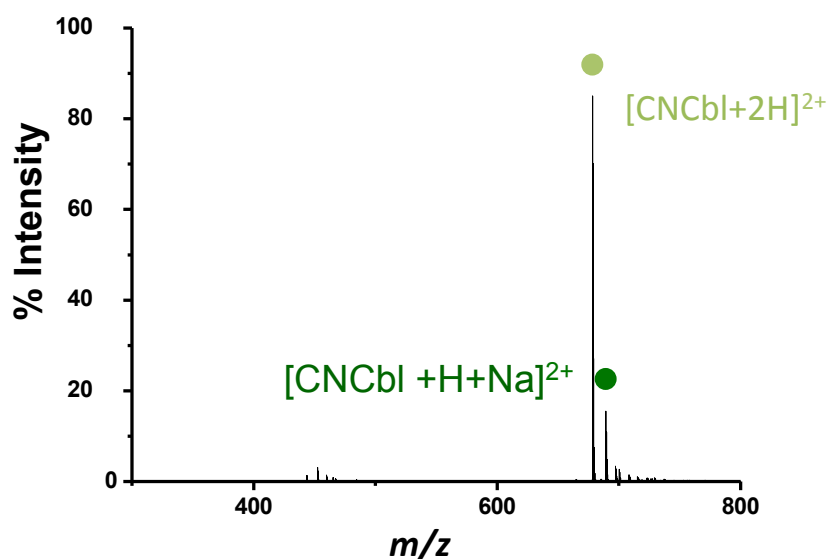


Figure 4.20 Spectrum of a 100 μM solution of vitamin B₁₂ in DDW at pH 1.7 in the dark, directly infused, the peak at 678.3 m/z was assigned as $[\text{CNCbl} + 2\text{H}]^{2+}$, and that at 689.3 m/z as $[\text{CNCbl} + \text{H} + \text{Na}]^{2+}$.

An aliquot taken from the same 100 μM stock solution was placed in a quartz cuvette and irradiated with 488 nm laser light for 10.00 h. This solution was then centrifuged for 10 min; and the supernatant was injected into the mass spectrometer. This spectrum (Figure 4.21) still contains the doubly protonated cyanocobalamin molecular ion (678.3 m/z) and a small amount of the doubly charged sodium adduct (689.3 m/z). The

following peaks appeared only in the spectrum of the irradiated solution: i.e., those at 664.8 m/z was assigned as the cyano free cobalamin species, $[\text{Cbl} + \text{H}]^{2+}$, and 673.8 m/z as aquacobalamin ($[\text{H}_2\text{OCbl} + \text{H}]^{2+}$) were observed showing that a photoreaction had occurred.

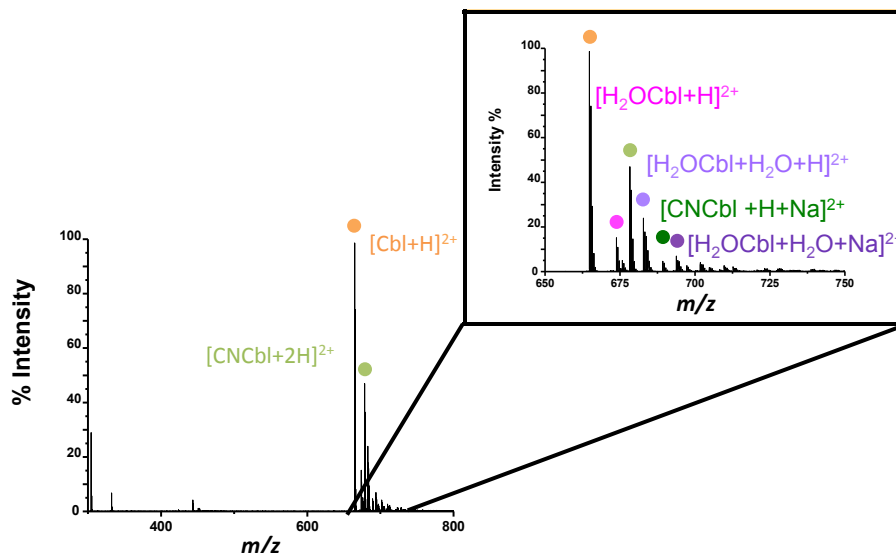


Figure 4.21 Spectrum of conventionally irradiated 100 μM solution of vitamin B_{12} in DDW (10 h, 488 nm) at pH 1. After irradiation the peaks at 664.8 m/z assigned as $[\text{Cbl} + \text{H}]^{2+}$, 673.8 m/z ($[\text{H}_2\text{OCbl} + \text{H}]^{2+}$), 682.8 m/z ($[\text{H}_2\text{OCbl} + \text{H}_2\text{O} + \text{H}]^{2+}$) and 693.8 m/z ($[\text{H}_2\text{OCbl} + \text{H}_2\text{O} + \text{Na}]^{2+}$) were observed.

4.3.2.2 Photoaquation of vitamin B_{12} at pH 1.7: PCF-MS system

The irradiation of vitamin B_{12} was then repeated within the PCF-MS system by flowing a 100 μM aqueous solution of vitamin B_{12} at pH 1.7 through the set-up. A signal was observed that was much more intense than anything achieved using previous samples or systems. After 15 min, the signal intensity had stabilized and reached a maximum value, at which point the spectrum of the solution in the dark was recorded (Figure 4.22 (A)). The 488 nm laser was then switched on and after a 15 min delay, species were observed at 664.8 m/z , and 673.8 m/z , which were

assigned as $[\text{Cbl} + \text{H}]^{2+}$, and $[\text{H}_2\text{OCbl} + \text{H}]^{2+}$ (Figure 4.22(B)), indicating the successful photoconversion of cyanocobalamin to its aqua adduct.

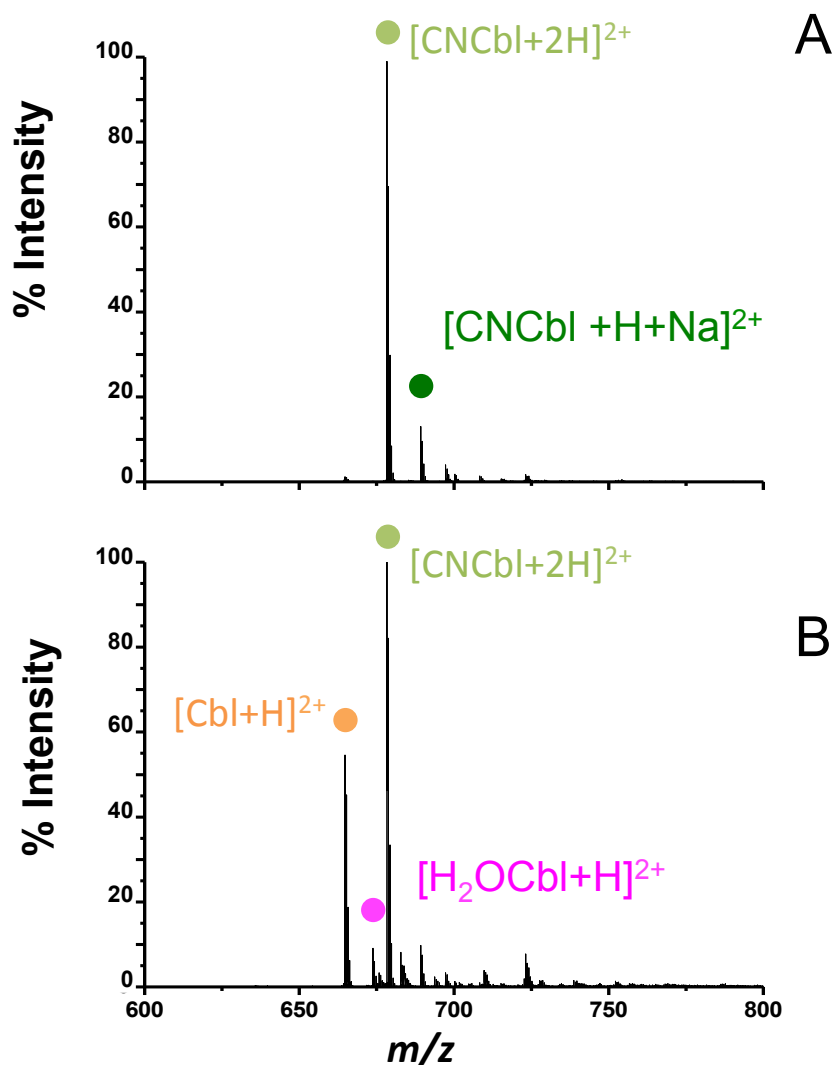


Figure 4.22: Mass spectra of vitamin B₁₂ (100 μM) in DDW at pH 1.7, obtained using the PCF-MS system. (A) Spectrum of vitamin B₁₂ in the dark; the peak at 678.3 m/z was assigned as $[\text{CNCbl} + 2\text{H}]^{2+}$ and 689.3 m/z as $[\text{CNCbl} + \text{H} + \text{Na}]^{2+}$. (B) After 15 min of irradiation at 488 nm; the 664.8 m/z peak was assigned as $[\text{Cbl} + \text{H}]^{2+}$, and that at 673.8 m/z as $[\text{H}_2\text{OCbl} + \text{H}]^{2+}$.

4.3.2.3 Photoaquation of vitamin B₁₂ at pH 7.9: conventional methods

As this is a pH dependent reaction and CNCbl is most stable to photodecomposition between pH 7 and 8, the cuvette and PCF-MS comparisons

were carried out within this pH range in order to investigate the possible superiority of the continuous flow set-up. The cuvette was again exposed to a minimum of 10 h irradiation with 488 nm light, but in this case the solution of vitamin B₁₂ was at pH 7.9. In this case, there was no difference between the spectra of the sample in the dark and that of the irradiated solution: an example is given in Figure 4.23. At the higher pH value, different ions are observed compared to the spectrum acquired for the lower pH solution. A lower proportion of protonated species is detected, with salt adducts such as sodium and potassium being more abundant. The peaks at 700.3 *m/z* and 734.3 *m/z* were assigned as [CNCbl + 2Na]²⁺ and [CNCbl + 2K + 2(H₂O)]²⁺ respectively.

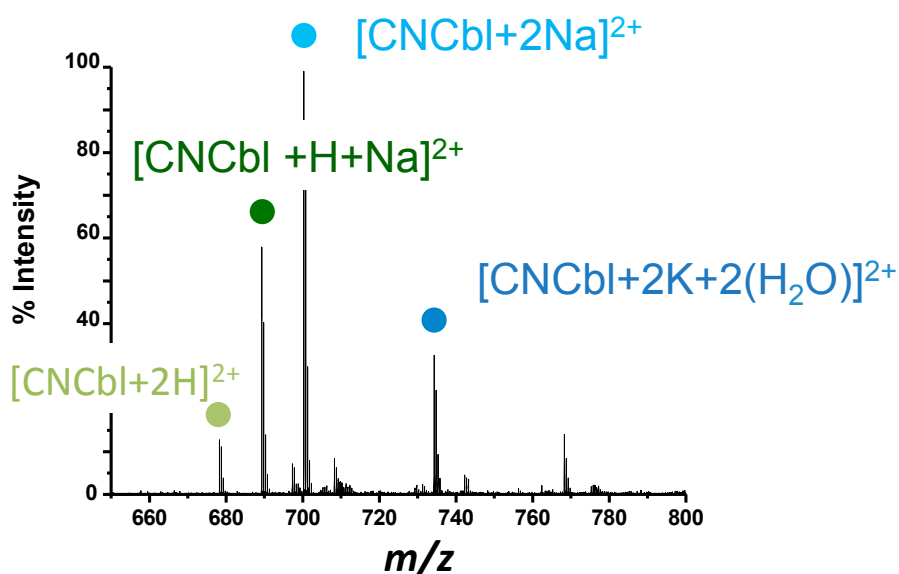


Figure 4.23 Mass spectrum from the direct infusion of 100 μ M vitamin B₁₂ in DDW at pH 7.9. The peak at 678.3 *m/z* was assigned as [CNCbl + 2H]²⁺, and those at 689.3 *m/z* as [CNCbl + H + Na]²⁺, 700.3 *m/z* as [CNCbl + 2Na]²⁺, and 734.3 *m/z* as [CNCbl + 2K + 2(H₂O)]²⁺.

4.3.2.4 Photoaquation of vitamin B₁₂ at pH 7.9: PCF-MS system

The same stock solution, at pH 7.9 was once again irradiated within the fibre-based system, and a similar spectrum of the solution in the dark was obtained, see Figure 4.24 A. The laser was switched on, and after 20 min the spectrum shown in Figure 4.24 B was recorded. Although not observed to the same extent as that at pH 1.7, a photoreaction is clearly observed here, and is attributable to the superior irradiance achieved within the fibre.

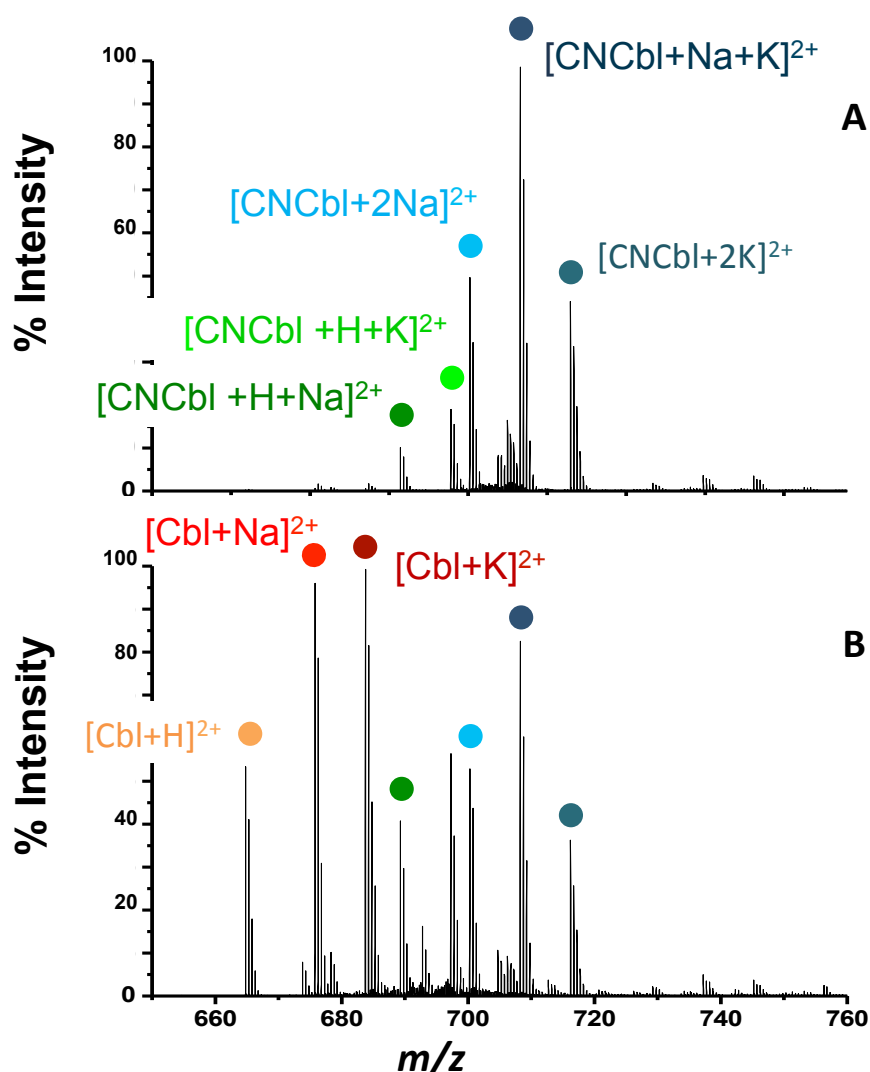


Figure 4. 24 Spectra from the PCF-MS system: 100 μM of vitamin B_{12} in DDW at pH 7.9 (A) the solution in the dark: peaks at 689.3 m/z were assigned as $[\text{CNCbl} + \text{H} + \text{Na}]^{2+}$, 697.3 m/z as $[\text{CNCbl} + \text{H} + \text{K}]^{2+}$, 700.3 m/z as $[\text{CNCbl} + 2\text{Na}]^{2+}$, 708.3 m/z as $[\text{CNCbl} + \text{Na} + \text{K}]^{2+}$ and 716.2 m/z $[\text{CNCbl} + 2\text{K}]^{2+}$. Spectrum (B) the solution irradiated for 20 min: peak at 664.8 m/z assigned as $[\text{Cbl} + \text{H}]^{2+}$, that at 675.8 m/z as $[\text{Cbl} + \text{Na}]^{2+}$, and that at 683.8 m/z as $[\text{Cbl} + \text{K}]^{2+}$.

4.3.3 PCF-MS system validation: Sodium nitroprusside - a model reaction for system validation in the negative-ion mode

The potential of the PCF-MS system to utilise the negative-ion mode was also explored using a well-characterised system. Sodium nitroprusside

$\text{Na}_2[\text{Fe}(\text{CN})_5\text{NO}] \cdot 2\text{H}_2\text{O}$ (SNP) is an iron-based vasodilator used in the clinic (structure shown in Figure 4.25).²⁹ The action of the drug is ascribable to the release of NO^\bullet from the complex into the blood stream. This process can be accelerated by exposure to light.^{30,31} There is some evidence to suggest this input of energy can also trigger the release of the remaining cyano groups.^{32,33,34}

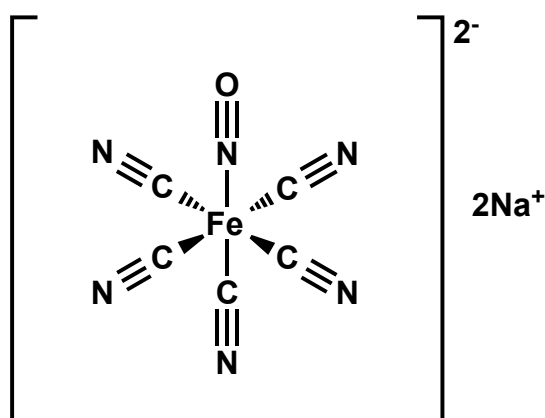


Figure 4.25 The structure of sodium nitroprusside (SNP).

Since this compound has been studied for many years, its behaviour upon ESI ionisation is well known.³⁵ Similar to the photoactivation of SNP, ionisation causes the loss of the NO^\bullet ligand followed by the loss of multiple CN^- ligands.³⁵ As fragmentation and light activation give such similar results, determination of photoactivation is dependent on the relative abundance of the fragment and molecular ions.

As with the experiments performed for validation of the PCF-MS system in the positive mode (see Section 4.2.2), the irradiation of SNP along with control solutions in the dark was analysed using both conventional methods and the PCF-MS system for comparative purposes. From the spectrum of the compound directly infused in the dark (Figure 4.26), it is apparent that even using this very soft

ionisation process, the complex undergoes a significant amount of fragmentation. The species at 238.9 m/z was assigned as $[[\text{Fe}(\text{CN})_5(\text{NO})]+\text{Na}]^-$, and the peaks 208.9 m/z as $[[\text{Fe}(\text{CN})_5]+\text{Na}]^-$, 133.9 m/z as $[[\text{Fe}(\text{CN})_3]]^-$ and 107.9 m/z as $[[\text{Fe}(\text{CN})_2]]^-$. When this 'dark' spectrum is compared to one of the same solution irradiated for several hours using 488 nm laser light, Figure 4.27, there is little observable difference between the peak intensities; the same was the case when the experiment was carried out using the PCF-MS system (results not shown).

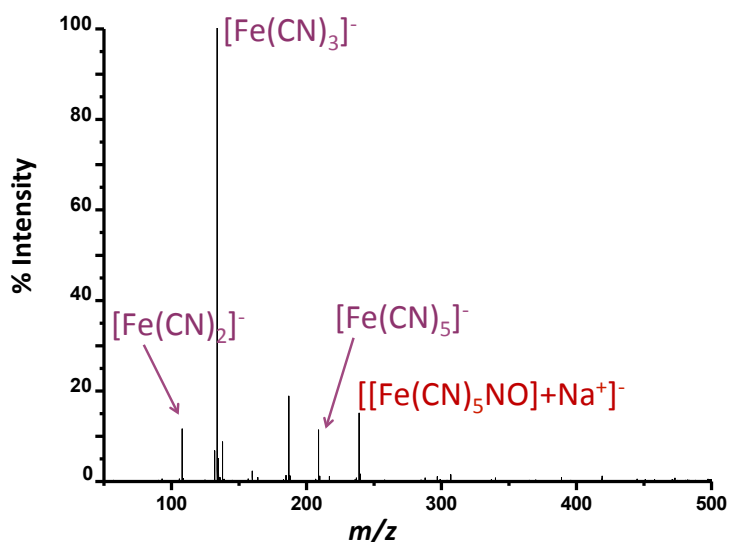


Figure 4.26 Mass spectrum of SNP, 500 μM in DDW, directly infused in the dark. The peak at 238.9 m/z is assigned as $[[\text{Fe}(\text{CN})_5(\text{NO})]+\text{Na}]^-$, that at 208.9 m/z as $[[\text{Fe}(\text{CN})_5]+\text{Na}]^-$, 133.9 m/z as $[[\text{Fe}(\text{CN})_3]]^-$, and 107.9 m/z as $[[\text{Fe}(\text{CN})_2]]^-$.

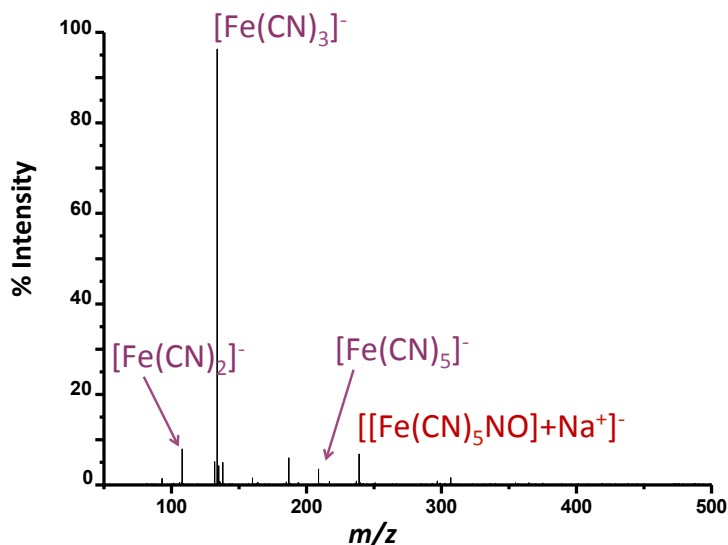


Figure 4.27 Mass spectrum of a 500 μM SNP solution in DDW irradiated for 3.00 h with 488 nm light and directly infused. The peak at 238.9 m/z was assigned as $[[\text{Fe}(\text{CN})_5(\text{NO})]+\text{Na}]^-$, that at 208.9 m/z as $[[\text{Fe}(\text{CN})_5]+\text{Na}]^-$, that at 133.9 m/z as $[[\text{Fe}(\text{CN})_3]]^-$ and 107.9 m/z as $[[\text{Fe}(\text{CN})_2]]^-$.

4.3.4 PCF-MS system application: photoactivation of ruthenium anticancer complexes

The unification of PCFs and mass spectrometry has, in the previous sections of this chapter, been shown to be superior to conventional methods of sample irradiation and analysis in some cases. This technique can now be extended to the study of photoactivatable ruthenium drugs. As shown in Section 4.3.1.4 Pt(IV)-diazido complexes are not good candidates for this system, in view of the fact that they are neutral and often only detected as salt adducts. This produces mass spectra from the PCF-MS that differ greatly from those obtained by conventional methods using similar conditions. Complex **24** is a doubly-charged ruthenium-based compound, see Figure 4.28, that loses a pyridine (py) ligand after being irradiated

with light for several hours.^{36,8} The fact that **24** is charged should mean that it is easier to detect in the mass spectrometer than a neutral compound that has to pick up a charge to be observed. The fact that **24** requires a longer period of irradiation to be activated by conventional methods than **8** allows for a more interesting comparison between the PCF-MS system and conventional irradiation methods; because of this, the organometallic arene complex **24** was selected.

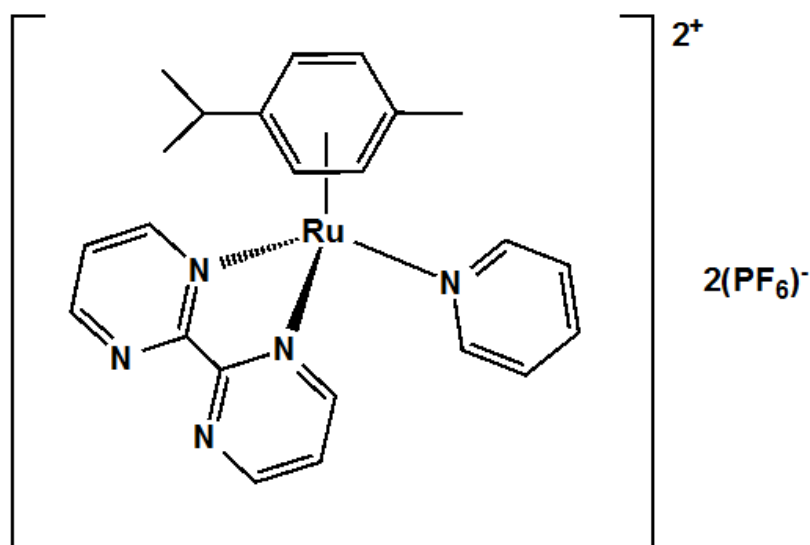


Figure 4.28 Structure of **24**, $[\text{Ru}(\eta^6\text{-p-cym})(2,2'\text{-bipyrimidine})(\text{py})]^{2+}$.

As with the system validation experiments (Sections 4.2.3 and 5.2.3), conventional methods were used as a comparison to test the efficacy of the PCF-MS system, as well as to those in the reported literature. Controls of the solutions in the dark were also analysed by both methods.

The direct infusion of a 250 μM solution of **24** in DDW in the dark results in the spectrum shown in Figure 4.29. The most abundant ion is 197.0 m/z , assigned as $[\text{M} - (\text{py})]^{2+}$; other significant peaks are 236.6 m/z $[\text{M}]^{2+}$ and at 618.1 m/z $[\text{M} + (\text{PF}_6)]^+$. The species at 197.0 m/z is what is expected to be produced upon

irradiation of **24** and was also detected in the spectrum of the sample after irradiation (Figure 4.30), as were the previously noted peaks. There was little observable difference before and after irradiation by conventional methods. The reaction was also carried out in the PCF-MS system, and the same result was obtained. This lack of distinction between the spectra of the complex in the dark and after irradiation made it a poor candidate for further investigation.

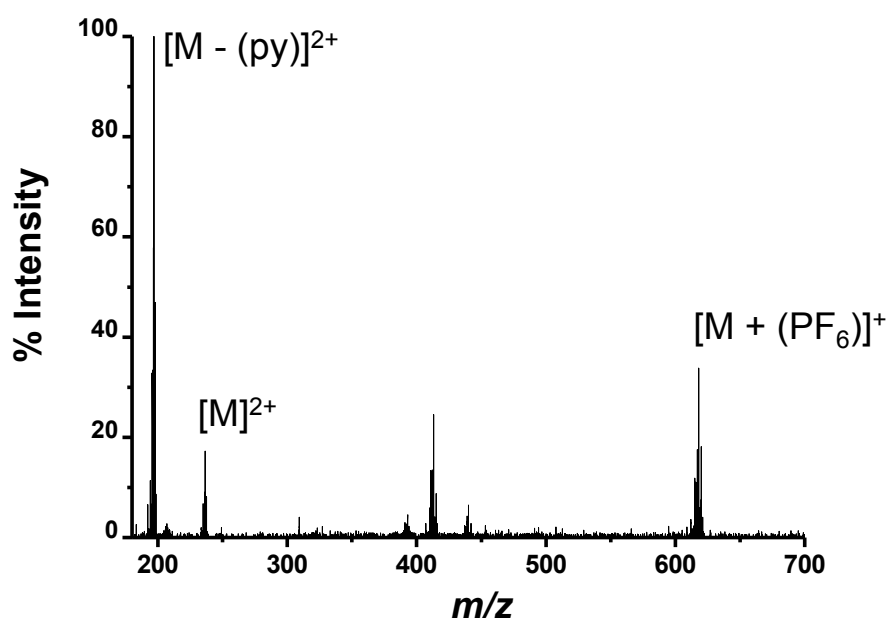


Figure 4.29 Mass spectrum of a directly infused dark solution (250 μ M in DDW), of complex **24**. Species at 197.0 m/z , assigned as $[M - (py)]^{2+}$, 236.6 m/z $[M]^{2+}$, and at 618.1 m/z as $[M + (PF_6)]^+$.

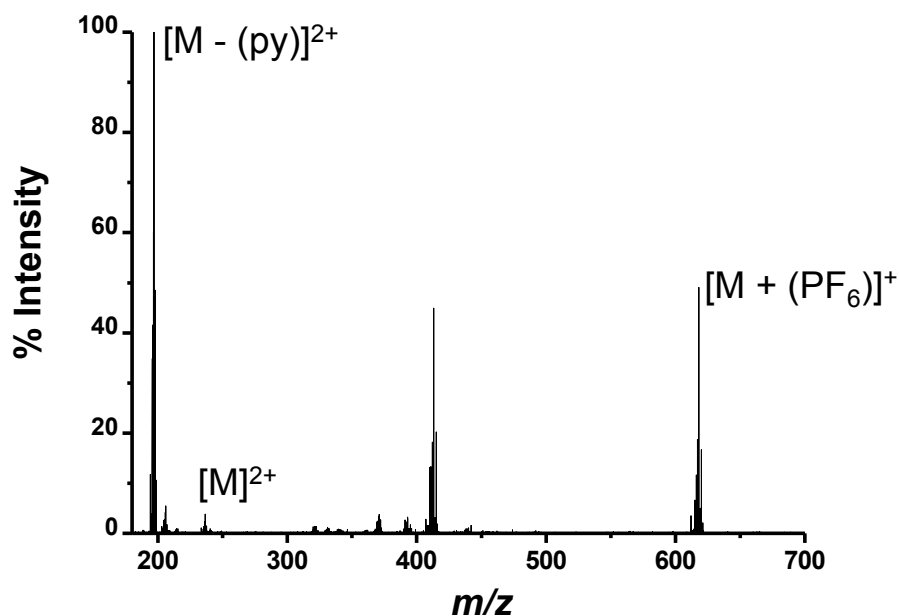


Figure 4.30 Mass spectrum of directly infused solution (250 μM in DDW), of **24**, irradiated with 488 nm light for 16 h. Species at 197.0 m/z , are assigned as $[\text{M} - (\text{py})]^{2+}$, 236.6 m/z $[\text{M}]^{2+}$, and at 618.1 m/z as $[\text{M} + (\text{PF}_6)]^+$.

4.3.5 PCF-MS system application as a rapid microreactor screening technique to gain insights into the mechanism of action of photoactivatable drugs

As outlined in Section 4.3.4, charged photoactivatable ruthenium-based complexes have been shown to be good candidates for PCF-MS, and after limited success with complex **24**, the dinuclear complex **25**, $[\{(\eta^6\text{-indan})\text{RuCl}\}_2(\mu\text{-}2,3\text{-dpp})](\text{PF}_6)_2$, see Figure 4.31, was selected for this study. The photoactivation, aquation and DNA binding properties of this compound have been previously reported,³⁷ and provide a good comparison to the findings of this work. The aim of this series of experiments was to use the PCF as a microreactor in order to photoactivate **25** in the presence of a range of small biomolecules that are present within the cell, or, alternatively, can act as a model for larger molecules, e.g. nucleobases and DNA.

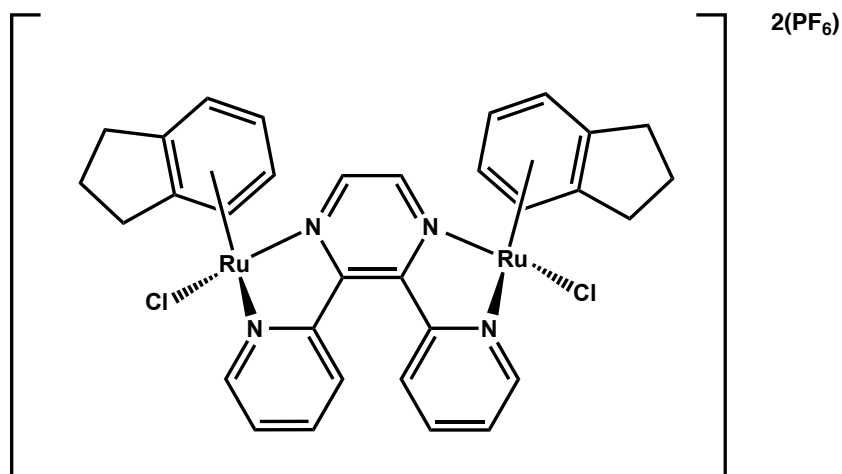


Figure 4.30 The structure of **25**, $[[\{\eta^6\text{-indan}\}\text{RuCl}]_2(\mu\text{-2,3-dpp})](\text{PF}_6)_2$.

Upon irradiation, **25** loses an indan ligand and will bind with DNA;³⁷ the complex can also undergo aquation when in aqueous solution. This may be prevented by the presence of a high concentration of Cl^- ions. However, for the PCF-MS system, this approach is impractical, as the mass spectrometer will not tolerate high levels of salt. As in the previous sections, there were controls using conventional methods for each experiment, and dark controls using both techniques. Since data from both the PCF-MS and the conventional methods were acquired over time in aqueous solution, they may be complicated by the aquation of **25**.

The direct infusion controls (Figure 4.31) indicate that the fragmentation process for this molecule is different from that of its photodissociation and aquation pathways. The main ions detected in the solution spectrum in the dark are the doubly charged molecular ion at $372.0\ m/z$ ($[\text{M}]^{2+}$), a singly-charged PF_6^- adduct at $888.96\ m/z$ ($[\text{M}+(\text{PF}_6)]^+$), and a singly charged fragment ion at $489.01\ m/z$ ($[(\eta^6\text{-indan})\text{RuCl}(\mu\text{-2,3-dpp})]^+$). There are also two sets of peaks just below the molecular

ion at 363.51 m/z and 353.00 m/z that are the result of aquation of **25**, and show the loss of at least one Cl^- ion. In summary, when in the dark, the spectrum of **25** will show the loss of chlorido ligands and may fragment into mononuclear species. However, there is no loss of an indan ligand from the ruthenium centre (Figure 4.32 A).

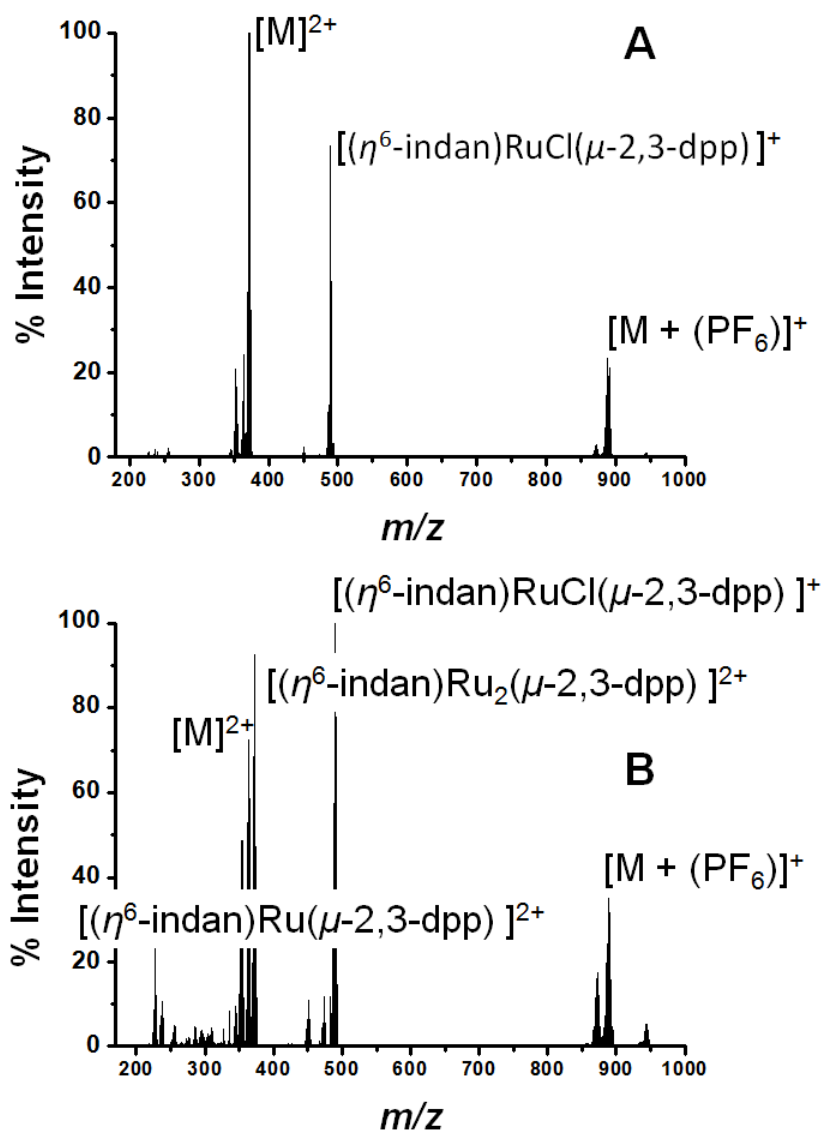


Figure 4.31 (A) Direct infusion of dimer complex **25** in the dark, 250 μM in DDW: peaks assigned 372.0 m/z as $[\text{M}]^{2+}$, 888.96 m/z as $[\text{M} + (\text{PF}_6)]^+$ and fragment ion at 489.01 m/z ($[(\eta^6\text{-indan})\text{RuCl}(\mu\text{-}2,3\text{-dpp})]^+$). (B) Spectrum of **25** (250 μM in DDW) irradiated 488 nm for 14 h and the appearance of a peak at 276.99 m/z as $[(\eta^6\text{-indan})\text{Ru}_2(\mu\text{-}2,3\text{-dpp})]^{2+}$.

A 250 μM solution of **25** in DDW was irradiated with 488 nm light for 14 h, and the resulting spectrum is shown in Figure 4.32B. The intensities of the peaks attributed to the aquation of **25** are higher in the spectrum of the irradiated solution than that of the complex in the dark. There is also a much larger increase in the intensity of the species at 227.04 m/z , assigned as $[(\eta^6\text{-indan})\text{Ru}(\mu\text{-2,3-dpp})]^{2+}$. The major difference in the spectra acquired is the peak at 276.99 m/z that is observed after irradiation, and is assigned as $[(\eta^6\text{-indan})\text{Ru}_2(\mu\text{-2,3-dpp})]^{2+}$. This is significant as it shows the loss of an indan ligand from **25**, and demonstrates that there can be easily achievable determination of a successful photoreaction, as the loss of this group is not observed under dark conditions.

The experiment was then repeated in the PCF-MS system (Figure 4.33), the only differences observed being that species resulting from aquation, such as 363.51 m/z , increase, but this is to be expected, as the compound has been in solution for a longer period of time. There is a drop in overall intensity for the PCF-MS spectrum, which is to be expected when a reaction is transferred to the system, as well as loss of intensity due to hydrolysis of the main peak species. The intensity of the species $[(\eta^6\text{-indan})\text{Ru}(\mu\text{-2,3-dpp})]^{2+}$ (227.04 m/z) is higher for the sample injected in the dark in PCF-MS experiment than when directly infused in the dark. Irradiation of the sample produces the same species as the control sample, and again an increase in the peak at 227.04 m/z .

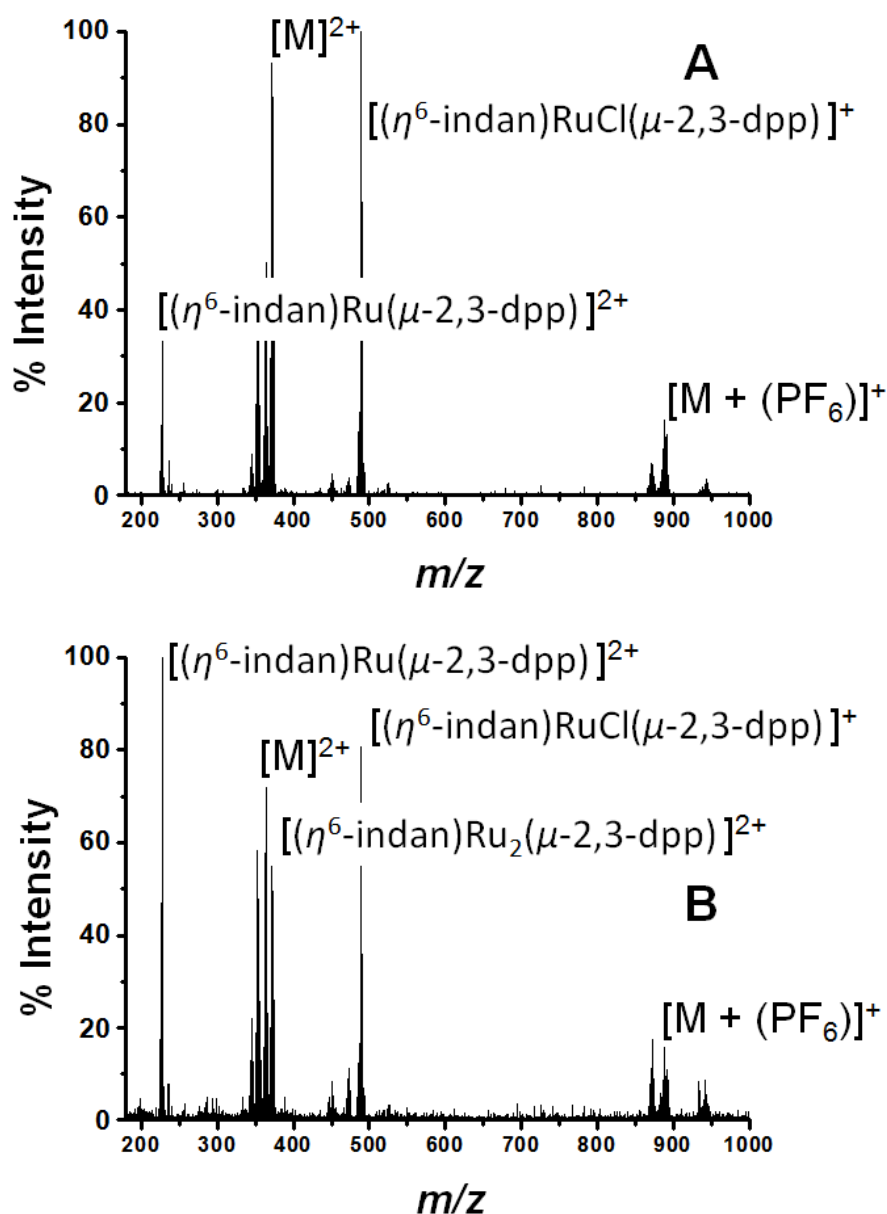


Figure 4.32 PCF-MS system mass spectra of **25** (250 μM) in DDW: (A) spectrum of the solution in the dark. Peaks assigned: 372.0 m/z as $[M]^{2+}$, 888.96 m/z as $[M+(\text{PF}_6)]^+$ and fragment ion at 489.01 m/z as $[(\eta^6\text{-indan})\text{RuCl}(\mu\text{-}2,3\text{-dpp})]^+$; (B) after 15 min of irradiation at 488 nm, a new peak at 276.99 m/z appears ($[(\eta^6\text{-indan})\text{Ru}_2(\mu\text{-}2,3\text{-dpp})]^{2+}$).

Since metal-based anticancer drugs that are currently in the clinic are known to bind to DNA,^{38,39,40} **25** was irradiated in the presence of two different nucleobases, to model its interaction with oligonucleotides. Initially, two

equivalents of 5'-GMP were added to an aqueous solution of **25** (500 μM nucleobase to 250 μM of complex). Spectra in the dark were obtained for both PCF-MS, and conventional experiments. The samples were irradiated: 14h in a cuvette for the conventional measurement, and 15 min in the PCF. Once again, there was close agreement between the conventional method control and the PCF-MS experiment, the only differences being a drop in peak intensity for the PCF-MS experiments and the appearance of the species at 658.6 m/z in just the PCF-MS irradiated spectrum.

In both dark spectra, and as shown in Figure 4.34, there is the appearance of a new peak is apparent at 517.6 m/z $[(\eta^6\text{-indan})\text{Ru}_2(\mu\text{-2,3-dpp}) + 5'\text{-GMP}]^{2+}$. This would suggest that 5'-GMP binds to **25** in the dark, presumably after aquation of the compound. This species would seem to be fragmented in the mass spectrometer, giving rise to the singly-charged ion at 582.03 m/z . Upon irradiation by conventional and PCF-MS methods, new peaks are observed at 458.51 m/z and 467.52 m/z that were assigned as $[(\eta^6\text{-indan})\text{Ru}_2(\mu\text{-2,3-dpp}) + 5'\text{-GMP}]^{2+}$ and $[(\eta^6\text{-indan})\text{Ru}_2(\mu\text{-2,3-dpp}) + 5'\text{-GMP} + \text{H}_2\text{O}]^{2+}$ respectively. These species are indicative of post-irradiation binding in view of the loss of an indan ring. This is further supported by the presence of a small amount of a 640.04 m/z peak, corresponding to a doubly charged species which is assigned as $[(\eta^6\text{-indan})\text{Ru}_2(\mu\text{-2,3-dpp}) + 2(5'\text{-GMP})]^{2+}$, and at 649.04 m/z , assigned as $[(\eta^6\text{-indan})\text{Ru}_2(\mu\text{-2,3-dpp}) + 2(5'\text{-GMP}) + \text{H}_2\text{O}]^{2+}$. The species at 658.6 m/z is only present in the PCF-MS spectrum, and is of relatively low intensity; this is assigned to $[(\eta^6\text{-indan})\text{Ru}_2(\mu\text{-2,3-dpp}) + 2(5'\text{-GMP}) +$

$\text{H}_2\text{O} + 2\text{H}^+]^{2+}$. The binding of 5'-GMP that occurs after aquation of the complex also increases in the post-irradiation spectra.

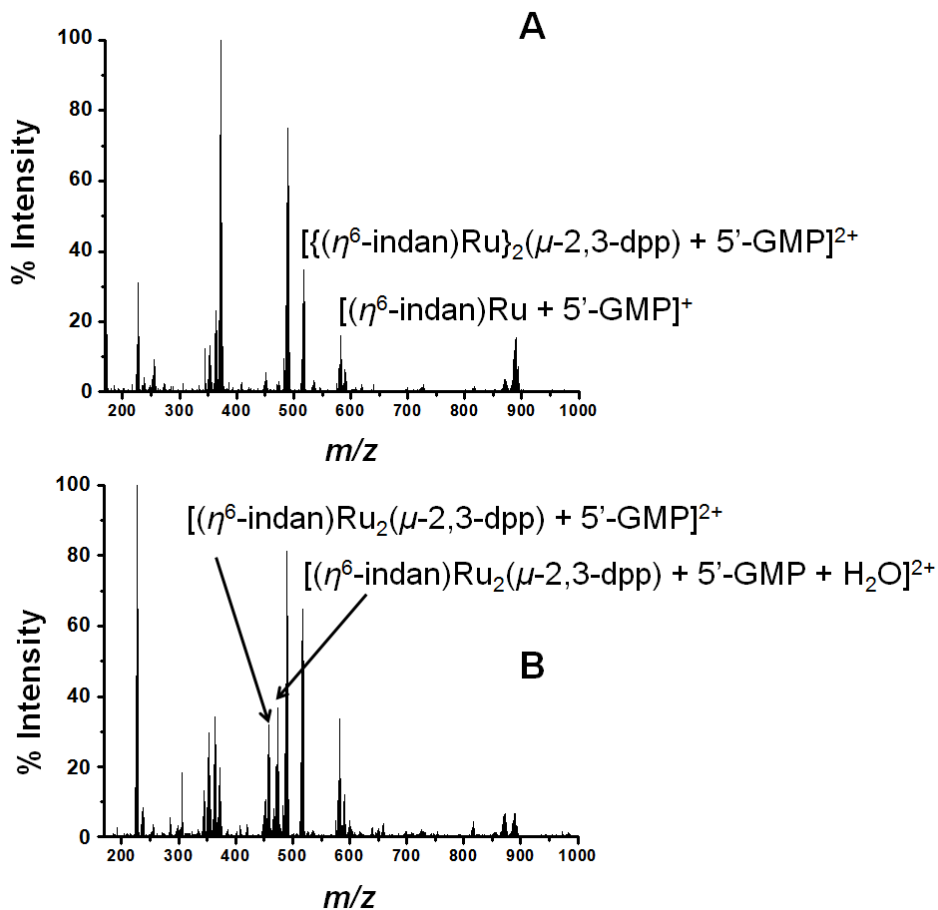


Figure 4.33 PCF-MS of 250 μM **25** and 500 μM 5'-GMP in DDW. Spectrum (A) is the dark solution peak at 517.6 m/z which is assigned as $[(\eta^6\text{-indan})\text{Ru}_2(\mu\text{-}2,3\text{-dpp}) + 5'\text{-GMP}]^{2+}$, the species at 582.03 m/z $[(\eta^6\text{-indan})\text{Ru} + 5'\text{-GMP}]^+$ and spectrum (B) is after 15 min irradiation at 488 nm light; new peaks at 640.04 m/z and 649.04 m/z are assigned as $[(\eta^6\text{-indan})\text{Ru}_2(\mu\text{-}2,3\text{-dpp}) + 2(5'\text{-GMP})]^{2+}$, and $[(\eta^6\text{-indan})\text{Ru}_2(\mu\text{-}2,3\text{-dpp}) + 2(5'\text{-GMP}) + \text{H}_2\text{O}]^{2+}$ respectively.

Complex **25** was then irradiated in the presence of 5'-AMP under the same conditions as those previously stated for 5'-GMP (250 μM **25** and 500 μM nucleobase). In the dark, there appears to be no reaction between **25** and 5'-AMP, see Figure 4.35. After irradiation by both methods, a species appears at 623.55 m/z ; this species is assigned as $[(\eta^6\text{-indan})\text{Ru}_2(\mu\text{-}2,3\text{-dpp}) + 2(5'\text{-AMP})]^{2+}$. The low

intensity of this peak in the PCF-MS spectrum indicated that the signal-to-noise ratio in this spectrum was too high to definitively assign the peak using these data alone. However, the assignment was confirmed using the sample irradiated by conventional methods. This is also the case for the peak at 566.04 m/z , assigned as $[(\eta^6\text{-indan})\text{Ru} + (5'\text{-AMP})]^+$.

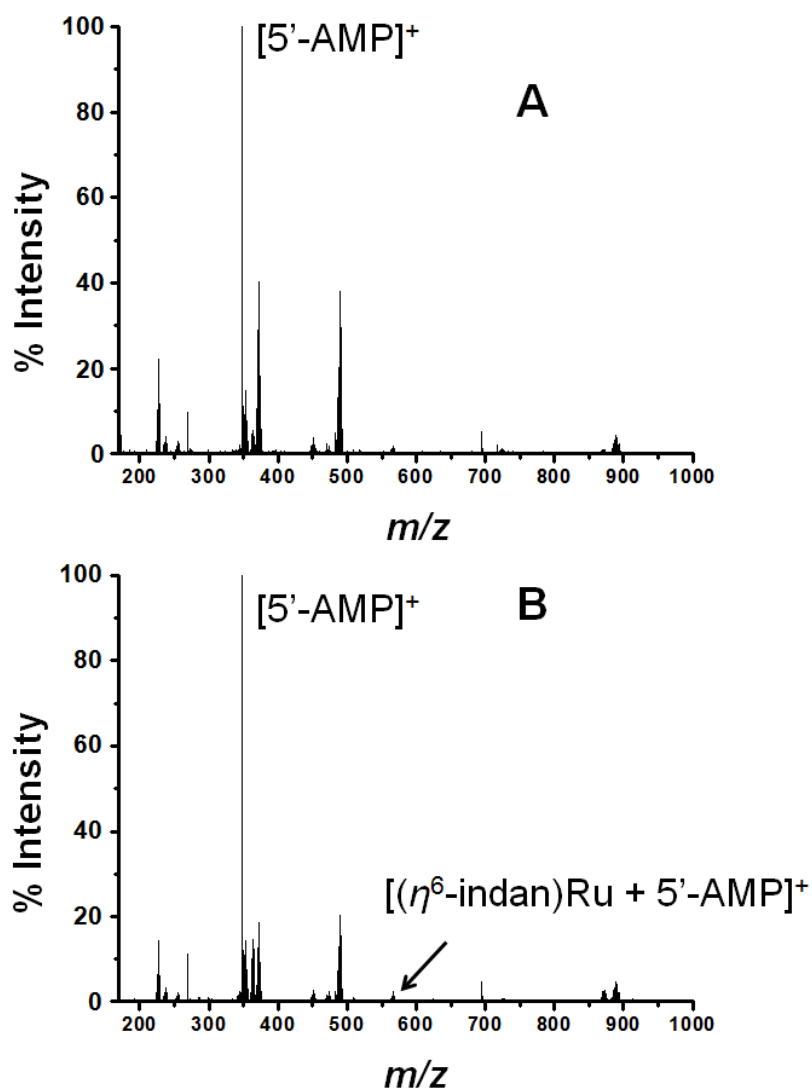


Figure 4.34 PCF-MS of 250 μM **25** and 500 μM 5'AMP in DDW. Spectrum (A) is the dark solution; a peak is detected at 348.07 m/z ($[5'\text{-AMP} + \text{H}]^+$), and spectrum (B) is after 15 min irradiation at 488 nm: the new peak at 566.04 m/z is assigned as $[(\eta^6\text{-indan})\text{Ru} + (5'\text{-AMP})]^+$.

In order to mimic the interaction of **25** with intracellular proteins, it was irradiated in the presence of the amino acid *L*-cysteine. A ratio of 2:1 amino acid to (500 μ M) complex (250 μ M) was used, and the sample was incubated at ambient temperature for the at least the time that it took to irradiate the solutions by both methods (30 min for the PCF-MS sample in the dark, and 14 h for the conventional measurement). There would appear to be no reaction in the dark between **25** and *L*-cysteine, see Figure 4.36. Upon irradiation by both conventional and PCF-MS methods, a series of peaks appear at 337-339 m/z . These are doubly-charged, and from their isotopic pattern, contain more than one Ru atom. These species are likely to be $[(\eta^6\text{-indan})\text{Ru}_2(\mu\text{-2,3-dpp}) + (\text{L-Cys})]^{2+}$ (338.49 m/z), and $[\text{Ru}_2(\mu\text{-2,3-dpp}) + 2(\text{L-Cys})]^{2+}$ (339.99 m/z). However, the low intensity of the signal and the overlap means that this is difficult to determine in view of the high signal to noise ratio and the complicated isotopic patterns of the species in question. Two other photoproducts were also detected, and are shown in Figure 4.36. These are $[(\eta^6\text{-indan})\text{Ru}(\mu\text{-2,3-dpp}) + (\text{L-Cys})]^+$ (574.09 m/z), and $[(\eta^6\text{-indan})\text{Ru}_2(\mu\text{-2,3-dpp}) + 2(\text{L-Cys})]^{2+}$ at 396.52 m/z .

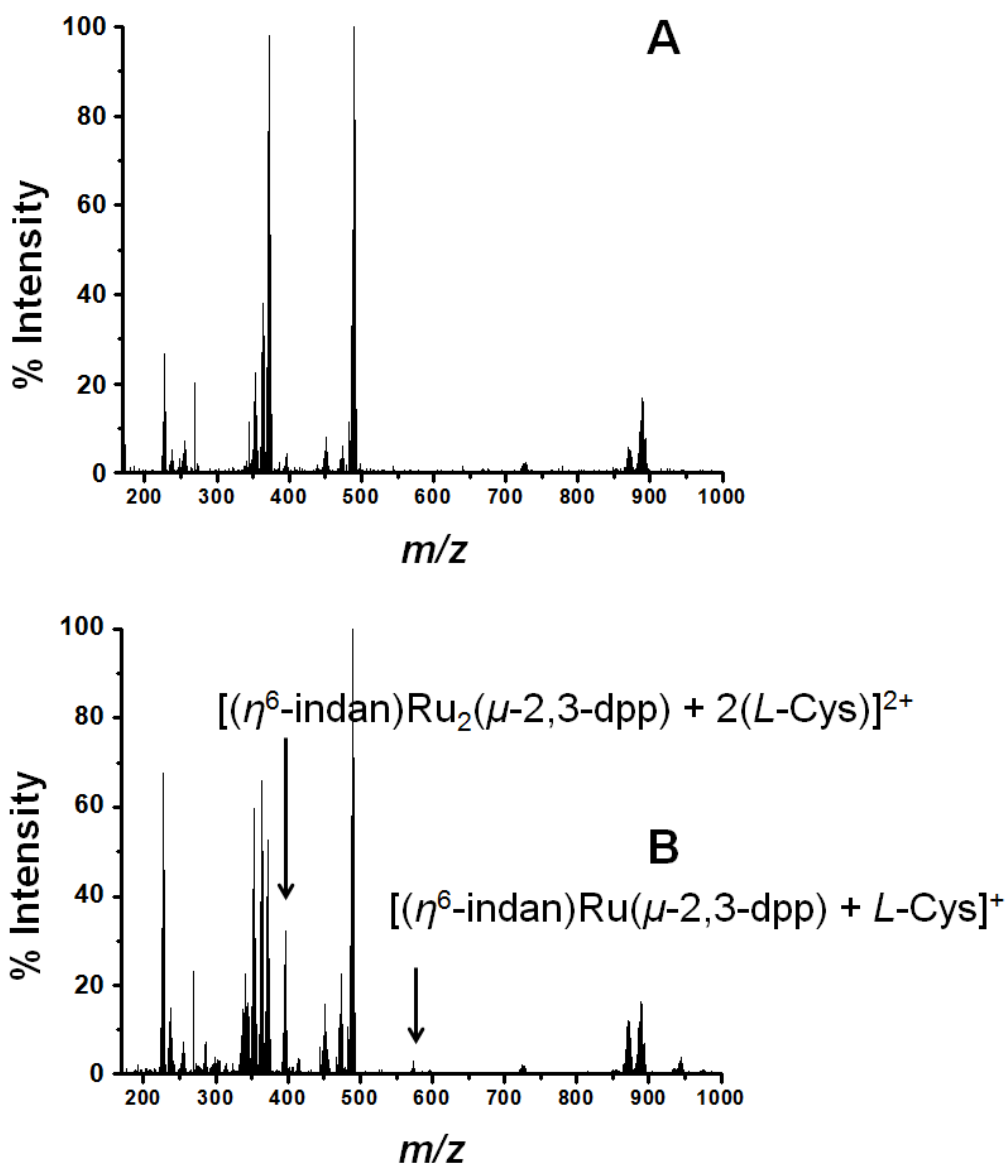


Figure 4.35 PCF-MS of 250 μM **25** and 500 μM *L*-Cys in DDW. Spectrum (A) is of the solution in the dark and spectrum (B) is after 15 min irradiation at 488 nm light. The peaks not observed before in spectrum B are assigned as 396.52 m/z , $[(\eta^6\text{-indan})\text{Ru}_2(\mu\text{-}2,3\text{-dpp}) + 2(\text{L-Cys})]^{2+}$ and 574.09 m/z , $[(\eta^6\text{-indan})\text{Ru}(\mu\text{-}2,3\text{-dpp}) + (\text{L-Cys})]^+$.

Reactions with the intracellular tripeptide glutathione were studied since it an important mechanism of resistance to metal-based drugs.^{41,42,43} Complex **25** (250 μM) was irradiated in the presence of two equivalents of glutathione (GSH), see Figure 4.37, with the dark controls again incubated for at least the same length

of time as the period of irradiation (30 min for the PCF-MS experiments, and 14 h for the sample analysed conventionally). In the dark, there was a new species generated at 408.56 m/z that contains one Ru atom, is doubly charged and would appear to contain one molecule of GSH and a fragment of GSH bound with the loss of an indan group, even in the dark (this peak decreased after irradiation). In the irradiated spectrum, further new species were observed including 430.52 m/z that was assigned as $[(\eta^6\text{-indan})\text{Ru}_2(\mu\text{-}2,3\text{-dpp}) + \text{GSH}]^{2+}$, and 526.06 m/z as $[(\eta^6\text{-indan})\text{Ru} + \text{GSH}]^+$. Species at *ca.* 580 and 584 m/z form a cluster of peaks in the PCF-MS spectrum, but in the conventionally irradiated spectrum only the 584.06 m/z species, $[(\eta^6\text{-indan})\text{Ru}_2(\mu\text{-}2,3\text{-dpp}) + 2\text{GSH}]^{2+}$, was present.

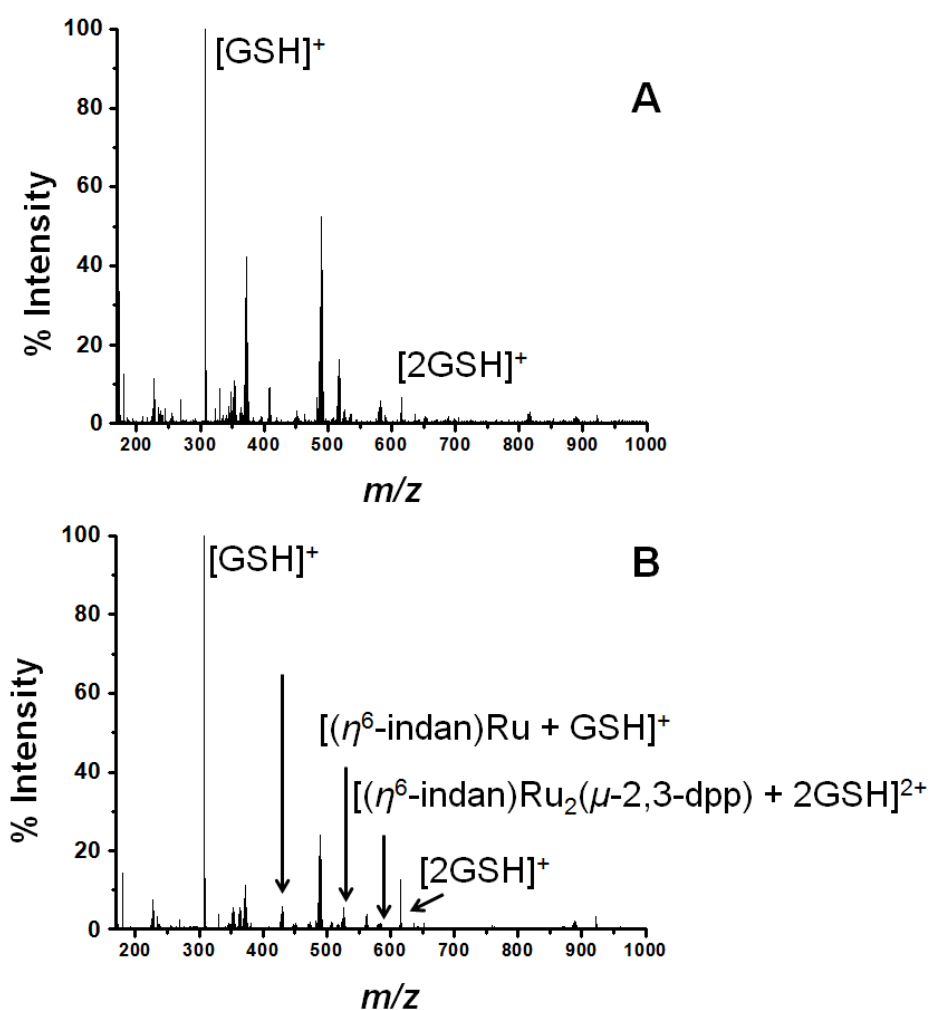


Figure 4.36 PCF-MS of 250 μM **25** and 500 μM GSH in DDW. Spectrum (A) is from the solution in the dark, with the peaks at 208.09 m/z assigned as $[\text{GSH} + \text{H}]^+$, 615.17 m/z as $[2\text{GSH} + \text{H}]^+$. Spectrum (B) is after 15 min irradiation at 488 nm; peaks at 430.52 m/z , 526.06 m/z and 584.06 m/z are attributed to $[(\eta^6\text{-indan})\text{Ru}_2(\mu\text{-2,3-dpp}) + \text{GSH}]^{2+}$, $[(\eta^6\text{-indan})\text{Ru} + \text{GSH}]^+$ and $[(\eta^6\text{-indan})\text{Ru}_2(\mu\text{-2,3-dpp}) + 2\text{GSH}]^{2+}$ respectively.

4.4 Discussion

4.4.1. Photonic crystal fibre mass spectrometry (PCF-MS) system design and development

Throughout the development of the PCF-MS system, several different coupling devices were used. The ideal coupling device would have a very small dead

volume to allow for rapid analysis, and also to minimise the possibility of short-lived species reacting with each other or solvent molecules. Changes to these devices were driven by the practicalities of the experiments involved and the problems encountered.

4.4.1.1 PCF-MS system design and development: metallic coupling devices

Preliminary experiments involving flowing a sample of **8** through the PCF and directly infusing it into the mass spectrometer (Section 4.3.1) showed that there was no difference between the resulting spectra. The inclusion of the metallic coupling devices to gain the ability to introduce light and sample to the fibre led to the appearance of new species in the mass spectrum of **8**, see Figure 4.4. The distinctive isotopic patterns of these new species suggests that they contain platinum. MS/MS of the peak at 750.2 m/z shows fragments at 383.1, 411.1, 579.2 and 732.2 m/z that all contain platinum. The ions 383.1 and 411.1 m/z are also observed in the spectrum of the direct infusion of **8**, Figure 4.5. The presence of these expected species within the unknown ions, along with the isotopic pattern of the peaks, suggests that complex **8** forms some kind of adduct with a low molecular weight contaminant introduced by the coupling device. However, the contaminant could not be identified since it was not possible to isolate it.

4.4.1.2 PCF-MS system design and development: plastic microfluidic coupling devices

The previous metallic coupling cells had a relatively large internal mixing volume of 60 μL . The change in both the construction and internal volume of the

coupling device to custom made teflon microfluidic devices was intended to improve the speed of analysis and remove the system contamination introduced by the metallic devices. However, the PEEK tubing that was glued into the device at the point of fabrication has an inner diameter that is too small to contain the PCF with its cladding, see Figure 4.9. As the fibre must reach the glass coverslip at the end of the device in order to maximise the amount of light that enters the PCF, the protective plastic coating had to be removed so that it could fit into this smaller tubing. The glass was left exposed and brittle. It had to pass through two sets of fingertight fittings (Figure 4.11) and there were many problems with the fibre breaking within the device. Consequently, many devices had to be employed, and the quality of the glass coverslip seemed to vary greatly. The removal of the cladding also lessened the ability of the PCF to guide the laser light along those sections of the fibre, and therefore it was not possible to guide any light into the core of the fibre.

4.4.1.3 PCF-MS system design and development: PVC coupling devices

The PVC coupling devices allowed the fibre to remain intact and be in contact with high quality glass windows to act as an interface between the laser light and the PCF, see **Figure 4.12**. This feature allowed the light to be successfully focused into the core of the fibre. The limiting feature of these coupling devices was not their light guiding ability, but their internal volume of 60 μL . With a total volume of 120 μL for the two devices alone, and a flow-rate of 100 $\mu\text{L}/\text{h}$, a sample took over an hour from the point of injection to reach the mass spectrometer. Although the flow rate was later doubled, the time of analysis did not improve

drastically as there was still the dead-time of the instrument, also and the time required for the electrospray to stabilise. It also became apparent that Pt(IV)-diazido complexes may not be the best compounds to test the efficacy of the system.

As promising new photoactivatable drug candidates, it was believed that this class of compound would be ideal for study by PCF-MS.^{44,45} Some previously reported photoproducts of complex **8** were detected by PCF-MS, such as $[\text{Pt}(\text{py})_2(\text{OH})(\text{H}_2\text{O})]^+$, but the spectra varied greatly from those obtained by conventional direct infusion.⁷ This may be attributable to the intrinsic properties of this particular type of complex, $[\text{Pt}(\text{py})_2(\text{N}_3)_2(\text{OH})_2]$, being a neutral species that is difficult to ionise, and is typically detected as a fragment of a salt adduct.²³ The difficulty in ionising these complexes results in decreased signal intensity, which is further exacerbated by the intrinsic loss of signal caused by the PCF-MS system. This problem may not have been appreciated during preliminary experiments as they were performed on an instrument requiring a much higher flow rate (240 $\mu\text{L}/\text{h}$ compared to 100 $\mu\text{L}/\text{h}$ when using the MaXis), minimising any interaction with the PCF.

4.4.1.4 PCF-MS system design and development: microfluidic devices using ‘off-the-shelf’ chips

To reduce the volume of the system, commercially available microfluidic chips were used as coupling devices in combination with PEEK fittings and custom-made mounts. The system volume was reduced to 3.1 μL , 40 times smaller than that required when either the metallic or Teflon devices were used (both volumes

do not include the PEEK tubing). The wavelength of light used was lengthened, and because of this the structure of the fibre was also altered. The change to 488 nm light was due to the improved light-guiding properties of PCFs at longer wavelengths, as well as achieving activation of **8** at longer, more desirable wavelengths. Complex **8** has also previously been shown to be activated at longer wavelengths.⁷ In this case, the longer the wavelength of activation the better, as the light will penetrate deeper into the tissue when administered in the clinic.

4.4.2 PCF-MS system validation: vitamin B₁₂ - a model reaction for system

validation in the positive mode

The photoaquation of vitamin B₁₂ is a well-characterised process that has been widely reported in the literature,^{24,19,27} making it an ideal reaction to test this novel system. The problems such as poor signal intensity and alterations in the mass spectra encountered with the use of Pt(IV)-diazido complexes were overcome by the use of a charged complex. The higher powers achieved within the core compared to conventional methods drastically reduce the time required to induce photoactivation of an acidic solution of vitamin B₁₂ from 10 h to 15 min. Comparing these two approaches to the irradiation of vitamin B₁₂ in terms of the light dosage received by the sample, the input power in the fibre experiment of $P_0^{\text{HC-PCF}} = 2.35$ mW is sufficient for photoconversion. In the case of the conventional experiment, a doubled input power of $P_0^{\text{CUV}} = 4.5$ mW still results in the intensity within the cuvette being 5 orders of magnitude lower in comparison to in the fibre ($I_0^{\text{CUV}} = 40$ mW/cm², $I_0^{\text{HC-PCF}} = 700$ W/cm²). This is the reason for the conventional experiment taking over 10 hours and still not reaching completion. In terms of sample volume

consumed, the PCF-MS approach is more advantageous than the conventional methods since it only requires 25 μL (volume required to carry out a 15 min analysis) of sample in comparison to at least 600 μL using a cuvette, a reduction of more than 20 times.

Sample volumes were also reduced from 600 μL to 25 μL . The increased light power even makes it possible to photoactivate a neutral solution of cyanocobalamin, which cannot be achieved by conventional methods (with 16 of irradiation) with less than 30 min of irradiation. The product of this reaction, aquacobalamin is only detected in small amounts. However, this is due to the stability of aquacobalamin, which even when directly infused in its pure form, very little of the molecular ion is detected, the dominant peak is cobalamin as noted in the irradiated PCF-MS spectra. There is also a small amount of cyanocobalamin present in the PCF-MS irradiated spectrum. This may be due to incomplete photoreaction of the starting material, but is more likely due to dilution of the sample irradiated within the core by the dark solution that passed through the cladding holes.

4.4.3 PCF-MS system validation: Sodium nitroprusside - a model reaction for system validation in the negative mode

Having proven the efficacy of the system in the positive-mode, its performance was also tested in the negative-mode using the vasodilator sodium nitroprusside. Once again high signal intensity was achieved and the spectra closely resembled those reported in the literature with the complex first losing NO^{\bullet} followed by sequential loss of the CN^- ligands.³⁵ Unfortunately, there was a lack of

distinction between dark and irradiated spectra. It was also not possible to observe this difference in the PCF-MS system. This could possibly be because even in the low levels of light present during sample preparation and injection, activation of the complex was induced. It could also just be possible that the fragmentation pathway of the complex in a mass spectrometer is very similar to its photactivation pathway. However, it has still been proven in principle that the system can work in the negative-ion mode.

4.4.4 PCF-MS system application: photoactivation of ruthenium potential anticancer complexes

As the system incorporating the 'off-the-shelf' chips was shown to work in positive-ion mode, it could be applied to the study of new potential drugs such as **24**. This particular compound is charged, resulting in a high signal intensity being detected, and produces fewer fragments than the Pt(IV) predecessors. Unfortunately, similarly to the case of SNP, the compound is highly fragmented upon ionisation in a similar manner to the effects of irradiation, resulting in the loss of the pyridine ligand. The peak intensity did not change significantly between spectra recorded in the dark and that of the complex once irradiated. Therefore, this could not be employed as an indicator of activation of the complex. In view of this ambiguity, it could not be determined whether or not photoactivation had occurred. The reaction yielded the same results when carried out in the PCF-MS system. Although the use of **24** for the purposes of monitoring a photoreaction was not successful, it has demonstrated that a metal-based drug can be flowed through the PCF-MS system, achieving a high enough signal, facilitating MS/MS analysis.

4.4.5 PCF-MS system application: PCF-MS as a rapid microreactor screening

technique to gain insights into the mechanism of action of photoactivatable drugs

The complex **25**, $[(\eta^6\text{-indan})\text{RuCl}]_2(\mu\text{-}2,3\text{-dpp})(\text{PF}_6)_2$, was proposed as another candidate for investigation by PCF-MS, as it is another photoactivatable positively charged metal-based drug. None of the previously encountered problems such as low signal intensity or ambiguous complex fragmentation were apparent when carrying out the controls using conventional methods. The PCF-MS spectra and controls based on conventional methods showed no differences other than a small reduction in intensity for the PCF-MS spectra. All of the detected species were the same by both methods. The time taken for the sample to be irradiated and the total sample volume was greatly reduced by using the PCF-MS method, from 16 h to 15 min. Upon irradiation of **25**, by both methods, there was an increase in the species at 227.04 m/z assigned as $[(\eta^6\text{-indan})\text{Ru}(\mu\text{-}2,3\text{-dpp})]^{2+}$, suggesting that exposure to light may result in the compound fragmenting in other ways as opposed to simple loss of the indan group. The further reactions with biological substrates will help to determine if this is the case

Having established the suitability of the PCF-MS system to study the irradiation of **25**, a short series of experiments using a range of small molecules to act as models for larger species present within cells was performed in order to gain insight into its intracellular behaviour. In the presence of the nucleobase 5'-GMP, a favoured binding site for other metal-based drugs,^{40,39} **25** undergoes aquation and forms a mono-adduct. This is supported by the findings of Magennis *et al.* who reported DNA binding of **25** in the dark.³⁷ When **25** was irradiated in the presence

of 5'-GMP, new 5'-GMP adducts were detected. The binding of 5'-GMP that occurs after aquation of the complex also increases in the post-irradiation spectra. This may arise from the concentration of the aqua adduct increasing over the time taken for the spectra to be acquired, or for the irradiation to be completed, depending on the method of analysis.

Similarly, when photoactivated in the presence of 5'-AMP, adducts of 5'-AMP were also detected but the peaks attributed to these are less intense than those due to 5'-GMP adducts. Magennis *et al.* also report an increase in DNA binding upon irradiation.³⁷ There is some binding with amino acids such as cysteine, but this binding occurs to a lesser extent than with nucleotides. This is supported by the findings of Wang *et al.* who reported that the complex $[(\eta^6\text{-biphenyl})\text{RuCl}(\text{en})]^+$ reacts slowly with L-cysteine in aqueous solution.⁴⁶ The complex does bind to other sulfur-containing species, as the detection of the species peaks at 430.52 m/z , 526.06 m/z and 584.06 m/z (attributed to $[(\eta^6\text{-indan})\text{Ru}_2(\mu\text{-}2,3\text{-dpp}) + \text{GSH}]^{2+}$, $[(\eta^6\text{-indan})\text{Ru} + \text{GSH}]^+$ and $[(\eta^6\text{-indan})\text{Ru}_2(\mu\text{-}2,3\text{-dpp}) + 2\text{GSH}]^{2+}$ respectively) indicates that it binds to GSH upon photoactivation. The presence of these species would suggest the photoactivation of **25** and subsequent binding of GSH. This may be the reason for the high IC_{50} value of the complex as GSH binding is a well-known detoxification mechanism for metal-based drugs.⁴²

4.5 Conclusions

In conclusion, a new technique for the rapid irradiation and analysis of photoactivatable metal complexes has been developed. The design of the system evolved greatly over the course of the work. The internal volume of the sample cells used to introduce liquid and light was decreased from 60 μL to 360 nL. This is a dramatic reduction in pre- and post-irradiation mixing within the system. The wavelength of light was also altered from 405 nm to 488 nm, and along with it the structure of the fiber used, to allow photoactivation at a slightly longer wavelength.

The system was then validated in the positive-ion mode using a known photoreaction, the photoaquation of cyanocobalamin, and the results were compared to those generated using conventional techniques. There appeared to be very little difference between the PCF-MS spectra and that of those from samples irradiated using conventional methods. There is however, a noticeable drop in peak intensity when working with the PCF-MS system compared to conventional methods. This may prove problematic in the case of identifying photoproducts generated by the system. Although the system was not properly validated using the vasodilator sodium nitroprusside, the data suggest that the methods should be applicable to the negative modes. The system did not generate any artefacts and a high signal intensity was observed in the negative-ion mode. The system in its current state has many advantages over conventional methods as it requires less than one twentieth of the sample and can irradiate samples forty times faster due to the high light powers achieved in the fibre core. However, the deadtime of the system is currently preventing truly rapid sample analysis. As although irradiation of

the sample should only take a matter of seconds the species are not detected for 15 min.

This new technique was subsequently used to gain insight into the mechanism of action of the photoactivatable ruthenium-based drug **25**, $[(\eta^6\text{-indan})\text{RuCl}]_2(\mu\text{-2,3-dpp})(\text{PF}_6)_2$. A series of models for intracellular components was used to predict how the complex might behave in cells (5'-GMP, 5'-AMP, L-Cys and GSH). The complex was found to bind to nucleobases in the dark and this binding increased upon irradiation. Compound **25** was also found to bind more to 5'GMP than 5'AMP. These findings are consistent with the work of Magennis *et al*, carried out using conventional methods.³⁷ The metal-based drug **25** also binds strongly to GSH after irradiation, a possible explanation for its lack of potency in cell line testing.

4.6 References

1. B. Rosenberg and L. VanCamp, *Cancer Res.*, 1970, **30**, 1799–802.
2. L. Kelland, *Nat. Rev. Cancer*, 2007, **7**, 573–584.
3. F. Barragán, D. Carrion-Salip, I. Gómez-Pinto, A. González-Cantó, P. J. Sadler, R. de Llorens, V. Moreno, C. González, A. Massaguer, and V. Marchán, *Bioconjugate Chem.*, 2012, **23**, 1838–1855.
4. L. Gaviglio, A. Gross, N. Metzler-Nolte, and M. Ravera, *Metallomics*, 2012, **4**, 260–266.
5. J. Della Rocca, R. C. Huxford, E. Comstock-Duggan, and W. Lin, *Angew. Chem. Int. Ed.*, 2011, **50**, 10330–10334.
6. L. J. Parker, L. C. Italiano, C. J. Morton, N. C. Hancock, D. B. Ascher, J. B. Aitken, H. H. Harris, P. Campomanes, U. Rothlisberger, A. De Luca, M. Lo Bello, W. H. Ang, P. J. Dyson, and M. W. Parker, *Chem. Eur. J.*, 2011, **17**, 7806–7816.
7. N. J. Farrer, J. A. Woods, L. Salassa, Y. Zhao, K. S. Robinson, G. Clarkson, F. S. Mackay, and P. J. Sadler, *Angew. Chem. Int. Ed.*, 2010, **49**, 8905–8908.
8. S. Betanzos-Lara and L. Salassa, *Organomet.*, 2012, **31**, 3466–3479.
9. R. S. Gohlke, *Anal. Chem.*, 1959, **31**, 535–541.
10. H. Zhang and R. M. Caprioli, *J. Mass Spectrom.*, 1996, **31**, 1039–1046.
11. M. Hollmann, J. Boertz, E. Dopp, J. Hippler, and A. V. Hirner, *Metallomics*, 2010, **2**, 52–56.
12. A. B. Theberge, F. Courtois, Y. Schaerli, M. Fischlechner, C. Abell, F. Hollfelder, and W. T. S. Huck, *Angew. Chem. Int. Ed.*, 2010, **49**, 5846–5868.
13. P. L. Urban, K. Jefimovs, A. Amantonico, S. R. Fagerer, T. Schmid, S. Mädler, J. Puigmarti-Luis, N. Goedecke, and R. Zenobi, *Lab Chip*, 2010, **10**, 3206–3209.
14. X. Sun, R. Kelly, K. Tang, and R. Smith, *Analyst*, 2010, **135**, 2296–2302.
15. D. L. Browne, S. Wright, B. J. Deadman, S. Dunnage, I. R. Baxendale, R. M. Turner, and S. V. Ley, *Rapid Comm. Mass Spectrom.*, 2012, **26**, 1999–2010.
16. A. M. Cubillas, S. Unterkofler, T. G. Euser, B. J. M. Etzold, A. C. Jones, P. J. Sadler, P. Wasserscheid, and P. S. J. Russell, *Chem. Soc. Rev.*, 2013, **42**, 8629–8648.
17. W. H. Reeves, D. V. Skryabin, F. Biancalana, J. C. Knight, P. S. J. Russell, F. G. Omenetto, A. Efimov, and a J. Taylor, *Nature*, 2003, **424**, 511–515.
18. R. Cregan, B. Mangan, J. Knight, T. Birks, P. Russell, P. Roberts, and D. Allan, *Science.*, 1999, **285**, 1537–1539.
19. J. S. Y. Chen, T. G. Euser, N. J. Farrer, P. J. Sadler, M. Scharrer, and P. S. J. Russell, *Chem. Eur. J.*, 2010, **16**, 5607–5612.

Chapter 4 – Photonic crystal fibre mass spectrometry

20. L. M. Fidalgo, G. Whyte, D. Bratton, C. F. Kaminski, C. Abell, and W. T. S. Huck, *Angew. Chem. Int. Ed.*, 2008, **47**, 2042–2045.
21. M. Ziehe, D. Esteban-Fernández, U. Hochkirch, J. Thomale, and M. W. Linscheid, *Metallomics*, 2012, **4**, 1098–1104.
22. A. F. Westendorf, A. Bodtke, and P. J. Bednarski, *Dalt. Trans.*, 2011, **40**, 5342–5351.
23. R. J. McQuitty, University of Warwick, 2008.
24. B. J. M. Pratt, *J. Chem. Soc.*, 1964, 5154–5160.
25. R. A. Firth and R. G. Thorp, *Chem Comm.*, 1967, 5694–5697.
26. S. M. Chemaly, *Dalt. Trans.*, 2008, 5766–5773.
27. W. H. and A. A. F. IQBAL AHMAD, 1992, **1**, 9–15.
28. J. S. Y. Chen, T. G. Euser, N. J. Farrer, P. J. Sadler, and P. S. J. Russell, *Chem. Eur. J.*, 2010, **16**, 5607–5612.
29. A. R. Butler and C. Glidewell, *Chem. Soc. Rev.*, 1987, **16**, 361–380.
30. S. K. Wolfe and J. H. Swinehart, *Inorg. Chem.*, 1975, **14**, 1049–1053.
31. S. H. Frank, M J, Johnson, M B and Rubin, *J. Pharma. Sci.*, **65**, 44–48.
32. M. G. De Oliveira, G. J. Langley, and A. J. Rest, *J. Chem. Soc. Dalt. Trans.*, 1995, **1995**, 2013–2019.
33. S. M. Shishido and M. G. de Oliveira, *Prog. React. Kinet. Mech.*, 2001, **26**, 239–261.
34. W. P. Arnold, D. E. Longnecker, and R. M. Epstein, *Anesthesiol.*, 1984, **61**, 254–260.
35. W. Henderson and J. S. McIndo, *Mass Spectrometry of Inorganic, Coordination and Organometallic Compounds*, John Wiley & Sons Ltd., Chichester, 2005.
36. S. Betanzos-Lara, L. Salassa, A. Habtemariam, and P. J. Sadler, *Chem. Comm.*, 2009, **2009**, 6622–6624.
37. S. W. Magennis, A. Habtemariam, O. Novakova, J. B. Henry, S. Meier, S. Parsons, I. D. H. Oswald, V. Brabec, and P. J. Sadler, *Inorg. Chem.*, 2007, **46**, 5059–5068.
38. S. E. Sherman and S. J. Lippard, *Chem. Rev.*, 1987, **87**, 1153–1181.
39. J. Reedijk, *Pure Appl. Chem.*, 2011, **83**, 1709–1719.
40. J. Reedijk, *Eur. J. Inorg. Chem.*, 2009, **2009**, 1303–1312.
41. B. Köberle, M. T. Tomicic, S. Usanova, and B. Kaina, *Biochim. Biophys. Acta*, 2010, **1806**, 172–182.
42. T. Shoeib and B. L. Sharp, *Metallomics*, 2012, **4**, 1308–1320.

Chapter 4 – Photonic crystal fibre mass spectrometry

43. A.-M. Florea and D. Büsselberg, *Cancers (Basel)*, 2011, **3**, 1351–1371.
44. J. Pracharova, L. Zerzankova, J. Stepankova, O. Novakova, N. J. Farrer, P. J. Sadler, V. Brabec, and J. Kasparkova, *Chem. Res. Toxicol.*, 2012, **25**, 1099–1111.
45. A. F. Westendorf, J. a Woods, K. Korpis, N. J. Farrer, L. Salassa, K. Robinson, V. Appleyard, K. Murray, R. Grünert, A. M. Thompson, P. J. Sadler, and P. J. Bednarski, *Mol. Cancer Ther.*, 2012, **11**, 1894–1904.
46. F. Wang, H. Chen, J. a Parkinson, P. D. S. Murdoch, and P. J. Sadler, *Inorg. Chem.*, 2002, **41**, 4509–4523.

Chapter 5

Conclusions and future work

5.1 Conclusions

In the course of this work analytical techniques, primarily high performance liquid chromatography (HPLC) and mass spectrometry (MS), have been applied to study various properties of metal-based anticancer drugs. In Chapter 2 the study of the intracellular accumulation of a new generation of platinum-based drugs is reported. The relative lipophilicity of a series of 10 platinum(IV) diazido complexes of the general formula *trans,trans,trans*-[Pt(N₃)₂(OH)₂(R)(R')] (where R and R' are NH₃, methylamine, ethylamine, pyridine, 2-picoline, 3-picoline or thiazole) was determined by HPLC. The trend predicted based on the lipophilicity of the R and R' ligands did not correlate with the observed lipophilicities. These observed values were then compared to the platinum accumulation of compounds **1-10** in A2780 human ovarian carcinoma cells. There appeared to be no overall trend relating hydrophobicity to the cellular accumulation of these complexes. Furthermore, the potency of these complexes in cancer cells (in the form of IC₅₀ values) also has no obvious relationship to their cellular accumulation. These studies suggest that active transport inside the cells is partly the cause. However, it is thought that other factors, such as the quantum yield of the complex, and the type of DNA adduct formed by the photoactivated species have a greater influence over the efficacy of this class of drug. Amino acids and reducing agents present in the cell media may have also reacted with the Pt(IV) diazido complexes in the dark, forming new Pt(II) species. This would explain the lack of correlation between the observed activity and the properties of the Pt(IV) complexes.

One of these complexes, **8** *trans,trans,trans*-[Pt(N₃)₂(OH)₂(py)₂] (where py is pyridine), was selected for further investigation in view of its low IC₅₀ value and

Chapter 5 – Conclusions and future work

high relative lipophilicity and cellular accumulation. Irradiation of **8** with UVA light in the presence of a single strand oligonucleotide, oligo 1 d'(ATACAT**G**CTACATA), led to a new species being detected by chromatography. Changing the oligonucleotide to d'(ATAC**G**T**G**CTACATA), oligo 3, gave similar results to those obtained using oligo 1. However, the amount of platinum bound to the DNA reduced by one third when the sequence of the oligonucleotide was changed to include the possibility of a 1,2-d(GpG) binding mode.

The $\{\text{Pt}(\text{py})_2\}^{2+}$ adduct formed by **8** upon photoactivation in the presence of oligo 1 was characterised by mass spectrometry. The species was assigned as {oligo 1 + $[\text{Pt}(\text{py})_2]$ } and ^{15}N labelled versions of **8**, *t,t,t*- $[\text{Pt}(\text{N}_3)_2(\text{OH})_2(^{15}\text{Npy})_2]$ (**8X**) and *t,t,t*- $[\text{Pt}(^{15}\text{N}_3)_2(\text{OH})_2(^{15}\text{Npy})_2]$ (**8Y**), were photoactivated in the presence of oligo 1 to confirm the formation of this species. Changing the wavelength of activation of **8** from 365 nm to 420 nm was found to cause decrease the rate platination of the oligonucleotide upon irradiation of **8**. Studies by both mass spectrometry and chromatography show that changing the wavelength of activation was found to have no affect on the type of DNA adduct formed.

In Chapter 3, normal-phase chiral HPLC was used to separate the enantiomers and diastereomers of a series of ruthenium, osmium and iridium organometallic anticancer complexes. Columns containing the amylose- and cellulose-based stationary phases CHIRALPAK IA and CHIRALPAK IC were used. Methods were developed and optimised through out the course of this work. The stability in solution of some of these separated enantiomers was investigated. All of the neutral Ir(III)pentamethylcyclopentadiene-based complexes tested reverted to

Chapter 5 – Conclusions and future work

a racemic mixture after a minimum of 2 h in ethanol at room temperature, but the Ru- and Os-based enantiomers maintained stability under the same conditions. Small changes in each of the ligands (i.e., halide leaving group, bidentate ligand and arene) resulted in changes to the retention times of the species eluted and hence, resolution of the separation. Changing the hydrophobicity of the bidentate ligand resulted in the largest changes of retention times.

In Chapter 4, the development and validation of photonic crystal fibre mass spectrometry as a novel technique for the rapid irradiation and analysis of photoactivatable drugs is reported. The internal volume of the sample cells used in the system was reduced from 60 μL to 360 nL over the course of the investigation. The photonic crystal fibre (PCF) used was improved in order to guide 488 nm light. The system was then validated in the positive mode using a known photoreaction, the photoaquation of cyanocobalamin, and the results were compared to those generated using conventional techniques. The spectra obtained using the PCF system differ only slightly from those obtained by the conventional method, the main difference being the drop in signal intensity when using the PCF system. Comparing this new method to conventional techniques, sample irradiation times are reduced from 8 h to 15 min and sample volumes are reduced by 20 times.

The system was then used to study the photoactivation of the ruthenium-based drug **26**, $[(\eta^6\text{-indan})\text{RuCl}_2(\mu\text{-}2,3\text{-dpp})](\text{PF}_6)_2$ (where $(\mu\text{-}2,3\text{-dpp})$ is (2,3-bis(2-pyridyl)pyrazine)). A series of small molecules was used as models for intracellular components to gain insight into how the complex might behave in cells (5'-GMP, 5'-AMP, L-Cys and GSH). The findings agree with the work of Magennis *et al.*, carried

Chapter 5 – Conclusions and future work

out using conventional methods. Complex **26** was found to bind to nucleobases in the dark, binding increased upon irradiation with 5'GMP, and this was favoured over 5'AMP binding.¹ After irradiation complex **26** was also found to bind strongly to GSH, a known deactivation pathway of metal-based drugs.^{2,3}

5.2 Future work

Future studies of the intracellular behaviour of platinum(IV)-diazido complexes of the general formula *trans,trans,trans*-[Pt(N₃)₂(OH)₂(R)(R')] could be extended to include a wider range of complexes to build a greater understanding of structure-activity relationships. Other properties of the complexes already included in the study should also be determined, such as the quantum yield and the DNA-binding properties. The use of HPLC retention times as a measure of relative hydrophobicity may prove useful for the comparison of other hydrophilic series of compounds.

Investigations of the nature of the DNA adduct formed by **8** have already been shown in Chapter 2 of this work. However, work is already under way to study it further using other techniques. Single molecule Förster resonance energy transfer, also known as single molecule fluorescence resonance energy transfer, describes the energy transfer between two chromophores, one donor and one acceptor. The energy is not transferred by fluorescence, but rather by non-radiative transfer. This transfer can take place over distances of 1 - 10 nm,^{4,5} and can be used to determine the relative distances between the donor and acceptor chromophores, and hence the bend induced by the platinum adduct. SM-FRET has previously been used to study structural features of DNA, and drug-induced

Chapter 5 – Conclusions and future work

with the literature reported values, then the technique can be applied to new, less well-characterised adducts such as those formed by platinum(IV) complex **8**.

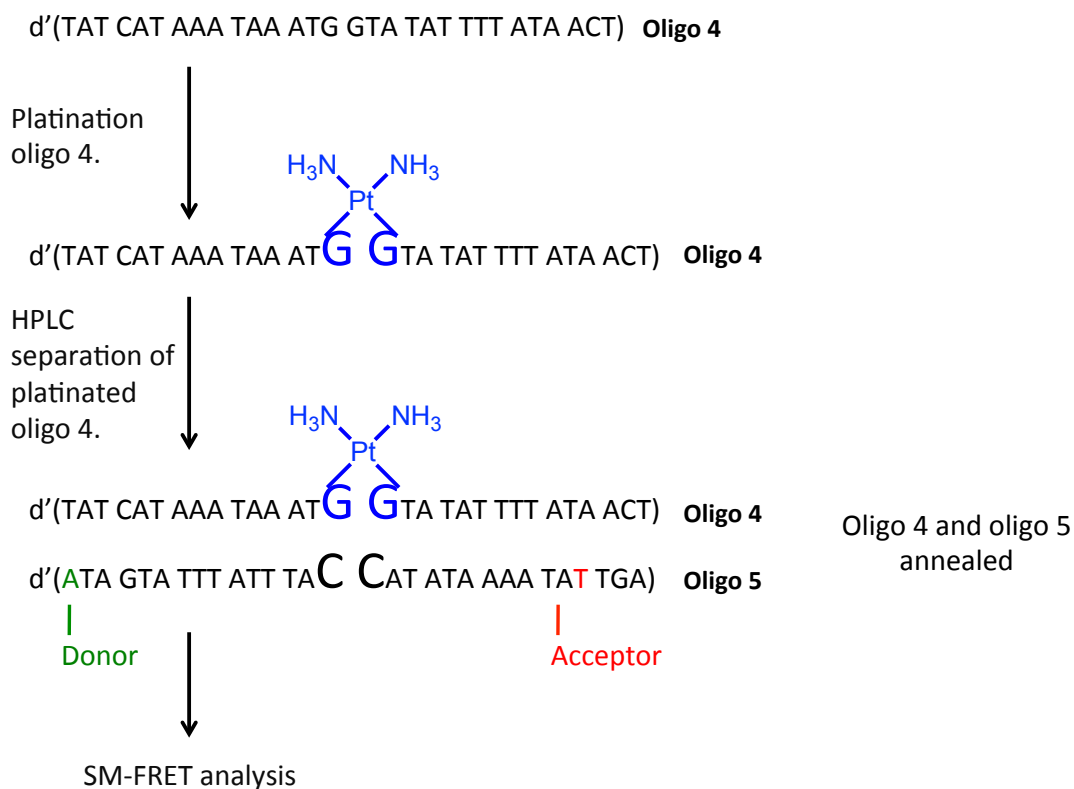


Figure 5.2 Outline of the overall SM-FRET experiment broken down into individual stages: the first and second stages in future work to be carried out at the University of Warwick and the third and fourth stages by our collaborators in Manchester.

Regarding the chiral separation of organometallic drugs, those separations shown to be successful in Chapter 3 and the isolation of stable separated enantiomers can be scaled up. This will allow for enough of the each isomer to be collected for biological assays to be carried out. In this manner the efficacy of each isomer can be assessed individually, allowing for further development of the selected anticancer drug.

Chapter 5 – Conclusions and future work

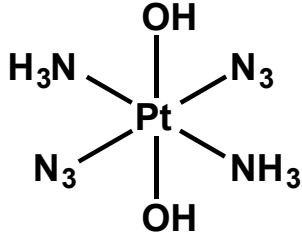
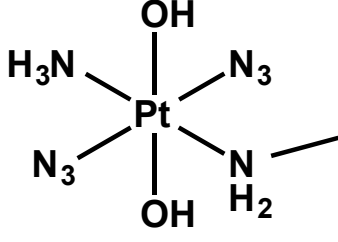
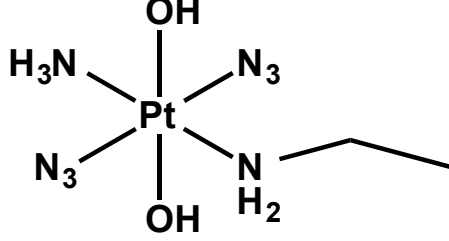
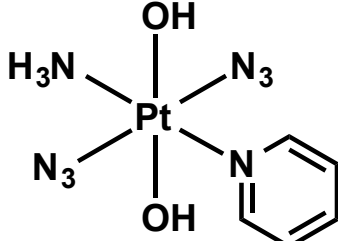
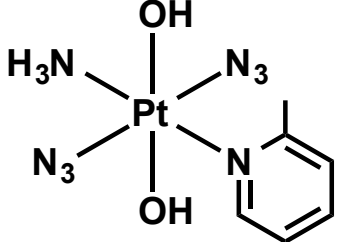
The photonic crystal fibre (PCF) system detailed in chapter 4 has shown great potential. It can now be used as a method to screen photoactivatable drugs for insights into their mechanism of action. Biological assays of complex **26** ($[(\eta^6\text{-indan})\text{RuCl}]_2(\mu\text{-}2,3\text{-dpp})]^{2+}$) should be carried out to see if predictions made using the PCF system screening are correct. Within the system itself, the deadtime has been minimised by reducing the length of tubing connecting the various components. To reduce what appears to be an intrinsic deadtime of 15 min in this system, it may prove useful to develop or adapt the electrospray ionisation device to better suit the flow-rates and pressures of the PCF system; since nano-flow technologies have already been reported as successfully coupled to mass spectrometers, this problem should be overcome.¹¹

5.4 References

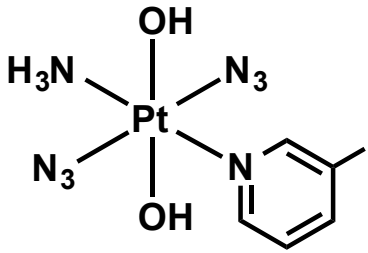
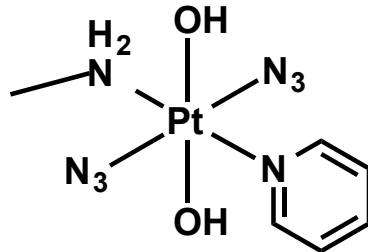
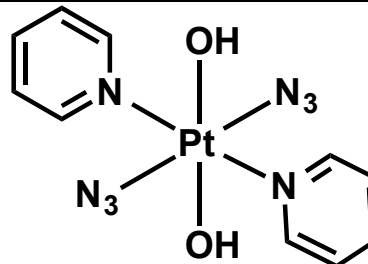
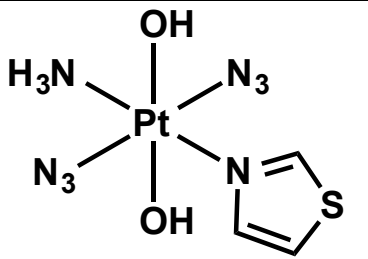
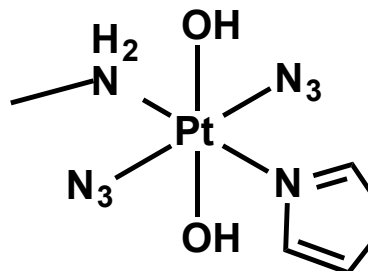
1. S. W. Magennis, A. Habtemariam, O. Novakova, J. B. Henry, S. Meier, S. Parsons, I. D. H. Oswald, V. Brabec, and P. J. Sadler, *Inorg. Chem.*, 2007, **46**, 5059–5068.
2. F. Arnesano and G. Natile, *Coord. Chem. Rev.*, 2009, **253**, 2070–2081.
3. A.-M. Florea and D. Büsselberg, *Cancers (Basel)*, 2011, **3**, 1351–1371.
4. S. Weiss, *Science (80-.)*, 1999, **283**, 1676–1683.
5. R. Roy, S. Hohng, and T. Ha, *Nat. Meth.*, 2008, **5**, 507–516.
6. L. E. Sass, C. Lanyi, K. Weninger, and D. a Erie, *Biochemistry*, 2010, **49**, 3174–3190.
7. S. Murata, Y. Mizumura, K. Hino, Y. Ueno, S. Ichikawa, and A. Matsuda, *J. Am. Chem. Soc.*, 2007, **129**, 10300–10301.
8. A. K. Wozniak, G. F. Schröder, H. Grubmüller, C. a M. Seidel, and F. Oesterhelt, *Proc. Nat. Acad. Sci.*, 2008, **105**, 18337–18342.
9. E. R. Jamieson, M. P. Jacobson, C. M. Barnes, C. S. Chow, and S. J. Lippard, *J. Biol. Chem.*, 1999, **274**, 12346–12354.
10. T. Sabir, G. F. Schröder, A. Toulmin, P. McGlynn, and S. W. Magennis, *J. Am. Chem. Soc.*, 2011, **133**, 1188–1191.
11. T. Köcher, P. Pichler, R. Swart, and K. Mechtler, *Nat. Protocl.*, 2012, **7**, 882–890.

Appendices

Appendix I

Complex	Structure
<p style="text-align: center;">1</p> <p style="text-align: center;"><i>trans,trans,trans</i>-[Pt(N₃)₂(OH)₂(NH₃)₂]</p>	
<p style="text-align: center;">2</p> <p style="text-align: center;"><i>trans,trans,trans</i>-[Pt(N₃)₂(OH)₂(NH₃)(NH₂CH₃)]</p>	
<p style="text-align: center;">3</p> <p style="text-align: center;"><i>trans,trans,trans</i>-[Pt(N₃)₂(OH)₂(NH₃)(NH₂CCH₂CH₃)]</p>	
<p style="text-align: center;">4</p> <p style="text-align: center;"><i>trans,trans,trans</i>-[Pt(N₃)₂(OH)₂(NH₃)(py)]</p>	
<p style="text-align: center;">5</p> <p style="text-align: center;"><i>trans,trans,trans</i>-[Pt(N₃)₂(OH)₂(NH₃)(2-pic)]</p>	

Appendices

<p style="text-align: center;">6</p> <p><i>trans,trans,trans</i>-[Pt(N₃)₂(OH)₂(NH₃)(4-pic)]</p>	 <p>The structure shows a central platinum (Pt) atom in an octahedral geometry. It is coordinated to two azido (N₃) groups in a trans configuration, two hydroxyl (OH) groups in a trans configuration, an ammonia (NH₃) group, and a 4-picoline (pic) ligand.</p>
<p style="text-align: center;">7</p> <p><i>trans,trans,trans</i>-[Pt(N₃)₂(OH)₂(NH₂CH₃)(py)]</p>	 <p>The structure shows a central platinum (Pt) atom in an octahedral geometry. It is coordinated to two azido (N₃) groups in a trans configuration, two hydroxyl (OH) groups in a trans configuration, a methylamino (NH₂CH₃) group, and a pyridine (py) ligand.</p>
<p style="text-align: center;">8</p> <p><i>trans,trans,trans</i>-[Pt(N₃)₂(OH)₂(py)₂]</p>	 <p>The structure shows a central platinum (Pt) atom in an octahedral geometry. It is coordinated to two azido (N₃) groups in a trans configuration, two hydroxyl (OH) groups in a trans configuration, and two pyridine (py) ligands.</p>
<p style="text-align: center;">9</p> <p><i>trans,trans,trans</i>-[Pt(N₃)₂(OH)₂(NH₃)(tz)]</p>	 <p>The structure shows a central platinum (Pt) atom in an octahedral geometry. It is coordinated to two azido (N₃) groups in a trans configuration, two hydroxyl (OH) groups in a trans configuration, an ammonia (NH₃) group, and a thiazole (tz) ligand.</p>
<p style="text-align: center;">10</p> <p><i>trans,trans,trans</i>-[Pt(N₃)₂(OH)₂(NH₂CH₃)(tz)]</p>	 <p>The structure shows a central platinum (Pt) atom in an octahedral geometry. It is coordinated to two azido (N₃) groups in a trans configuration, two hydroxyl (OH) groups in a trans configuration, a methylamino (NH₂CH₃) group, and a thiazole (tz) ligand.</p>

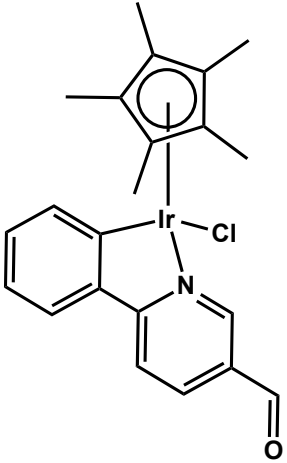
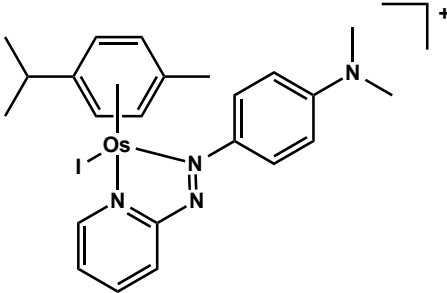
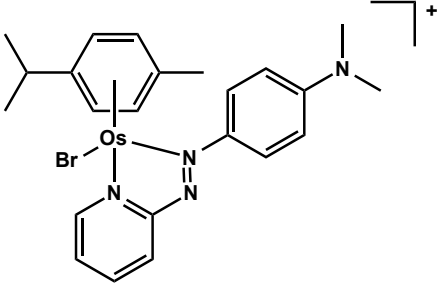
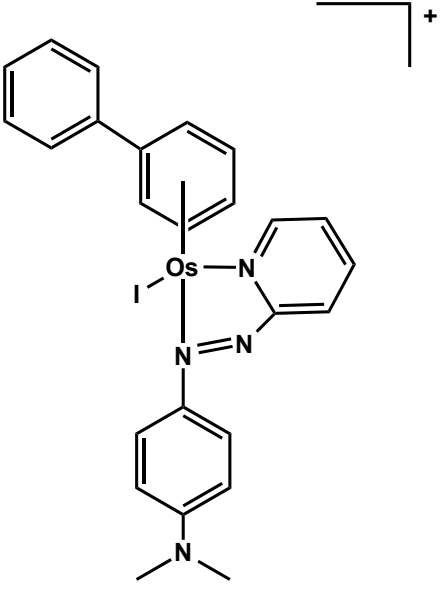
Appendices

<p>11</p> <p>$[\text{Ir}(\eta^5\text{-Cp}^{\text{xbph}})(\text{phenpy})\text{Cl}]$</p>	<p>The structure shows an iridium (Ir) center coordinated to a chloride (Cl) ligand, a pentamethylcyclopentadienyl (Cp*) ring, and a phenpyridine (phenpy) ligand. The phenpyridine ligand consists of a phenyl ring connected to a pyridine ring. The Cp* ring is substituted with a 4-phenylphenyl group.</p>
<p>12</p> <p>$[\text{Ir}(\eta^5\text{-Cp}^*) (\text{benzq})\text{Cl}]$</p>	<p>The structure shows an iridium (Ir) center coordinated to a chloride (Cl) ligand, a pentamethylcyclopentadienyl (Cp*) ring, and a benzquinoxaline (benzq) ligand. The benzq ligand is a tricyclic system consisting of a benzene ring fused to a quinoxaline ring system.</p>
<p>13</p> <p>$[\text{Ir}(\eta^5\text{-Cp}^*) (\text{dfphpy})\text{Cl}]$</p>	<p>The structure shows an iridium (Ir) center coordinated to a chloride (Cl) ligand, a pentamethylcyclopentadienyl (Cp*) ring, and a difluorophenylpyridine (dfphpy) ligand. The dfphpy ligand consists of a pyridine ring connected to a benzene ring substituted with two fluorine (F) atoms.</p>

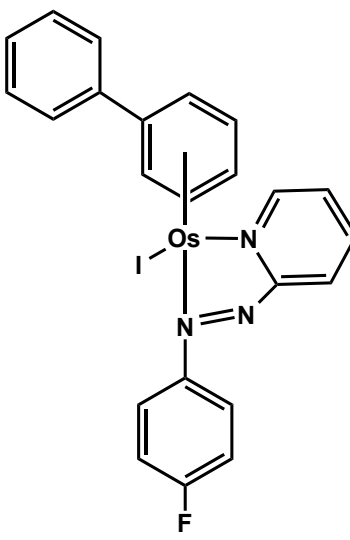
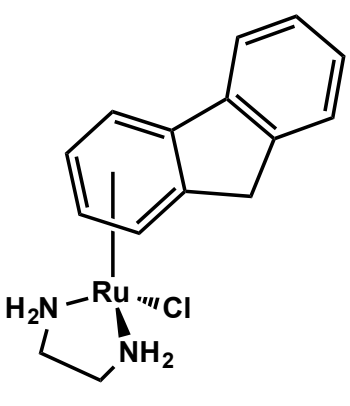
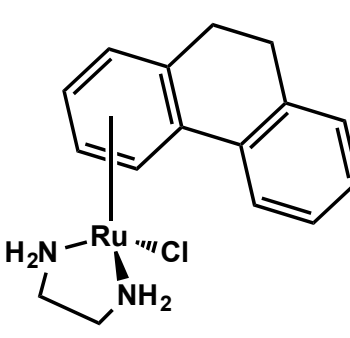
Appendices

<p style="text-align: center;">14</p> <p style="text-align: center;">$[\text{Ir}(\eta^5\text{-Cp}^*)(\text{py},4\text{-}(2\text{fph}))\text{Cl}]$</p>	<p>The structure shows an iridium (Ir) center coordinated to a pentamethylcyclopentadienyl (Cp*) ligand, a chlorine (Cl) atom, and a bidentate ligand. The bidentate ligand consists of a pyridine ring and a benzene ring. The benzene ring has a fluorine (F) atom at the 2-position relative to the Ir-C bond.</p>
<p style="text-align: center;">15</p> <p style="text-align: center;">$[\text{Ir}(\eta^5\text{-Cp}^*)(\text{py},4\text{-}(4\text{fph}))\text{Cl}]$</p>	<p>The structure shows an iridium (Ir) center coordinated to a pentamethylcyclopentadienyl (Cp*) ligand, a chlorine (Cl) atom, and a bidentate ligand. The bidentate ligand consists of a pyridine ring and a benzene ring. The benzene ring has a fluorine (F) atom at the 4-position relative to the Ir-C bond.</p>
<p style="text-align: center;">16</p> <p style="text-align: center;">$[\text{Ir}(\eta^5\text{-Cp}^*)(\text{py},4\text{-}(4\text{tfmph}))\text{Cl}]$</p>	<p>The structure shows an iridium (Ir) center coordinated to a pentamethylcyclopentadienyl (Cp*) ligand, a chlorine (Cl) atom, and a bidentate ligand. The bidentate ligand consists of a pyridine ring and a benzene ring. The benzene ring has a trifluoromethyl (F₃C) group at the 4-position relative to the Ir-C bond.</p>

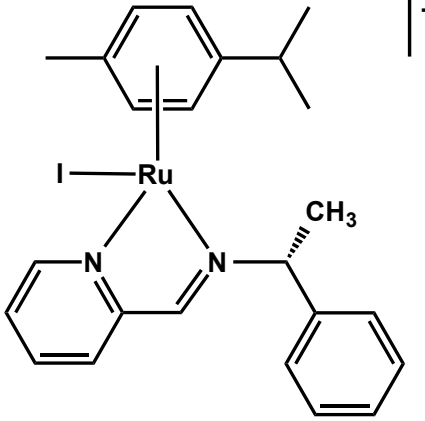
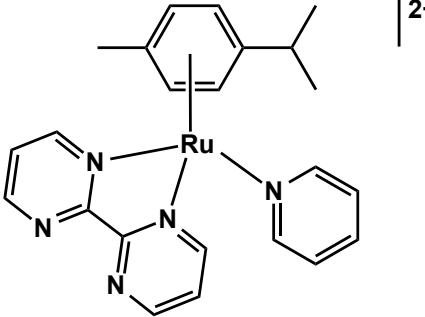
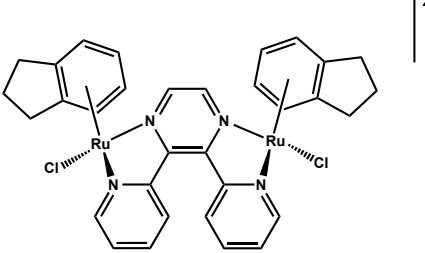
Appendices

<p style="text-align: center;">17</p> <p style="text-align: center;">$[\text{Ir}(\eta^5\text{-Cp}^*)(\text{py},4\text{-(4tfmph)})\text{Cl}]$</p>	
<p style="text-align: center;">18</p> <p style="text-align: center;">$[\text{Os}(\eta^6\text{-p-cym})(\text{azpy-NMe}_2)\text{I}]^+$</p>	
<p style="text-align: center;">19</p> <p style="text-align: center;">$[\text{Os}(\eta^6\text{-p-cym})(\text{azpy-NMe}_2)\text{Br}]^+$</p>	
<p style="text-align: center;">20</p> <p style="text-align: center;">$[\text{Os}(\eta^6\text{-bip})(\text{azpy-NMe}_2)\text{I}]^+$</p>	

Appendices

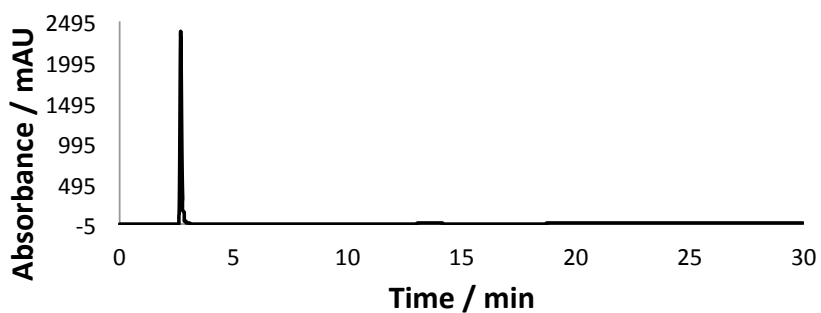
<p style="text-align: center;">21</p> <p style="text-align: center;">$[\text{Os}(\eta^6\text{-bip})(\text{azpy-f})\text{I}]^+$</p>	<p style="text-align: right;">+</p> 
<p style="text-align: center;">22</p> <p style="text-align: center;">$[\text{Ru}(\eta^6\text{-flu})(\text{en})\text{Cl}]^+$</p>	<p style="text-align: right;">+</p> 
<p style="text-align: center;">23</p> <p style="text-align: center;">$[\text{Ru}(\eta^6\text{-phent})(\text{en})\text{Cl}]^+$</p>	<p style="text-align: right;">+</p> 

Appendices

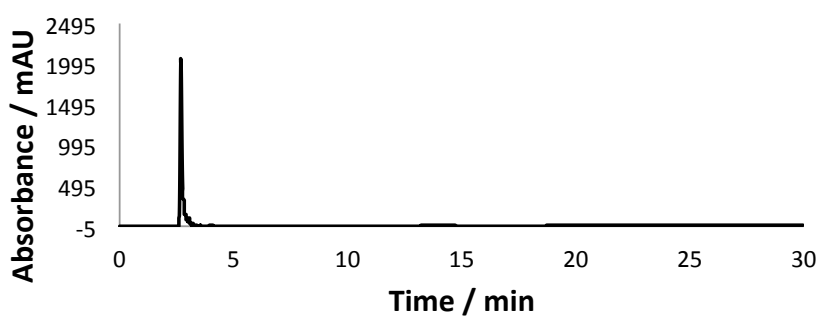
<p style="text-align: center;">24</p> <p style="text-align: center;">$[\text{Ru}(\eta^6\text{-p-cym})(\text{Impy})\text{I}]^+$</p>	
<p style="text-align: center;">24</p> <p style="text-align: center;">$[\text{Ru}(\eta^6\text{-p-cym})(\text{bpm})(\text{py})]^{2+}$</p>	
<p style="text-align: center;">25</p> <p style="text-align: center;">$[\{\text{Ru}(\eta^6\text{-indan})\text{Cl}\}_2(\mu\text{-2,3-dpp})]^{2+}$</p>	

Appendix II

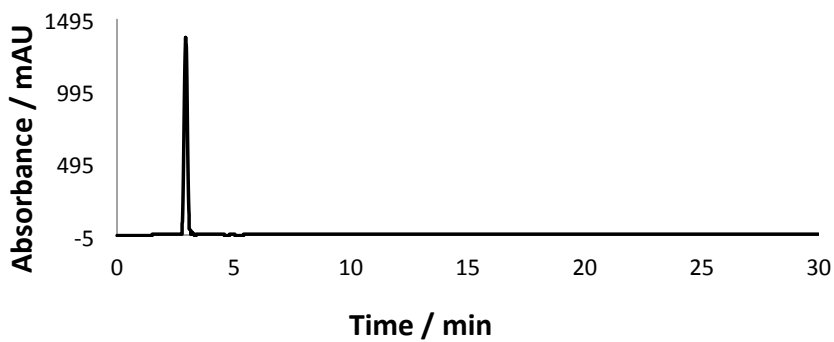
Complex 1 t = 0 h



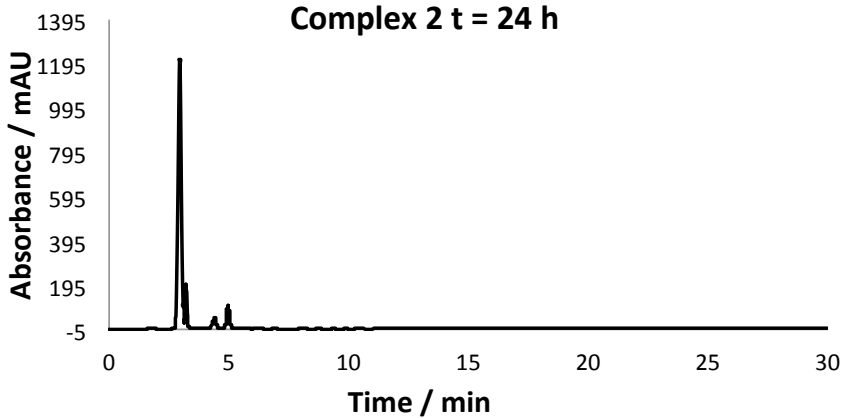
Complex 1 t = 24 h



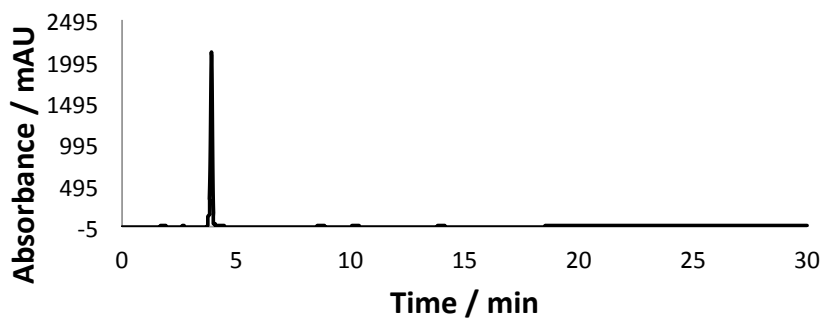
Complex 2 t = 0 h



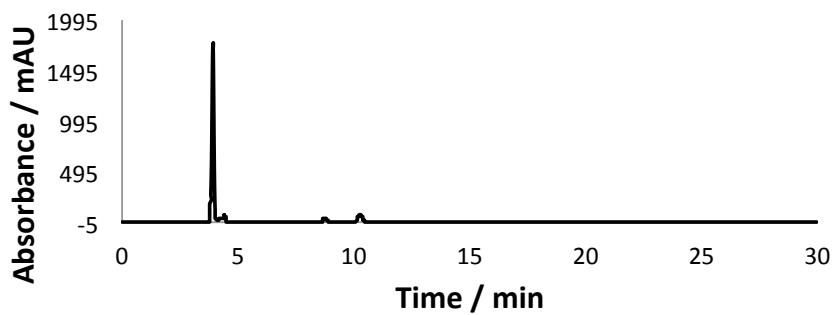
Complex 2 t = 24 h



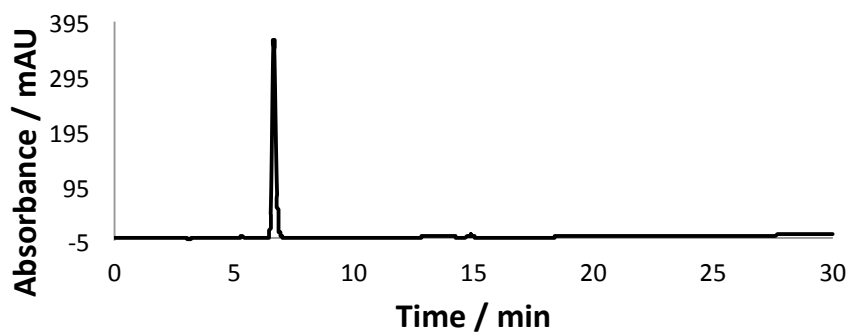
Complex 3 t = 0 h



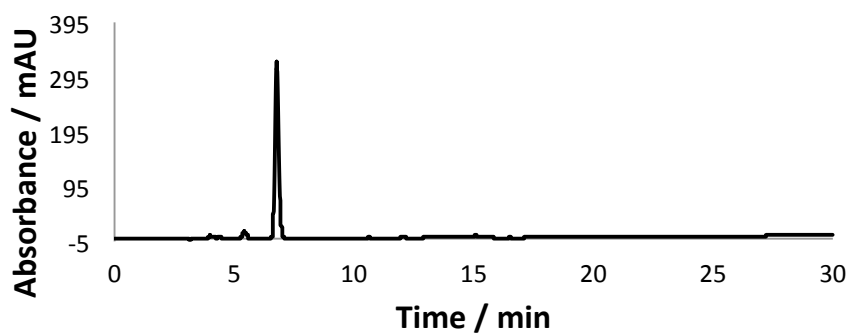
Complex 3 t = 24 h



Complex 4 t = 0 h

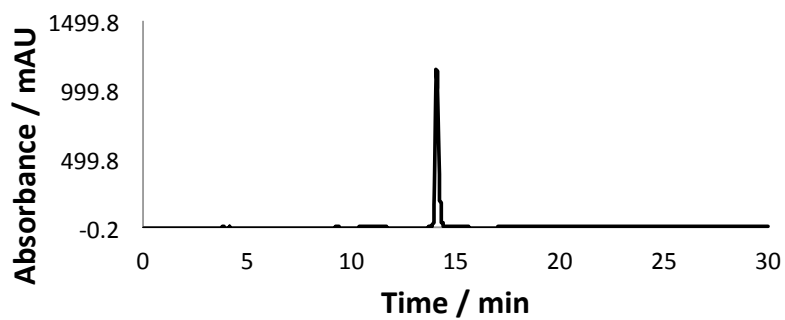


Complex 4 t = 24 h

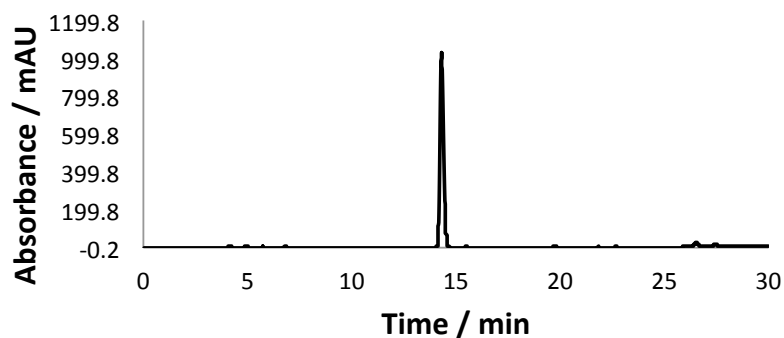


Appendices

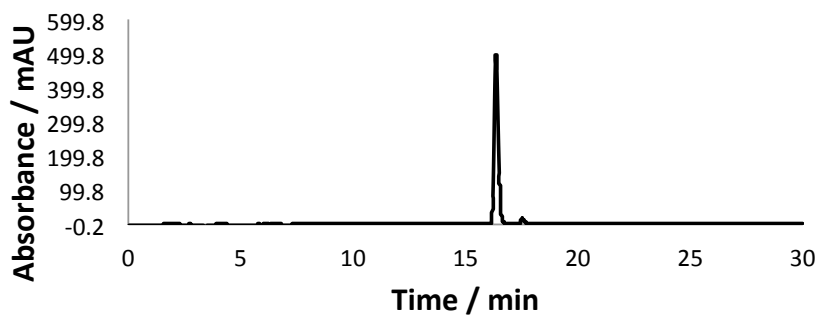
Complex 5 t = 0h



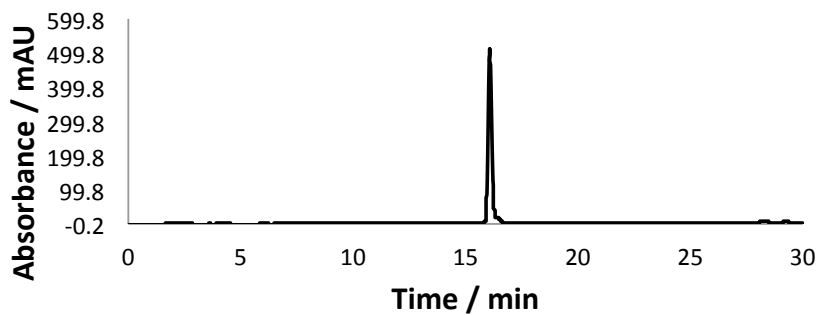
Complex 5 t = 24 h



Complex 6 t = 0 h

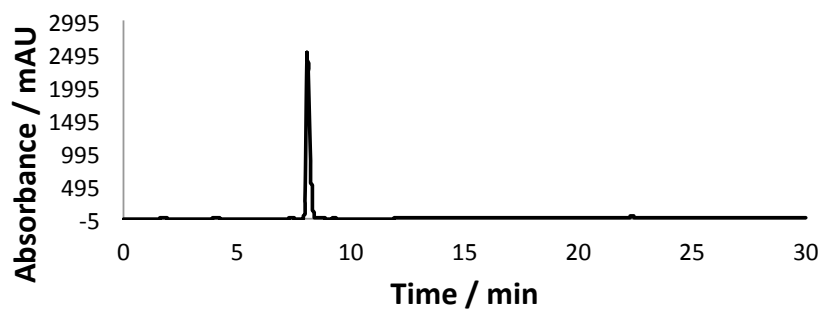


Complex 6 t = 24 h

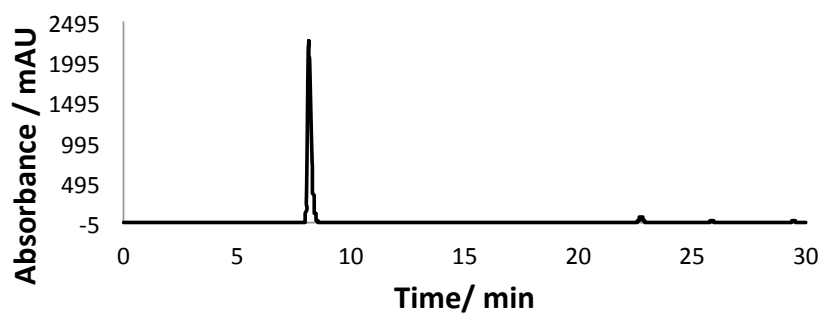


Appendices

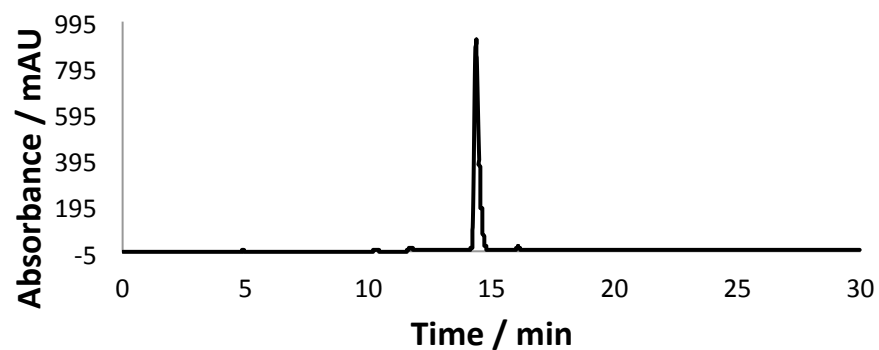
Complex 7 t = 0 h



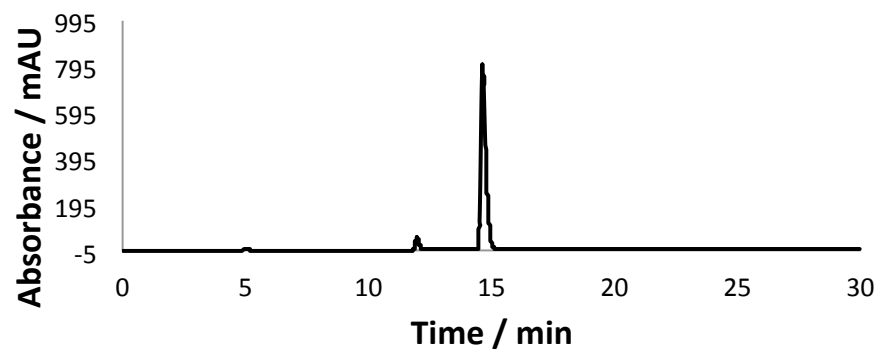
Complex 7 t = 24 h



Complex 8 t = 0

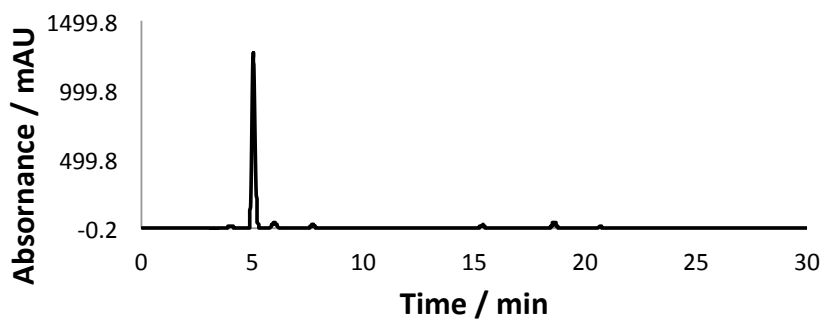


Complex 8 t = 24

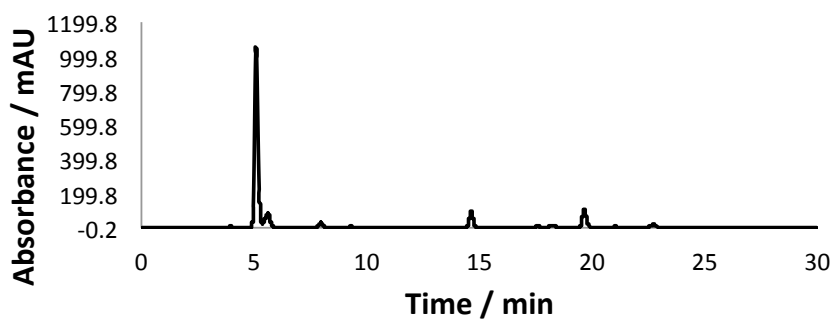


Appendices

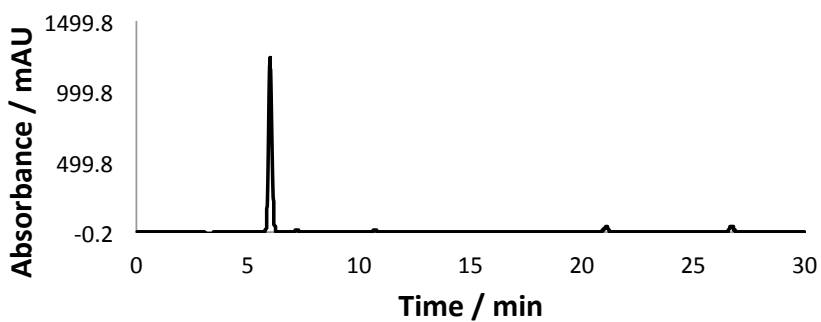
Complex 9 t = 0 h



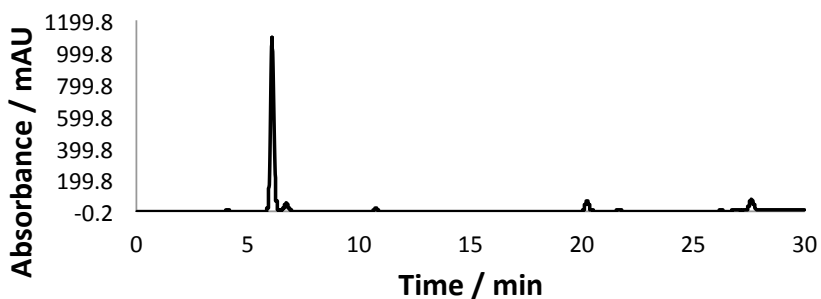
Complex 9 t = 24 h



Complex 10 t = 0 h



Complex 10 t = 24 h

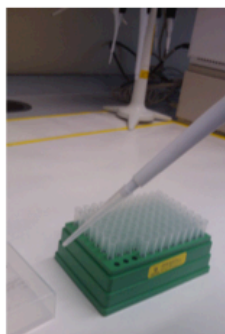


Appendix III

Appendix III part A: desalting methods

In this thesis two methods of desalting are used, and they are compared in this section. The methods used were: Omix pipette tips, that uses the adherence of the oligonucleotide to C18 to remove salt, and an Amicon stirred cell, employing a 1 kDa cut off filter disc. The two devices are shown below in Figure III-A. The recoveries of oligonucleotide from the devices, as well as the amount of salt adducts detected via mass spectrometry, were compared.

Omix pipette tips



- C18 stationary phase in tip
- Sample volume of 10 – 100 μL

Amicon stirred cell



- Membrane with 1 kDa cut off
- Sample volume of 0.75 – 3 mL

Figure III-A Left, Omix pipette tips, and right, the Amicon stirred cell.

The Omix pipette tips use a series of buffers and solutions to allow adherence of the oligonucleotide to the C18 within the tip, and its subsequent removal. This can be repeated for multiple 'cycles' (up to 10 times, according to the manufacturer) to increase sample recovery, in this comparison 3 cycles are used. The tips are recommended for use with peptides, and the manufacturer

recommends that the sample is acidified and that the tips are prepared for use using trifluoroacetic acid (TFA) buffer. The UV-Visible spectra in Figure III-B show a 4% recovery of the oligonucleotide (ATACATGCTACATA) by this method.

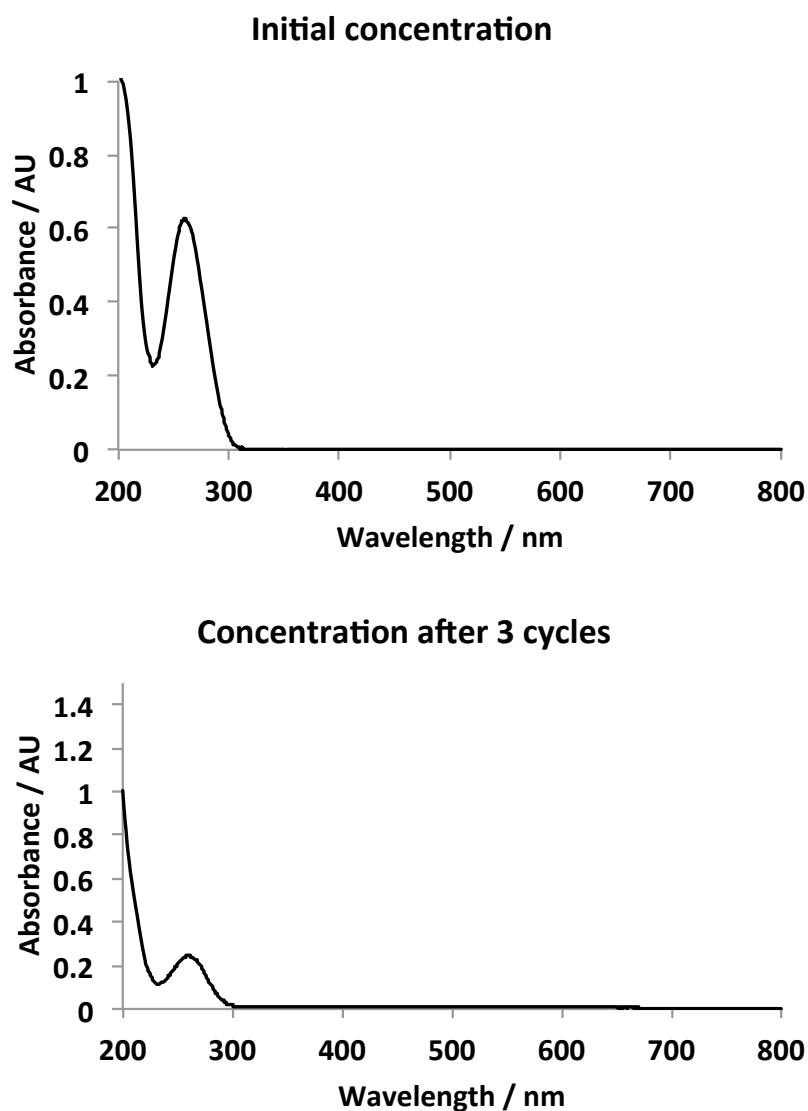


Figure III-B Top: initial concentration of 200 μm , bottom: oligonucleotide concentration of 8 μm eluted after a total of 3 cycles. Total recovery of oligonucleotide by this method was 4%.

The poor recovery from the manufacturers protocol led me to change the TFA (pH 1.7) containing buffer used to prepare the C18 for a less acidic solution 40

mM solution of NH_4OAc . The sample was no longer acidified before desalting, rather it is diluted 1 in 2 in a solution of 80 mM NH_4OAc . Ammonium acetate has the advantage of not only being less damaging to the mass spectrometer than TFA, but it also still displaces the Na^+ and K^+ ions associated with the oligonucleotide and will disassociate during the ionisation process. This ion-pairing also allows for interaction with the non-polar C18 and adherence to its surface. This change of solvents improved recovery by 5 times, giving an overall oligonucleotide recovery of 20% for this method of desalting (Figure III-C).

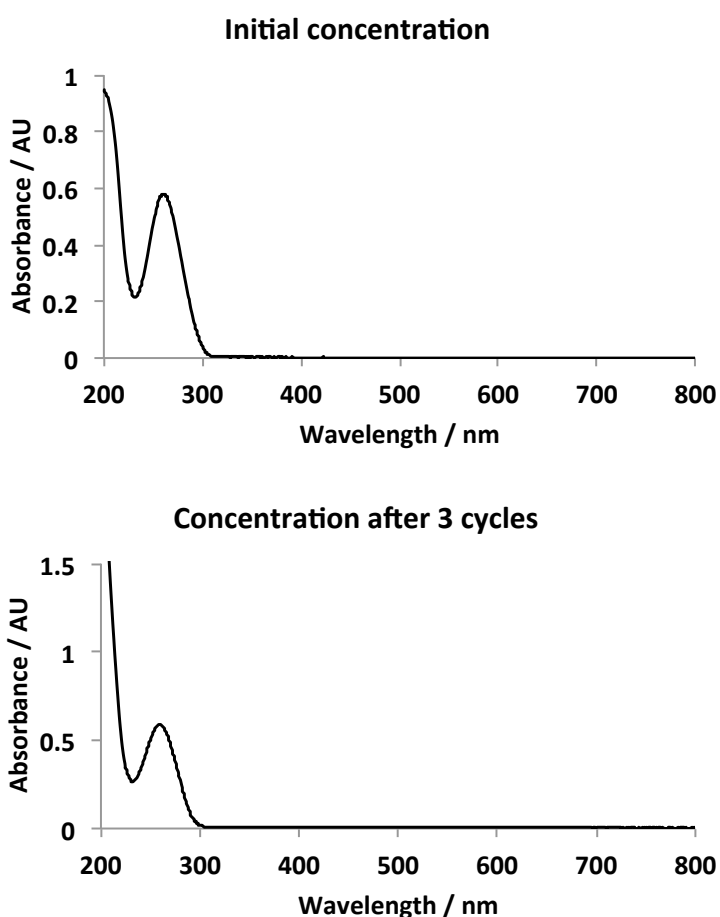


Figure III-C Top: initial concentration (200 μm), bottom: after 3 cycles using NH_4OAc buffer (40 μm). Giving an overall recovery of 20%.

The other desalting method used in this thesis was the Amicon stirred cell, fitted with a 1kDa cut-off filter disc. This device uses the filter disc to retain the 14 base-long oligonucleotide, whilst the excess salt in solution is forced through the membrane by nitrogen gas as the sample is slowly stirred. Using this method, the sample can be washed to remove salts associated with the oligonucleotide. After this ammonium acetate is added to help displace Na^+ and K^+ ions. The recovery from this method was found to be 67% after one wash and 24% overall recovery after 2 washes, see Figure III-D. This device can also be used to concentrate more dilute samples for analysis.

The resulting mass spectra of these solutions are shown in Figure III-E. The samples desalted using the Amicon stirred cell contain fewer salt adducts than the sample desalted using the Omix tips. The number of washes that the stirred cell sample undergoes also decreases the number of salt adducts detected. Other ways to improve the mass spectra of oligonucleotides are to leave the sample overnight in ammonium acetate and to use up to 50% isopropanol as the solvent used to spray the sample. The Amicon stirred cell method was then used to obtain high-resolution mass spectrometry data for this thesis, allowing for the accurate determination of new platinum-DNA adducts. The Omix tips were used in conjunction with an ion-trap mass spectrometer to determine if they were the correct molecular weight during the oligonucleotide quality control process.

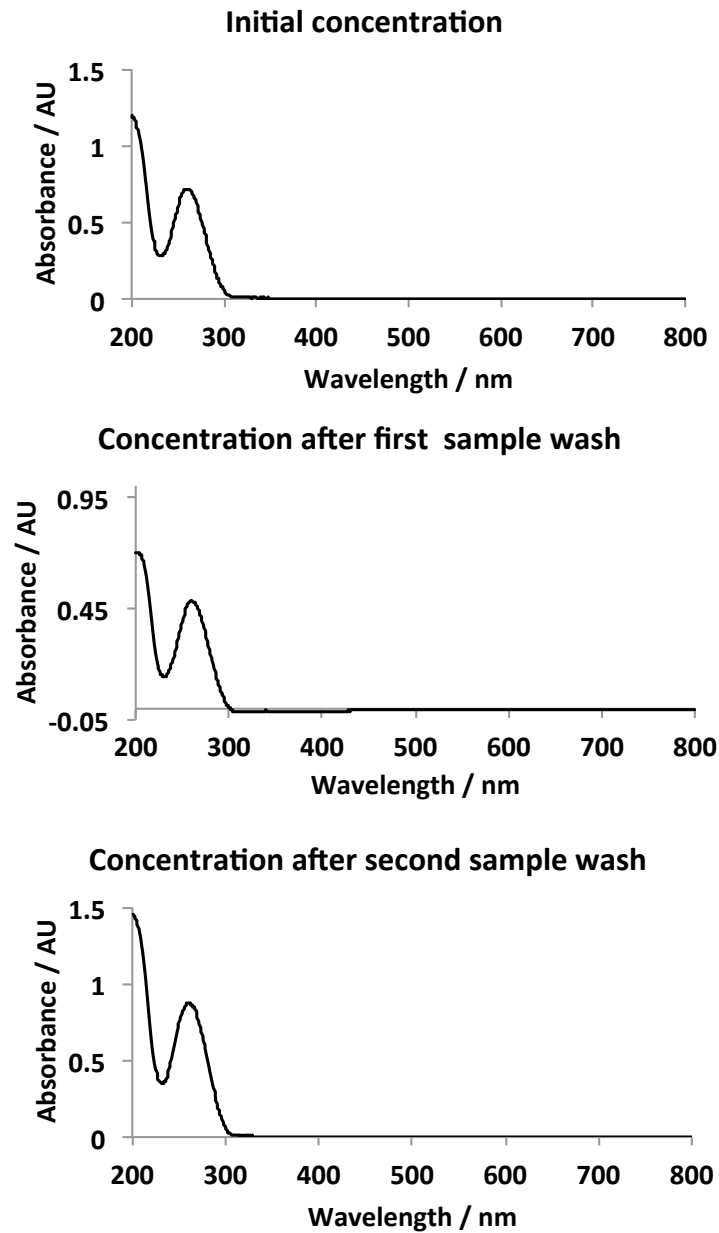


Figure III-D Oligonucleotide recovery from the Amicon stirred cell desalting method. Top: initial concentration (200 μm), middle: recovery after first wash (167 μm), and bottom: recovery after 2 washes (60 μm).

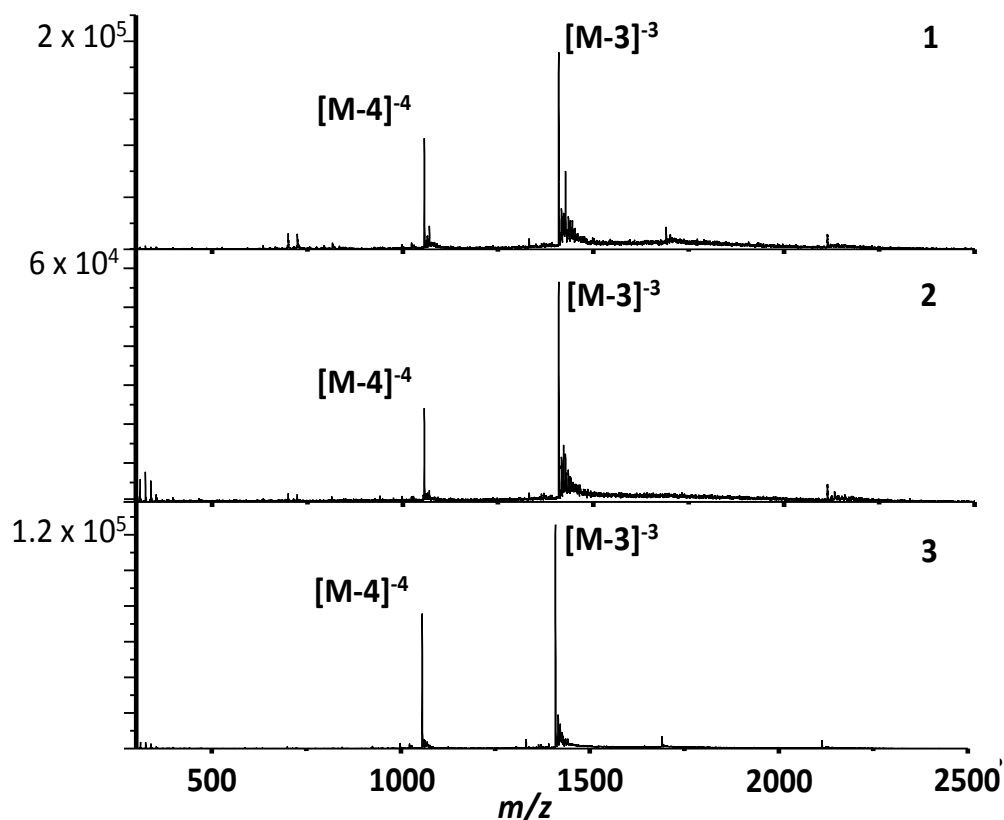


Figure III-E Mass spectra of the oligonucleotide (ATACATGCTACATA) desalted using: **1** Omix pipette tips, **2** an Amicon stirred cell with 1 kDa filter and one sample wash, **3** using the Amicon stirred cell and washing the sample twice.

Appendix III part B: method optimisation of the separation of free oligonucleotide from oligonucleotide with platinum adducts.

The analysis of the photoactivation of complex **8** (t,t,t -[Pt(N₃)₂(OH)₂(py)₂) in the presence of an oligonucleotide by chromatography required the development of a separation method. This began with the selection of the column and the mobile phase used. A longer column, 250 mm rather than 150 mm, to increase the number of theoretical plates, was chosen. The increased number of theoretical plates (N) results an increase in the resolving power of the column (Equation 1), where N is

the number of plates, α is the separation factor ($\alpha = k_2/k_1$), k_{av} is the average retention factor ($k_{av} = (k_1 + k_2)/2$), and R_s is the peak resolution.¹

$$\sqrt{N} = \frac{2(\alpha+1)}{\alpha-1} \cdot \frac{1+k_{av}}{k_{av}} \cdot R_s \quad (1)^1$$

The type of chromatography was reversed phase, as a hydrophilic mobile phase is more biologically relevant and offers the best solubility for DNA. This requires the use of a hydrophobic stationary phase. The stationary phases used for the work in this thesis are silica-based and are functionalised with carbon chains (C8 and C18 respectively). To allow the long oligonucleotides to interact with the stationary phase, particles with a larger pore size (300 Å) were used.

Reversed phase chromatography does; however, pose a problem as the separation of analytes is reliant upon the interaction on the charged oligonucleotides with the non-ionic hydrophobic stationary phase. To overcome this an ion-pairing agent can be added to the mobile phase, which will associate with the oligonucleotide, creating a neutral species, and allow interaction with the stationary phase. Common ion-pairing agents for DNA chromatography are triethylammonium acetate (TEAA) and ammonium acetate. There are many examples of NH_4OAc containing mobile phase being used to analyse Pt-DNA interactions by chromatography.²⁻⁴ This along with the 'sticky' nature of TEAA, meaning that it is more difficult to flush out of instruments, mean that NH_4OAc was selected as the ion-pairing agent. The concentration of the additive is also important, as was highlighted by A. Eastman (1986).⁵ He observed a separation of two formerly unresolved peaks by lowering the concentration of ammonium

acetate from 0.1 M to 0.02 M. The salt interacts with the oligonucleotide, sharpening peaks, reducing retention times. At lower concentrations of cation, adducts elute later and produce broader peaks but previously unresolved species can be separated. As a result of this a concentration of 10 mM NH_4OAc in both solvents was chosen. The pH of the mobile phases was also lowered to 5.5 to improve peak sharpness by increasing likelihood of phosphate backbone protonation.

The wavelength of detection used (260 nm) was selected, as this is the wavelength at which the extinction coefficient of DNA is the highest. The instrument used had a fault with the column thermostat fault, resulting in the ability to only heat the column and not the eluent entering it as well. This has resulted in the reporting of higher temperatures that one would normally use in the HPLC of oligonucleotides, as the solution had to be heated through the column rather than directly. The flow rate used throughout the method development was 1.00 mL/min.

A solvent gradient was required to separate the unreacted oligonucleotide from that with a platinum species bound. Initially separations were carried out on a Zorbax eclipse C18 strong-bond 25 x 4.6 mm 5 μm particle size with a 300 Å pore size. The development of the method began using a simple 0 – 80 % B (v/v) over 80 min gradient (80/80 gradient). This is a useful starting point for the development of new methods as for every minute of the method the percentage of B is increased by 1 %. So it is easy to isolate points of interest in the gradient and adapt them. The resulting chromatogram is not shown here.

The early elution of the unresolved peaks using the 80/80 gradient indicated that they elute with only a small proportion of acetonitrile present in the solvent mix. The starting percentage of acetonitrile was set to just below that at which the unreacted oligonucleotide is eluted and then kept isocratic for some time and then gradually increased. This was done with the aim of separating the unreacted DNA from the slightly more hydrophobic platinated DNA. The height and steepness of this gradient was refined to achieve the best possible separation conditions on this column. Both the gradient and the resulting chromatogram are shown in Figure III-F. The solvent was isocratic for the first 15 min at 6 % B, increased to 15 % B between 15 and 18 min, with a flow rate of 1 mL/min. The gradient remained isocratic at 15 % until 30 min into the run, then increased to 80 % B by 31 min, where it remained until the end of the run at 35 min. For this separation the column oven was to 35°C.

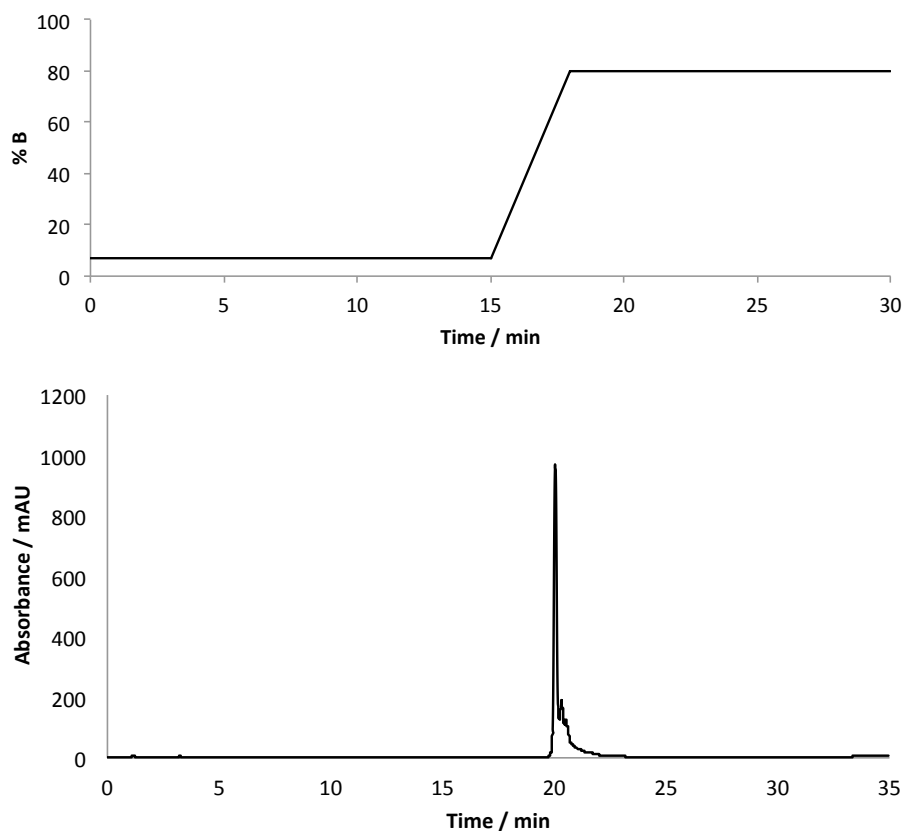


Figure III-F Top: solvent gradient used for separation, bottom: chromatogram of oligonucleotide d'(ATACATGCTACATA) irradiated in the presence of $[\text{Pt}(\text{N}_3)_2(\text{OH})_2(\text{py})_2]^{2+}$ for 5 h at 37°C with 420 nm. Separated using the above gradient A: NH_4OAc 10 mM H_2O , B: NH_4OAc 10 mM ACN), flow rate 1.00 mL / min, wavelength of detection 260 nm.

The Gradient shown in Figure III-F gives a better separation than the 80/80 gradient but still not complete resolution. The other options to improve resolution were: to change the stationary phase for one functionalised with a shorter carbon chain, e.g. C8; or to change the mobile phase. Increasing the concentration of ammonium acetate would increase ion suppression, sharpening peaks but reducing resolution. As such this would not be a useful strategy. The same can be said for decreasing the concentration as it is already quite low and reducing the ion suppression and causing the already quite broad peaks to broaden further. The most attractive option was to change the stationary phase to C8 as this could

increase the interaction of the analyte with the stationary phase and improve separation.

An 80/80 gradient was then run using a C8 column, shown in Figure III-G. A peak due to the unreacted oligonucleotide is observed and a shoulder attributable to the oligonucleotide with the adduct formed by photoactivated **8**.

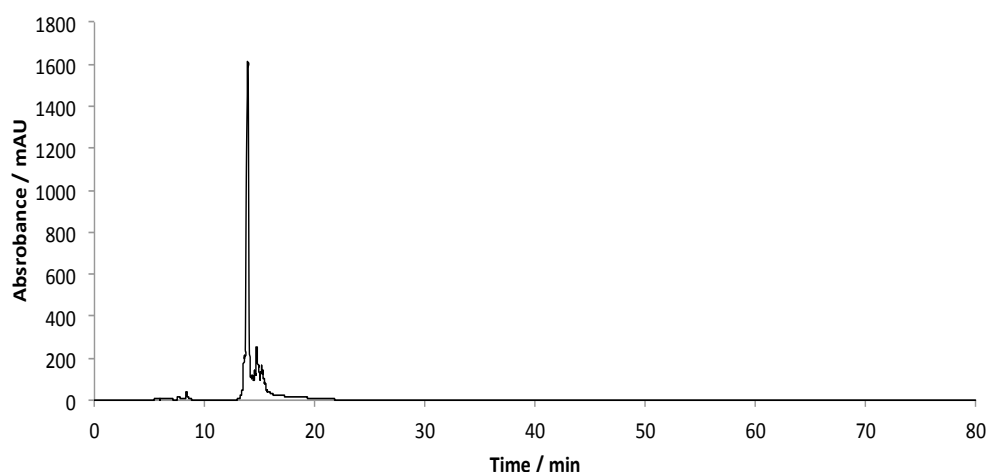


Figure III-G Chromatogram of the oligonucleotide d'(TATCATAAATAAATGGTATATTTATAACT) incubated with $[\text{Pt}(\text{NH}_3)_2(\text{H}_2\text{O})_2]^{2+}$ separated using a gradient from 0 – 80 %B; A: NH_4OAc 10 mM H_2O , B: NH_4OAc 10 mM ACN), flow rate 1.00 mL / min, wavelength of detection 260 nm, column thermostat 35°C.

A new gradient was then used to try to separate the shoulder from the peak, similar to that shown in Figure III-F. This gradient is shown in Figure II-H, and begins at 6% B remaining isocratic for some time. After which, B is increased by 9 % over 3 min with the intention of separating the two. The peaks appear to be resolved but there is another shoulder on the peak at around 19 min that is may be possible to resolve.

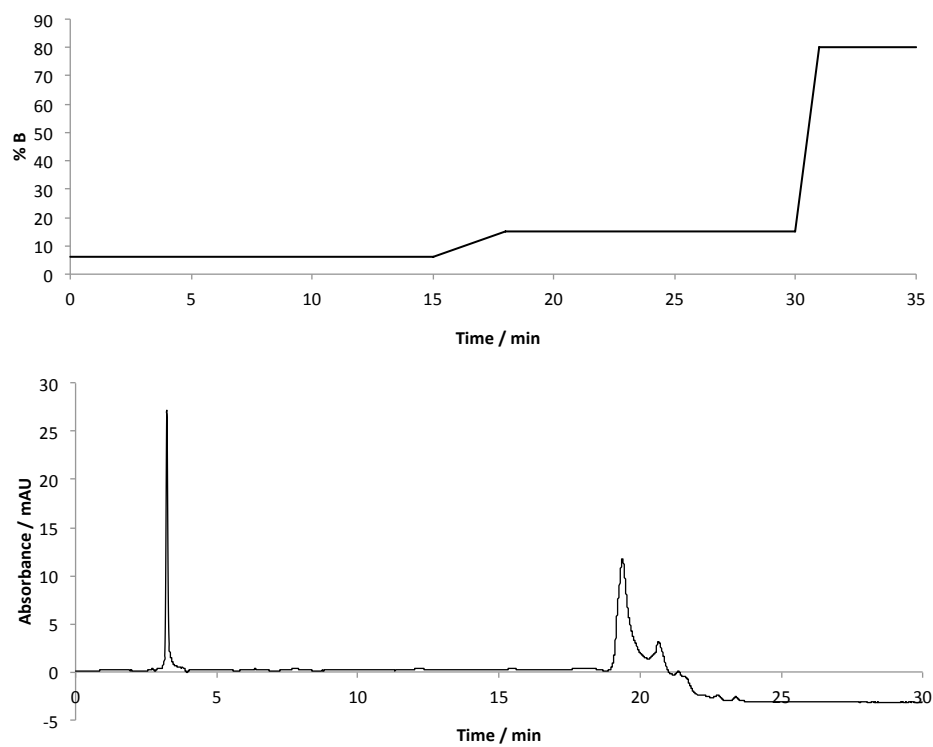


Figure III-H Top: gradient used for the separation shown below: chromatogram of oligonucleotide d'(ATACATGCTACATA) irradiated in the presence of $[\text{Pt}(\text{N}_3)_2(\text{OH})_2(\text{py})_2]^{2+}$ for 60 min at 37°C with 420 nm. Separated using the above gradient A: NH_4OAc 10 mM H_2O , B: NH_4OAc 10 mM ACN), flow rate 1.00 mL / min, wavelength of detection 260 nm.

The method was then altered many times to optimise this separation as far as possible, again adjusting the length of the isocratic period and the slope and extent of the gradient that followed. The temperature of the column thermostat was also increased to reduce the possibility of oligonucleotide folding, and hence improving the separation. The resulting optimised gradient is shown in Figure III-I and is the method outlined in Chapter 2, Section 2.2.2.4. However, there was not a very efficient transfer of heat to the analyte (as outlined previously in this appendix) and this may be the reason for the folded oligonucleotide structures observed in Chapter 2.

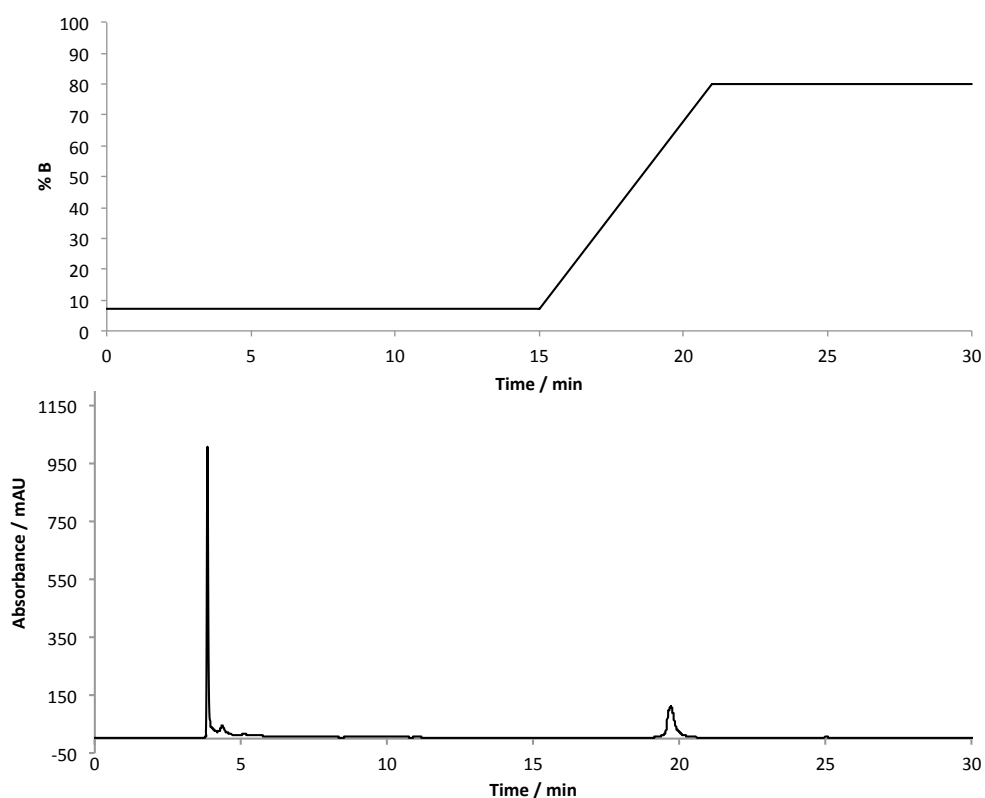


Figure III-I Top: gradient used for the separation shown below: chromatogram of oligonucleotide d'(ATACATGCTACATA) irradiated in the presence of $[\text{Pt}(\text{N}_3)_2(\text{OH})_2(\text{py})_2]^{2+}$ for 60 min at 37°C with 420 nm. Separated using the above gradient A: NH_4OAc 10 mM H_2O , B: NH_4OAc 10 mM ACN), flow rate 1.00 mL / min, wavelength of detection 260 nm.

Appendix III part C: oligonucleotide quality control (QC) procedure

The following are the quality control procedures carried out for all of the custom oligonucleotides detailed in this thesis.

Quantisation

UV-Vis spectroscopy

Using the Beer-Lambert law and a calculated molar absorption coefficient from Tataurov *et al.*⁶ the concentration of a solution of an oligonucleotide can be calculated. Here is an example of the dilution steps required to obtain a good UV-Visible spectrum for a 5 μM oligonucleotide synthesis in 1 mL DDW:

Total 1 in 400 dilution.

1 in 10 dilution of stock



1 in 10 dilution of previous stock dilution



1 in 4 dilution of previous solution (UV-Vis sample, ca. 5 μM)

Purity tests

HPLC

Using the Agilent 1100 series HPLC with a Rheodyne 7725i manual injector fitted with a 100 μL loop and a variable wavelength UV detector.

Mobile phase for all analyses: solvent A, H₂O 10 mM NH₄OAc (pH 5.5); solvent, B ACN 10 mM NH₄OAc.

Column PJS 54 (Zorbax eclipse C18 strong-bond 25 x 4.6 mm 5 µm particle size with a 300 Å pore)

Method folder: RM_2011

Method file: 3030

Flow rate 1 mL/min

Wavelength of absorption is 260 nm

Gradient: 0 - 30 % B over 30 min

Column oven temperature 40 °C

Sample:

45 µL injections of a ~ 1 in 150 dilution of the stock (ca. 16 µM)

Molecular mass confirmation

Mass Spectrometry

Analysis using the HCT Ultra (ion-trap)

Sample preparation

Perform a 1 in 10 dilution of stock (ca. 250 µM) for a total volume of 50 µL (ca. 25 µM). This solution is then diluted 1 in 2 in at least 80 mM NH₄OAc to give a total volume of 100 µL (ca. 12.5 µM). This solution then undergoes 5 cycles of Omix tip

desalting (adapted) protocol, eluting 20 μL each round. The resulting solution is then directly infused in to the MS without any further dilution.

Adapted Omix protocol (1 cycle)

1. Aspirate 100 μL of 50:50 ACN H_2O and discard, repeat.
2. Aspirate 100 μL of 40 mM NH_4OAc (in H_2O) and discard, repeat.
3. Aspirate 100 μL of sample and expel, repeat 4-5 times.
4. Change pipetting volume to 10 μL .
5. Aspirate 10 μL of 40 mM NH_4OAc (60:40 MeOH/ H_2O).
6. Dispense sample for analysis.
7. Repeat steps 2 – 6 for another 4 cycles.

References

1. D. Gjerde, D. J., Hanna, C. P., Hornby, *DNA Chromatography*, WILEY-VCH, Weinheim, Germany, 2002.
2. A. P. Silverman, W. Bu, S. M. Cohen, and S. J. Lippard, *J. Biol. Chem.*, 2002, **277**, 49743–49749.
3. A. Eastman, *Biochemistry*, 1983, **22**, 3927–3933.
4. Y. Wu, D. Bhattacharyya, C. L. King, I. Baskerville-abraham, S. Huh, G. Boysen, J. A. Swenberg, B. Temple, S. L. Campbell, S. G. Chaney, V. Recci, V. No, V. Re, M. Recci, and V. February, *Biochemistry*, 2007, **46**, 6477–6487.
5. A. Eastman, *Biochemistry*, 1986, **25**, 3912–3915.
6. A. V Tataurov, Y. You, and R. Owczarzy, *Biophys. Chem.*, 2008, **133**, 66–70.

